ULB Faculté des Sciences

Development of an Automated Assembly Line, DAQ Test Systems, and In-Beam Characterization of 2S Silicon Modules for the CMS Phase-2 Tracker Upgrade at the HL-LHC

Thesis submitted by Ali KHALILZADEH
in fulfilment of the requirements of the PhD Degree in Science
("Docteur en Sciences")
Academic year 2025-2026

Supervisor: Professor Pascal VANLAER
Co-supervisor: Professor Gilles DE LENTDECKER
Service de Physique des Particules Elémentaires
Interuniversity Institute for High Energies (ULB/VUB)

Thesis jury:

Prof. Simona Toscano (Université libre de Bruxelles, Chair)
Prof. Pascal Vanlaer (Université libre de Bruxelles, Secretary)
Prof. Gilles De Lentdecker (Université libre de Bruxelles)
Prof. Christophe Delaere (Université catholique de Louvain)
Prof. Fairouz Malek (Université de Grenoble Alpes)
Prof. Nicolas Pauly (Université libre de Bruxelles)
Prof. Laurent Thomas (Université libre de Bruxelles)
Prof. Michael Tytgat (Vrije Universiteit Brussel)

fnrs FREEDOM TO RESEARCH

Acknowledgement

Reaching the end of this PhD journey has been both a challenging and deeply rewarding experience. It would not have been possible without the support, guidance, and encouragement of many individuals and institutions. This section is a humble attempt to express my heartfelt gratitude to all those who contributed to the completion of these results and to my personal and professional growth throughout these years.

First and foremost, I would like to sincerely thank Pascal and Gilles, whose consistent support and mentorship were extremely valuable throughout my PhD journey. This thesis would not have been possible without your support and encouragement, for which I am deeply grateful. Your help, guidance, and efforts opened a new chapter in my life, and words fall short in expressing my appreciation. I am especially thankful for your support, time and constructive feedback and comments. It has been a great honor to learn from you, and my life has truly been inspired by your presence and guidance.

I am also thankful to the respected jury members for their time, thoughtful review, and valuable comments on this thesis.

A very special thanks goes to Martin. This thesis deserves an extra chapter just to thank you. Your help, guidance, and feedback have been exceptional. You were always available and supportive, generously dedicating your time to patiently explain everything in detail. I always enjoyed our conversations and learned so much from you. You truly brought color to this journey.

I also thank all the members of the Tracker group at the IIHE for their continuous support.

In the development of the DAQ system test firmware, I gratefully acknowledge the contributions of Stefano, Sara, and Fabio at CERN, and Jarne and Yifan in Belgium.

I express my sincere gratitude to the Fonds de la Recherche Scientifique - FNRS for their financial support throughout my PhD. Their contribution made this research journey possible.

I would like to thank my friends at IIHE for all the memories we shared together, especially: Eliott, Felix, Franco, Goodwin, Hugues, Ilia, Katka and Marta. I am happy to have made a friend like Pierre and Pierre-Alexandre, whose kindness and support helped me immensely.

To my friends at CERN who supported me during my tracker DOC shifts especially Ivan and Lesya, thank you. I also appreciate Alexander and Erik for their constructive feedback.

Warm thanks go to Mojtaba and his family at CERN for their generous hospitality. I always enjoyed and benefited from our conversations.

I also want to thank Bugra, who always supported me at CERN and gave me

the opportunity to visit many experiments including CMS for the first time which meant a great deal to me.

I would like to thank the secretaries at the IIHE—Audrey and Sofie—for their help and support, as well as the IT team, whose assistance I could always count on.

To my dear friends in Belgium who supported me throughout this journey: Pegah, Amin, Sara, Safa, Mohammad, Mahya, Mehdi, Fatemeh, and Golnaz—your presence always gave me strength and comfort. Thank you.

Finally, Mostafa, I am so grateful to have had a supportive friend like you in Belgium. Your help and guidance began even before I arrived and continued throughout. I remember those early days when I frequently called you about everything, and even later, when I sometimes disturbed you late at night. You and Shiva, with your warmth and kindness, made me feel at home.

Lastly, I would like to express my deepest gratitude to my family. Though physically distant, their unwavering love, care, and encouragement were always with me and sustained me during this long and challenging journey.

Contents

Acronyms

ADC Analog to Digital Converter. (Page 115, 116, 120, 126, 128, 130, 176)

AlCF Aluminum-Carbon Fiber. (Page 67–72, 74, 75, 77, 78, 80, 81, 90–92, 130–133, 144)

AMC Advanced Mezzanine Card. (Page 178, 179)

BER Bit Error Rate. (Page 171, 172, 175, 203–207, 209, 213)

BX bunch crossing. (Page 52, 56, 57, 60, 61, 142, 147, 163)

CBC CMS Binary Chip version 3.1. (Page 49–51, 54–62)

CIC Concentrator Integrated Circuit. (Page 49, 56, 58–63)

CMS Compact Muon Solenoid. (Page 3, 4, 7, 8, 10–13, 18–22, 25, 27, 28, 30, 31, 34, 42–44, 211, 212)

CSC Cathode Strip Chambers. (Page 19–21, 29)

DAQ Data acquisition. (Page 4, 13, 18, 21, 65, 83, 85, 141, 171–173, 178, 180, 181, 184, 209, 213)

DDMI Digital Diagnostic Monitoring Interface. (Page 171, 172, 176, 178, 181–184, 186, 196, 203, 208, 209, 213)

DLL Delay Locked Loop. (Page 52, 53, 58, 167, 168)

DT Drift Tubes. (Page 19–21, 29)

DUT Device Under Test. (Page 135, 139, 140, 144–168)

ECAL Electromagnetic Calorimeter. (Page 16, 17, 28)

FEH Front-End Hybrid. (Page 30, 31, 67, 68, 71, 79–81, 192)

FWHM Full Width at Half Maximum. (Page 104, 106, 113, 147)

GCT Global Calorimeter Trigger. (Page 21)

GEM Gas Electron Multipliers. (Page 19, 20, 29)

HCAL Hadron Calorimeter. (Page 16, 17)

HGCAL High Granularity Calorimeter. (Page 28, 29)

HL-LHC High-Luminosity LHC. (Page 3–5, 7, 21–25, 27, 29, 32, 43, 45, 65, 145, 172, 211, 213)

HLT High-Level Trigger. (Page 20, 21, 29)

I2C Inter-Integrated Circuit. (Page 12, 173, 176, 182, 183, 185)

IIHE Interuniversity Institute for High Energies. (Page 4, 5, 73, 87, 144, 148, 149, 172, 211–213)

LC Lucent Connector. (Page 187, 189, 190)

LDD Laser Diode Driver. (Page 172, 174–176)

LHC Large Hadron Collider. (Page 3–5, 7, 8, 10, 21, 22)

lpGBT Low Power Gigabit Transceiver. (Page 49, 58–60, 63, 64, 172, 173, 203, 204)

MIP Minimum Ionizing Particles. (Page 38, 39, 43, 166)

MPA Macro Pixel ASIC. (Page 30, 31, 58, 59, 61, 62)

OMA Optical Modulation Amplitude. (Page 175, 192, 194)

OPL Optical Path Length. (Page 197, 199)

ph2acf Phase-2 Acquisition and Control Framework. (Page 184, 190, 191, 203, 208)

PI Polyimide Isolators. (Page 67–71, 74, 75, 77, 83)

PRBS Pseudo Random Binary Sequence. (Page 175, 203)

ROSA Receiver Optical Sub-Assembly. (Page 172, 175, 176, 186)

RPC Resistive Plate Chambers. (Page 19–21, 29)

RSSI Received Signal Strength Indicator. (Page 174, 193, 196, 197, 200, 208, 209)

SCL Serial Clock. (Page 183)

SCR space charge region. (Page 41–43, 157)

SDA Serial Data. (Page 183)

SEH Service Hybrid. (Page 31, 67, 68, 71, 79, 172, 173)

SFP Small Form-factor Pluggable. (Page 172, 173, 175, 176, 178, 180, 182–186, 189–191, 196, 200, 201, 203, 208)

SiPMs silicon photomultipliers. (Page 28)

SPS Super Proton Synchrotron. (Page 137–139)

TIA Trans-Impedance Amplifier. (Page 65, 172, 174–176)

TOSA Transmit Optical Sub-Assembly. (Page 172, 174–176, 186)

uDTC micro Data, Trigger and Control. (Page 180–182, 184, 208)

UPC Ultra Physical Contact. (Page 187, 190)

V_{CTH} Comparator Threshold. (Page 142, 144, 147, 155, 157, 160–164, 166, 170)

VCSEL vertical-cavity surface-emitting laser. (Page 65, 66, 172, 174, 196, 200, 201, 209, 213)

VTRx+ Versatile Transceiver plus. (Page 30, 49, 63, 65, 82, 83, 171–175, 186, 190, 192–197, 199–201, 203–205, 208, 209, 213)

Chapter 1

Introduction

The Large Hadron Collider (LHC) at CERN is the largest particle physics facility in the world and one at the forefront of high-energy physics research, aiming for new insights into the structure of matter and enabling major discoveries such as the Higgs boson. To further expand our understanding of fundamental interactions and to search for new physics beyond the Standard Model, the LHC is undergoing a significant luminosity upgrade known as the High-Luminosity LHC (HL-LHC). This upgrade aims to increase the instantaneous luminosity of proton-proton collisions to about 5×10^{34} cm^{-2}s^{-1}, with possible future upgrades reaching up to 7.5×10^{34} cm^{-2}s^{-1}. By the end of the HL-LHC's program, integrated luminosities of $3000 - 4000 fb^{-1}$ are expected—about ten times higher than the original design goal of the LHC.

This increase in luminosity will allow more collisions to be recorded, improving the statistical accuracy of measurements and increasing the chances of discovering new particles and rare processes. However, the number of interactions per bunch crossing will also rise, often exceeding 140-200 simultaneous collisions. This makes detector design and data processing much more complex. Therefore, existing detectors need major upgrades to maintain their performance and to remain radiation-hard under these extreme conditions.

The Compact Muon Solenoid (CMS) experiment, one of the four main detectors at the LHC, has played a key role in many important discoveries and precise measurements. As the HL-LHC era approaches, the CMS detector requires significant upgrades to handle the higher collision rates and radiation levels. One of the most important upgrades involves the tracker subsystem—the part responsible for reconstructing the paths of charged particles produced in collisions.

The Outer Tracker upgrade project aims to replace the current silicon-based tracker with a new architecture that provides better spatial resolution, a lower material budget, greater radiation tolerance, extended acceptance and the ability to participate in the Level-1 (L1) trigger system.

The Interuniversity Institute for High Energies (IIHE) in Brussels, uniting the particle physics groups of the ULB and VUB universities, is committed to being one of the seven centers responsible for assembling the 2S modules and will build, and fully test, about 1520 modules plus spares out of 13322 of the total Outer Tracker modules, together with colleagues from University of Antwerpen and University of Gent.

This PhD thesis focuses on multiple aspects of the 2S module assembly, including the development of the assembly line, quality assurance, characterization of the modules in a high-energy particle beam, and integration of optical diagnostic tools into the Data acquisition (DAQ) system.

When I joined the IIHE in 2019, only a very simple first prototype of the gluing robot was available. One of the key challenges identified early on successful module assembly was the need for reliable, high-precision measurement of the glue robot head's height relative to the sensor surface. I investigated two non-contact height measurement methods: one based on optical sharpness using image processing algorithms, and another using a triangular displacement laser sensor.

Another major task for our group was to establish a complete and consistent procedure for assembling a fully functional 2S module. I contributed by helping evaluate the performance of a full-size module prototype, assembled with close-to final components in an asynchronous particle beam. In addition, we gained valuable insights into how the module behaves under these unconventional conditions, which are particularly interesting for the MUonE experiment, that plans to use about 200 2S modules from the CMS production [1] and pre-commissioning of the CMS Outer Tracker for the HL-LHC with cosmic rays.

Furthermore, it is important to have diagnostic tools, in real-time during data taking, as well as at detector assembly centers for systematic studies and debugging the long-term behavior of the optical transceivers under high radiation conditions and low temperatures.

In the following each chapter is briefly summarized:

Chapter 2: LHC, CMS, HL-LHC, and Outer Tracker Upgrade
This chapter provides a summary of the HL-LHC project, its physics motivations, and the overarching goals of the CMS experiment and the Outer Tracker upgrade. It describes the design principles and technical requirements for the new CMS Outer Tracker, including an introduction to the layout and functionality of the 2S modules.

Chapter 3: Silicon Sensors for 2S Modules
This chapter reviews the fundamental physics of silicon sensors and the principles of charged particle detection. It includes a discussion on the properties of the silicon sensors used in the 2S modules.

Chapter 4: Readout Electronics of 2S Modules

The readout electronics of the 2S modules are introduced in this chapter. Their architecture, functionality, and roles in data acquisition and triggering are explained in detail.

Chapter 5: Mechanics of 2S Modules

This chapter describes the mechanical structure of the 2S modules and the assembly process carried out at IIHE. It discusses the adhesives, custom jigs, assembly procedures, and alignment tools used to ensure high mechanical precision and reproducibility.

Chapter 6: Non-Contact Height Measurement Techniques

The chapter outlines the requirements for precise height measurement of the glue robot head relative to the target surface during the assembly process. It presents two non-contact approaches that have been studied in this thesis—optical sharpness analysis and triangular displacement laser sensing. The chapter concludes with a justification for selecting the laser-based solution and describes its successful integration into the gluing robot system.

Chapter 7: 2S Module Performance in an Asynchronous Beam

This chapter details the experimental setup and methodology used during tests of the 2S modules in a beam where particles are not synchronized with the readout clock, unlike at the LHC. It presents the performance results—such as efficiency, occupancy, and cluster multiplicity—under different bias voltages and comparator thresholds. The chapter also examines the influence of asynchronous data-taking on module performance, offering insights relevant for future applications like the MUonE experiment.

Chapter 8: Digital Diagnostic Monitoring Interface

This chapter documents the architecture of the Digital Diagnostic Monitoring Interface (DDMI), including its hardware, firmware, and software components for the monitoring of the received and transmitted optical power. It presents measurements of optical power versus temperature, transient thermal responses, and bit error rates, demonstrating the effectiveness of the diagnostic tools for studying reliable communication within the optical readout chain.

Chapter 9: Conclusions and Outlook

The final chapter summarizes the main findings of this work in the context of the HL-LHC Outer Tracker upgrade. It discusses the overall impact of the tools and procedures developed, and outlines potential directions for further research and improvement within the tracker upgrade program.

Chapter 2

LHC, CMS and HL-LHC Upgrade

In this chapter, an overview of the LHC and the CMS experiment is presented. The general structure of the CMS detector, including its primary components such as the magnet system and the various subdetectors arranged from the innermost to the outermost layers, is described. The CMS trigger system, responsible for the real-time selection of events of interest, is also introduced. Subsequently, the HL-LHC project is explained. The motivation for this major upgrade is discussed. Following this, a brief overview of the various CMS subsystems that are planned to undergo upgrades in preparation for HL-LHC operations is provided. Finally, a detailed description of the upgrade of the CMS Outer Tracker is given.

2.1 LHC

The LHC[2] is the most powerful particle accelerator in the world. It was designed to expand our understanding of the fundamental elements of matter and the interactions between them. The LHC is located at the European Organization for Nuclear Research (CERN), located on the border between Switzerland and France near Geneva. It is in a circular tunnel with a circumference of 26.7 kilometers, approximately 100 meters underground.

The LHC started operation in 2009 [3]. Run 1 (2010-2012) was conducted at center-of-mass energies of 7-8 TeV[4], during which the CMS experiment collected an integrated luminosity of approximately 29.4 fb^{-1}[5], leading to the discovery of the Higgs boson in 2012. Following the upgrades performed during Long Shutdown 1 (2013-2015), Run 2 (2015-2018) increased the collision center-of-mass energy to 13 TeV and delivered an additional 163.6 fb^{-1}. This enabled more precise investigations of the Standard Model and improved searches for physics beyond the Standard Model. After Long Shutdown 2 (2019-2021), Run 3 started in 2022 at an increased collision center-of-mass energy of 13.6 TeV with higher beam inten-

sities. As of mid-2025, Run 3 has contributed a further 220.3 fb^{-1}. Consequently, the cumulative integrated luminosity delivered to CMS since the start of LHC operations amounts to approximately 413.3 fb^{-1}, as illustrated in Figure 2.1.

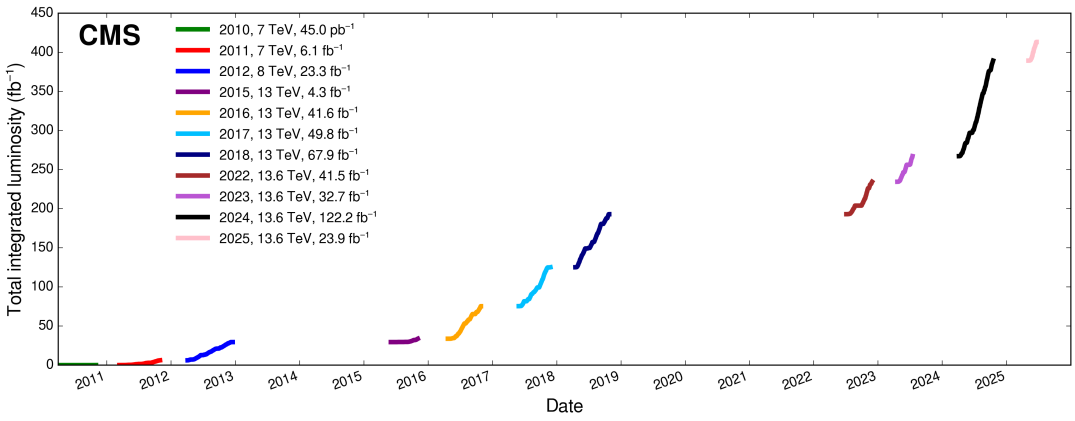

Figure 2.1: Integrated luminosity provided to CMS per day during stable pp collisions at the nominal center-of-mass energy[5].

The particle acceleration process begins with linear accelerators (LINAC), which deliver negative hydrogen ions at an energy of 160 MeV. Electrons are then removed from these ions, and the resulting protons are injected into the Proton Synchrotron Booster (PSB), where they are accelerated to 2 GeV. The protons then enter the Proton Synchrotron (PS) and are further accelerated to 26 GeV. They are then transferred to the Super Proton Synchrotron (SPS), where they reach 450 GeV before being injected into the LHC. In the main LHC ring, two counter-rotating beams are accelerated to a maximum energy of 6.8 TeV per beam during Run 3, using superconducting radio-frequency (RF) cavities operating at 400 MHz. Each beam contains more than 2,000 bunches of particles, with each bunch comprising approximately 1.1×10^{11} protons on the nominal operating conditions. The beams circulate in two separate beam pipes, located in a cryogenic chamber, and are guided by over 1,200 superconducting dipole magnets, each 15 meters in length, that generate magnetic fields up to 8.33 Tesla. These magnets operate at an ultra-low temperature of 1.9 K, cooled using liquid helium. In addition, more than 400 superconducting quadrupole magnets focus the beams to achieve optimal collision conditions. The beam pipes are maintained under an ultrahigh vacuum with pressures below 10^{-13} atm. The entire accelerator complex is synchronized with a sophisticated timing and control system. Figure 2.2 presents a schematic of the accelerator complex, highlighting its key subsystems and experimental setups.

The LHC hosts four major experiments, each designed for specific research

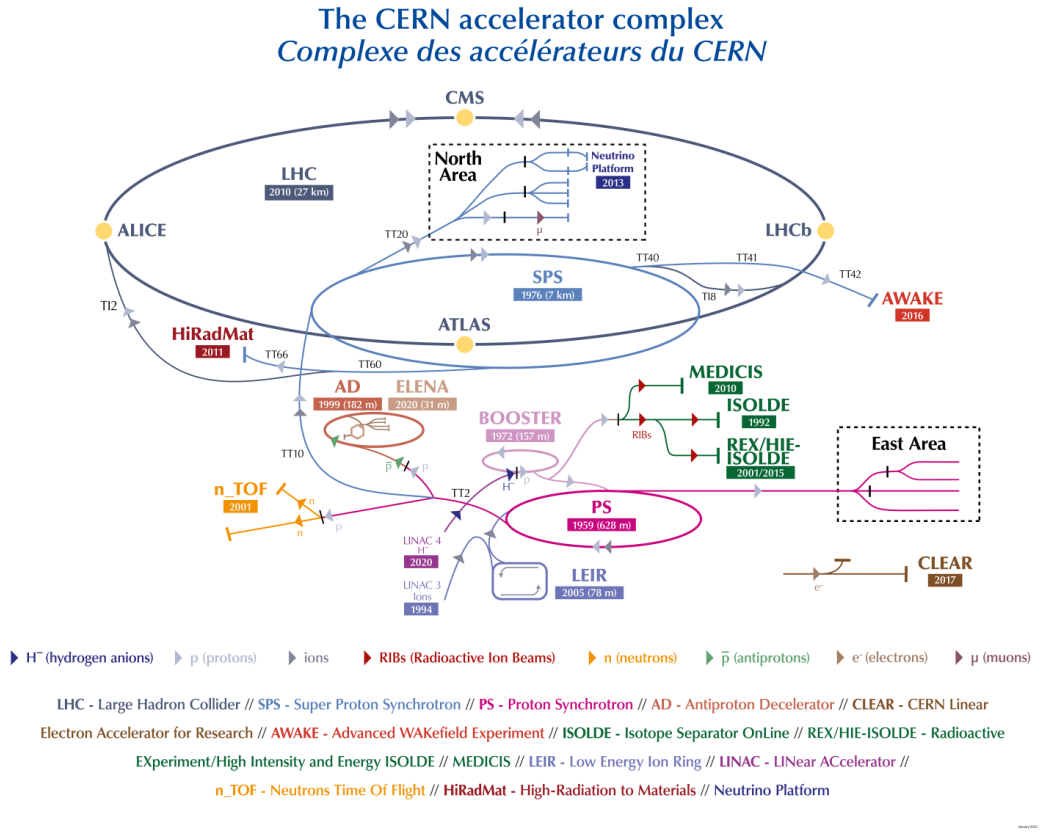

Figure 2.2: Schematic representation of the CERN accelerator complex, including its main subsystems and experimental facilities[6].

goals:

- **A Toroidal LHC ApparatuS (ATLAS) and CMS** are general-purpose detectors, designed to explore a wide range of physics phenomena, including precision tests of the Standard Model and beyond the Standard Model.
- **A Large Ion Collider Experiment. (ALICE)** focuses on the study of quark-gluon plasma in heavy-ion collisions.
- **Large Hadron Collider beauty (LHCb)** specializes in the study of b-quark.

The LHC represents a technical achievement and a global scientific collaboration, involving over 10,000 researchers from more than 80 countries. Beyond its contributions to fundamental physics, the LHC has guided multiple projects in scientific and industrial domains like superconducting magnet technology, cryogenics, RF engineering, large-scale data acquisition, and computing infrastructure, with broad applications in science and industry.

2.2 CMS

2.2.1 General view

The CMS detector is one of the largest experiments at CERN and was designed to study a wide range of physics phenomena[4]. It played a major role in the discovery of the Higgs boson in 2012. The schematic of the CMS detector is shown in Figure 2.3.

The CMS detector has a diameter of 15 meters, a length of 22 meters, and weighs approximately 14,000 tonnes. It consists of a superconducting solenoid magnet, various detector systems, and supporting mechanical structures.

The primary role of the superconducting solenoid magnet in the CMS detector is to generate a strong magnetic field that bends the trajectories of charged particles produced after each collision. By measuring this bending with the tracker detectors, the momentum of charged particles can be determined precisely through their curvature in the magnetic field. This measurement is essential for identifying particles and reconstructing their kinematic properties. The superconducting solenoid magnet[8] consists of four layers of cold-mass windings made from NbTi (niobium-titanium) conductors. When operated at a current of 18,164 A, it generates a magnetic field of 3.8 T. The magnetic flux is returned via five barrel wheels and six endcap yokes located outside the solenoid. The inner diameter of the magnet is 6 meters, and its length is 12.5 meters. The cooling system of the

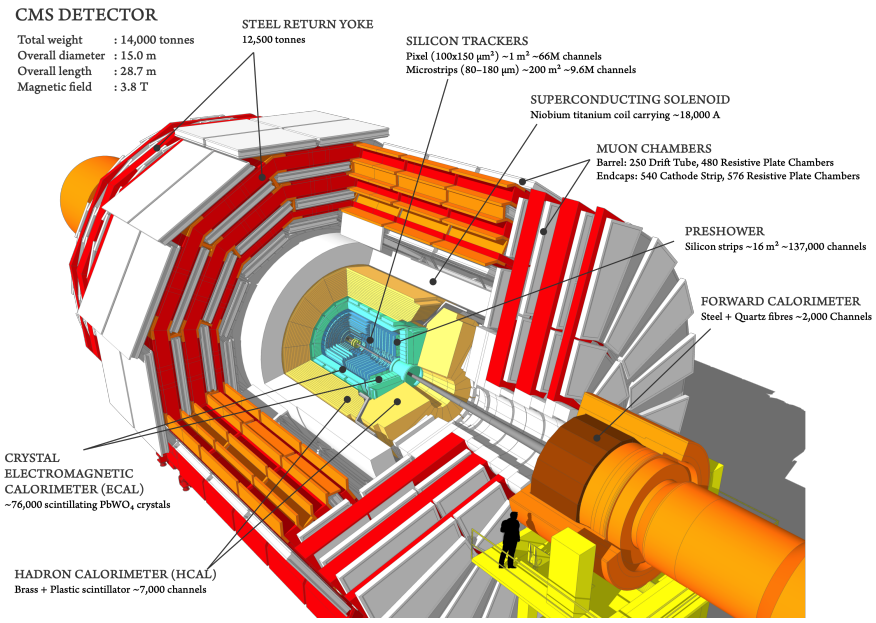

Figure 2.3: Schematic of CMS detector including different layers of detectors and the magnets [7].

superconducting magnet is based on liquid helium, and it takes approximately 4 hours to ramp up the magnet to its nominal field strength.

In the following sections, the different layers of the CMS detector and their characteristics will be discussed.

2.2.2 Tracker

The tracker is the innermost detector system of CMS, consisting of silicon pixel and silicon strip detectors. The schematic of one quadrant of the CMS tracker is shown in Figure 2.4. It provides precise position information of charged particles, which allows tracking of their trajectories and the reconstruction of primary and secondary vertices [4]. The current four-point tracking pixel detector was installed in 2017 as part of the Phase-1 upgrade program[9]. It consists of four barrel layers located at radii of 29 mm, 68 mm, 109 mm, and 160 mm from the beam pipe, and three endcap disks positioned at distances of 291 mm, 396 mm, and 516 mm from the detector center.

The pixel detector consists of the Pixel Barrel (BPIX) and the Pixel Forward (FPIX) Disks. Both BPIX and FPIX sensors use pixels with dimensions of 100 × 150 μm.

The Readout Chip (ROC) used in the CMS pixel detector is responsible for

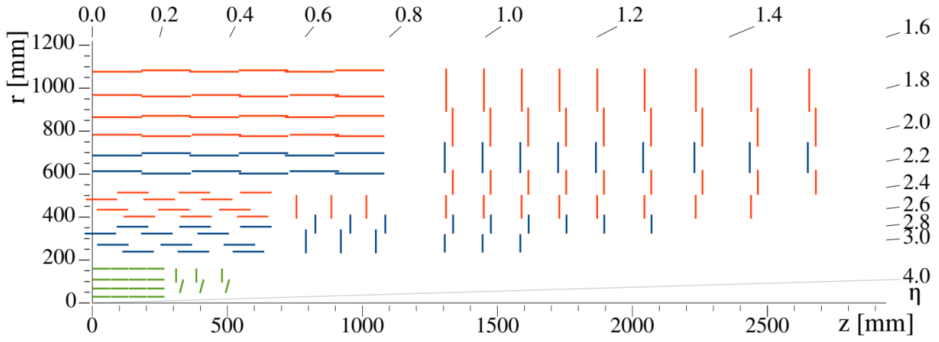

Figure 2.4: One quadrant of the CMS tracker is shown schematically in the r-z view. Single-sided strip modules are shown in red, while double-sided ones are shown in blue. The pixel detector is illustrated in green [4].

amplifying, discriminating, and digitizing the signals generated by the pixel sensors. Each ROC includes an array of pixel unit cells, analog front-end circuits, and buffers for temporary data storage during the trigger latency period (approximately 4 μs). The upgraded version of the ROC, known as psi46dig, provides digital output at a rate of 160 Mbit/s. The Token Bit Manager (TBM) controls the readout of the ROC modules. It distributes clock, trigger, reset, and Inter-Integrated Circuit (I2C) signals across the module and manages data flow by passing a readout token between ROCs. TMB transforms up to four 160 Mbit/s ROC data streams into one or two high-speed outputs (160 or 320 Mbit/s). Versions include single-core and dual-core TMBs, depending on module data rate requirements for the innermost layer (L1) or outer layers (L2-L4) and FPIX.

Each group of eight BPIX modules is mounted on a ladder made of Carbon-Fiber Reinforced Polymer (CFRP)[10]. These ladders are installed on service half-cylinders corresponding to each layer. By shifting slightly the ladders between smaller and larger radii, an overlap is created for continuous coverage. The FPIX modules are mounted on two concentric rings of half-disks, each tilted slightly to form a turbine-like mechanical structure. This arrangement also provides overlap between sensors.

The low-voltage supply for the pixel modules is delivered by DC-DC converters, which provide 2.4 V for the analog circuits and either 3.3 V or 3.5 V for the digital components. Each pair of converters serves between one and four pixel modules, depending on the configuration. The high-voltage (HV) supplies are independent and are provided by CAEN power supply modules. Due to the accumulation of radiation damage over time, the bias voltages of the CMS pixel detectors are progressively increased to maintain full depletion and charge collection efficiency. By the end of Run 3, the bias voltage is expected to reach its maximum value (800

V) for the innermost barrel layer (BPIX L1).

The readout system of the pixel detector is based on the FC7 board, which transfers data at a rate of 10 Gb/s via an optical network to the DAQ system. In the DAQ, pixel hit information is decoded by Front-End Driver (FED) modules. Slow control of the detector is managed by Front-End Controller (FEC) modules, while clock and timing signals are distributed by AMC13 cards.

The strip detectors are located outside the pixel detectors, extending from a radius of approximately 20 cm to 1.1 m, with a total length of about 5 m. The Pixel and strip detectors provide coverage up to $|\eta| < 3.0$. The barrel tracker consists of four inner layers (TIB) composed of 300 μm-thick modules and six outer layers (TOB) made of 500 μm-thick modules, all positioned parallel to the beam pipe. Adjacent to the TIB on each side are three disks, each comprising three concentric rings of modules with the same 300 μm thickness. On both ends of the barrel tracker, the endcap detectors (TEC) are positioned, each consisting of nine disks. Each disk is structured from four to seven rings of modules. The first four rings (when present) use 320 μm-thick modules, while the remaining rings use 500 μm-thick modules. From Disk 4 onward, the number of rings decreases, as the inner rings are progressively omitted.

Certain modules of strip detectors are made of two independent single-sided modules glued together back-to-back (double-sided modules) with a 100 mrad rotation respect to each other which allows full space determination[11]. These double-sided modules are installed in the first two layers of the TIB and TOB, in the first two TID rings, and in rings 1, 2 and 5 of the TEC structure.

The detectors used are p-on-n microstrips, with pitch sizes ranging from 80 μm to 205 μm depending on the sensor. A carbon-fiber frame supports the modules, which include the front-end hybrids and one or two sensors depending on the location, while a layer of Kapton isolates the silicon sensors and provides both bias voltage to the sensor backplane and efficient thermal handling [12].

The readout system uses APV25 chips to amplify, shape, and store signals from 128 strips at 40 MHz. Signals are multiplexed, converted to optical form by Analog Opto-Hybrids (AOH), and sent to FEDs for digitization and data processing. Control and configuration are managed by FECs and Communication and Control Units (CCU), while power groups supply regulated low (1.25 V and 2.5 V) and high voltages (up to 600 V) to the modules.

The cooling system is based on evaporative CO_2 and uses a network of thin-walled stainless steel pipes routed within the detector volume. To suppress leakage current and prevent thermal runaway caused by radiation damage, the cooling system operated the strip tracker at $-20°C$ during Run 3, gradually decreasing the temperature to $-25°C$.

Despite aging and radiation-induced effects, the CMS tracker has maintained

excellent performance, as will be discussed in the following section. The performance results are based on data collected during Run 3 in 2024 from proton-proton collisions at a centre-of-mass energy of 13.6 TeV[13], Otherwise, it will be mentioned.

Approximately 95% of the detector modules were operable during Run 3. The hit efficiency is presented in Figure 2.5 for various layers of the TIB and TOB as a function of instantaneous luminosity [14]. The efficiency was reported to be greater than 99% for the typical instantaneous luminosity of $1.11 \times 10^{34}\ cm^{-2}s^{-1}$.

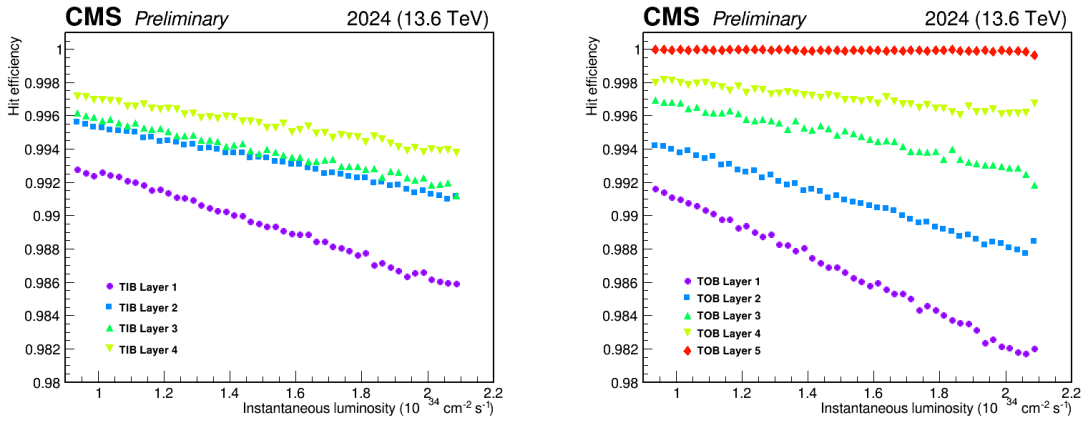

Figure 2.5: Left: Hit efficiency as a function of instantaneous luminosity in different layers of TIB and right, in different layers of TOB[14].

The signal-to-noise ratio (S/N) as a function of the integrated luminosity is shown in Figure 2.6 for different layers of the strip tracker. A gradual decrease in S/N is observed with increasing integrated luminosity, reflecting the effects of accumulated radiation damage. Extrapolating the observed trend, the signal-to-noise ratio (S/N) by the end of Run 3 (at an integrated luminosity of 500 fb^{-1}) is expected to reach approximately 12 for thin sensors and 18 for thick sensors, which remains sufficient for the tracker to continue collecting data effectively.

The evolution of the leakage current per cubic centimeter as a function of integrated luminosity (early Run 3) along the simulation data is shown in Figure 2.7 for various layers of TIB[15]. The data is scaled to $0°C$. An increasing trend is observed, consistent with cumulative radiation exposure. This rise in leakage current increases the risk of thermal runaway. As expected, some detectors in the innermost layer of the TIB experienced thermal runaway by the end of Run 3 (at an integrated luminosity of 400 fb^{-1}). In addition, studies show that the detectors in Layer 1 of the TIB reached the inversion point by the end of LHC Run 2.

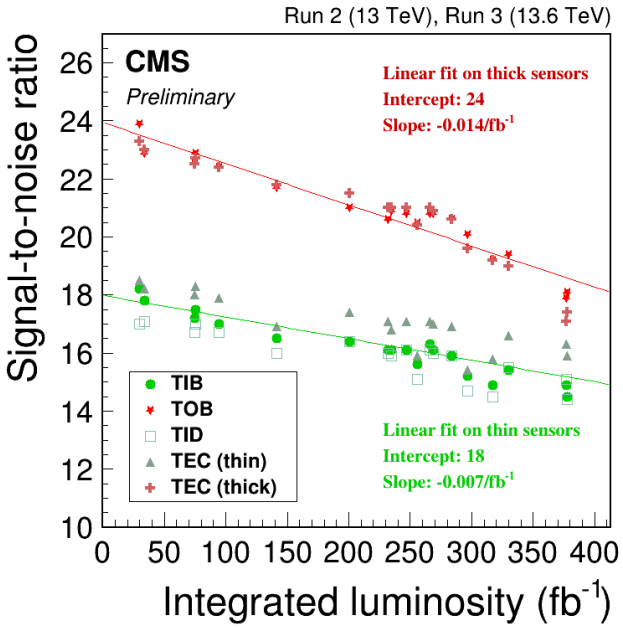

Figure 2.6: Signal-to-noise ratio as a function of integrated luminosity. Triangles show the results for TEC sensors with a thickness of 320 μm, and crosses show the results for 500 μm sensors[13].

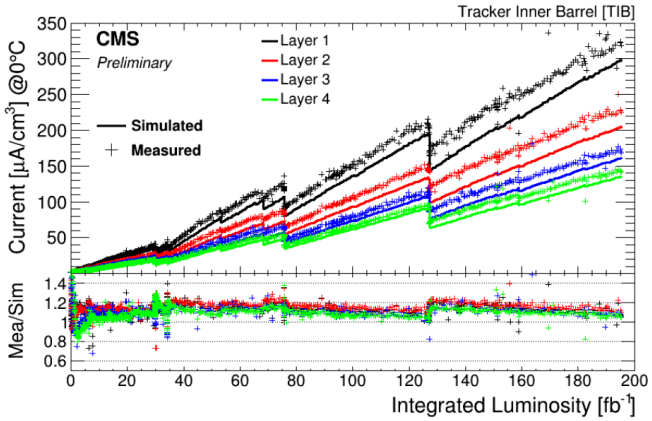

Figure 2.7: Leakage current per cubic centimeter in the TIB layers as a function of integrated luminosity, including simulation results. The data are normalized to 0 $°C$[15].

2.2.3 Electromagnetic calorimeter

After the tracker system, the preshower detectors are located. These consist of two planes of silicon sensors interleaved with layers of lead. Following the preshower detectors, the Electromagnetic Calorimeter (ECAL) is positioned. The ECAL is made of lead tungstate ($PbWO_4$) crystals[16], each with a depth of approximately 23 cm. It provides measurements of the energy, impact position, and arrival time of electrons and photons.

The ECAL comprises 61,200 crystals in the barrel region (EB) and 7,324 crystals in each of the endcap regions (EE), providing a pseudorapidity coverage of $|\eta| < 3.0$. These crystals are grouped into strips, each consisting of 5×1 crystals. The signals from the crystals are read out by photodetectors—specifically, avalanche photodiodes (APDs). Each strip is managed by an electronic chip called FENIX, which performs several functions: energy intercalibration, conversion of the deposited energy into transverse energy (ET), signal amplitude estimation, and assignment of the signal to the correct bunch crossing (BX). Five strips are then combined to form a trigger tower.

For each trigger tower, the FENIX chip also evaluates whether the observed energy corresponds to an actual electromagnetic shower or to a fake signal (spike) deposited directly in the APD. Spikes are rejected based on the signal distribution across the tower's cells and predefined thresholds, in order to prevent false triggers. Also, the rate of baseline updates (originally twice per year in 2018) was increased and applied periodically, which allowed the ECAL L1 trigger to operate with high efficiency.

Finally, the processed energy information is sent to the Trigger Concentrator Card (TCC), which gathers data from all regions of the detector and transmits it via optical links (through oSLB cards) to the central Level-1 (L1) calorimeter trigger system. There, it contributes to the global L1 trigger decision.

2.2.4 Hadronic calorimeter

After the ECAL, the Hadron Calorimeter (HCAL) detectors are located. The HCAL is designed to detect and measure hadronic jets and missing transverse energy (MET). The HCAL consists of four main sections: the Barrel Calorimeter (HB), the Endcap Calorimeter (HE), the Outer Calorimeter (HO), and the Forward Hadron Calorimeter (HF). In total, the HCAL consists of approximately 70,000 scintillating tiles. A schematic longitudinal view of the HCAL layout is shown in Figure 2.9. The structure and function of each section in addition to readout system are described below.

- **HB and HE:** The HB is located inside the solenoid magnet and covers the central region of the detector with pseudorapidity $|\eta| < 1.392$. It extends

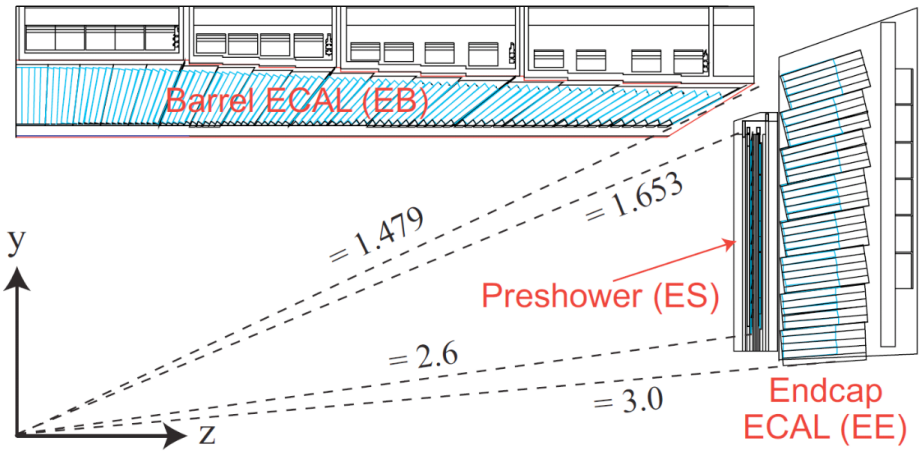

Figure 2.8: Schematic view of one quarter of the ECAL[17].

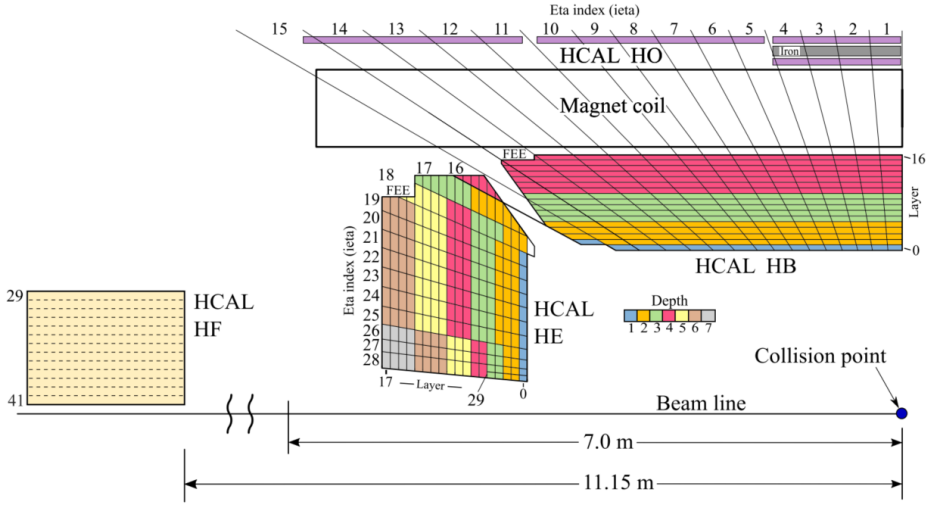

Figure 2.9: The HCAL is segmented longitudinally and transversely. Layers of the same color inside a tower connect to the same SiPM[4].

radially from 1.77 m to 2.95 m. The HE, positioned at the ends of the barrel, covers the region $1.305 < |\eta| < 3.0$. Both HB and HE are composed of alternating layers of brass (as the absorber material) and plastic scintillators. The number of layers varies between 17 and 18 depending on the η region. These layers form structures known as towers. Each scintillator tile is coupled with a Wavelength-shifting (WLS) fiber, which collects the scintillation light and transmits it to the Silicon Photomultipliers (SiPMs) for signal readout.

- **HO:** The HO is located outside the solenoid magnet and is designed to detect the tails of hadronic showers. It covers the region $|\eta| < 1.26$. This section uses steel as the absorber and the same type of plastic scintillators as in HB and HE. WLS fibers are placed in grooves carved into the scintillator tiles to collect the emitted light. These fibers transmit the light through pigtails and optical connectors to SiPMs.

- **HF:** The HF is located 11.5 meters from the interaction point on both sides of the detector and covers the high pseudorapidity region $3.0 < |\eta| < 5.2$. It has a cylindrical geometry with a radius of approximately 130 cm. The HF utilizes grooved steel as the absorber, with quartz fibers embedded in the grooves to detect Cherenkov radiation produced by relativistic charged particles. Two types of quartz fibers—with different lengths—are used to distinguish electromagnetic (e.g., electrons and photons) showers from hadronic showers based on the depth at which the signal is produced. The collected Cherenkov light is then guided to photomultiplier tubes (PMTs) for conversion into electrical signals.

- **Signal Readout and DAQ:** Once the optical signals are collected by the photodetectors, they are converted into analog electrical signals, which are subsequently digitized by frontend electronics equipped with Charge Integrator and Encoder (QIE) chips. These chips digitize signals via Analog to Digital Converter (ADC) and process signals. The digitized data, along with calibration and monitoring information, are transmitted via gigabit optical links to the underground service cavern. There, the data are received and analysed by the micro HCAL Trigger and Readout (μHTR) system. In the backend electronics, the AMC13 card collects data from multiple μHTR modules and transmits it to the CMS central DAQ system and the Level-1 trigger system. Additionally, the AMC13 card is responsible for distributing fast timing and control commands issued by the CMS Timing, Control, and Distribution System (TCDS).

2.2.5 Muon detectors

The outermost layer of the CMS detector contains the muon detection system[4], which is embedded within the steel flux-return yoke of the solenoid. These detectors span a wide range of pseudorapidity (η) and play an important role in the physics performance of CMS, particularly in muon identification and momentum measurement. Their signals are also essential components of the CMS trigger system. A schematic view of the muon detectors in the r-z plane of a CMS quadrant is shown in Figure 2.10. The muon system is composed of four types of gaseous detectors, all operating based on the collection of ionization electrons produced when charged particles pass through the detector medium: Drift Tubes (DT), Cathode Strip Chambers (CSC), Resistive Plate Chambers (RPC), Gas Electron Multipliers (GEM). Further details of each detector type are provided below.

- **DT:** The DT system is located in the barrel region of the CMS detector ($|\eta| < 1.2$). It consists of drift chambers with rectangular cells filled with a gas mixture of Ar and CO_2. These chambers provide precise spatial resolution ranging from 80 to 120 μm and deliver both tracking and trigger information. The DT system is optimized for operation in the relatively low magnetic field and low particle flux conditions of the barrel.

- **CSC:** CSCs are used in the endcap regions, covering $0.9 < |\eta| < 2.4$. Each CSC is a proportional chamber containing multiple anode wires oriented perpendicular to cathode strips, which are arranged in the (R-ϕ) geometry. They are filled with a gas mixture of Ar, CO_2, and CF_4. CSCs offer both precision position measurements, with spatial resolution between 40 and 150 μm, and trigger information. Their design is well-suited for the high magnetic field and particle flux found in the endcaps.

- **RPC:** The RPC system is deployed in both the barrel and the endcap regions. These detectors are double-gap chambers operated in avalanche mode, providing fast timing and aiding in the bunch crossing identification necessary for the Level-1 trigger. Although their spatial resolution is lower than that of DTs or CSCs, RPCs complement the muon system by offering excellent time resolution. They are filled with a gas mixture consisting of $C_2H_2F_4$, $i-C_4H_{10}$, and SF_6.

- **GEM:** GEM detectors are advanced micro-pattern gaseous detectors that have recently been added to the CMS muon system (LS2, 2019-2021). They are located in the endcap regions, specifically in front of the inner rings of the CSC chambers. Each GEM detector consists of four gas gaps separated by three GEM foils, which are perforated insulating polymer sheets coated with conductive material on both sides. They operate with an Ar and CO_2

gas mixture. GEM detectors provide both excellent spatial resolution and rapid signal response, enhancing the performance of muon identification and triggering in high-rate environments.

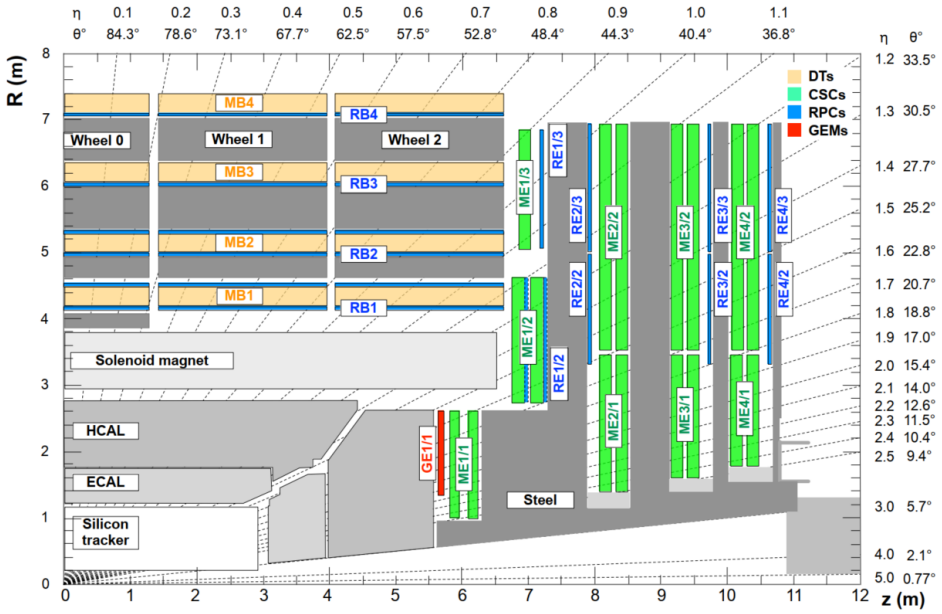

Figure 2.10: Schematic view of a CMS detector quadrant. The positions of the different muon stations are indicated by color in the image. In the labeling convention, M stands for Muon, B for Barrel, and E for Endcap. The detector technologies are color-coded as follows: DTs are shown in orange, CSCs in green, RPCs in blue, and GEMs in red[4].

2.2.6 The trigger system

The rate of collisions and data production at CMS is extremely high, requiring a large storage capacity. Since only a small fraction of the data—typically those involving high-energy particles such as electrons, muons, taus, photons, missing transverse energy, or jets— we are mostly interested in, and the background must be efficiently rejected. To achieve this, CMS employs a two-level trigger system[18]. The first level is the Level-1 (L1) Trigger, which is hardware-based and very fast. The second level is the High-Level Trigger (HLT), which runs more complex software algorithms. These triggers reduce the event rate from the initial 40 MHz down to approximately 100 kHz after the L1 trigger, and to the order of a few kHz after the HLT.

The input to the L1 trigger is provided by the calorimeters and muon detectors. The first stage of data received by the L1 trigger from these detectors is called Trigger Primitives (TP). These TPs are used to reconstruct physics objects, which are then evaluated to determine whether an event should be passed on to the next trigger level. The calorimeter system sends TP data to the Regional Calorimeter Trigger (RCT). The RCT finds interesting regions and looks for particles. The Global Calorimeter Trigger (GCT) combines data from the RCT and sends the results to the Global Trigger.

RPC hits are sent to the Pattern Comparator, which compares them to predefined patterns to help identify muons. DT and CSC hits go to segment finders, which find small parts of muon tracks. Then, the segment finders pass data to track finders, which look for full muon tracks. The Global Muon Trigger collects muon tracks from the DT, CSC, and RPC detectors. It makes a decision about muon candidates. The Global Trigger makes the final Level-1 trigger decision based on information from the GCT and the Global Muon Trigger. The full event data are stored in the pipelines of the detector readout systems. If the event is accepted, the decision signal is sent to the Timing, Trigger, and Control system (TTC), which forwards it to all sub-detectors to send the data to the counting room. The DAQ system collects the data and saves it for further processing.

All should be less than L1 latency ($\sim 4\ \mu s$). L1 latency must be less than the front-end electronics' pipeline depth and also should be deterministic in time. A schematic of the L1 trigger system is shown in Figure 2.11.

In the HLT, the full detector event data are processed by flexible software algorithms that run on a computing farm. The HLT then makes the final decision on which events are selected for offline storage. The selected data are initially written to local disk storage. Subsequently, the data are transferred to computing centers, where another offline reconstruction is performed, and the data are archived permanently.

2.3 HL-LHC

To improve the precision of measurements of rare Standard Model processes and to explore physics beyond the Standard Model, it is necessary to increase the instantaneous luminosity. The HL-LHC program [3] aims to collide protons at a center-of-mass energy of 14 TeV and reach a peak instantaneous luminosity of 5-7.5×10^{34} $cm^{-2}s^{-1}$, with an average number of pileup events between 140 and 200. The LHC road map from 2011 to 2040, including the integrated luminosity and energy of collision, is shown in Figure 2.12.

The CMS and ATLAS experiments are expected to collect an integrated luminosity of 3000 to 4000 fb^{-1} over the period of the project life (10 years). To

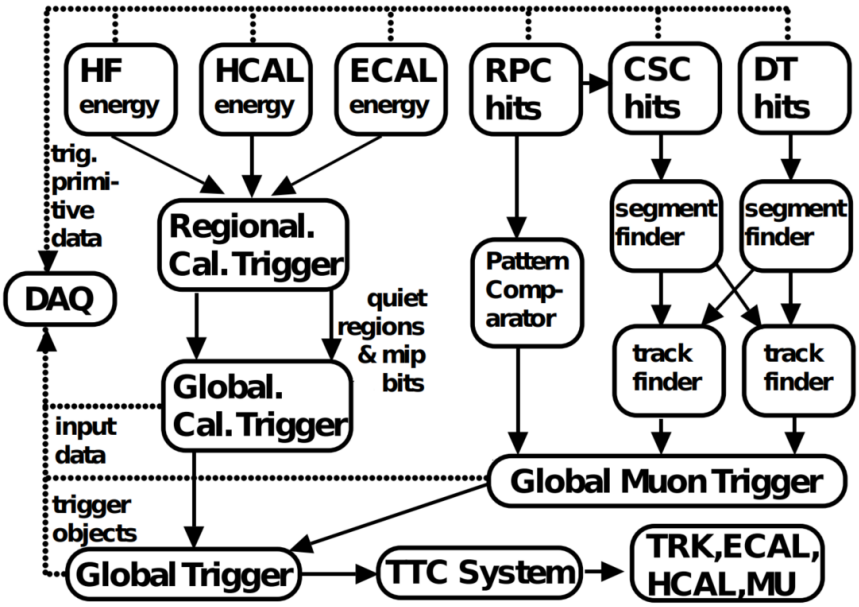

Figure 2.11: Schematic of the CMS L1 trigger system[18].

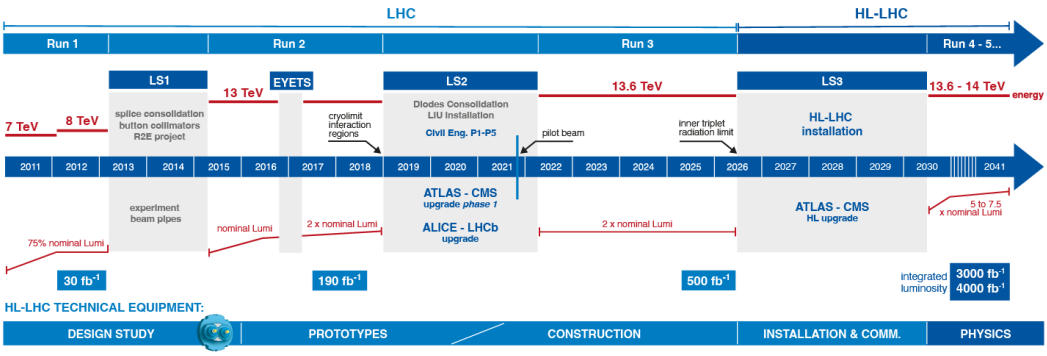

Figure 2.12: Planned operational schedule of the LHC from its beginning through the HL-LHC era[19].

achieve this performance and overcome the challenges, the LHC must undergo several upgrades[20] which will be discussed in the following section.

2.3.1 Physics motivation of the HL-LHC

The number of physics events increases with higher luminosity, thereby enhancing the potential to observe rare particles within the Standard Model (SM) as well as phenomena predicted Beyond the Standard Model (BSM).

Data from the HL-LHC are expected to significantly improve the precision of Higgs boson coupling measurements in the SM, particularly its coupling to light fermions such as muons[3]. Figure 2.13 illustrates the Higgs boson couplings to fermions and bosons as a function of their masses, including the associated uncertainties. The left plot shows results obtained with Run 1 data, while the right plot presents the projections for the HL-LHC at an integrated luminosity of 3000 fb^{-1}.

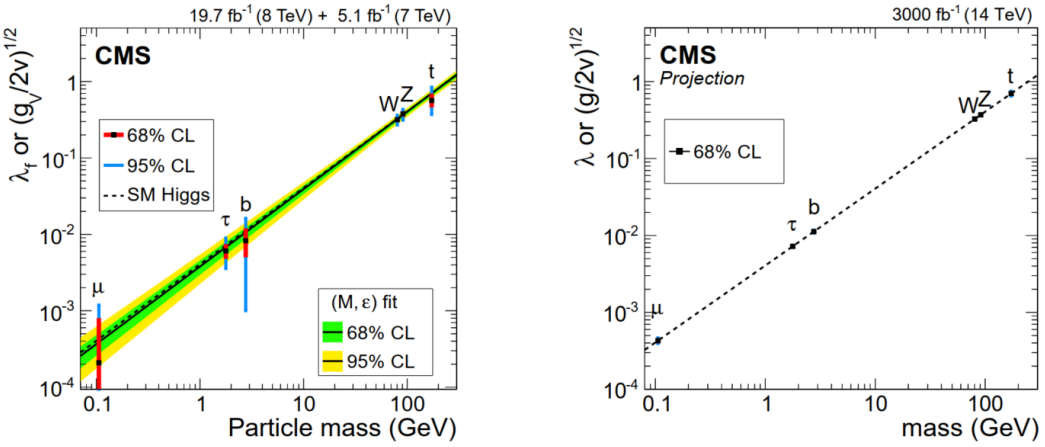

Figure 2.13: Higgs boson couplings to fermions and bosons as a function of their masses, including uncertainties. The left panel shows results from Run 1 data, while the right panel displays the expected precision at the HL-LHC for an integrated luminosity of 3000 fb^{-1}[3].

The decay $H \to \mu^+\mu^-$ offers the greatest potential for measuring the Higgs boson's coupling to second-generation fermions[3]. The di-muon invariant mass resolution is determined by fitting the $H \to \mu^+\mu^-$ spectrum in the range 122.5-127.5 GeV with a Gaussian. Figure 2.14 shows that the Phase-2 upgrade improves the resolution by about 65% thanks to reduced material and enhanced tracker precision. This leads to a projected 5% uncertainty on the Higgs-muon coupling, corresponding to a 10% precision on the cross-section measurement.

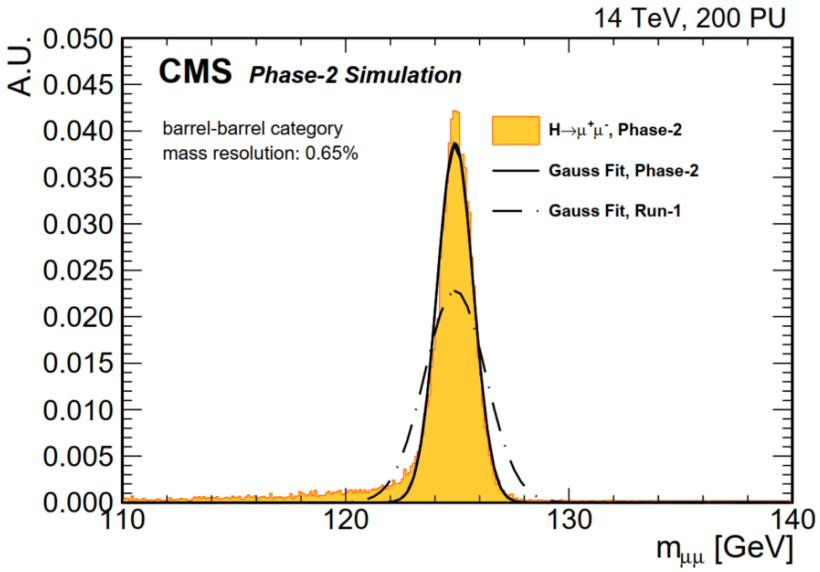

Figure 2.14: The invariant mass spectrum of central-region muons from $H \to \mu^+\mu^-$ decays is simulated with the Phase-2 detector for the central region[3].

Moreover, HL-LHC data will enable the measurement of the Higgs boson self-coupling, providing deeper insights into the Higgs potential. By defining the modified coupling κ_3 as the ratio of the Higgs self-coupling to its Standard Model prediction, one expects $\kappa_3 \approx 1$ within the SM [21]. Any significant deviation from unity would indicate possible new physics beyond the SM. Figure 2.15 shows the expected ATLAS+CMS likelihood scans of the Higgs self-coupling modifier for different decay channels and their combination, assuming $\sqrt{s}$ = 14 TeV, an integrated luminosity of 3 ab^{-1} per experiment, and the S3 scenario. This demonstrates that the HL-LHC will have sufficient sensitivity to directly probe the Higgs potential by measuring the trilinear self-coupling through double-Higgs production, with the 68% confidence interval given by $\kappa_3 \in [0.74, , 1.29]$.

To fully exploit these opportunities for rare processes and BSM physics at the HL-LHC, advanced detector capabilities are required, in particular improvements in the tracking system that enhance sensitivity to displaced signatures of long-lived particles.

Increasing luminosity will also allow the exploration of weak boson scattering channels with small cross-sections, which are essential to probe electroweak symmetry breaking and the role of the Higgs boson.

In addition, searches for BSM scenarios including supersymmetry (SUSY), extra spatial dimensions, and new heavy gauge bosons will be extended to higher mass scales at the HL-LHC, enabling the study of processes with very small cross-

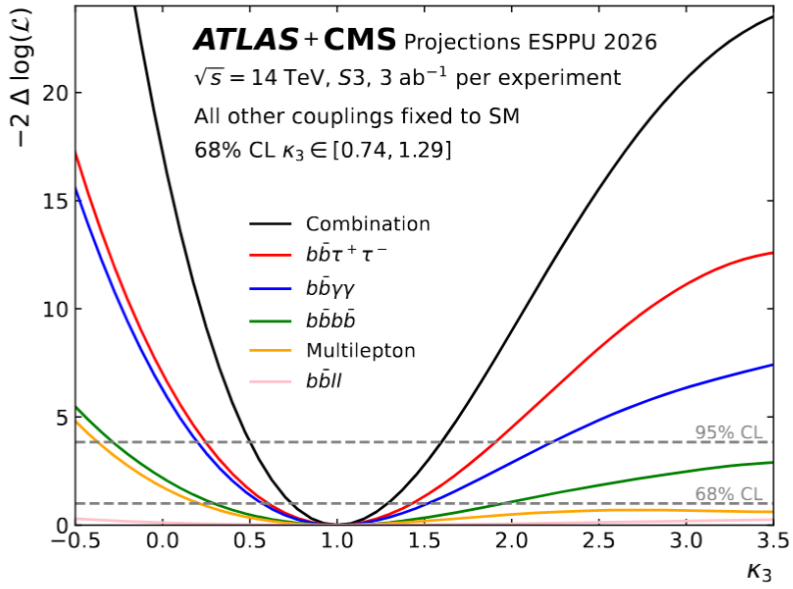

Figure 2.15: Expected ATLAS and CMS likelihood scans of the Higgs self-coupling modifier κ_3 for individual decay channels and their combination in the S3 scenario, assuming $\sqrt{s}$ = 14 TeV and an integrated luminosity of 3 ab^{-1} per experiment [21].

sections.

2.3.2 An overview of the LHC upgrade

One major upgrade is the installation of new triplet quadrupole focusing magnets[22] based on the Nb_3Sn superconductor. These magnets are more radiation-tolerant and can generate magnetic fields up to 12 Tesla, which is necessary for the final focusing of beams before collisions in the ATLAS and CMS detectors. They will replace the current NbTi-based magnets, which can only provide up to 8 Tesla.

New beam optics will also be introduced to help maintain a steady collision rate.

"Crab" cavities will be installed for both the ATLAS and CMS experiments. These devices give the particle bunches a small transverse kick just before collision, increasing the probability of collisions between particles.

The stored beam energy in the HL-LHC will be twice that of the current LHC. To protect the machine, additional collimators with better performance will be added or upgraded. These collimators will absorb particles that deviate from the beam path, preventing damage to the machine.

New crystal collimators will also be installed in the cleaning insertion to im-

prove cleaning efficiency during operation with ion beams.

In addition, the magnets require superconducting power lines to carry high direct current from the power supply systems. The new superconducting power lines, each about 100 meters long, are made of magnesium diboride (MgB_2). When cooled below 50 Kelvin using helium, these cables can carry currents up to 100 kA.

During Long Shutdown 2 (LS2), the injector chain, which pre-accelerates the beams before injection into the main LHC ring, was upgraded. Civil engineering work was also carried out, including the construction of new service tunnels near the ATLAS and CMS detectors to prepare for the HL-LHC era.

The high luminosity expected at HL-LHC will also introduce experimental challenges for both ATLAS and CMS, including high pileup and increased radiation levels.

In the following section, the CMS upgrade for HL-LHC will be discussed. This includes a detailed look at the Outer Tracker upgrade, with a specific focus on the 2S module.

2.3.3 An overview of the CMS upgrade

For the HL-LHC, the CMS detector is being upgraded to cope with higher radiation levels and more pileups (~ 140 to 200). One main focus is upgrading the Level-1 trigger system. To achieve this, the system will be updated to increase latency time (12.5 μs) to give more time to the L1 trigger to select events and increase its accept rate (750 kHz). This requires a complete replacement and redesign of the readout electronics inside the detector, with larger pipeline depth and faster data transfer.

The pixel detector, which is the closest to the collision point, will be completely replaced. The new detector will use much smaller (100×25) and thinner pixels (100-150 μm) to provide more precise tracking and to cope with high radiation (1.2 Grad) and data rates[23]. It will also cover a larger area along the beam direction to increase η acceptance, with more disks added at each endcap, which is illustrated in Figure 2.20. Additionally, the first layer of the Inner Tracker will be equipped with a new 3D pixel modules.

The strip tracker, which surrounds the pixel detector, will also be fully replaced with a new "Outer Tracker" that participate in the Level-1 trigger. The tracking system for the CMS not only contributes at the Level-1 trigger stage by improving event selection and background rejection, but also provides the capability to reconstruct displaced tracks from particles with relatively long lifetimes, which can arise in theories beyond the Standard Model. The extended L1 tracking examines trajectories that do not necessarily originate from the beamspot and is able to determine the transverse impact parameter (d_0) of the track. A significant

improvement in the track-finding efficiency is observed for particles with d_0 up to about ±5 cm, as illustrated in Figure 2.16. This part will be discussed in more

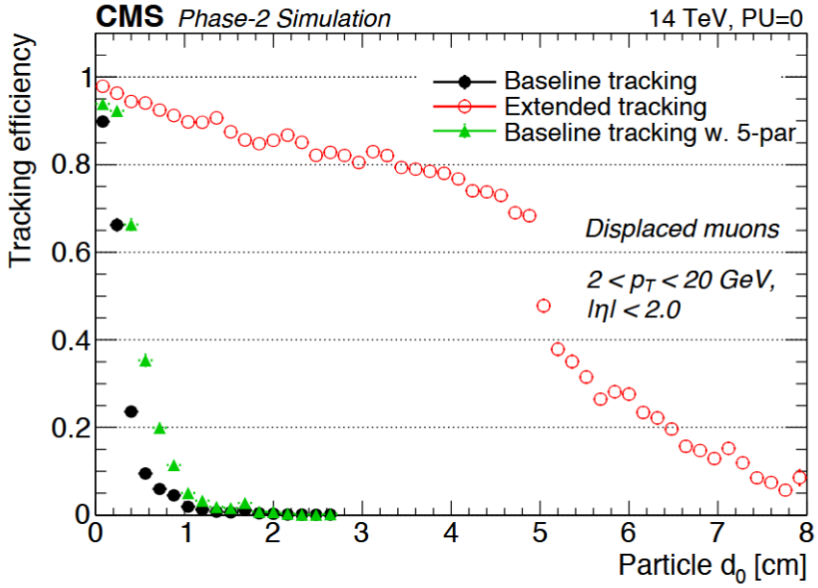

Figure 2.16: L1 tracking efficiency as a function of transverse impact parameter (d_0) for displaced muons with $2 < p_T < 20$ GeV and $|\eta| < 2.0$ in events without pileup. The extended tracking using triplet seeds (red) shows a significant improvement compared to the baseline algorithms (black, green) [24].

detail in section 2.3.4, where the advantages of both the inner tracker and the outer tracker, in terms of resolution and material budget, will also be presented.

A new detector, capable of measuring time with a resolution of a few tens of picoseconds, called the Minimum Ionizing Particle (MIP) Timing Detector (MTD), is included in the CMS upgrade plan[25]. Its purpose is to measure the time of arrival of charged tracks originating in the luminous region (approximately 5 cm and duration of the order of 200 ps). By utilizing the time coordinate to distinguish spatially overlapping vertices, it should be possible to reduce the line density of vertices in different time frames to a level comparable to the current one. This is made possible by determining the time of origin of charged tracks with an uncertainty approximately five times smaller than the 200 ps temporal spread of primary vertices in the luminous region. In addition, the MTD will enhance the study of long-lived and heavy stable charged particles by providing precise time-of-flight measurements, allowing discrimination of slow-moving, massive particles from relativistic backgrounds. This detector will cover both the barrel and endcap regions. The barrel section, covering the pseudorapidity range of $|\eta| < 1.45$, will be

installed between the tracker and the ECAL. It will be constructed from fast scintillators, specifically cerium-doped lutetium-yttrium oxyorthosilicate (LYSO:Ce), which will be read out using silicon photomultipliers (SiPMs). The endcap section will extend the coverage to $|\eta| < 3$ and will be equipped with Low Gain Avalanche Diode (LGAD) sensors. It will be installed between the endcaps of tracker and the High Granularity Calorimeter (HGCAL).

The electronics of the ECAL in the barrel region will undergo an upgrade, while the crystals and photodiodes will remain unchanged. The data sampling rate will be increased by a factor of 4 to enhance spike rejection at the Level-1 trigger stage and to improve the timing resolution for signals with energies greater than 50 GeV, achieving a resolution of approximately 30 ps[26]. Additionally, the operating temperature will be lowered from $18°C$ to $9°C$ to reduce noise caused by the dark current of the photodiodes, which is made worse by radiation effects. As part of the upgrade plan, each crystal will be read out individually and will contribute to the trigger system[27]. The endcap calorimeters will be replaced with a new detector known as the HGCAL, which is composed of 47 layers, including silicon sensors in high-radiation regions and scintillator modules equipped with SiPMs in lower-radiation areas. The HGCAL has more than 6 million read-out channels. This design enables the precise measurement of both transverse and longitudinal shower profiles, as well as high-resolution timing information which significantly improves object reconstruction, particle identification, and pileup mitigation in the forward region. The electromagnetic section of HGCAL utilizes absorbers made of copper, copper-tungsten, and lead, interleaved with layers of silicon sensor modules, while the absorbers in the hadronic section are made of steel. The silicon sensors are hexagonal in shape, with surface areas of 0.5 cm^2 in the innermost regions and 1.2 cm^2 in the outer regions[28]. The entire system will operate at a temperature of -35$°C$.

The muon detectors will stay mostly the same, since tests show they still work well even under HL-LHC conditions[29]. However, their front-end electronics will be upgraded to handle higher data rates, better resist radiation, and improved background rejection capabilities[30]. In the case of the DT and CSC detectors, some parts of the trigger logic will be moved to the back-end system to enhance flexibility and maintainability. The new DT electronics digitize full time-resolved signals, enabling better resolution for segment timing and improving background rejection. Upgraded CSC electronics include larger memory, higher bandwidth, and radiation-hard optical links. The RPC system, which helps detect muons, will also be upgraded. The legacy readout links are being replaced with a new system based on FPGAs and Time-to-Digital Converters (TDCs) with 2.5 ns resolution, enabling improved trigger timing performance. The RPC coverage will be extended to a larger area (up to $\eta < 2.4$), and new, improved RPC chambers (called iRPCs)

will be installed. These use different materials and designs to handle the harsher environment and offer better position and timing measurements. In addition to these, new Triple-GEM detectors will be installed in the forward region. These complement the CSCs and extend the muon system's pseudorapidity coverage to $|\eta| < 2.8$.

Following the upgrades, the average event size is expected to increase to approximately 7.4 MB [31], compared to 2 MB during RUN 3 [4] which is about 3.7 times larger than the current event size. The system must be capable of handling a data flow of several terabytes per second. The HLT will reduce this, but ultimately, around 5.3 petabytes of data per day [31] will need to be processed and stored.

2.3.4 Outer tracker upgrade

The status of the current tracker is described in Section 2.2.2. The current tracker has been designed for an integrated luminosity of up to 450 fb^{-1} maximum. In addition, a new readout system is required to overcome limitations in bandwidth and trigger latency caused by the high pileup environment at the HL-LHC.

The new Outer Tracker consists of two types of modules: 2S modules and PS modules. Images of both the PS and 2S modules are shown in Figure 2.17.

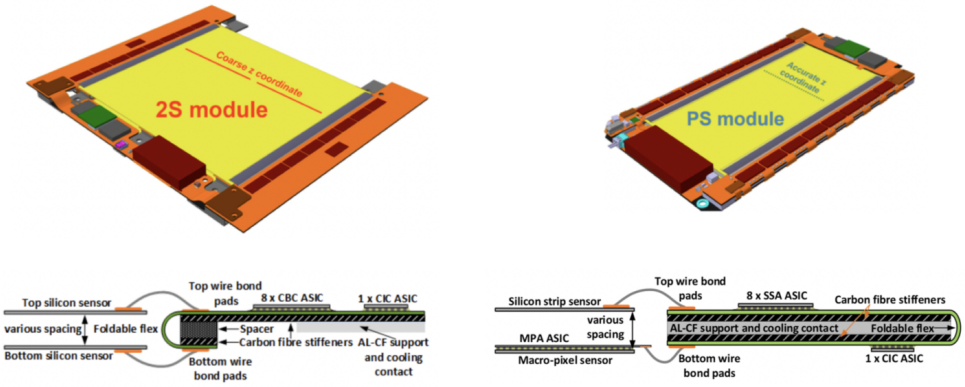

Figure 2.17: Image of 2S module (left) and PS module (right). In the bottom, corresponding Front-End Hybrid (FEH) schematic along section of sensors and wire bonds are shown[3].

Each 2S module is composed of two closely spaced microstrip sensors, each with a strip length of 5 cm and a pitch of 90 μm. The spacing between the sensors is maintained by high-precision ALCF spacers, available in two versions: 1.8 mm and 4 mm. These spacers provide mechanical stability and, due to their high thermal conductivity, also help dissipate heat generated within the module.

A more detailed discussion of the 2S module sensor specifications is provided in Chapter 3.

Each 2S module contains two FEHs, located on opposite ends of the sensors. Each FEH contains eight readout chips (CBCs), each of which reads signals from 127 strips on the top sensor and 127 strips on the bottom sensor. The CBC chips process the signals, format the data, and send them to the CIC. The CIC aggregates the data from all eight CBCs and transmits them to the Service Hybrid.

The Service Hybrid includes a DC-DC converter, a high-voltage distribution circuit, a Low Power GigaBit Transceiver (LpGBT), and an optical transmitter (Versatile Transceiver plus (VTRx+)) to transmit the data via optical fibers to the CMS trigger and data acquisition system. Further details regarding the electronics and readout architecture of the 2S module are presented in Chapter 4 while the mechanical design and assembly of the 2S module are discussed in Chapter 5.

The PS module consists of a macro-pixel sensor (PS-P) with a pixel size of 1.5 mm × 100 μm and a microstrip sensor (PS-S) with a strip size of 2.5 cm × 100 μm. These two sensors are closely spaced using AlN spacers, available in three configurations with gaps of 1.6 mm, 2.6 mm, and 4 mm.

In the PS module, the Strip Sensor ASIC (SSA) reads signals from 254 strip channels, while the Macro Pixel ASIC (MPA), which is bump-bonded to the macro-pixel sensor, reads signals from the pixel side.

Similar to the 2S module, the CIC on the FEH collects and formats stub and cluster data received from the MPAs and transmits this data to the readout Service Hybrid (SEH).

The PS module includes two service hybrids, placed on the two other sides of the module—one dedicated to power delivery and the other for data readout.

The electronics on the FEH are capable of performing correlation checks between the hits on two sensors to form a stub. At each bunch crossing, they transmit the stub data. When a strip or pixel collects a charge above a programmable threshold, it is marked as a '1' (hit), while others are marked as '0' (no hit). When a hit is detected in the seed sensor, a logic search is performed within a configurable acceptance window in the second sensor, at the corresponding position with a configurable offset, by the CBC (see Figure 2.18).

Due to the magnetic field of the CMS detector, charged particles bend in the transverse plane depending on their p_T. High-p_T particles pass through the module at nearly normal incidence and fall within the acceptance window, thereby forming a stub. In contrast, low-p_T particles are bent more and fall outside the acceptance window, resulting in no stub formation. The width of this window, along with the spacing between the sensors, determines the transverse momentum (p_T) range of the particles selected.

This stub-forming capability helps reduce the data volume and provides track-

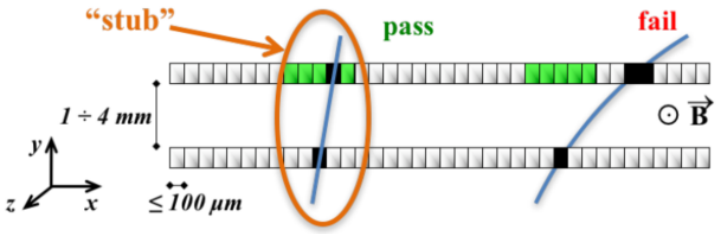

Figure 2.18: Depiction of the p_T module concept: Correlation of signals across two stacked positioned sensors facilitates the exclusion of particles with low transverse momentum (p_T). The channels highlighted in green serve as the criteria window for identifying an approved stub[3].

ing information directly to the Level-1 (L1) trigger at the full LHC bunch-crossing rate of 40 MHz.

Stub data from each module is sent to a hardware-based track-finding system for pattern recognition and track fitting. The maximum trigger rates are expected to reach 750 kHz for the L1 trigger and 7.5 kHz for the High-Level Trigger (HLT), with an L1 trigger latency of approximately 12.5 μs [3]. For comparison, the L1 trigger in the current system during Run 3 operated at 110 kHz, and the HLT at 5 kHz, with an L1 latency of approximately 4 μs [13].

The new sensor is based on n-type strips on a p-type bulk with an active thickness of 290 μm. This sensor design has been demonstrated to offer improved radiation tolerance [32]. It can maintain full efficiency up to an integrated luminosity of 3000 fb^{-1} when operated at 600 V, and still has the potential to collect charge and provide a measurable signal at 800 V in the ultimate luminosity scenario.

To keep the channel occupancy around or below the cent level for efficient tracking under high pileup conditions in the Outer Tracker, the granularity of the detector has been increased. By decreasing the pitch and increasing the channel density, the hit resolution has improved. The resolution of the tracking parameters is defined as the root mean square (RMS) of the differences between the reconstructed and simulated values. Figure 2.19 illustrates the resolution of the transverse momentum (left) and resolution of the transverse impact parameter (right) as a function of pseudorapidity for single muons with p_T = 10 GeV, comparing the Phase-2 Tracker to the current tracker. The improved hit resolution, together with the reduced material budget, leads to a significantly enhanced transverse momentum resolution.

The Outer Tracker detector designed for the HL-LHC consists of three cylindrical layers of PS modules, called TBPS, followed by three cylindrical layers of 2S modules, called TB2S, in the barrel section. This is complemented by five double-

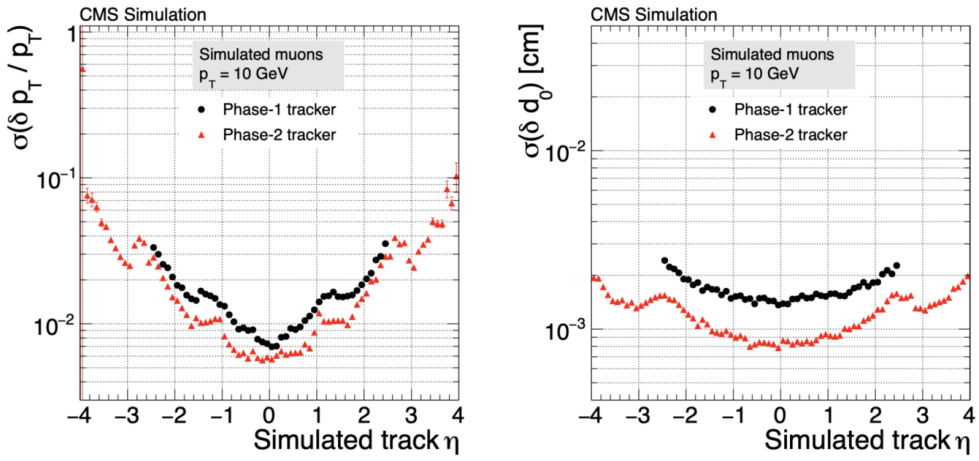

Figure 2.19: Comparison of the relative transverse momentum resolution (left) and resolution of the transverse impact parameter (right) as a function of pseudorapidity for the Phase-1 tracker (black dots) and the upgraded Phase-2 tracker (red triangles). For the simulation, single isolated muons with a transverse momentum of 10 GeV were used[3].

disc layers, known as TEDD, on each side of the detector endcaps. A schematic of a quarter of the tracker in the r-z view is shown in Figure 2.20. The TBPS layers are geometrically tilted as a function of pseudorapidity to ensure good hermetic coverage and improved trigger performance. Different sensor spacings are used in different regions of the detector to achieve a uniform level of transverse momentum discrimination. The tracker layout has also been extended to cover the forward region, thereby increasing tracking acceptance in high-$|\eta|$ areas and providing valuable information for physics analyses that rely on forward particle detection. In this new layout of outer tracker, all particles within the pseudorapidity range $|\eta| < 2.4$ intersect with at least six module layers, except for a small transition region between the barrel and endcap around $\eta = 1$, where the coverage drops to five layers.

The material budget in the new Outer Tracker has been significantly reduced, which minimizes multiple Coulomb scattering and reduces the production of secondary particles resulting from unwanted interactions such as photon conversions and hadronic interactions. These improvements lead to better energy and momentum resolution as well as enhanced tracking efficiency. This improvement is the result of several key optimizations, including a decrease in the total number of layers, a more efficient routing of services, a new lightweight support structure, a low-mass CO_2 cooling system, and an updated DC-DC converter architecture. The comparison between the material budget of the current tracker and that of

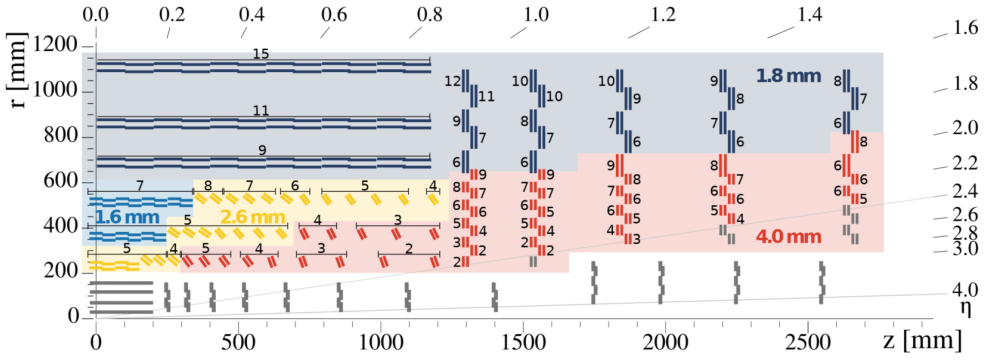

Figure 2.20: The 2S modules come in two types: one with sensors 1.8 mm apart and another with sensors 4.0 mm apart. In the tracker diagram, these sections are marked in dark blue and red respectively. The PS modules also have three types: with sensors 1.6 mm, 2.6 mm, or 4.0 mm apart. These are shown in light blue, yellow, and red. Numbers near these modules explain acceptance windows for selecting particles with $p_T > 2GeV/c$[3].

the HL-LHC tracker is presented in Figure 2.21.

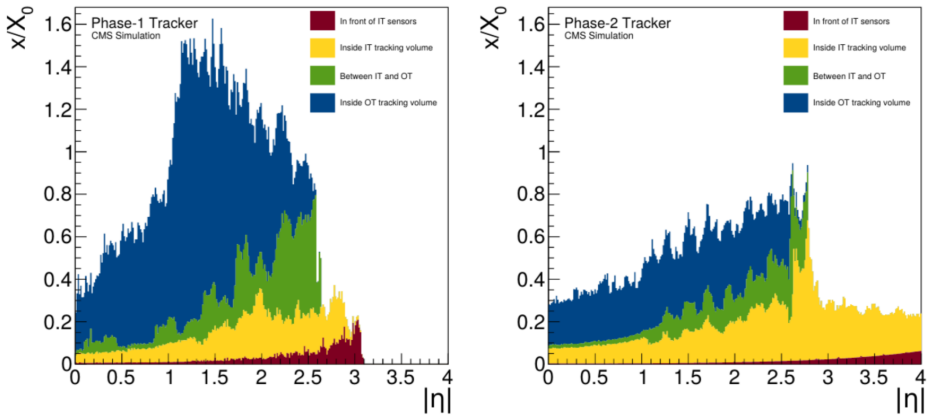

Figure 2.21: Comparison of material budget for the current CMS tracker (left) and the phase-2 upgrade tracker (right)[3].

Finally, Table 2.1 lists the number of each module type produced per participating institute and Figure 2.22 shows the distribution of it. The outer pie chart corresponds to the 2S modules (a total of 7,608), while the inner pie chart corresponds to the PS modules (a total of 5,714).

Table 2.1: Number of Outer Tracker modules per type and production institute.

Institute	2S 1.8 mm	2S 4.0 mm	PS 1.6 mm	PS 2.6 mm	PS 4.0 mm
Brussels	1192	320	0	0	0
KIT[a]	1288	0	0	0	0
Aachen	696	104	0	0	0
Brown	900	0	0	0	1310
FNAL[b]	900	0	826	126	290
Perugia	0	0	0	1336	584
NISER[c]	1104	0	0	0	0
NCP[d]	1104	0	826	126	290

[a]Karlsruhe Institute of Technology
[b]Fermi National Accelerator Laboratory
[c]National Institute of Science Education and Research
[d]National Centre for Physics

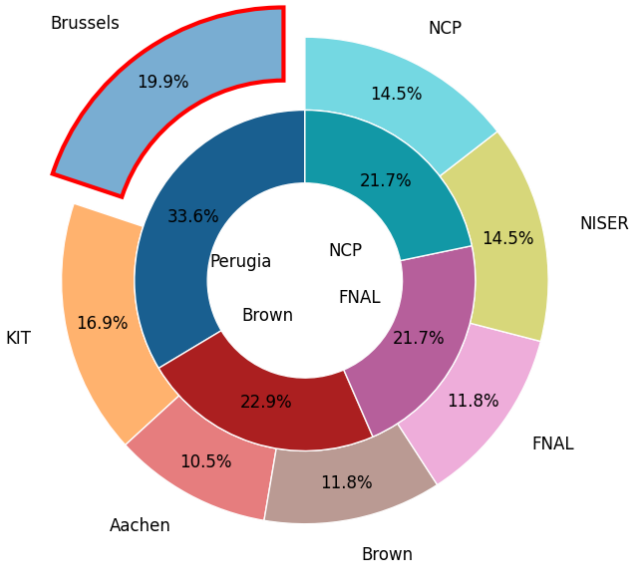

Figure 2.22: Distribution of 2S (outer pie chart) and PS (inner pie chart) modules production per institute (total: 7,608 2S modules and 5,714 PS modules).

Chapter 3

Silicon Sensor for 2S Modules

In this chapter, we will introduce how silicon sensors are used to detect charged particles. We will begin by describing how charged particles interact with matter, then explain the working principles of silicon detectors by introducing the p-n junction and space charge region, followed by a discussion of signal formation. Later the structure and specification of 2S module sensor will be reviewed. Finally, we will review their radiation resistance.

3.1 Heavy charged particle interactions with matter

In this context, the term heavy refers to all charged particles produced after the collision, excluding the electron. When a heavy charged particle traverses matter, it interacts with atomic electrons primarily through Coulomb interactions. These interactions cause excitation and ionization. As a result, free charge carriers are produced, as seen in gases or semiconductors.

The average energy loss of such a charged particle as it passes through a medium is described by the Bethe-Bloch formula[33], given below:

$$\left\langle \frac{dE}{dx} \right\rangle = K \frac{z^2 Z}{A\beta^2} \left[\frac{1}{2} \ln \frac{2m_e c^2 \beta^2 \gamma^2 W_{\max}}{I^2} - \beta^2 - \frac{\delta(\beta\gamma)}{2} \right] \tag{3.1}$$

where K is a coefficient for dE/dx (0.307075 $MeV\ mol^{-1}\ cm^2$), z is the charge of the incoming particle, Z is atomic number of the material, A is the atomic mass of the material, β is the ratio of the particle's velocity to the speed of light, m_e is the electron rest mass, c is the speed of light in vacuum, γ is the Lorentz factor of particle, W_{max} is the maximum energy transfer in a single collision, I is the mean excitation potential, and $\delta(\beta\gamma)$ is the density correction factor. The Bethe-Bloch plot is shown in Figure 3.1.

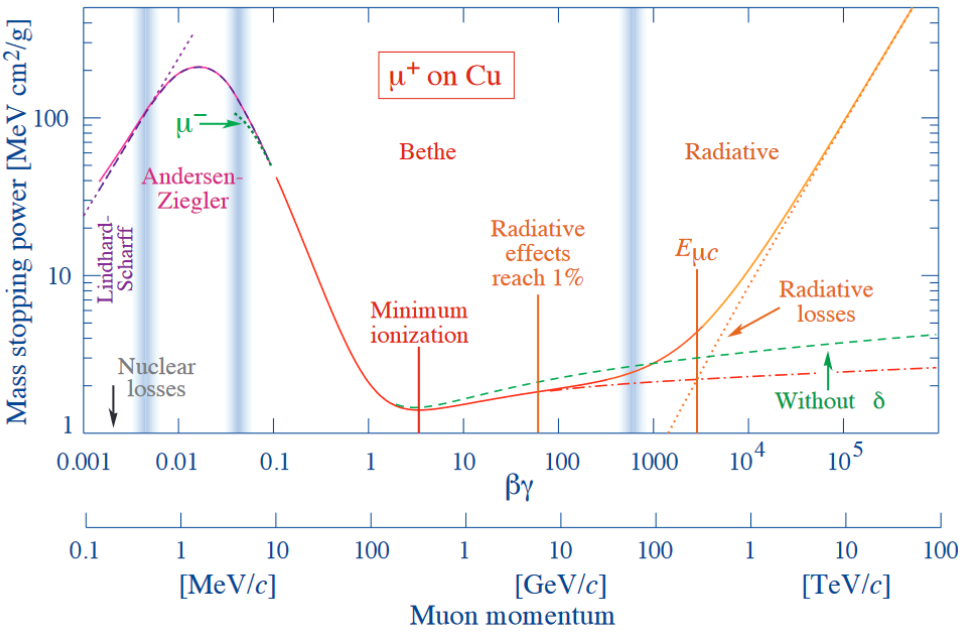

Figure 3.1: The graph illustrates the stopping power of copper for muons passing through it. It includes adjustments to the Bethe-Bloch formula to account for both low and high energy levels[33].

At low energies, additional correction terms must be considered. These arise from the atomic binding of electrons in the material and changes in the effective charge of the incident particle. A key feature in the interaction of charged particles with matter is the presence of a minimum in the energy deposition curve. This occurs at approximately $\beta\gamma \approx 3$. This point is known as the Minimum Ionizing Particles (MIP) regime. It defines the minimum energy loss needed for reliable detection in typical tracking detectors. At high energies, radiative losses, particularly bremsstrahlung, become important. These effects are especially relevant for light particles like electrons. It is important to note that the average energy loss is proportional to the square of the charge of the traversing particle, z^2, as shown in the Bethe-Bloch formula. The electron density of the medium also affects the total ionization energy loss. The energy loss of a charged particle passing through a thin absorber shows statistical fluctuations. These are due to variations in both the number and magnitude of individual ionizing collisions. Landau studied this behavior and derived a straggling function—an asymmetric distribution that describes the total energy loss. In rare events, large energy transfers can produce δ-electrons (also called knock-on electrons). These electrons create a high-energy tail in the energy loss or charge deposition distribution.

Low-energy heavy ions can be produced in nuclear interactions, such as those involving protons, neutrons, and pions traversing matter. These ions usually have energies below 10 MeV and short ranges less than 10 μm[34]. They deposit energy on the order of 2 MeV/μm in silicon, which is much higher than the energy loss of a MIP. And these particles are important because they can induce significant single event upsets (SEUs) in ICs.

Electrons are light charged particles that mainly interact with the electronic structure of atoms. In each collision, they tend to lose a large fraction of their energy and are strongly deflected. This often leads to a zigzag path. Electrons also experience radiative energy loss through bremsstrahlung. This process becomes more important at high energies due to interactions with atomic nuclei.

Muons, are much heavier than electrons. They lose less energy through ionization and, at higher energies, through radiative processes. Due to their large mass and small interaction cross-section, muons can travel through dense materials over distances of several meters.

When a MIP with $\beta\gamma > 3$ traverses silicon, it deposits energy at an average rate of approximately 3.87 MeV/cm. In the case of a 2S module with an active silicon thickness of 290 μm, this corresponds to an average deposited energy of 112.23 keV. Given that the average energy required to create an electron-hole pair in silicon is 3.6 eV, this energy loss results in the creation of approximately 31.175×10^3 e-h pairs. However, for thin silicon layers like this, the Landau distribution of energy loss becomes significant due to statistical fluctuations. As a result, the most probable value (MPV) of the energy loss is a more relevant metric than the mean. The MPV is approximately 70% of the average energy loss. This corresponds to about 21.878×10^3 e-h pairs.

3.2 Silicon detector

The lattice structure plays an important role in the properties of semiconductors. Semiconductors such as silicon and germanium are structured in diamond lattices, which are composed of two interpenetrating face-centered cubic (FCC) sublattices. In this arrangement, each atom is tetrahedrally surrounded by four neighbors and forms covalent bonds. This structure plays a critical role in determining the behavior of semiconductor devices. A schematic of a silicon lattice is shown in Figure 3.2. This structure affects the band gap, which is the energy difference between the valence band and the conduction band. The band gap determines how easily electrons can move from one band to another, and whether a material behaves as an insulator, conductor, or semiconductor. In semiconductors, the valence band is filled at low temperatures, while the conduction band is empty. As the temperature increases, some electrons gain enough energy to move into

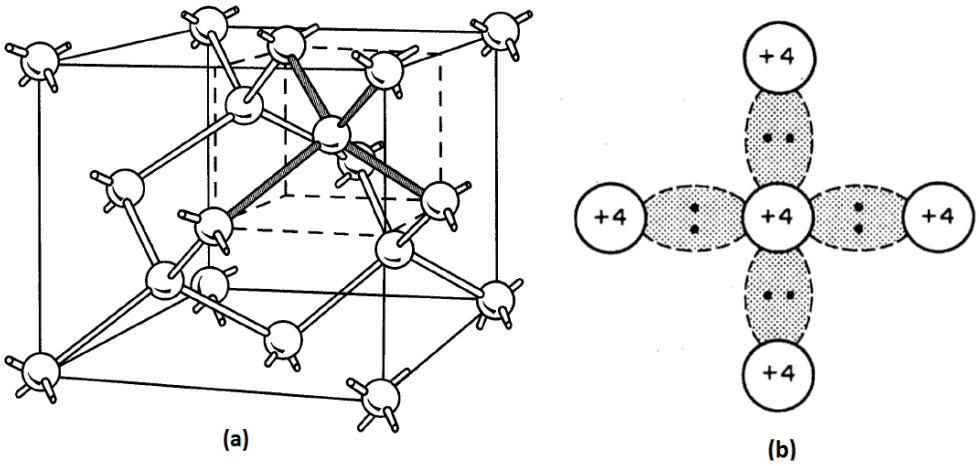

Figure 3.2: (a) A tetrahedron bond lattice. (b) A two-dimensional diagram illustrating a tetrahedron bond.

the conduction band, leaving behind "holes" (vacant energy states) in the valence band. These free electrons and holes contribute to electrical conduction. The lattice structure also affects charge carrier mobility, such as for electrons and holes. Charge carriers move through the lattice with an effective mass, which differs from that of free electrons. A higher mobility means faster signal collection and lower noise in the detector. Therefore, maintaining a high-quality lattice with minimal defects and impurities is essential. The conductivity of semiconductors ranges from 10^{-6} to $10^{4}\ \Omega^{-1}\,\mathrm{m}^{-1}$ and is influenced by temperature and doping. To modify the conductivity of silicon, a process called "doping" is used. This introduces additional energy states by adding specific atoms (dopants), which transforms silicon into either n-type or p-type material.

To create n-type silicon, which has an excess of electrons as the majority charge carriers, group V elements like phosphorus are added. These elements have five valence electrons. Conversely, group III elements such as boron, which have three valence electrons, are used to create p-type silicon. In this case, holes become the majority charge carriers. Many semiconductor devices are built using combinations of these two doped silicon types.

When the system is in thermal equilibrium, the Fermi-Dirac statistics describe the probability that a certain energy state with energy E is occupied by a particle. This probability follows the Pauli exclusion principle, which limits the number of identical fermions that can occupy the same quantum state. The Fermi level represents the energy at which exactly half of the available energy levels are filled. In intrinsic silicon, this level is located in the middle of the band gap. When impurities are introduced, the Fermi level shifts and is positioned between the

impurity levels and the nearest energy band. This shift in the Fermi level becomes important, especially when two different materials come into contact. It sets the relative alignment of all other energy bands in the system. Conductivity, σ, is the inverse of resistivity and is defined as

$$\sigma = e \cdot N \cdot \frac{\nu}{E} \tag{3.2}$$

where e is the elementary charge, N is the number of charge carriers, ν is the drift velocity of the carriers, and E is the electric field. By defining mobility as $\mu = \frac{\nu}{E}$ and considering both types of carriers in semiconductors, the conductivity can also be expressed as

$$\sigma = e \cdot (N_e \cdot \mu_e + N_p \cdot \mu_p) \tag{3.3}$$

where N_e and N_p are the concentrations of electrons and holes, and μ_e and μ_p are their respective mobilities. The mobilities in silicon are relatively high, making it a suitable material for use in high energy physics detectors. The electron mobility in silicon is $\mu_e = 1350\,\mathrm{cm}^2/(\mathrm{V}\cdot\mathrm{s})$, and the hole mobility is $\mu_p = 450\,\mathrm{cm}^2/(\mathrm{V}\cdot\mathrm{s})$. These values result in a typical charge collection time of approximately 2 ns and 6 ns for respectively electron and holes in silicon layers with an active thickness of 290 μm and bias voltage of 300 V. In an intrinsic silicon substrate, there are around 10^9 free charge carriers (background), compared to only approximately 2×10^4 electrons generated by an ionizing particle. The number of free charge carriers can be reduced either by cooling the silicon to very low temperatures or by depleting the silicon volume using a reverse-biased pn-junction composed of p-type and n-type silicon. Cryogenic cooling is not practical for large detectors, so the basic principles of pn-junctions are used instead.

3.3 PN junction as charged particle detector

In thermal equilibrium, the Fermi energy remains constant throughout the semiconductor structure. At a pn-junction, equilibrium is achieved by the diffusion of majority carriers—electrons from the n-type region and holes from the p-type region—into the opposite side of the junction, where they recombine with opposite carriers. As carriers diffuse, they leave behind ionized donor and acceptor atoms fixed in the crystal lattice. This forms a region without mobile charge carriers, known as the depletion region or space charge region (SCR). An internal electric field $|E|$ develops from the n-side to the p-side, opposing further diffusion. The system reaches dynamic equilibrium when the diffusive current of carriers is exactly balanced by the drift current caused by the electric field. As a result, no net current flows, and the Fermi level becomes flat across the junction. Solving the Poisson equation in the SCR, assuming uniform doping on both sides and an

abrupt junction, yields an electric field $E(x)$ that varies linearly with position within each region (p-side and n-side). The electric potential $\phi(x)$ varies quadratically with position. The total electrostatic potential difference across the SCR is called the built-in potential or diffusion potential, denoted by V_{bi}. This potential depends on temperature and doping levels and is given by

$$V_{\text{bi}} = \frac{kT}{q} \ln\left(\frac{N_A N_D}{n_i^2}\right) \tag{3.4}$$

where k is Boltzmann's constant, T is the absolute temperature, q is the elementary charge, N_A and N_D are the acceptor and donor concentrations, and n_i is the intrinsic carrier concentration of silicon. An external voltage $\pm V$ changes the intrinsic potential barrier of the pn-junction. The depletion width either decreases or increases, depending on whether a forward or reverse bias voltage is applied.

To increase the depleted volume, a reverse bias voltage is used. This extends the SCR, enhancing the separation and collection of charge carriers generated by ionizing radiation through the electric field. To ensure full charge collection efficiency, the applied external reverse bias voltage V_{external} must be large enough to fully deplete the sensitive volume of the sensor. The voltage required to deplete a layer of thickness w is given by

$$V_{\text{depletion}} = \frac{q \cdot |N_{\text{eff}}| \cdot w^2}{\varepsilon} \tag{3.5}$$

where w is the width of the depletion layer, ε is the permittivity of silicon, and N_{eff} is the effective space charge density. The full depletion voltage V_{FD} corresponds to the value of $V_{\text{depletion}}$ when w equals the full thickness of the detector. It is an important design parameter that determines the minimum bias voltage needed for optimal detector performance. For example, in the CMS Outer Tracker sensors, with a thickness of 290 μm and a resistivity above 3.5 kΩ cm, the full depletion voltage—considering holes as the dominant charge carriers (i.e., a p-type bulk)—is calculated to be approximately 241.6 V.When the applied bias voltage V_{bias} exceeds the full depletion voltage V_{FD}, the depletion region extends across the entire active thickness of the sensor and creates a strong electric field. Electron-hole pairs generated thermally within this region are immediately separated and collected by the electrodes before recombination, resulting in a small but measurable leakage current.

Below the breakdown voltage, the leakage current in a non-irradiated sensor is primarily determined by Shockley-Read-Hall (SRH)[35] bulk generation due to impurities. Irradiation introduces additional defect states, reduces the generation lifetime, and increases the leakage current. Lowering the temperature reduces the leakage current, making cooling an effective mitigation strategy.

The total capacitance of a sensor can be determined by considering the two planes of the SCR as the plates of a capacitor, with silicon serving as the dielectric material. The capacitance of the sensor is given by the following equation:

$$C_{bulk} = \begin{cases} A\sqrt{\frac{\varepsilon_{Si}}{2.\rho.\mu.V_{bias}}} & V_{bias} \leq V_{FD} \\ A\frac{\varepsilon_{Si}}{w_{depletion}} = const. & V_{bias} > V_{FD} \end{cases} \tag{3.6}$$

The capacitance-voltage characteristic, also known as the CV curve, or the behavior of $1/C^2$ versus the applied voltage, is a standard method used to determine the full depletion voltage V_{FD}.

Electron-hole pairs generated by a MIP drift along the electric field with a velocity proportional to that field, while also diffusing laterally from the particle track. The carriers spread outward until they are collected at their respective electrodes, leading to charge sharing and cluster broadening. The width of the charge cloud is given by

$$\sigma = \sqrt{2Dt}$$

where D is the diffusion coefficient (assumed to be $35\,\mathrm{cm^2\,s^{-1}}$ for electrons in silicon), and t is the drift time (approximately 3 ns under nominal conditions). These values correspond to a spread of about $4.5\,\mu$m, which is small compared to the $90\,\mu$m strip pitch of the CMS 2S sensor. The movement of charge carriers toward the electrodes and the backplane of the detector induces a signal on the electrode surface. This signal can be recorded and is described by the Shockley-Ramo theorem[36, 37]. For high-energy particles that deposit charge across two adjacent strips, the center-of-charge method can be applied to improve the position resolution. In a detector with binary readout, the position resolution is given by

$$\sigma_x = \frac{\text{pitch}}{\sqrt{12}}$$

which yields a resolution of approximately $26\,\mu$m for the CMS 2S sensor with a $90\,\mu$m pitch.

3.4 HL-LHC outer tracker sensors design

The Outer Tracker of the HL-LHC consists of two types of detector modules[38]. The inner part uses PS modules, which combine DC-coupled macro-pixel sensors (PS-P) and AC-coupled strip sensors (PS-S). For the outer part, the 2S module is used, consisting of two AC-coupled strip sensors. These sensors are designed to

operate at a temperature of −20 °C, withstand fluences as high as 3×10^{14} n_{eq}/cm^2, and function within a magnetic field of 4 T under dry air conditions. The PS-S sensor has approximately 2000 readout channels with a pitch of 100 μm. Its physical dimensions are 10 cm × 5 cm. The PS-P sensor consists of rows of very short strips, known as macro-pixels, each with a length of 1.4 mm. These are directly read through DC coupling. The overall size of the PS-P sensor is similar to that of the PS-S sensor.

The strip sensor used in the 2S module also has around 2000 channels with a pitch of 90 μm, and its dimensions are approximately 10 cm × 10 cm. In both types of strip sensors, the strips are divided into segments, with each half being read out from opposite ends. During module assembly, the strip pads are connected to the readout board pads via wire bonding.

3.5 2S Module sensor structure

As this thesis focuses on the 2S module, we emphasize the specific properties of the silicon sensors used in this module, as specified by the CMS collaboration. A schematic illustration is shown in Figure 3.3, and detailed specifications are listed in Table 3.1.

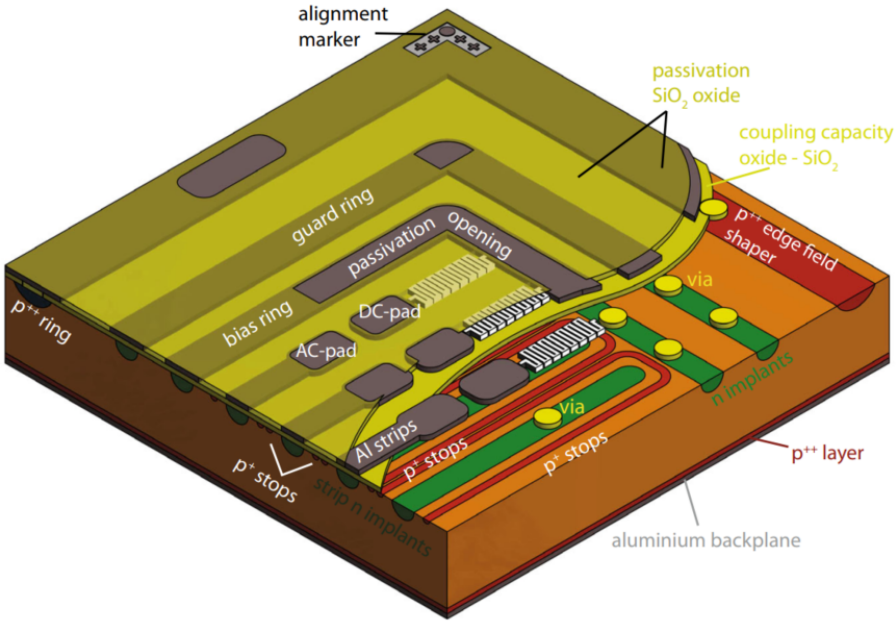

Figure 3.3: A three-dimensional diagram illustrating an n-in-p sensor's schematic. Within this schematic, an 'atoll' configuration is illustrated, wherein each individual strip is encircled by its own p-stop[39].

The structure of the 2S module sensor is described in the following. These sensors are of the n-in-p type, meaning they consist of highly n-doped readout strips implanted in a p-doped silicon bulk[39]. Strip isolation is achieved using a p-stop implantation. The sensor material is Float Zone (FZ) silicon manufactured by Hamamatsu. The total thickness of the sensor is 320 μm, with an active region of 290 μm and a 30 μm p++ doped backside layer. This highly doped layer makes the back surface less sensitive to mechanical scratches. The readout electrodes are aluminum strips. These are capacitively coupled to the underlying n-implant via a thin dielectric layer of Si-SiO_2. The aluminum strips are connected to the readout electronics for signal processing. To ensure good ohmic contact and lower resistivity, the backplane of the sensor includes a p++ layer. A thin aluminum layer is deposited over this backplane. The bias voltage is applied to the backplane, while the bias ring is kept at ground potential. Signals from the strips are read from the AC pads.

To enhance electrical isolation between the strips, a p+ implant surrounds each n-type strip implant. Around the entire active area, there is a bias ring designed to provide a uniform electric potential across all strips. This ring supplies voltage to each individual n-strip implant through polysilicon bias resistors. To reduce edge effects, shape the electric field, and ensure a homogeneous potential distribution for both edge and central strips, the sensor includes a floating guard ring. The guard ring is located outside the bias ring. It is supported by an n+ implant beneath it, which is connected via vias to the guard ring. To mitigate the effects of sidewall defects caused during the sensor dicing process, a broad p++ implant is applied around the sensor's front face. This region is known as the active edge ring or edge field shaper. The sensor surface is covered with a protective SiO_2 layer. This passivation layer provides surface insulation, environmental stability, and protection against damage. Openings in the passivation layer are created over selected areas of aluminum, such as bonding pads and test points, to allow electrical contact. The sensor includes alignment marks located at its corners. Strip numbers are printed on both outer ends of the strips, following a counter-clockwise ordering scheme.

3.6 Radiation damage

One of the major challenges at the HL-LHC is the high level of radiation, especially for the tracking detectors, which are located closest to the interaction point (see Table 3.2). Radiation can cause displacement damage in the silicon bulk by creating charge carrier traps and introducing new energy levels [39]. This leads to an increase in leakage current, which raises the noise level and, in the absence of proper cooling, can result in thermal runaway. In addition, radiation alters the ef-

Table 3.1: Main specifications for non-irradiated 2S module sensors[38]

Main specifications for 2S sensors	
Sensor Type	AC coupled strips with atoll p-stop isolation and polysilicon bias
Material	p-type $FZ290$
Crystal orientation	$< 100 >$
Thickness (physical)	320 μm
Thickness (active)	290 μm
Thickness tolerance	$\pm 5\%$
Physical dimensions	94183×102700 μm^2
Strip pitch	90 μm
Width-to-pitch	0.25
Strip implant length	50205 μm
Number of strips	2×1016
Full depletion voltage	< 350 V
Current at 600 V	≤ 2.5 nA/mm^3
Resistivity	> 3.5 $k\Omega cm$
Polysilicon bias resistor	1.5 ± 0.5 $M\Omega$
Interstrip capacitance $C_{int,1N}$	< 0.5 pF/cm
Coupling capacitance	> 1.2 $pF/(cm\ \mu m)$
Radiation hardness	*up to* $3.8 \times 10^{14} \mathrm{n_{eq}/cm^2}$

fective doping concentration, potentially causing type inversion, which affects the full depletion voltage. The current tracker detectors (operational in Run 3) use n-type bulk, which eventually undergoes type inversion to p-type under radiation. It has been reported that by the end of Run 2, many strip silicon sensors had approached or reached type inversion. Overall, these effects degrade tracking efficiency and hit resolution. Radiation can also cause surface damage; more details can be found in [39].

To address these challenges, the new sensors are fabricated using n-in-p technology with float zone (FZ) silicon and have a standard active thickness of 290 μm[32]. In the p-type bulk, type inversion does not occur. Furthermore, charge collection is improved due to electron collection on the n-side. The sensor thickness was chosen based on the fact that thinner sensors exhibit improved radiation hardness. Thinner sensors also benefit from lower full depletion voltage and reduced leakage current. Additionally, the new sensors are capable of operating at high bias voltages (up to 800 V) to ensure full depletion even after exposure to high radiation fluence. Enrichment of the silicon bulk with oxygen also helps to mitigate radiation-induced defects.

Table 3.2: Maximum fluence after 3000 and 4000 fb^{-1} assigned to the different module types and their positions in the tracker based on FLUKA v3.7.20.1 simulation results[38].

Type / location	No. of modules	z position (mm)	Radius (mm)	Max. module fluence (n_{eq}/cm^2)	
				3000 fb^{-1}	4000 fb^{-1}
1.8 mm 2S barrel	4416	1127	669	2.8×10^{14}	3.7×10^{14}
1.8 mm 2S endcap	2768	2239	768	2.9×10^{14}	3.8×10^{14}
4.0 mm 2S endcap	424	2643	665	3.7×10^{14}	4.9×10^{14}

In the next chapter, the electronics and readout system of the 2S module will be discussed.

Chapter 4

Readout Electronics of 2S Modules

In this section, we review the electronic components used to capture signals in the silicon detector. These signals are generated by the passage of ionizing particles through the silicon. The electronics of the 2S module include front-end binary readout chips called CMS Binary Chip version 3.1 (CBC), which are connected to the sensors. Each module also has a Concentrator Integrated Circuit (CIC) concentrator on both sides. An Low Power Gigabit Transceiver (lpGBT) chip is used for data serialization and deserialization, module control, and monitoring. The VTRx+ chip handles the interface between the electrical signals of the module and the optical transfer link (see Figure 4.1). The following sections provide more information about each chip.

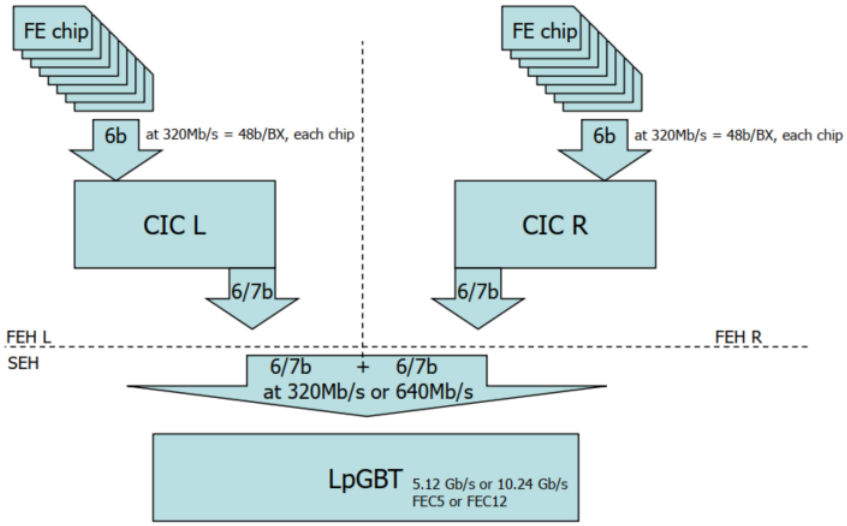

Figure 4.1: The diagram shows the data flow at the front-end of the modules[3].

4.1 CBC

The CBC[40] is fabricated using 130nm Complementary Metal-Oxide-Semiconductor (CMOS) technology. It is designed to read the electrical charges generated by ionizing particles in the silicon strips of the CMS detector. These signals are converted into binary outputs, indicating either the presence ("hit") or absence ("no hit") of an event for each channel. The resulting data, called Triggered Data, is synchronized with the bunch crossing interval, which occurs every 25 ns.

The CBC is designed to store data from each event for up to 512 bunch crossing intervals, corresponding to 12.8 μs, based on a 25 ns clock cycle. This storage period, known as trigger latency, is essential to allow the external system enough time to determine which event data should be read out from the chip.

Upon receiving a trigger signal, the CBC retrieves the Triggered Data corresponding to the event that occurred one trigger latency period earlier. This data is temporarily stored in a buffer with a depth of 32 events, waiting for serial readout from the chip at a clock rate of 320 MHz. The serial readout process, which includes data from 254 channels, the event address, and housekeeping bits, takes 950 ns to complete. At the same time, the CBC continues acquiring data at each bunch crossing. Despite an average trigger rate of 750 kHz, the CBC is designed to handle trigger rates up to 1 MHz, ensuring that the data buffer prevents event loss.

A key feature of the CBC, which distinguishes it from earlier versions, is the ability to identify high-momentum tracks in each event. This feature is important

for physics analysis. The chip includes logic that checks for coincidences between hits in different sensor layers to generate positional information, called Stub Data. The Stub Data, which is critical for the Level-1 Trigger decision process, is sent from the CBC with minimal delay. To enable this fast transfer, the Stub Data is limited in amount and transmitted through five parallel digital outputs running at 320 MHz. Each CBC chip can send up to three sets of Stub Data per event, balancing detection efficiency with output bandwidth constraints. From the sig-

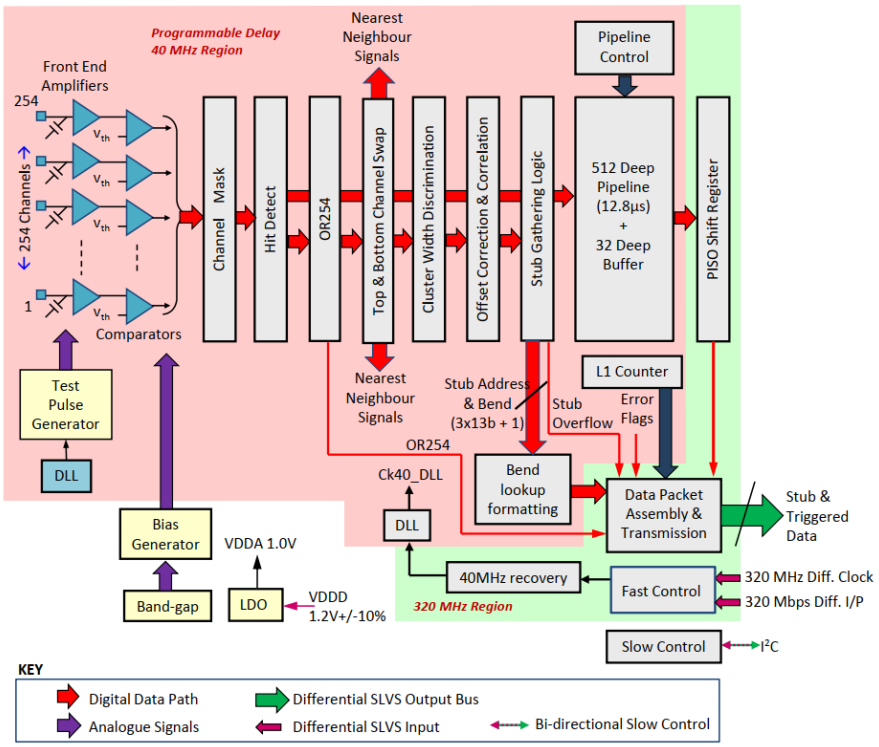

Figure 4.2: Block Diagram of CBC architecture[40].

nal point of view, the top-level architecture is divided into an analog front-end and a digital front-end. The different sections of the analog front-end are shown in Figure 4.3. The analog front-end is designed to amplify incoming signals so they are strong enough to be processed accurately. The combined gain from the pre-amplifier and post-amplifier is designed to be 50 mV/fC at the input of the comparator. The comparator compares the incoming signal level to a predefined reference level.

The design targets to keep the noise level below 1000 electrons for detector strips that are 5 centimeters long with a leakage current of up to 1 μA. This low noise level is achievable even with an external capacitance, including the sensor and any stray capacitance, of up to 10 pF. The shape of the electrical pulse is designed

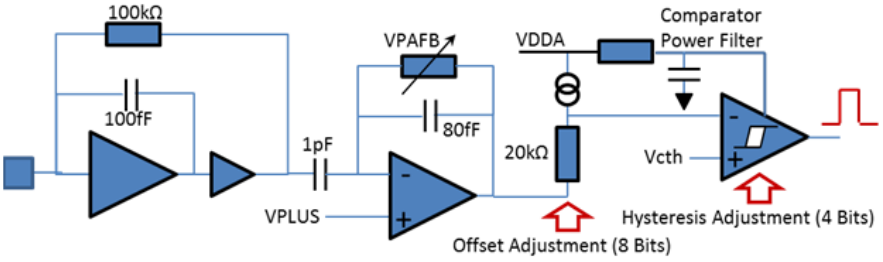

Figure 4.3: CBC3 Analogue Front-End[40].

to peak in less than 20 ns and return to the baseline within 50 ns. This fast response is important for the chip to process signals quickly and accurately. To compensate for variations between channels, the analog front-end includes a mechanism called Post-amp Offset Adjustment to fine-tune the signal level entering the comparator. This is done by adjusting the current in the post-amplifier, which changes the output voltage. The analog front-end can recover quickly from large signals, such as those caused by heavily ionizing particles, and be ready to process normal signals within 2.5 μs. It is also designed so that the time difference in the comparator's response to different signal sizes is no more than 16 ns, ensuring consistent timing for signal processing. The comparator threshold voltage, which determines the signal level at which the comparator reacts, can be finely adjusted using a 10-bit resistor ladder Digital-to-Analog Converter (DAC). This allows precise control of the comparator's sensitivity. After the comparator, the chip handles digital signals, which are passed to the digital front-end.

The on-chip 40 MHz clock, derived from the serial fast command input, serves as the timing source for the data pathway starting from the comparator outputs to the Output Data Serializer and the Data Assembly Logic at the back-end. This pathway requires a transition to the 320 MHz clock domain. Since the derived 40 MHz clock may not be optimally phase-aligned with the data produced by the bunch crossing (BX), a Delay Locked Loop (DLL) circuit is integrated to adjust the phase of the 40 MHz clock used by the Hit Detect and Pipelined Data Logic. The clock phase is controlled by a programmable register, accessible via the I2C interface, with phase adjustments possible in 1 ns steps ranging from 0 to 25 ns. The operational frequency range of the DLL is limited, so a bypass option is provided for low-frequency wafer-level tests. This bypass allows the use of the unadjusted derived clock instead of the phase-shifted version. To synchronize the fast control commands with the phase-shifted clock, these commands are also routed through the DLL circuit. This ensures they are automatically aligned with the adjusted clock. The Channel Mask is a 254-bit register programmable via the I2C slow control interface. The outputs of this register are used to disable the Hit

Detect circuits individually for each channel.

The Hit Detect Logic is an important part that interprets the signals from the channel's comparator circuit. It is configurable and can provide four distinct outputs, each with specific characteristics described below. These modes are also illustrated in Figure 4.4:

- **Fixed Pulse Width Output (Latched Mode):** This output captures the signal from the hit comparator for an entire 25 ns clock cycle. It ensures that any transitions in the comparator's output that are not aligned with the clock are still recorded. The result is a fixed 25 ns pulse, independent of the actual pulse duration of the comparator. Consecutive hits in successive clock cycles are registered, provided that the signal drops below the comparator's threshold between hits.

- **40 MHz Sampled Output:** In this mode, the comparator's output is sampled with the 40 MHz clock derived from the DLL. The output is latched if the comparator is high at the rising edge of the clock and is reset to zero only when the comparator goes low and the next rising clock edge occurs. The minimum pulse duration is one clock cycle. Hits occurring in consecutive clock cycles are registered, even if the signal does not fall below the threshold between them.

- **Logical OR Output:** This output is the logical OR combination of the Fixed Pulse Width Output and the 40 MHz Sampled Output. It captures any hits detected by either mode.

- **HIP Suppressed Output:** This mode is based on the 40 MHz Sampled Output and includes an optional Highly Ionizing Particle (HIP) suppression feature. If the output pulse exceeds a configurable number of clock cycles, the circuit forces the output to reset to zero. The maximum pulse length before suppression is set via a three-bit register accessible through the I2C interface. HIP suppression can be applied either to the 40 MHz Sampled Output or to the Logical OR Output, based on the selection made using a multiplexer.

Each of these outputs can be independently directed to the Stub Logic or to the Pipeline Memory, allowing flexible data processing and management within the system. The data generated by the hit detection logic is forwarded to the digital section of the chip. Within the digital domain, two types of logic operate: one for the full-event data and one dedicated to stub generation. The configuration of the hit detection outputs is independently selectable for the full-event logic and for the stub logic, allowing the system to be tailored to specific operational requirements.

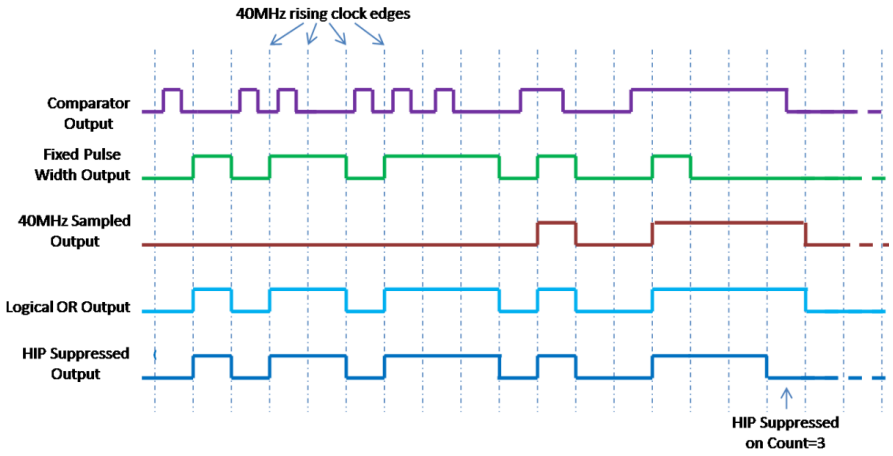

Figure 4.4: CBC sampling modes[40].

The timing mechanisms for the Fixed Pulse Width Output and the 40 MHz Sampled Output show small differences within the circuitry. There is a limitation on the minimum detectable pulse width. The hit detect circuit can only recognize pulses that are at least 300 ps wide. Any pulse narrower than this may not be detected or correctly processed. Additionally, a minimum setup time of 300 ps is required between the comparator output going high and the rising edge of the clock for the stub to be detected. The hit detect circuit has a setup and hold blind spot, which corresponds to the period after the clock edge when new data cannot be reliably latched. This happens because the data must remain stable both before (setup time) and after (hold time) the clock edge to be captured correctly. This blind spot creates a dead time during which the circuit is unable to detect hits due to clock timing constraints. If a hit occurs within this blind spot, approximately 2.7 ns around the clock edge, it will not be detected. These timing constraints are illustrated in Figure 4.5.

The CBC is responsible for processing data sampled from both the top (superior) and bottom (inferior) sensor channels. It can synchronize clusters detected in both channels, enabling the generation of stubs. The architecture also supports inter-chip communication, allowing clusters to be correlated even when they span across multiple chips. The pathway through which stub data flows is shown in Figure 4.2.

Once the full sample is received from the sensor, the data passes through a logical OR network. This network produces an active-high signal (denoted as OR254) if one or more channels register a hit. This signal is included in the stub data output packet.

The data containing hits from the entire sensor then passes to a layer swapping mechanism. This function allows the user to select either the top or bottom sensor

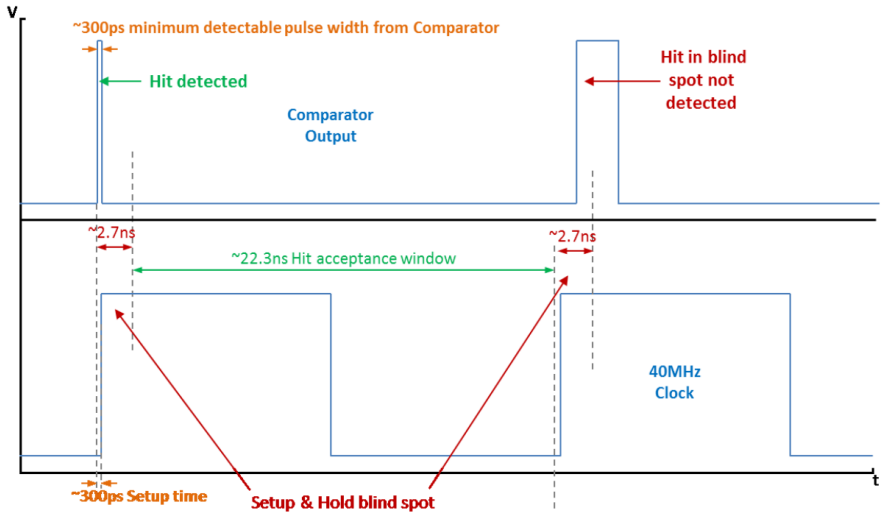

Figure 4.5: Timing restrictions for the Fixed Pulse Width segment of the hit identification circuitry[40].

channels as the seed layer, depending on the operational requirements.

Following this, the cluster width discrimination process excludes clusters that exceed a user-defined width threshold (up to 4 channels) which is applied to both layers. This threshold is programmable to match specific operational needs. Clusters that pass this filter are forwarded to the offset correction and cluster correlation logic. This system allows programming of an offset between the seed layer and the correlation layer to correct for Geometrical correction due to module placement in the $r - \phi$ plane. Each CBC chip is divided into four sectors, and each sector can have its own independently programmed offset. The offset adjustment range is ±3 channels, with a resolution of half a strip. The CBC algorithm searches for a cluster in the correlation layer that aligns with each cluster detected in the seed layer. This search occurs within a programmable correlation window centered on the seed cluster. The width of the correlation window can be set up to ±7 channels, with half-strip resolution for precise matching.

When the CBC identifies a matching cluster within this window, it generates a stub. The width of the correlation window directly determines the transverse momentum (p_T) threshold for the stubs. Examples of the correlation window and offset configurations are shown in Figure 4.6.

Upon successfully identifying a stub, the CBC determines the central location of the seed cluster. For clusters larger than a single strip, the position resolution improves, achieving what is known as half-strip resolution.

In addition, the CBC calculates the deviation between clusters in the seed and correlation layers, which represents the bend. Given the maximum range of the

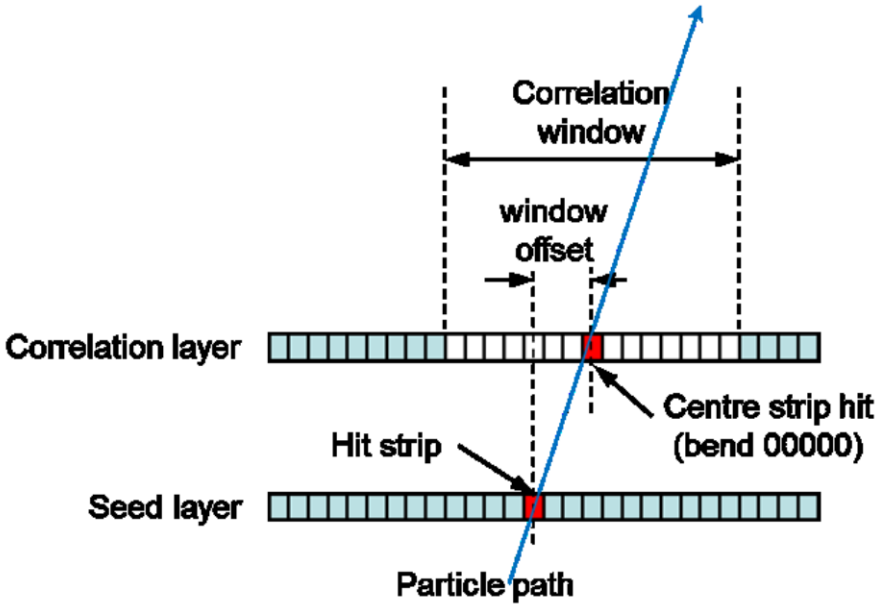

Figure 4.6: This picture illustrates Correlation Window and Offset Correction[40].

correlation window and the resolution, this bend is quantified with a 5-bit value. However, this detailed bend information is used only internally within the chip. To reduce the output bandwidth, the 5-bit bend value is converted into a 4-bit bend code using a programmable bend Look-Up Table (LUT). The CBC outputs the position and bend information for up to three stubs per BX, transmitted over five lines at a data rate of 320 Mbps, as shown in Figure 4.7.

It is important to note that stub data is transmitted in an unsequenced order. If more than three stubs are detected within a single BX, the CBC prioritizes those with the lowest strip address. In such cases, an overflow flag is set in the stub data packet to indicate that more than three stubs were detected.

The output data frame also includes a synchronization bit, which is always set to high. This bit allows the CIC or backend systems to verify data alignment. Additionally, the frame contains the OR254 bit and an error indicator. The error indicator is the logical OR of two conditions: the full-event First-In, First-Out (FIFO) full flag and the latency error flag.

During each bunch crossing, the sampling logic captures data from every channel and stores it in the CBC's internal memory. This process is managed by a 9-bit write pointer that determines the memory address for incoming data. Additionally, a trigger pointer—controlled by a trigger counter that starts counting after a preset latency from the start of the write pointer—is used to retrieve the data at the correct time. When a Level-1 Accept (L1A) trigger is received, the

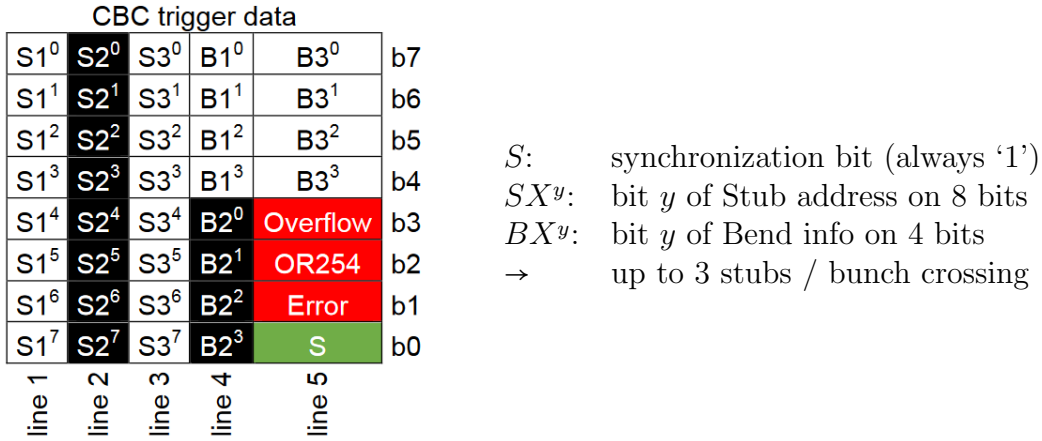

Figure 4.7: CBC output trigger data format[40].

CBC retrieves the data from the memory location indicated by the trigger pointer. The internal memory supports a maximum L1 latency of 512 BXs. The retrieved full-event data is transferred to an output FIFO buffer with a capacity of 32 entries. From there, the data is serialized, appended with a header, and transmitted at 320 Mbps through a differential line to the backend systems.

The structure of the full-event output data frame is shown in Figure 4.8. The frame starts with a two-bit header, followed by two error flag bits—one indicating a latency mismatch between the trigger and write pointers, and another indicating if the FIFO buffer is full. This is followed by a 9-bit pipeline counter and a 9-bit L1 counter, which increments with each L1A trigger. The next 254 bits represent the sensor image. Each full-event data frame requires 950 ns to be transmitted. This allows for a maximum continuous output data rate of 1 MHz. The first bit of the full-event output frame is synchronized with the synchronization bit in the stub data frame.

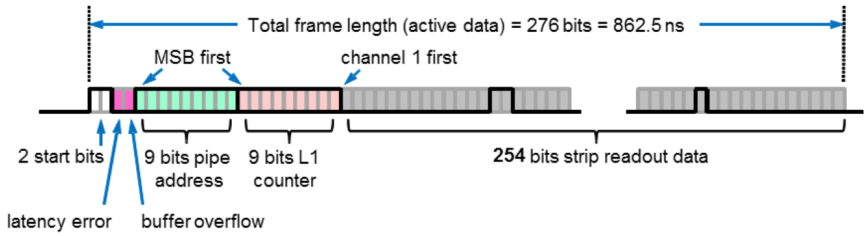

Figure 4.8: This picture illustration of the serial Triggered Data packet[40].

The CBC architecture is divided into two distinct clock domains, showed with color-coded regions in Figure 4.2. The primary domain operates at 320 MHz

(shown in pink in the architecture diagram) and controls all Input/Output interface functions, except for the slow-control interface, which uses a 1 MHz I2C-type interface for register initialization. The secondary domain operates at 40 MHz (shown in green), derived from the Fast Control Interface (FCI), and is synchronized with the 25 ns bunch crossing interval. This 40 MHz domain is widely used throughout the chip's internal circuits. Timing alignment with the bunch crossing is achieved using a DLL, which allows phase tuning of the 40 MHz clock. Users can select the optimal clock phase to synchronize internal operations with the bunch crossing. The ASIC also provides a 40 MHz clock output for testing purposes. The CBC consists of 254 channels, each equipped with a pre-amplifier, post-amplifier, and comparator. These circuits convert the charge from the silicon sensors into binary hit data. The ASIC services 127 strips from each of two sensor layers, with multiplexing logic that supports layer swapping. The analog front-end amplifiers can be stimulated by an on-chip test pulse generator, triggered by a fast command from the FCI. After hit detection, the data follows two paths: one path goes directly to a 512-depth pipeline memory, while the other is sent to the Stub Finding Logic (SFL) for stub generation.

4.2 CIC

The primary function of the CIC [41] is to collect digital data from sensor signals processed by the front-end (FE) chips. Each CIC chip manages data from a group of eight FE chips. In 2S modules, the FE chips are CBCs, while in PS modules, they are MPAs. The CIC is responsible for transmitting the collected data to the lpGBT.

To ensure signal integrity and minimize noise—particularly noise induced by the large number of lines on the hybrid—all connections between the FE chips and the CIC, as well as between the CIC and the lpGBT, are differential, operating at a data rate of 320 Mbps. Each FE chip connects to the CIC through six differential lines at 320 Mbps, totaling 48 lines per CIC. Additionally, there are 6 or 7 differential lines between each CIC and the lpGBT, operating at either 320 Mbps or 640 Mbps, depending on the configuration.

Each module is equipped with two CIC chips to handle data from both sides of the module. The top-level architecture of the CIC is primarily divided into two main components: the Front-End (FE) blocks and the Output block.

- **Front-End (FE) Blocks:** These blocks process data received from the eight FE chips connected to the CIC. A dedicated block is implemented for each FE chip, and each FE block handles both trigger data and L1 data independently. The processing of trigger data is identical for both types

of FE chips (CBC and MPA). However, there are three distinct modes for handling L1 data:

  - **CBC Sparsified:** In this mode, the CBC L1 data is received by the CIC in unsparsified form, and sparsification is performed within the FE block to achieve the necessary data compression for output.
  - **CBC Deserialized:** This is a debug mode that allows the transmission of raw CBC data directly from the CIC without sparsification. It supports operation up to an L1 Acceptance (L1A) rate of 100 kHz.
  - **MPA Deserialized:** For MPA chips, the L1 data is already sparsified before reaching the CIC, so no further processing is needed within the FE block.

- **Output Block:** This block aggregates the data from the eight FE blocks and formats the combined data into an output packet suitable for transmission to the lpGBT.

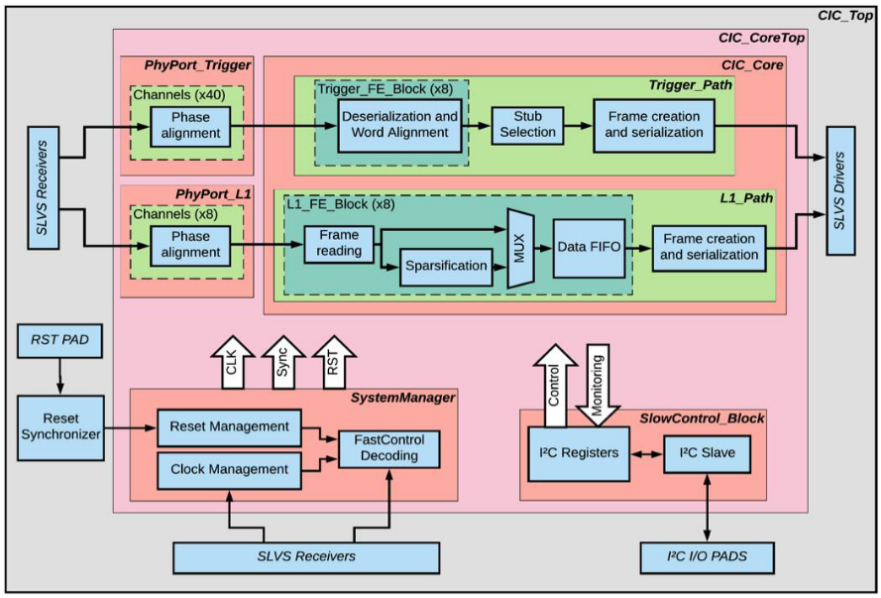

Figure 4.9: CIC2 Block diagram[41].

The CIC initially interacts with incoming data through its physical (phy) ports, as illustrated in the top-level diagram in Figure 4.9. These ports synchronize the incoming data with the CIC's internal 320 MHz clock. This synchronization is essential because, although all ASICs on the module operate on a common clock

sourced from the lpGBT, the CIC must determine the precise phase for accurate sampling.

The phase aligner blocks used in the CIC are derived from those developed for the lpGBT. Within these blocks, the input lines are grouped into phy ports, with each port handling four input data lines that operate at the same frequency but may have different phases. In the CIC, while the data line frequencies are identical, the optimal sampling phase can differ due to timing mismatches between front-end ASICs or routing delays on the hybrid. The CIC's phy ports can fine-tune the sampling phase with a resolution of 391 ps, corresponding to one-eighth of the 3.125 ns clock period at 320 MHz.

During the setup process, the system automatically determines the best sampling phase values. Only values that span the duration of a complete clock cycle are valid. To identify the optimal alignment, the CIC requires a consistent input data pattern. Once the phase tuning process is initiated, the chip confirms whether the alignment is successful for each of the 48 input lines. When the CIC is mounted on a hybrid, this alignment is typically a one-time operation, as the timing delays across lines remain stable. Once established, the optimal sampling phase settings can be programmed via the I2C interface.

Additionally, the CIC includes the capability to bypass both the phy ports and the core logic. This feature allows data from one selected phy port to be routed directly to the CIC's output lines. The user can configure which phy port is bypassed, providing direct access to raw, unprocessed input data from the front-end chips. This diagnostic tool is valuable for troubleshooting and verifying signal integrity from the front-end ASICs.

4.2.1 CIC stub data path and formats

Stub data arrives at a frequency of 40 MHz. To correctly identify the initial bit of each word, the CIC requires word alignment patterns for each of the five stub data lines. Confirmation of successful word alignment is provided via an I2C register, and the alignment pattern may differ between lines. This alignment process compensates for timing discrepancies of up to 9.375 ns between lines from different chips and is also essential for BX0 alignment.

The CIC contains eight stub reconstruction blocks, one for each front-end chip, which output up to six stubs per CBC at a rate of 20 MHz to the stub selection logic. In this stage, stubs from eight consecutive BXs are collected and sorted based on their bend values. The selected stubs are then passed to the frame creation and serialization process, where a header is added, and the stub data is formatted for output. The exact output format depends on the CIC configuration, with all available options listed in Table 4.1.

The configuration of the CIC depends not only on the type of front-end chip

Table 4.1: 320 MHz stub data configurations for the CIC for CBC of 2S module[41].

Bend info	Bend info present		Bend info not present	
#Output lines	5	6	5	6
Width of a single stub (bits)	18		14	
Max #stubs/boxcar	16	19	20	25
#Output (bits)	320	384	320	384

but also on the number of output lines selected, which is five in FEC12 mode. Additionally, there is an option to include or exclude bend information in the payload. Selecting more output lines or omitting bend information allows the CIC to transmit more stubs. However, bend information is typically not required for standard operation since the Level-1 (L1) trigger system is unlikely to use it for track reconstruction. Nevertheless, including bend information can be valuable for validating the stub sorting logic within the CIC.

Figure 4.10 shows an example of the stub data format output by the CIC. A data frame includes eight consecutive bunch crossings, referred to as a boxcar in CMS DAQ terminology. To ensure the stub packages from the front-end chips are compiled starting from the correct bunch crossing, BX0 alignment is performed. The alignment status is accessible via an I2C register. Accurate BX0 alignment is essential to ensure that all CICs in the Outer Tracker synchronize their starting bunch crossing as BX0.

Each stub boxcar begins with a header that indicates the CIC configuration—whether operating in PS or 2S mode—along with nine status bits representing the CIC and the front-end chips. The CIC error bit is set if a stub overflow occurs or if an incorrect synchronization bit is received. For CBC front-end chips, the status bits reflect any error flags from the eight CBC stub packages or indicate synchronization errors. The header also contains the bunch crossing ID and the total number of stubs in the payload. The payload itself includes the stub data as delivered from the front-end chips. Each stub entry contains the address and bend information. Additionally, the payload is tagged with the chip ID and the timing offset of the stub within the CIC stub boxcar.

4.2.2 CIC full-event data path and formats

The CIC's frame reading section actively searches for the header of the full-event data frame emitted by the front-end chip within a predefined time window following the reception of the L1A trigger. If the header is not identified within this window, the system flags a time-out error. For data generated by the MPA, which is sparsified, it is directly transferred to the data FIFO assigned to each chip. In

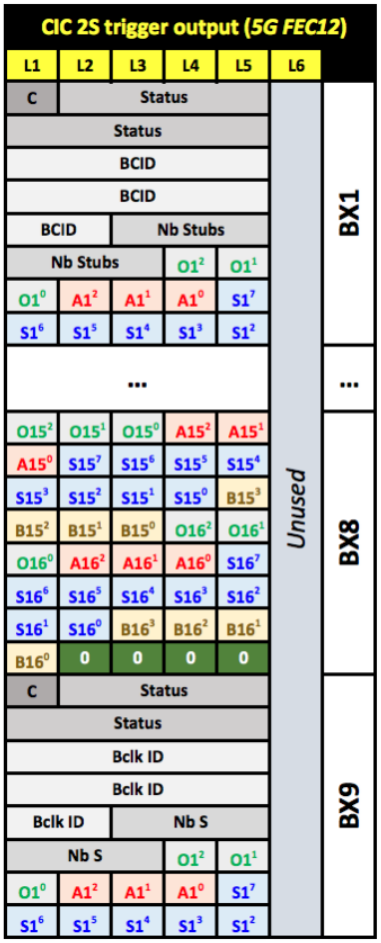

C	CIC configuration: MPA or CBC
Status	Status bits
BCID	Bunch clock ID
Nb Stubs	Number of stubs in block
OX^Y	BX offset for stub X (bit Y)
AX^Y	Chip ID for stub X (bit Y)
SX^Y	Stub address for stub X (bit Y)
BX^Y	Bend info for stub X (bit Y)
ZX^Y	Z-info for stub X (bit Y)

Figure 4.10: CIC output trigger data format[41].

contrast, data from the CBC can be processed in two ways: either by saving the entire unsparsified data frame into the FIFO or by performing clusterization on the CBC full-event data frame and storing the resulting sparsified data.

Data is written to the FIFO only if the CIC's internal L1 counter matches the L1 counter in the incoming full-event frame and if the trailer bit is valid. If there is a mismatch or an invalid trailer bit, an empty frame with error flags is written to the FIFO. The width of the FIFO defines the maximum cluster occupancy that can be stored per chip, while its depth limits the short-term trigger rate handling capability of the CIC. Specifically, in CIC1, each front-end chip is equipped with a FIFO of depth 10 and width 550 bits, allowing it to store the entire unsparsified CBC full-event frame.

The frame creation block then retrieves data from the FIFOs to assemble the full-event data packet, which represents the sensor image for half of a module.

The output configuration for this process is shown in Figure 4.11. The serialized full-event data is transmitted through a single output line from the CIC. The maximum number of clusters that can be contained in one CIC package is limited to 127.

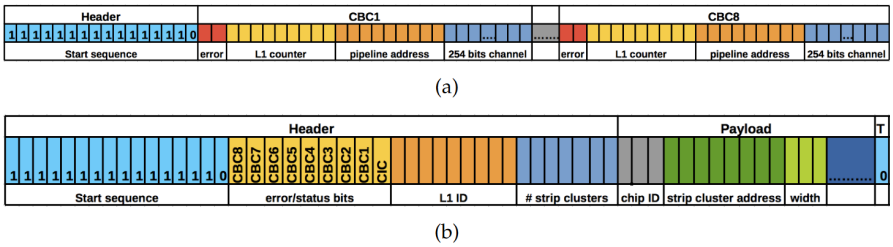

Figure 4.11: The full-event data frame format output by the CIC chip: TOP: CIC-2S in unsparsified mode; Bottom: CIC-2S in sparsified mode[41].

However, this level of occupancy exceeds what the CIC bandwidth can continuously support. The available bandwidth allows for a sustained cluster occupancy of approximately 25 clusters per CIC for each L1A trigger, assuming the CIC operates at a frequency of 320 MHz [41].

4.3 Service hybrid

Every tracker module within the CMS framework is designed to operate independently, with its own dedicated suite of services. The services hybrid [3] acts as the central hub for all connections to the backend and its associated electronic components. This includes the DC-DC converters, which generate the required voltages for both the front-end electronics—set at 1.0 V and 1.25 V—and the optoelectronics, set at 2.55 V, following a dual-stage power supply architecture.

Additionally, the services hybrid incorporates miniature high-voltage (HV) connectors for the sensor bias circuits; the lpGBT chip, which handles serialization and deserialization of data to and from the backend, manages front-end ASIC communication, distributes clock and trigger signals, and performs local monitoring functions; and the VTRx+ transceiver, which converts all bidirectional data between optical and electrical domains.

4.4 lpGBT

The lpGBT [42] is a radiation-tolerant ASIC designed to enable high-speed bidirectional data transfer in high-energy physics experiments.

Some key functionalities of the lpGBT are outlined below:

- **High-Speed Data Transfer:** The lpGBT supports downlink data rates of 2.56 Gbps and uplink data rates of either 5.12 Gbps or 10.24 Gbps, depending on the operational mode.

- **Diverse Data Paths:** It incorporates three primary data paths: Timing, Trigger, and Control (TTC); Data Acquisition (DAQ); and Slow Control. Each path is designed to meet the specific bandwidth and latency requirements of its corresponding data type, ensuring efficient and reliable data handling.

- **Radiation Hardness:** Fabricated using advanced 65 nm CMOS technology, the lpGBT employs specialized layout techniques to withstand Total Ionizing Dose (TID), Non-Ionizing Energy Loss (NIEL), and Single-Event Upsets (SEU), ensuring reliable operation in harsh radiation environments.

- **Error Correction:** To mitigate data corruption in radiation-prone environments, the lpGBT is equipped with robust error detection and correction mechanisms, including Forward Error Correction (FEC), to maintain data integrity during long-distance transmissions.

- **Advanced Clock Management:** The ASIC features sophisticated clock management systems, including Clock and Data Recovery (CDR) and a Phase-Locked Loop (PLL), to recover clock signals from incoming data streams with high precision.

- **Versatile Interfaces:** The lpGBT offers multiple interfaces, including high-speed electrical links for front-end modules, a programmable general-purpose I/O port, and I2C master interfaces for controlling external devices. These interfaces provide flexibility for diverse control, communication, and monitoring tasks.

- **Integrated Peripherals:** The chip includes integrated peripherals such as a 10-bit Analog-to-Digital Converter (ADC) with multiple input channels, on-chip temperature sensors, and programmable current sources, enhancing its capabilities for sensor readout and environmental monitoring.

- **Configurability and Monitoring:** The lpGBT features extensive configurability via a comprehensive set of programmable registers. It also provides diagnostic functions and real-time status monitoring, which are crucial for ensuring reliable data transmission [42].

4.5 VTRX+

The VTRx+ module [43] is an advanced optical transceiver developed for the Versatile Link Plus (VL+) project, designed to support multi-gigabit-per-second optical data transmission in HL-LHC experiments.

The VTRx+ offers a versatile configuration, adaptable either at the time of assembly or by disabling unused channels according to user requirements. This flexibility enables various operational modes tailored to different transmission needs. The module integrates a vertical-cavity surface-emitting laser (VCSEL) (Vertical-Cavity Surface-Emitting Laser), radiation-tolerant laser driver ASICs, PIN photodiodes, and a radiation-tolerant transimpedance amplifier (Trans-Impedance Amplifier (TIA)).

The VTRx+ facilitates high-speed optical data transmission. Upstream channels (Tx, from the 2S module to the DAQ) support data rates of up to 10.24 Gbps, while downstream channels (Rx, from the DAQ to the 2S module) operate at up to 2.56 Gbps. This capacity ensures efficient data transfer in demanding experimental environments. The module supports bidirectional communication, with the number of uplink (front-end to back-end) and downlink (back-end to front-end) channels configurable. The default configuration includes four transmitters (Tx) and one receiver (Rx), but alternative setups, such as 4 Tx only or 1 Tx and 1 Rx, are possible by modifying the channel allocation.

Figure 4.12 illustrates the Versatile Link Plus system and the key components of the VTRx+. The module is engineered for reliable operation under extreme environmental conditions, including exposure to high levels of ionizing radiation (1 MGy total dose, 1×10^{15} n/cm^2 and 1×10^{15} h/cm^2 total fluence) and a wide temperature range from −35 °C to 65 °C. These characteristics make the VTRx+ suitable for the harsh conditions expected at the HL-LHC.

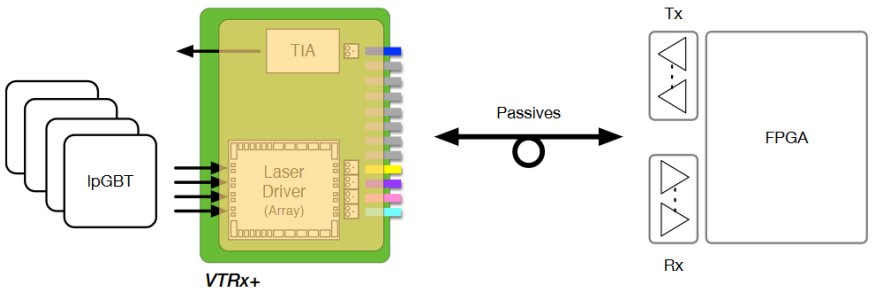

Figure 4.12: Overview of the Versatile Link + system showing the components of the VTRx+[43].

The module's optical interface is designed to manage vertically-emitted light

from the VCSEL, redirecting it through 90 degrees into the optical fiber. This precise optical coupling is essential for ensuring efficient signal transmission.

Chapter 5

Assembly of 2S Modules

The assembly of the 2S module involves several techniques and tools that must guarantee strict quality criteria for the assembled module. In the following sections, at first the mechanical structure and specifications of the 2S module will be introduced, then different steps involved in the assembly procedure and testing will be explained as they are implemented at the time of writing. Several steps in module assembly, prior to glue dispensing, require height measurements. These include the automatic localization of 12 jigs, jig tilt measurement, and the determination of the height between the dispenser tip and the sensor backside. The implementation of these height measurement procedures in the gluing robot, which constitutes part of the author's contribution, will be described in Chapter 6.

5.1 Mechanical structure of the 2S Module

In this section, we focus on the mechanical components of the 2S module and discuss its structure and main mechanical specifications[44]. These include the Aluminum-Carbon Fiber (AlCF) bridges, Polyimide Isolators (PI) isolators, and High Voltage (HV) tails. An exploded view of the 2S module is shown in Figure 5.1.

The two sensors are mounted back-to-back via the AlCF bridges, forming the bare module. Then on a larger scale, they provide mechanical connections between the bare module and the FEH and SEH, completing the 2S module structure. The bridges are made of AlCF, which offers two key advantages. First, it has a high thermal conductivity(~230 W/m·K [45]), allowing heat dissipation through contact with cooling pipes. Second, its coefficient of thermal expansion is similar to that of silicon (~2.4 ppm/K [45]), which helps to minimize mechanical stresses on sensors due to temperature change. Depending on the module's location in

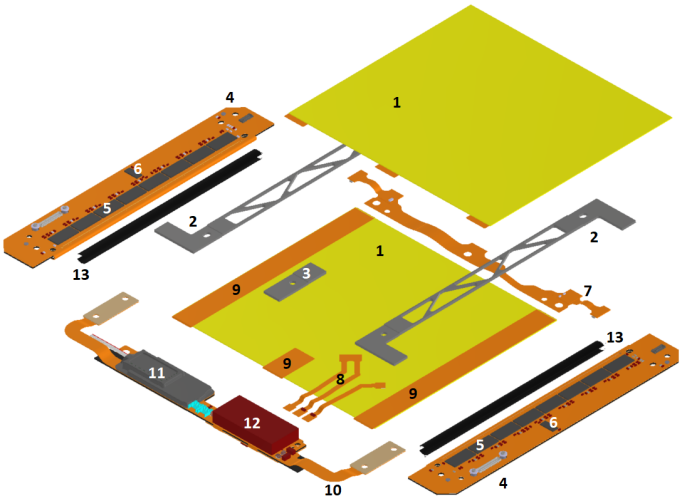

1 Silicon strip sensor
2 Al-CF spacer
3 Al-CF short spacer
4 Front-End Hybrid
5 CBC
6 CIC
7 Ground balancer
8 HV pigtails
9 PI strips
10 Service hybrid
11 VTRx+
12 DC-DC converter
13 Wire bounded

Figure 5.1: An exploded view of the Strip Sensors (2S) module components with 1.8 mm bridges and five cooling contacts.

the outer tracker layers and the level of radiation exposure, 2S modules may include either five or six cooling contact points. Accordingly, AlCF bridges come in two thicknesses—1.8 mm and 4.0 mm—which determine the spacing between the sensors. In terms of length, there are two types of bridges: long (also called main bridges) and short (also called stump bridges). As shown in Figure 5.1, each module includes two long AlCF bridges (annotated as item 2) and two short AlCF bridges (annotated as item 3). The long AlCF bridges are positioned near the FEH side of the sensors. The short AlCF bridges are placed near the SEH side, in the middle of the module. In configurations with six cooling contacts, an additional short bridge is placed opposite the SEH side.

Since the backside of each sensor is biased with high voltage, it must be electrically insulated from the conductive AlCF bridges. This insulation strips (annotated as item 9 in Figure 5.1) are DuPont Kapton®MT [46] and made of PI, which has a thermal conductivity of 0.45 W/(m·K) and a nominal thickness of approximately 25 μm. Two different lengths of PI strips are used to cover the lengths of the long and short AlCF bridges. The dimensions of the polyimide strips are listed in Table 5.1.

The HV tails, annotated as item 8 in Figure 5.1, deliver high voltage from the SEH to the backside of the sensor via bonding wires that will be placed during module assembly. Two designs exist: a U-shaped HV tail for the top sensor and an I-shaped HV tail for the bottom sensor. The U-shaped HV tail also includes an integrated temperature sensor for measuring the temperature of the sensor.

Figure 5.2 also shows a sectional view of the two strip sensors glued to the AlCF

Table 5.1: Specifications of PI strips used for 2S module assembly.

Components	Specification
Short PI strips	$10.1^{+1.00}_{-0.55}$ mm × $17.26^{+1.00}_{-0.65}$ mm
Long PI strips	$9.8^{+1.00}_{-0.10}$ mm × $95.59^{+1.00}_{-0.10}$ mm

bridges while electrically isolated by the PI strips. In this view, the reference frame is also depicted, which helps define the tilt of the module and geometrical criteria of the module. The tilt is defined as the angle between the strip orientations of the two sensors in the x-y plane. The mechanical tolerances and criteria of the 2S

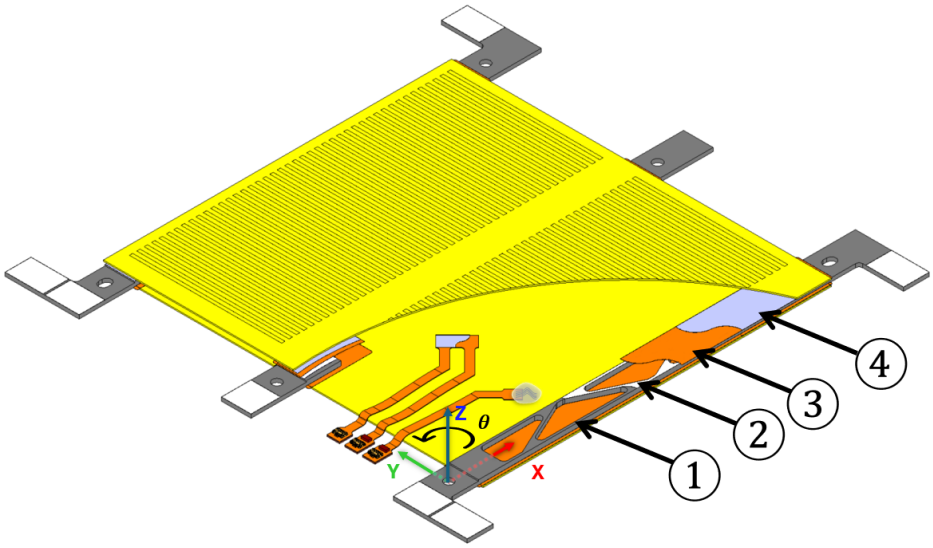

1 Al-CF spacer 3 Polyimide strips (PI)
2 Polytec TC437 4 Polytec 601-LV

Figure 5.2: Section view of bare 2S module with six of 1.8 mm AlCF bridges and the reference frame.The image is not on scale and some strip symbol are placed to show the sensor oriantation.

module components are listed in Table 5.2.

5.2 Assembly procedure

The assembly of 2S modules involves multiple stages and performed in parallel production mode (gluing of 12 sensors in one day, corresponding to the assembly

Table 5.2: Key Mechanical Specifications of the 2S Module[44].

Components placement	**Value**
Angular misalignment between top and bottom sensor strips (projected on XY plane, see 5.2)	< 400 μrad
Maximum out-of-plane deviation of main bridge cooling contact points	< 1 mm
Maximum longitudinal offset between top and bottom sensor strips (along strip direction, Y direction in 5.2)	< 100 μm
Maximum transverse offset between top and bottom sensor strips (orthogonal direction, X direction in 5.2)	< 50 μm
Maximum XY positional error of stump corners and bridge mounting holes	≤ 100 μm
Maximum alignment error between sensor and hybrid bond pads in the direction perpendicular to strips	< 180 μm
Gap between sensor edges and readout hybrid	200 ± 100 μm
Placement accuracy of PI with respect to sensor edges	≤ 200 μm
Glue thickness	
Minimum encapsulant thickness above wire loop (Sylgard 186)	> 100 μm
Maximum encapsulant thickness above wire loop (Sylgard 186)	< 300 μm
Maximum total encapsulant mass for readout wires (Sylgard 186)	< 5 g
Average glue layer thickness between PI and sensors (Polytec 601-LV)	< 25 μm
Average glue layer thickness between AlCF bridges and PI (Polytec TC437)	< 50 μm
Average glue layer thickness between hybrids and AlCF bridges (Polytec TC437)	< 50 μm

of 6 modules in parallel), the complete workflow typically requires approximately 8 working days. This extended timeframe is necessary to accommodate the curing periods of the two-component adhesives used during assembly. To ensure precise alignment of components, custom jigs are employed at various stages of the module assembly. These jigs, characterized by their precise and reliable design, enable the parallel execution of on batches of modules that are at different stage of the assembly steps. This section describes the various steps, tools, and tests involved in the assembly of 2S modules. Before initiating the assembly process, it is essential to perform a thorough quality inspection of all components. This inspection is conducted according to the criteria defined by CMS. This step minimizes the loss of good components that would otherwise be discarded if assembled with non-conforming parts.

5.2.1 Preparation and components check

The first step in the module assembly process involves the inspection of various components[47] to ensure that all received parts are undamaged and meet the required quality standards. This includes checking the IV curve of the sensors to ensure their electrical integrity. The IV measurement setup is shown in Figure 5.4. It featured a light-tight box, flashed with dry air, because the sensors are sensitive to humidity and to light. Measurement are taken after 10 minutes in an ambient relative humidity below 20%. The bias voltage is provided by a Keithley 6517A source and measure unit [48]. This apparatus also measure the leakage current with a resolution of $100pA$ in range of $0 - 20\mu A$. The leakage current must not exceed 7.25 μA and 10 μA at 600 V and 800 V, respectively[49].

A visual inspection of the sensors is also performed to detect any scratches on the top and bottom surfaces. The noise levels of the individual channels of the FEHs must be measured to determine whether they fall within acceptable ranges, as deviations in noise levels may indicate underlying issues or potential malfunctions in the electronic circuitry of the FEHs. All electrical components, including the SEHs, must be inspected for missing or damaged electronic components, cracks on the PCBs, or contamination of contact pads. The dimensions of the PI strips are measured using image processing techniques to verify compliance with the specified tolerances.

The flatness of the AlCF main bridges and stumps is evaluated to ensure mechanical conformity. Flatness is defined as the maximum distance between the highest and lowest points on a surface relative to the best-fit reference plane across that surface. The CAD schematic of the bridges, showing the flatness constraints on the surfaces intended for gluing, is presented in Figure 5.3 and Table 6.16.

Table 5.3: Tolerances of the different sections of the AlCF bridges and stumps[50][51]. A schematic diagram of them are shown in Figure 5.3

Section	Specification (mm)
Area A	< 0.5
Area B and C	< 0.01
Common zone	< 0.1
Stump	< 0.01

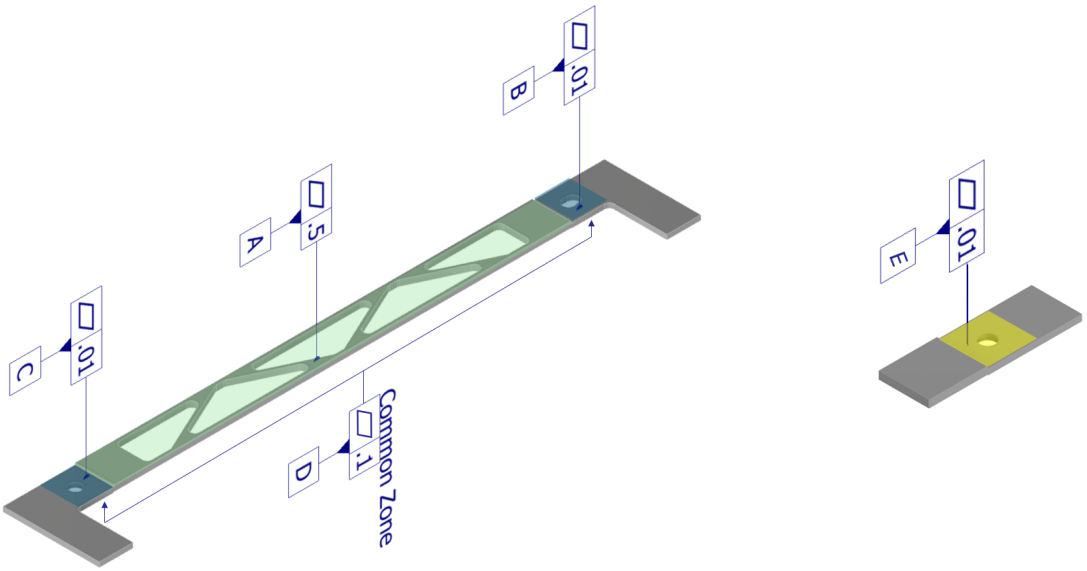

Figure 5.3: Flatness constraints for different parts of the 1.8 mm AlCF bridges. Units are in mm. Left: Long AlCF bridges. Right: Stump AlCF bridges.

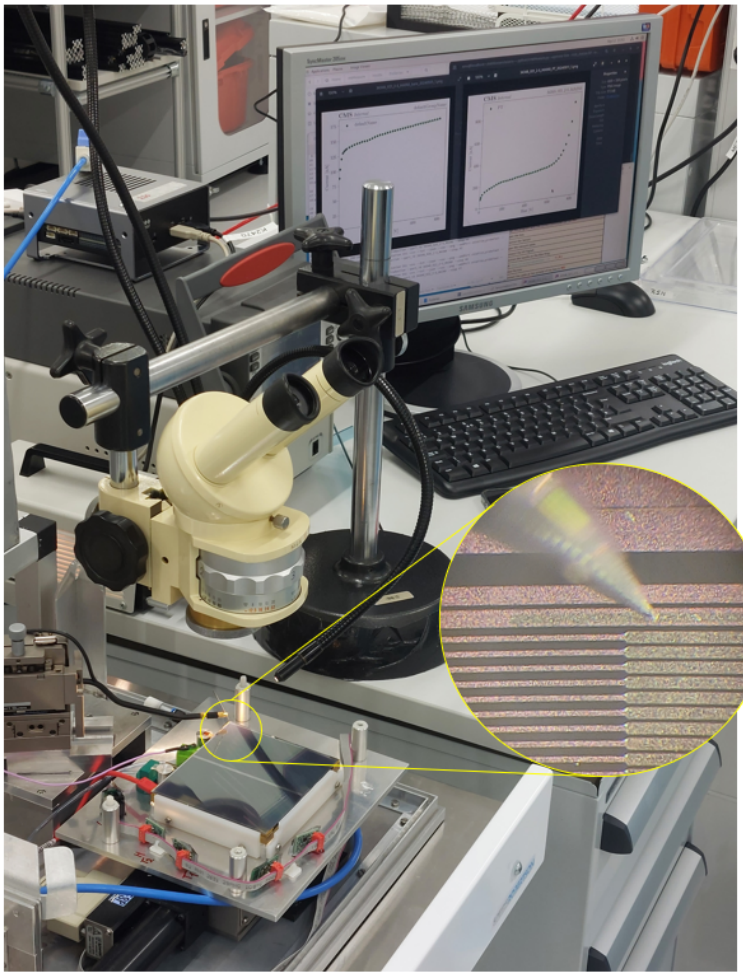

Figure 5.4: A picture of the IV measurement setup in the clean room at the IIHE. In this image, the light-tight cover has been removed to adjust the Karl Suss probe needle onto the sensor bias ring using a microscope. The bias voltage is provided by a Keithley 6517A Source and Measure Unit, connected either directly to the backplane of the bare sensor or via a High-voltage (HV) pigtail added to the backplane of the sensor.

5.2.2 PI and HV tails gluing

The first assembly step consist in gluing PI isolator strips and HV tails to the backside of the sensors, with precision of the order of 100 μm in x and y. This is done for 12 sensors in parallel on the robot shown in Figure 5.5. The glue is dispensed by a syringe that needs to be always at the same distance from the sensor backside with a precision of also 100 μm, to maintain a uniform glue line and a 95 % wetting of the surface to be glued. Therefore, each jig must be located in position and orientation, relative to the tip of the glue-dispensing syringe. The jig position calibration relies on a laser sensor that is one of the contribution of the author of this thesis, and is further discussed in Chapter 6. The sensors themselves are positioned on the jig against stoppers, and maintained fixed by vacuum during glue curing.

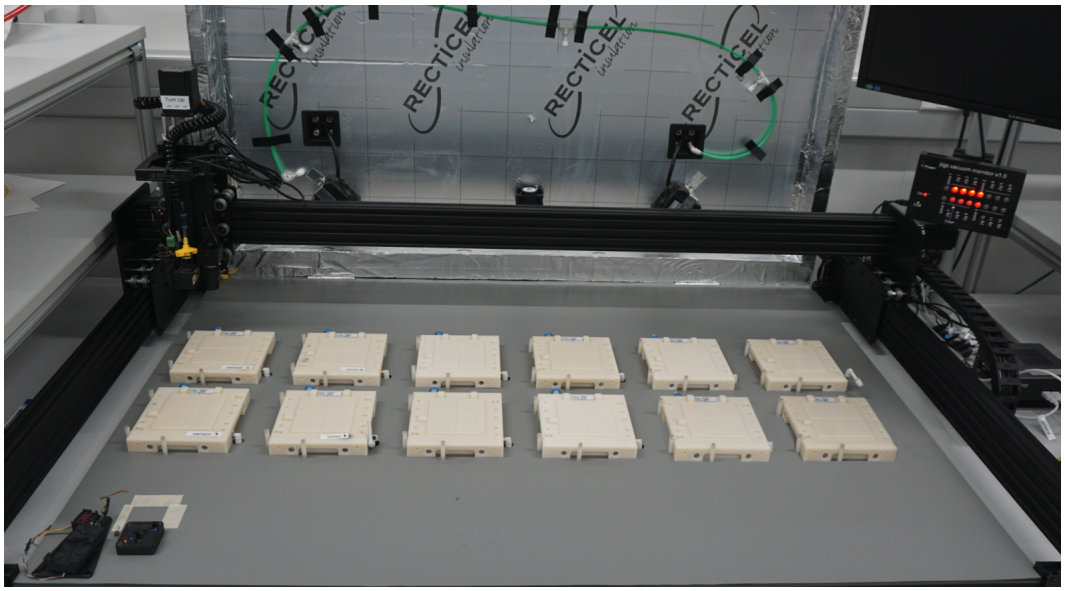

Figure 5.5: A picture of the gluing robot with 12 sensor gluing jigs.

The gluing robot then dispenses glue lines on the backside of the sensor for the long and short PI strips, and dispenses short line glue for the HV tails. Once glue dispensing is complete, each PI strip is positioned on an aluminum pickup bar, aligned using an L-shaped mechanical stopper. A few drops of isopropyl alcohol are applied to the bar surface to temporarily hold the strip. Once the PI strip is aligned, the stopper is removed, and the strip is transferred to the sensor gluing jig using the pickup bar. These bars have alignment pins on both sides that fit into precisely drilled holes on the jig to ensure correct positioning. The schematic image of the nominal position of the AlCF and PI on backside of the sensor is shown in image 5.6. After the strips are in place, the HV tails are transferred to

the back side of the sensors. A dedicated aluminum pickup bar with a magnetic holder is used to transfer each HV tail to its respective position. After curing, a specialized key tool is then used to detach the magnetic holder. The strips and HV tails are transferred one by one. The entire process must be completed within a few hours, as the glue begins to cure. PI and HV tail gluing processes are shown in image 5.7. The PI and HV tails gluing jig was co-designed by IIHE and KIT, and was machined in the bulk of an ESD-safe polymer plate at UCLouvain.

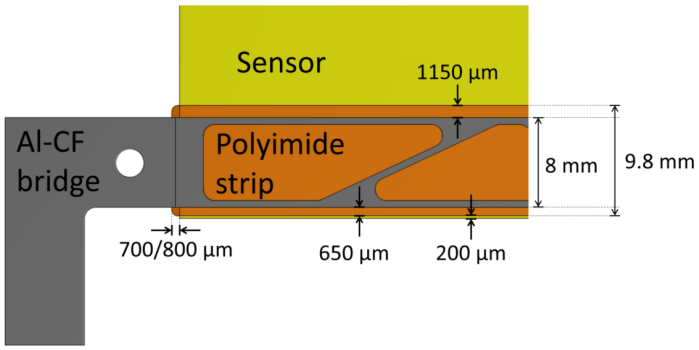

Figure 5.6: The nominal placement of the long PI strip and AlCF on the sensor backplane.

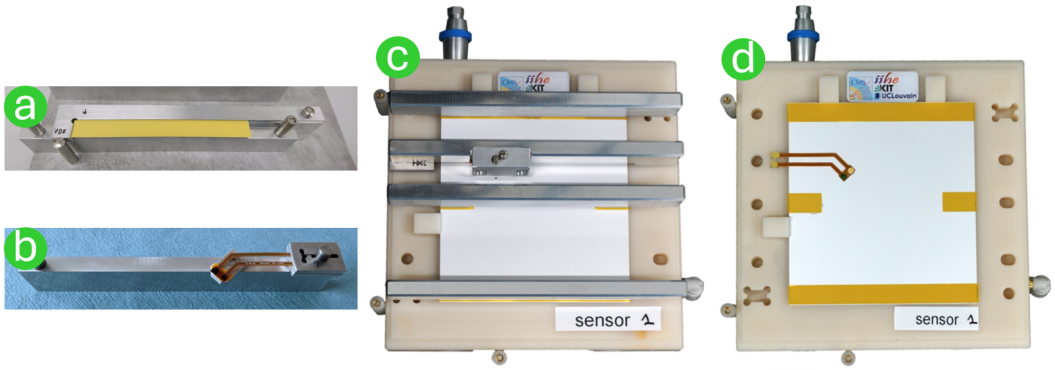

Figure 5.7: The process of PI strip and HV tail gluing is illustrated in this image. (a): the long PI pickup tool equipped with an L-shaped stopper. (b): the HV tail pickup tool with magnetic holders. (c): all pickup tools are placed on the backside of a glued functional sensor, which is mounted on an ESD-safe gluing jig. (d): the final configuration of PI strips and HV tail after curing and removal of the pickup tools.

5.2.3 HV tails wire bonding

To establish the electrical connection between the backside of the sensor and the HV tails, between 10 and 20 wire bonds are made in accordance with the specified requirements. Wire bonding is performed using a commercial Hesse BondJet 820 bonding machine [52]. For the encapsulation of the wire bonds, Sylgard 186 [53] is used. The encapsulation is prepared using appropriate dosing and mixing devices. A volumetric hand-operated glue dispenser is used to manually apply a drop of glue on top of the bonded wires, ensuring mechanical protection and insulation. The process of HV tails wire bonding and encapsulating are shown in Figure 5.8. One day is required for curing the glue however, it could be accelerated by the curing system. After wire bonding the HV tails, the IV of the modules is measured to evaluate the quality of them.

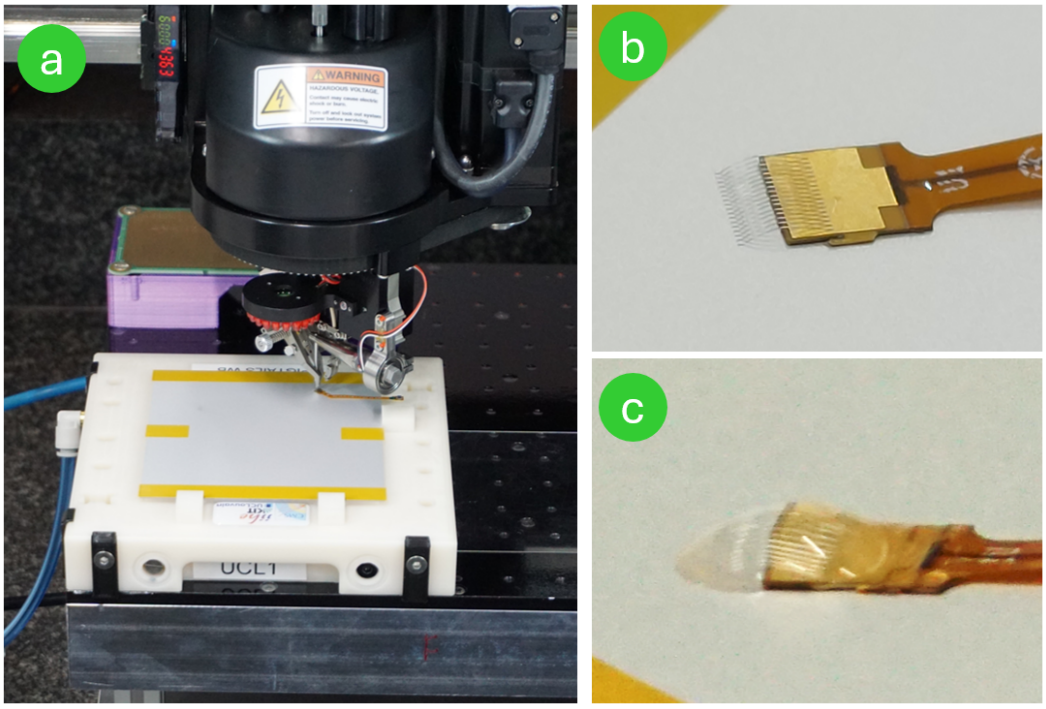

Figure 5.8: High-voltage (HV) tail wire bonding and encapsulation process is illustrated in this image. (a) The photo shows the HV tail glued to the bottom sensor backplane, while a wire bonding machine is placing between 10 and 20 wires connecting the HV tail pad to the sensor backplane. (b) The HV tail pad and the sensor backplane after wire bonding and (c) encapsulation.

5.2.4 Sensor sandwich gluing

The process of attaching the sensors to the AlCF bridges to form a sensor sandwich is performed using a specialized gluing jig, as illustrated in Figure 5.9. This procedure requires high precision, particularly in the alignment of the two sensors. To maintain proper alignment:

- The displacement offset perpendicular to the strip direction must not exceed 50 μm,
- The displacement along the strip direction is limited to 100 μm, and
- The rotational misalignment, defined as the angular difference between the top and bottom sensor strips, must be less than 400 μrad.

The assembly begins with the bottom sensor, which is positioned on the jig so that its edges contact three mechanical stoppers. The alignment is verified using a microscope mounted on a rail system. Once aligned, vacuum suction is applied from the base plate to hold the sensor securely in place. For the gluing procedure, Polytec TC437[54] is used. After dosing and mixing, the glue is transferred onto a special application plate and spread evenly using a bar to form a layer with a thickness of 100 μm. After inserting the alignment pins into the bar, four AlCF bridges—two long and two stump—for a single module with six cooling contact points are placed on the glue layer to be coated. The bridges are then moved to another slot on the plate so that both sides are coated. Once coated, the bridges are precisely aligned using guiding pins and placed onto the glued PI strips on the backside of the bottom sensor. The top sensor is then positioned similarly by aligning its edges with the three stoppers and held in place by gently applied springs. The stopper-to-sensor edge contact is again verified under the microscope. A weight plate is carefully placed on top to apply uniform pressure during curing. Guiding pins ensure accurate placement of the weight plate, preventing scratches and ensuring an even force distribution on the assembly. The glue requires one day to cure at room temperature. However, this setup is equipped with an isolator cover to increase the temperature to accelerate curing. After curing, the weight is removed, completing the sensor sandwich structure and the bare module is transferred to the carrier plate.

5.2.5 Metrology

After curing, sensor alignment is evaluated using the metrology setup, which is shown in Figure 5.10. This setup features a fully automated system that controls an XYZ stage and, through image processing, measures the positions of fiducial markers located at the four corners of the sensor, as well as reference points given

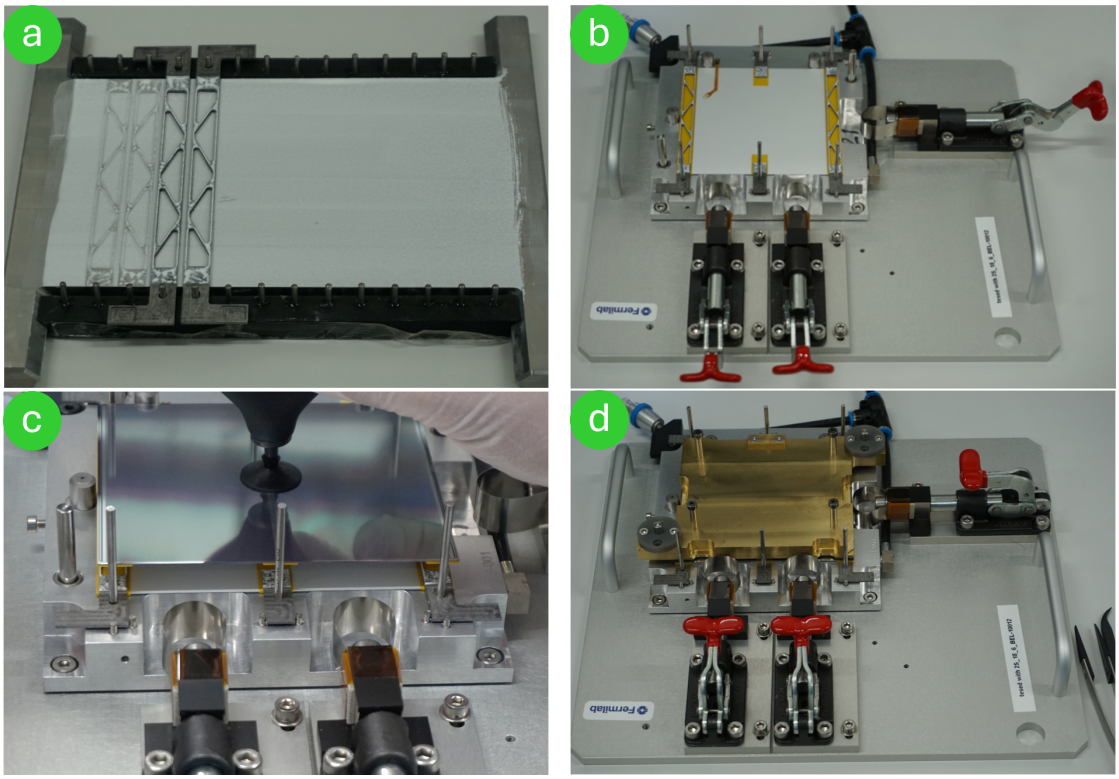

Figure 5.9: Some images of the sandwich gluing process is illustrated step-by-step: (a) Long AlCF bridges are positioned on the gluing plate and aligned using pins. One side of each bridge is coated with Polytec TC437 adhesive. (b) A bottom sensor is placed onto the gluing setup, and the pre-glued AlCF bridges are positioned on top of it, aligned precisely with the guide pins. (c) A top sensor is carefully placed onto the AlCF bridges using a vacuum pickup bulb. (d) A weight plate is placed on top while the springs are engaged.

by the tips of four needles mounted on the carrier plate and visible from both sides of the carrier plate. By repeating this measurement for both the top and bottom sides of the bare module, the rotational tilt between the two sensors can be calculated with high accuracy of 40 μrad (2σ)[55] to ensure reliable and repeatable sensor alignment verification.

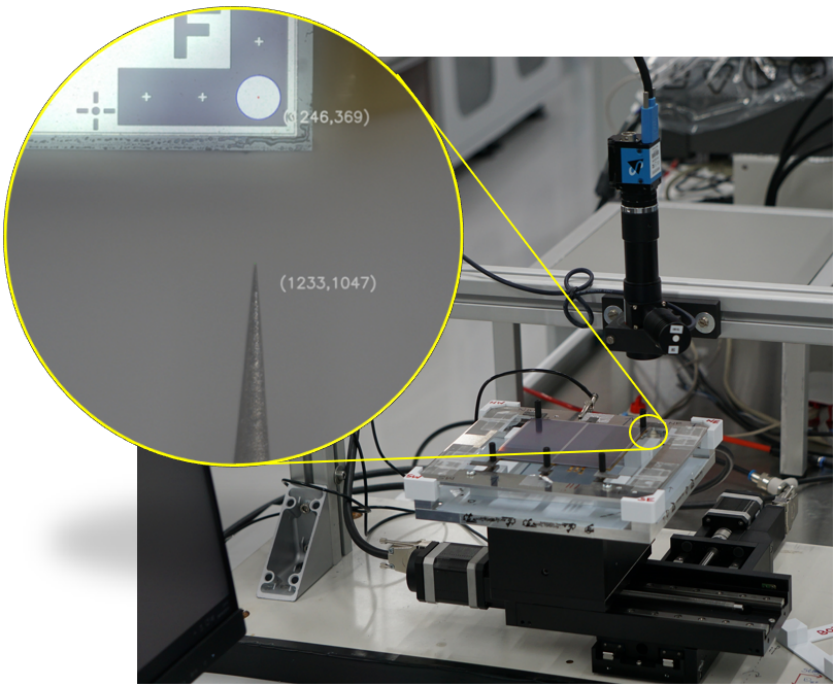

Figure 5.10: The metrology setup is shown in this image. It consists of a high-precision XYZ stage with a microscope mounted above it. The relative alignment of the top and bottom sensors is determined by measuring the positions of fiducial marks located at the four corners of each sensor with respect to the tips of four alignment needles, one placed at each corner.

5.2.6 Hybrid gluing

Following the precise alignment and attachment of the sensors, the next step involves attaching and gluing the hybrids to the sensor sandwich. At this stage, it is necessary to prepare and bend the tails of the SEH and the ground balancer to compensate for any misalignment with the FEHs. By employing a set of dedicated bending tools, the tails on both sides of the SEH and the ground balancer are bent twice to form an S-shape, allowing proper mechanical fit and connector alignment. The next step is to glue and attach the FEHs and SEH to the bare module using a dedicated hybrid gluing jig. A key feature of this jig is the presence of adjustable

brass rails with precision-drilled holes, which align with the FEH pins to set the distance between the FEHs and the bare module to approximately 100 μm. On the hybrid gluing jig, the bare module is placed first, followed by the skeleton. After aligning and adjusting the jig with all components in position, the alignment of the bonding pads between the FEHs and the sensor is checked at all corners using a microscope. If the alignment is confirmed, the skeleton is temporarily removed, and a small amount of Polytec TC437 adhesive (approximately 3 mg) is carefully brushed onto each "ear" of the AlCF bridges. The skeleton, including the ground balancer, is then repositioned onto the glue-coated contact areas and aligned using guide pins. The glued contact points are secured using magnetic pushers to ensure proper pressure during curing. The process of hybrid gluing is shown in image 5.11. After approximately one day, the glue is fully cured, and the module can be transferred to the carrier plate. However, the gluing jig is equipped with a thermal cover and integrated heater, which can be used to accelerate the curing process if required.

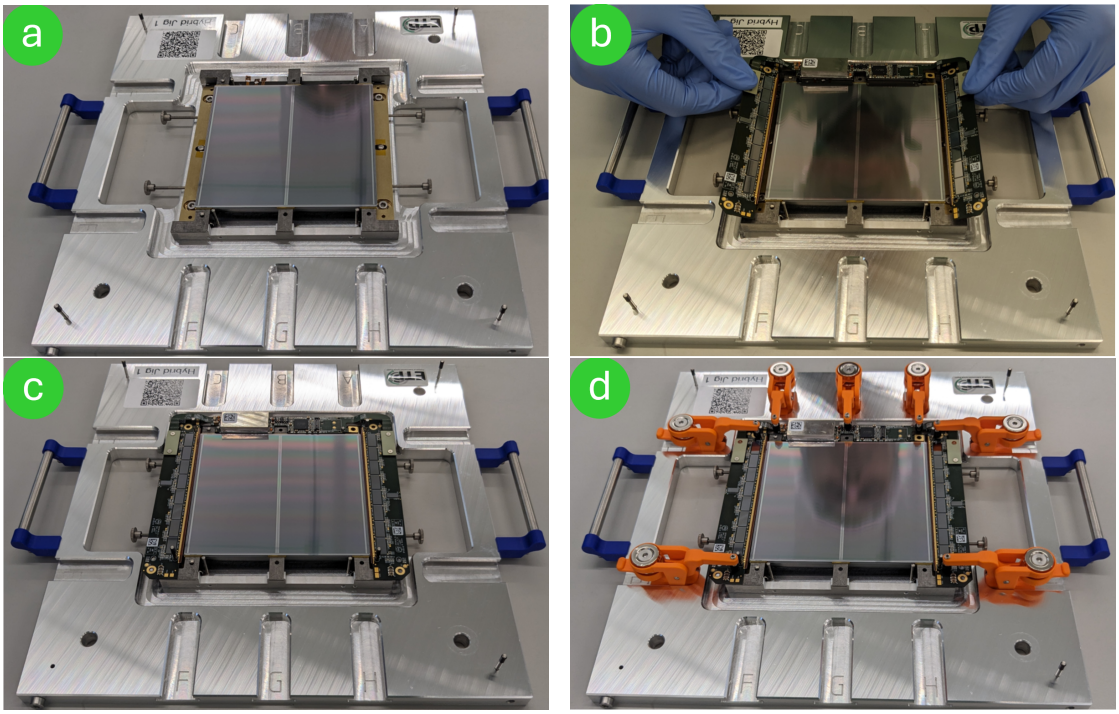

Figure 5.11: The images of the hybrid gluing process are shown: (a) The bare module is placed on the hybrid gluing jig and aligned using pins. (b) The skeleton is positioned on top of the bare module after applying Polytec TC437 adhesive to the AlCF ear areas. (c) The hybrids are aligned, and pushers are engaged to ensure uniform pressure during the bonding process.

5.2.7 Pull test and wire bonding

At this stage of assembly, to connect the sensor strips to the readout chips located on the FEHs, the module is transferred to the wire bonding jig. The jig is equipped with alignment pins that fit into the AlCF bridge holes and features rubber feet connected to a vacuum system, which firmly holds the module in place from the bottom side. After completing the calibration process, ten test bonds are placed on each FEH on dedicated test pads, one bond for each CBC chip, and one bond on each side of the FEH. The wires are made of aluminum with a diameter of 25 μm, and the bonding machine uses ultrasonic vibration to weld the wire to the bond pad as shown in image 5.12-a. Following this initial bonding, the module is moved to the pull-test machine[56], where the wire bonds are tested to evaluate their mechanical strength and bonding quality (see Figure 5.12-b and c). The performance criteria for the pull test are defined as follows:

- A mean pull force greater than 8 g,
- A Root Mean Square (RMS) less than 10% of the mean,
- Bond lift occurs in fewer than 20% of the tests.

Once the wire bond quality is confirmed, the module is returned to the wire bonding machine for full-scale bonding. At this stage, all sensor channels are bonded, with 1,016 wires per FEH. Additionally, the ground pads of the FEHs are bonded to the sensor bias ring to put the sensor strips to ground potential. Once bonding on the top sensor is completed, the module is flipped to repeat the bonding process on the bottom sensor.

Table 5.4: Key dimensional specifications of the 2S Module bonds.

Specification	**Value**
Number of backplane bias wires per sensor	10 to 20
Maximum bond wire height above sensor surface (backplane bias)	< 400 μm
Maximum bond wire height above sensor surface (readout)	< 700 μm
Minimum bond wire height from sensor cut edge (readout)	> 200 μm

5.2.8 Readout system

After completing the full electrical connection between the sensor strips and the readout system via wire bonding, the module is tested again in the readout test box as shown in Figure 5.13. The readout system includes a Karlsruher InfraRed

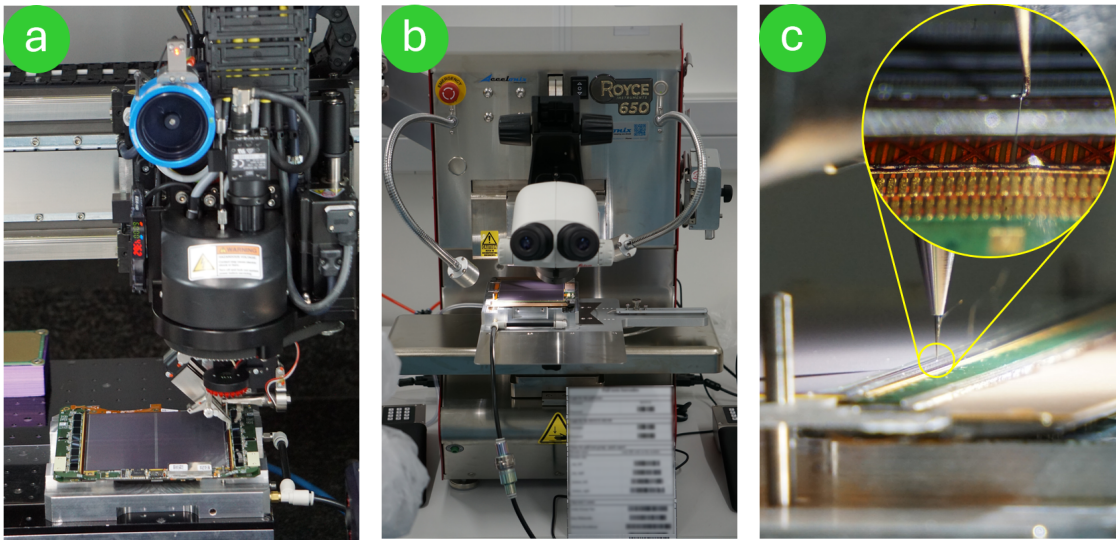

Figure 5.12: The wire bonding and pull testing process are shown: (a) A module placed inside the wire bonding machine during the placement of test bonds. (b) A photograph of the pull tester machine used for bond strength evaluation. (c) A close-up image showing the hook of the pull tester positioned below a test wire just before force application.

Array (KIRA) box and a graphical interface known as the Graphical Interface for Phase-2 Tracker Objects (GIPHT)[57]. The infrared arrays can be used to stimulate charge in the silicon detector for further investigations on the strips, whereas they were not employed during the standard readout tests. To read out a module, the system requires external power supplies, including a low voltage source (Rhode & Schwarz HMP4040)[58], a high voltage source (Keithley 2410)[59], and an FC7 readout board. Through a standard communication protocol, (GIPHT) provides full control over these devices and the associated measurement processes. It enables the measurement of channel noise levels, the IV characteristics of the module, and visualizes the results through integrated plotting tools. Additionally, the measurement data can be uploaded directly to a centralized database for tracking and documentation purposes. During this step, low voltage (LV) cables and VTRx+ are added between the module and the carrier plate connector. Then by connecting LV, HV and optical connectors to the carrier plate, and applying LV, HV at a safe value of 350 V, the integrity of the wire bonds is evaluated, and any issues such as shorts or disconnected pads are identified. The verification is performed by analyzing the noise levels on each channel, as the noise level is directly related to channel capacitance. A lower-than-expected noise level typically indicates a disconnected channel, while higher noise levels may suggest that adjacent channels are shorted together.

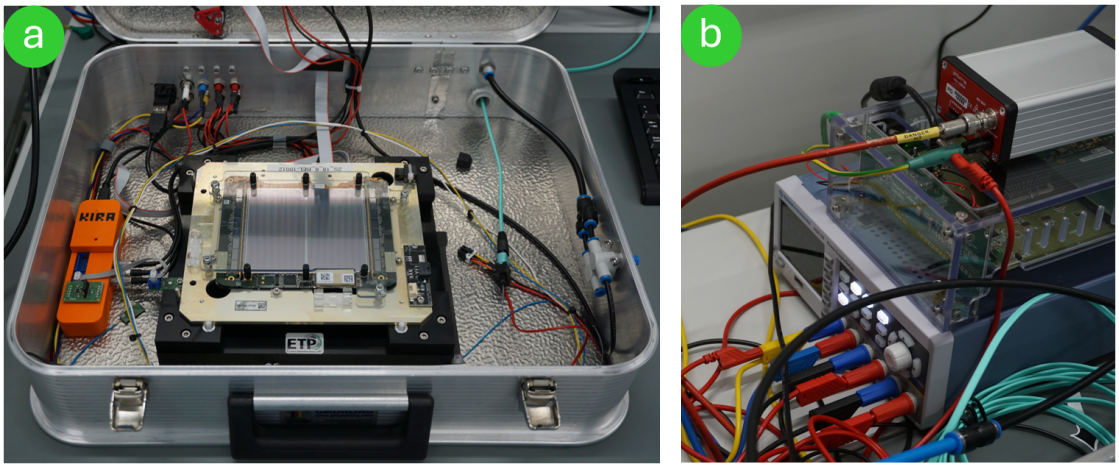

Figure 5.13: Images of the readout test system are shown: (a) A wire-bonded module placed inside the (KIRA) box for testing. (b) The electronic equipment used in the test setup: (Top) High-voltage supply unit; (Middle) FC7 DAQ system; (Bottom) Low-voltage power supply.

5.2.9 Bonded wire encapsulation

After wire bonding and verification of the connections using the readout test system, the bond wires must be protected from mechanical damage by encapsulation. For this purpose, the same robot as used for PI gluing is used. The carrier plate with the module is placed onto the table of the dispensing machine and aligned using three mechanical stopper bolts and located in 3D as for the PI gluing jig.Once the machine is calibrated, the encapsulation glue is dispensed along the bond rows on both the left and right sides of the module (see Figure 5.14). This process covers the wire bonds connected to the sensor strips as well as those on the sensor bias ring. The glue is applied in a spiral pattern, with the dispenser tip maintained approximately 200 μm above the bond wires to ensure a continuous glue line. The total encapsulation mass on the module is 2.2 g. At the end of the process, the VTRx+ shield must also be manually glued using a glue gun, applying adhesive around the VTRx+ transceiver to prevent light leakage from its embedded laser (At present, it is not clear whether the light shield will be glued onto the VTRx+, as this is still under evaluation by the CMS Outer Tracker group). Although, the curing time of the Sylgard 186 is 48 hours at room temperature, the module, after undergoes a 24-hour curing period, can be repositioned upside down in the carrier to encapsulate the bond wires of the bottom sensor, followed by an additional 24-hour curing cycle. At present, the curing time is reduced by warming the modules to 25$^{\circ}C$. After 24 hours, the module undergoes the final readout test and IV measurement up to 800 V.

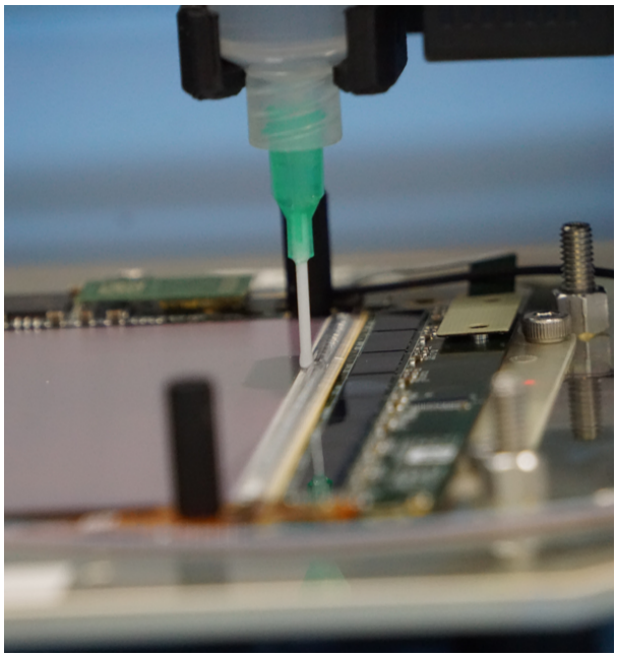

Figure 5.14: Image showing the encapsulation needle positioned above the bonded wires during the application of Sylgard 186.

5.2.10 Burn-in setup

The burn-in setup is designed to ensure the long-term reliability and functionality of the 2S module which is shown in Figure 5.15. During burn-in testing, the module is subjected to multiple thermal cycles, transitioning from the assembly temperature down to the operational temperature of -35°C, typically for a minimum of 10 complete cycles which takes about 32 hours. The burn-in setup has a capacity of 10 modules. Between thermal cycles, the noise levels of the readout channels are measured to evaluate the potential impact of thermal stress on the electrical performance. Variations in noise levels can reveal degradation in sensor performance, bound integrity, ASIC stability, or interconnect integrity. This procedure helps to identify early failures or latent defects in the sensors, bounds, front-end electronics, and other critical components of the module, ensuring only robust modules proceed to final integration.

It is notable that the measurement data from various tests are stored in both local and central databases, ensuring accessibility for review whenever required.

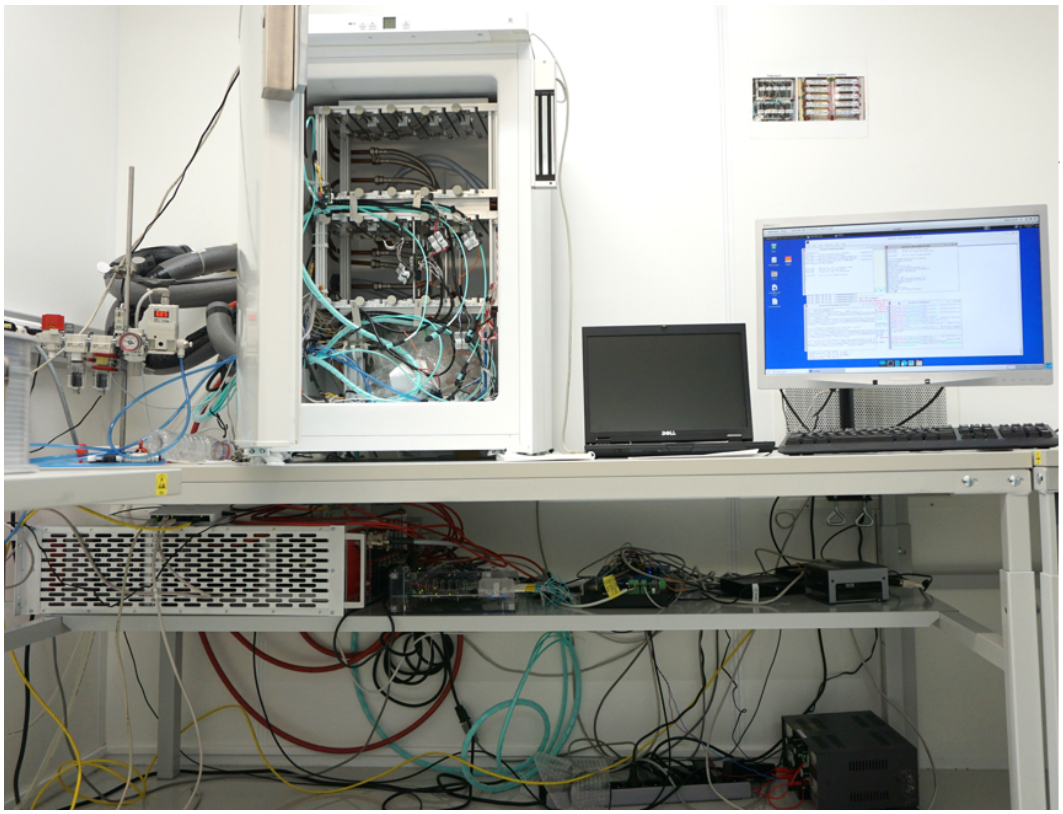

Figure 5.15: Image of the burn-in test setup, including the refrigerator and screen located on top of the table. The bottom of the table contains the high-voltage supply, DAQ system, controller, and interconnecting cables are shown.

5.2.11 Storage and shipment

After completing all assembly steps, the modules that successfully pass all required tests and meet the acceptance criteria defined by CMS are transferred to a dry cabinet for storage until shipment to the integration site. For transportation, the modules are placed in the OT Module Transport Box, a dedicated container designed specifically for Outer Tracker modules. This transport box contains eight compartments, each formed from ESD-safe foam, providing both mechanical protection and electrostatic discharge shielding during shipment.

Chapter 6

Height Measurement

In this chapter, at first we will give a general overview on the gluing robot and importance of height measurement then discuss various methods for measuring height for the gluing robot. We will begin by examining the criteria necessary for an effective height measurement technique. Following this, we will propose and analyse two distinct methods. The first is established by the identification of the sharpest image at the working distance range of an optical setup. The second method employs a triangular displacement laser sensor. Both methods will be rigorously evaluated to determine the most appropriate solution for the gluing robot's operations. However, various industrial state-of-the-art methods for non-contact height measurement, such as confocal displacement sensors and interferometric techniques, offer superior precision and robustness. Nevertheless, the sensors required for these methods are considerably more expensive compared to optical image-based height measurement and triangulation laser displacement sensors.

6.1 Gluing robot

The gluing robot is an advanced, highly flexible machine designed to precisely apply glue to a target surface. It is fully designed in IIHE, specially for the assembly of 2S modules. It is composed of several sections and controllers that work together to achieve this task. The robot's primary components are:

- Glue Dispenser: This is located in the head of the robot and is responsible for dispensing glue. A syringe filled with glue is connected to an air pressure regulator to control the flow of glue. A dedicated controller manages the glue flow, which is governed by the central controller.
- Motors: The robot is equipped with motors that move the glue dispenser

in X, Y and Z over the desired surface. These motors are managed by a controller board, which is also controlled by the central controller.

- Camera: A camera is installed on the robot head to capture images for further quality check.
- Scale for Glue Flow Calibration: A digital scale is used to calibrate the flow of glue, ensuring accurate dispensing. This scale is connected and controlled by the central controller.
- Z Calibration Sensor: A switch is directly linked to the motors' controller, stopping the motor during Z calibration of the dispensing needle upon detecting touch.
- XY Calibration: An optical sensor is used for XY calibration of dispensing needle, further increasing the precision and speed of the calibration. Also, the controller can send signals directly to the motors' controller.

The image 6.1 illustrates a section of the gluing robot, highlighting various fixture components and the robotic head. Key elements are marked with color outlines: the camera in green, the triangular displacement laser sensor in red, the glue syringe dispenser in pink, the digital scale for glue flow calibration in orange, the optoelectric sensors for X and Y calibration in cyan, and the motors in blue. Figure 6.2 illustrates a general block diagram of the different sections and controllers of the gluing robot, providing an overview of how these components are interconnected and managed.

6.2 Height measurement requirements

Direct calibration of the needle position in the Z direction on the sensitive surface, such as the fragile sensor surface or bonding wires, is not feasible due to the risk of damage. Consequently, the height setting for gluing above these surfaces is approximate and lacks full accuracy. Maintaining a continuous flow of glue, which is essential for 2S module assembly, requires precise control of the dispensing needle's height. This is because the glue's wetting behavior depends on its viscosity and surface tension. There is therefore a crucial need for a non-contact precise height measurement system. The stage at which the gluing machine is used in the module assembly is depicted in the workflow diagram of the 2S module assembly, as shown in Figure 8.1. For the application of Kapton strips and Pigtails gluing, the machine must dispense adhesive onto the back side of the sensor. Silicon sensors are particularly sensitive; any scratches can lead to leakage current and noise, compromising the sensor's efficiency. To prevent scratches on the sensor's

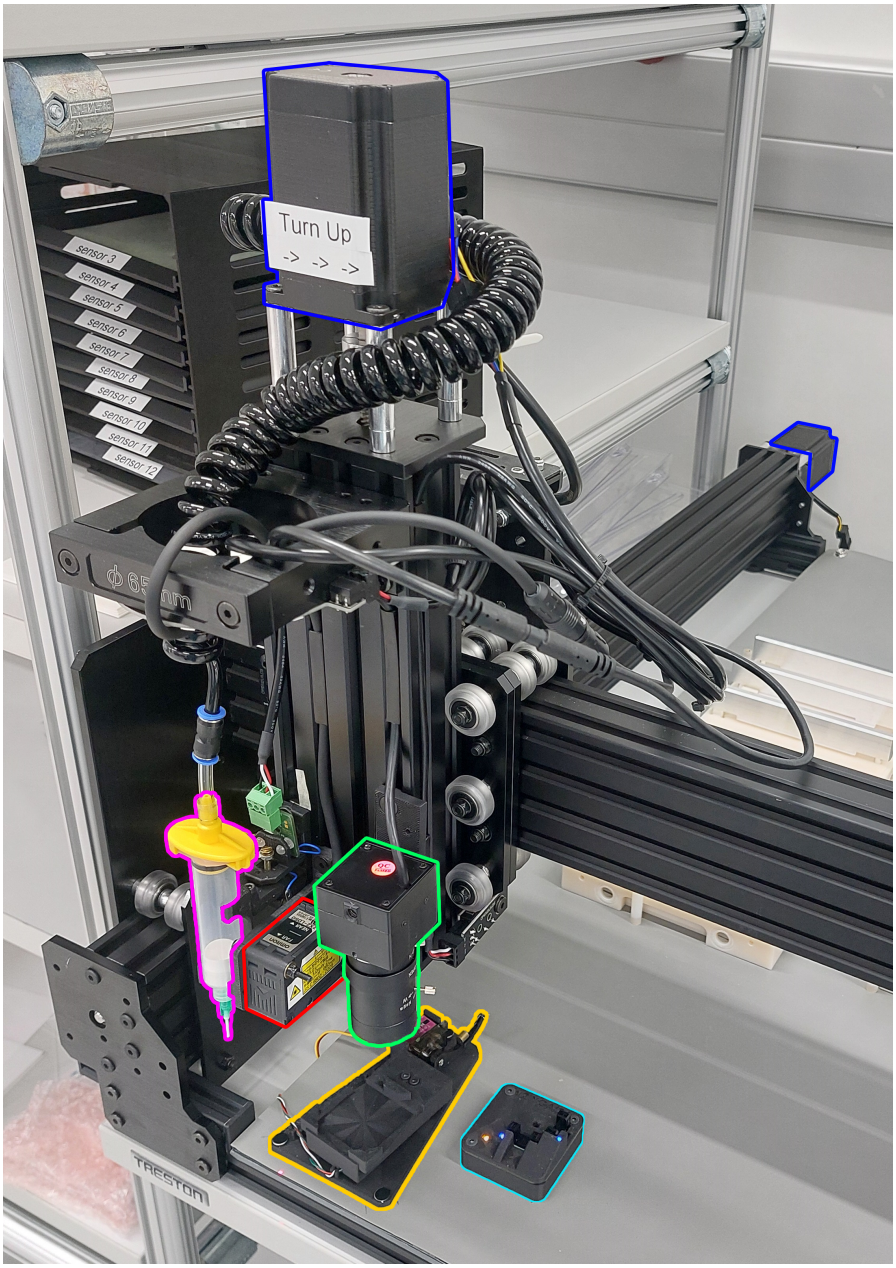

Figure 6.1: A part of the gluing robot including fixture parts and the head are shown in the image. The camera is outlined in green, the triangular displacement laser sensor in red, the dispenser glue syringe in pink, the digital scale for glue flow calibration in orange, the optoelectric sensors for X and Y calibration in cyan, and the motors in blue.

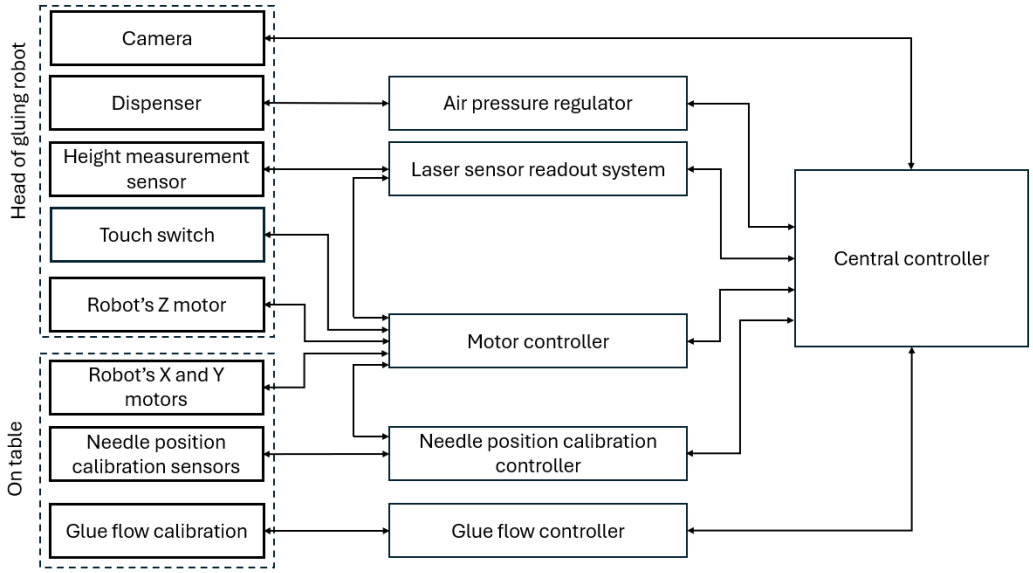

Figure 6.2: A detailed block diagram presenting the different sections and controllers of the gluing robot, as well as the interconnection of components. The controllers are located outside of the gluing robot workspace (under the table).

back side, the height must not be less than $100\mu m$. This height ensures that vibrations and movements of the machine do not cause damage.

In addition, for kapton strip gluing, the height at which the dispensing needle operates impacts the quality of the glue line. A height of $300\mu m$ is roughly the point at which droplets begin to form, resulting in an uneven line[60]. At greater heights, reproducibility decreases, hence the optimal height for gluing is $200 \pm 100\mu m$.

During encapsulation, the gluing robot must operate above wires over a distance of $10cm$ with a minimal margin of error. The target height for encapsulation near bonds is also $200 \pm 100\mu m$. The height of the needle above the wire loops should ideally be measured.

During prototyping, we checked flatness of AlCF bridges using the height measurement system, the surface of which is black and absorb light. However, the backside of the sensors is diffusely reflective, whereas the dummy sensors used during practice have specular reflection, which poses a challenge. Also, calibration and object detection is performed on the surface of jigs made from brushed metal, which is shiny and has irregular reflection.

The working distance of the height measurement method must exceed the height of the tallest object in the setup to prevent the dispensing needle from colliding with objects in the targeted gluing area.

Measurements indicate that the tallest objects are the aligning pins on the kapton strip jig, with a height of approximately $11mm$ and for flexibility of using different type of jigs, the working distance of the height measurement method should be higher than this value.

However, while the minimum step size of movement in the z-direction ($2.5\mu m$) or a smaller value could be the ideal target for the precision of the height measurement method, a maximum acceptable precision of $20\mu m$ (one-tenth of the measurement range) is considered.

Another aspect to consider is the weight of the height measurement system. Since it needs to be installed on the head with other equipments, it should be as lightweight as possible. Additionally, the response time is critical, as the system must perform several measurements at different stages. Therefore, it should be as fast as possible, ideally less than 10 seconds. The summary of the height measurements requirements are listed in Table 6.1. The different surfaces are depicted in Figures 6.3.

Table 6.1: Summary of height measurement's requirements.

Measurement method type	non-contact
Precision	$\sim 2.5\mu m$ Maximum $20\mu m$
Working distance	$\geq 11mm$
Weight	As light as possible
Measurement time	$\leq 10s$
Surface type	AlCF bridges back and front side of functional sensor brushed metal jig ESD safe polymer jig

6.3 Optical height measurement

In this study, we measure height by analyzing the sharpness of images captured sequentially at different heights to identify the point of maximum sharpness[61]. We first introduce the principle and various methods for measuring image sharpness. We then compare these methods under different conditions, including the presence of noise, execution time, sensitivity, precision and accuracy, image size, and brightness. Finally, we select the most robust method based on these comparative analyses.

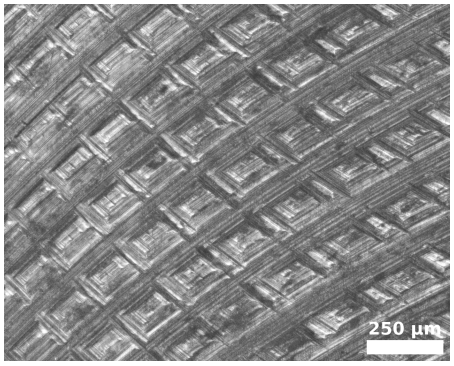

(a) Jig's surface.

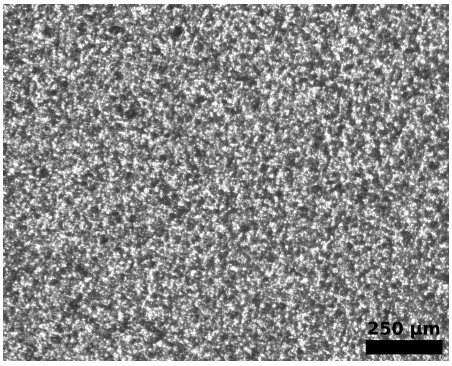

(b) Backside of sensor's surface.

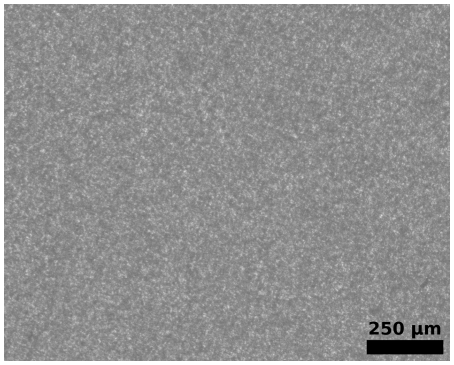

(c) Kapton's surface.

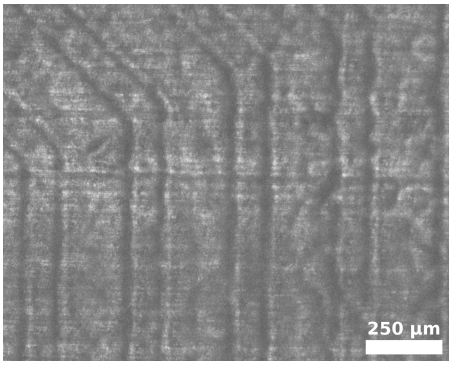

(d) Front end hybrid's surface.

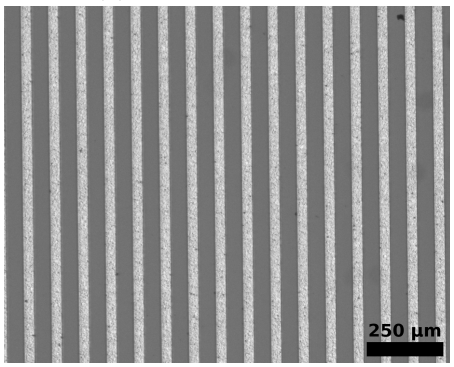

(e) Topside of sensor's surface.

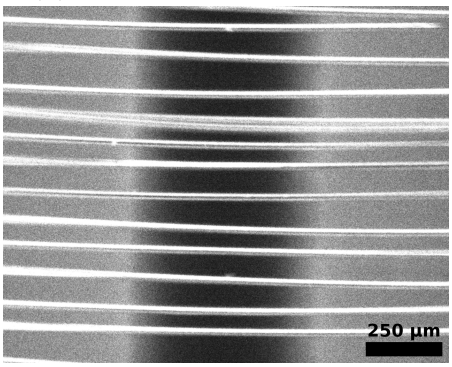

(f) Row of bonding wires.

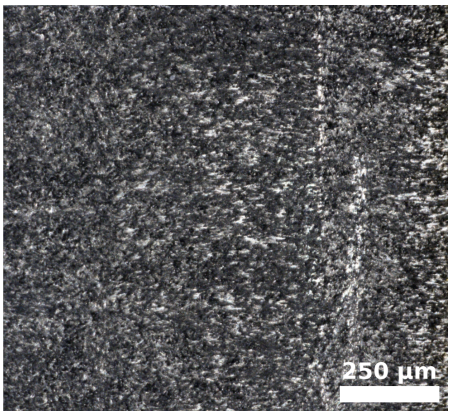

(g) AlCF bridge's surface.

Figure 6.3: Surface of different parts of 2S module which required height measurement during assembly process.

6.3.1 Principle of working

Sharpness is achieved when fine details within the image are clear and distinctly visible. The depth of field is defined as the range of working distance for which a sharp image is obtained. Working distance, depth of field are showed in Figure 6.4. The system consists of a camera for capturing images, an optical lens, and a motorized stage to adjust the position of the camera and lens. By incrementally moving the camera and lens along the Z-axis relative to the object and capturing images at various intervals, the system can compute the sharpness for each image. A graph of sharpness versus the Z-axis position is then generated. Figure 6.5 illustrates Z scanning and measuring sharpness to find the maximum value which occur in focal point.

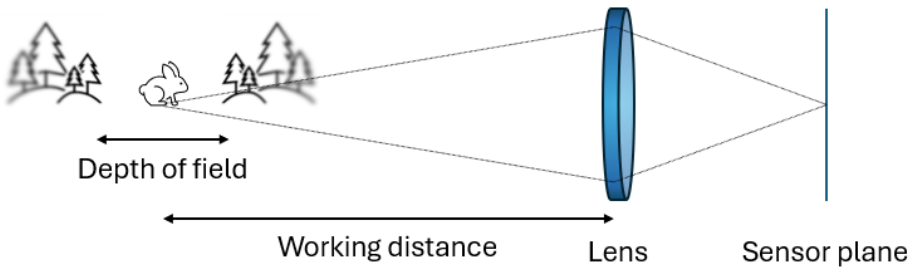

Figure 6.4: The effect of depth of field on sharpness and working distance are illustrated in this picture.

To study and examine this method we used a metrology setup in the clean room. The setup contains a CMOS camera (IMX264LQR)[62] equipped with a telecentric lens (TC5M-30-65C)[63] and two precision linear stages in X and Y (LTM 80-75-HSM)[64] and an elevator stage in Z direction (HVM 60N-12-HIDS)[65]. The long working distance and shallow depth of field of the optical setup make it ideal to investigate the potential of optical height measurement. In this setup, instead of moving the optical parts, there is an elevator stage with a controller to move the object. For image processing the OpenCV library was deployed and for simplicity the images turned to gray scale for image processing. A picture of the metrology setup in the cleanroom is depicted in Figure 6.6. Important specifications of each part of the setup are given shown in Tables 6.2, 6.3 and 6.4.

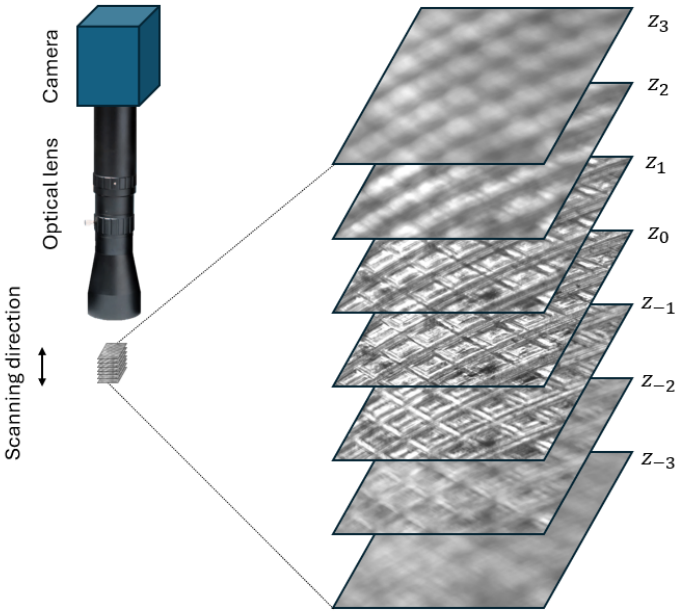

Figure 6.5: Principle of height measurement based on maximum sharpness at focal point is depicted here.

Table 6.2: Specifications of the camera.

Technical Data	Specification
Part number	DFK 33UX264
Resolution	2448×2048
Frame Rate at Full Resolution	38
Sensor Type	Sony IMX264LQR-C
Sensor Format	$\frac{2}{3} inch$
Pixel Size	$3.45 \mu m$
Interface	$USB3.0$
Weight	$65g$
Price[1]	$933.00 Euro$

[1]Price as quoted by nl.sales@stemmer-imaging.com on 25/02/2020.

Table 6.3: Specification of the optical lens.

Technical Data	Specification
Part number	TC5M-30-65C
Magnification	3×
Working Distance (WD)	$65mm$
Depth of Field (DOF)	$42.7\mu m$
Resolution (Object Side)	$2.15\mu m$
Megapixel (max.)	$5MP$
Field of View (FOV)	$2.8mm \times 2.4mm$
Telecentricity	0.02°
Weight	$211g$
Price[2]	$3148.49Euro$

Table 6.4: Specifications of the Z stage and controller.

Technical Data	Specification
Part number	OWIS-HVM 60N-12-HiSM
Motor type	step motor
Range of travel	$12mm$
Load capacity	$max.90N$
Repeatability (bidirectional)	$< 6\mu m$
Positioning error	$< 80\mu m$
Travel per motor revolution	$200\mu m$
Steps/pulses per motor revolution	200

To compute sharpness, it is essential first to ascertain whether the focal point of the optical lens falls within the range of motion of the Z-elevator stage, upon which the targeted surface is placed. Once this has been confirmed, the program may be executed. Initially, the program calibrates the stage and camera, then relocates the stage to the lowest predefined position. From there, it commences the process of image capture, computing the sharpness, and recording the correlation between sharpness and the absolute position of the stage. Subsequently, the stage is incrementally moved in Z direction by defined steps until it reaches the upper limit of the defined range and the range should be at least in order of the lens' depth of field.

The optimal sharpness value, can then be selected straightforwardly. In cases where the optical system features a broad rather than a shallow depth of field, the graph of sharpness versus position will exhibit a plateau instead of a singular

[2]Price as quoted by order@sedeco.nl on 24/02/2020.

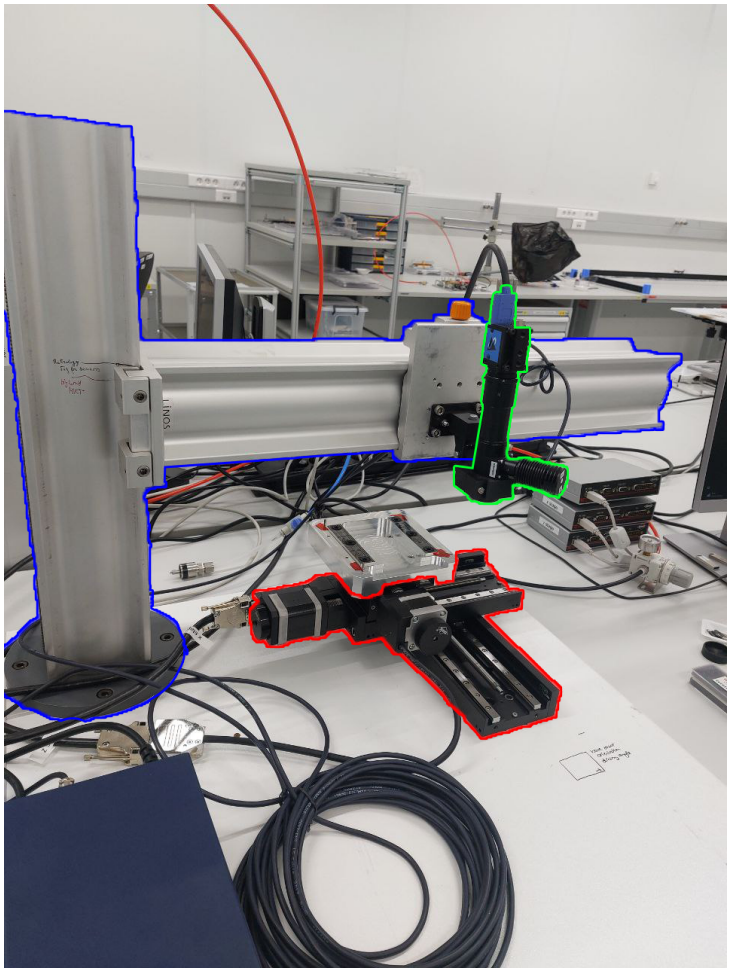

Figure 6.6: Picture of the metrology setup including a camera and optical lens (green color), XYZ linear positioning stage (red color) and a stand (blue color).

maximum. Increasing the aperture of the lens reduces the depth of field but necessitates the use of a larger, heavier and more expensive lens. For more precise measurement, a Gaussian function is fitted to the data, and the mean of this function is designated as the focal point.

6.3.2 Sharpness metrics

The sharpness of an imaging system, which significantly influences its ability to reproduce details, is directly proportional to the system's resolution capability.

Several methods are utilized for measuring sharpness, including edge-based detection, analysis of spatial and frequency domains, and statistical methods. Subsequently, these methods will be examined in detail, and their performance will be evaluated under different conditions relevant to our application.

a) Statistical methods

- **Standard Deviation:** Standard deviation is a measure of variability or dispersion around the mean. Higher standard deviation values indicate more contrast between pixels in an image, which has been linked to sharper images.

$$\sigma = \sqrt{\frac{1}{N}\sum_{i=1}^{N}(I_i - \mu)^2} \tag{6.1}$$

  Here, σ is the standard deviation of the pixel intensities, N is the total number of pixels in the image, I_i represents the intensity of the i^{th} pixel, and μ is the mean intensity of all pixels in the image. Since an in-focus image has more details, then it has larger standard deviation. The sharpness based on standard deviation of images is shown in Figure 6.9a for a variety of photos taken at a range of distances from the back side of the functional sensor.

  Sharpness is intrinsically a spatial attribute, and it depends on the representation of edge transitions and small details. The spatial distribution is not taken into account when measuring overall contrast and variability using the standard deviation of pixel values. Furthermore, higher amounts of noise can distort the standard deviation, creating the appearance of increased sharpness. It is possible for a large amount of noise in an image to be mistakenly seen as sharper than a cleaner image with finer features. It is not very efficient on Kapton strip which are the most homogeneous surface we will encounter.

- **Entropy:** Quantifying the amount of information or unpredictability in the pixel intensity distribution, or quantifying entropy, is another technique based on pixel statics to assess image sharpness. More complexity or information richness is indicated by higher entropy values, which can occasionally, though

not always, directly correlate with perceived sharpness or detail. The process of calculating entropy involves first calculating the image's pixel intensity histogram and then applying the entropy formula to it. The formula for entropy in this context is

$$H = -\sum_{i=1}^{n} p(x_i) \log_2 p(x_i) \tag{6.2}$$

Here, n is the number of distinct pixel intensity values, $p(x_i)$ is the probability that an intensity value x_i will occur, and the formula is applied to all distinct pixel intensity values. [66] This method focuses on the distribution of pixel values rather than their absolute or relative brightness, making it more robust against changes in illumination or exposure that do not affect the actual content information. This method doesn't directly quantify edge sharpness or focus quality. Therefore, it might not always correlate with sharpness, especially when noise contributes significantly to the entropy.

b) Frequency-domain method

- **Energy Ratio:** Another category of studying image sharpness is analyzing the image in the frequency domain. Frequency domain analysis is a powerful technique in image processing and signal analysis that involves converting spatial or time-domain signals into the frequency domain. This transformation provides insights into the different spatial frequency components that make up the signal or image, allowing for a detailed understanding of its characteristics. Frequency domain analysis can reveal the distribution and intensity of various spatial frequencies present, when applied to images, which correspond to different levels of detail within the image.

  The cornerstone of frequency domain analysis is the Fourier Transform. The Fourier Transform decomposes an image into its sinusoidal components, essentially representing it as a sum of waves with varying frequencies and amplitudes. The 2D Fourier Transform of an image produces a 2D spectrum that shows the frequencies present in the image along two main axes.

  In the context of detecting sharpness, frequency domain analysis offers a distinct advantage by providing a way to directly observe the frequency components that characterize sharp edges (high frequencies) versus smooth transitions (low frequencies). Metrics such as the energy ratio of different frequency bands can be calculated to provide a more quantitative assessment of image sharpness. Comparing the energy in the higher frequency bands relative to the entire spectrum can yield a sharpness metric. For example, a higher ratio of high-frequency energy might indicate a sharper image, while a predominance of low-frequency energy could suggest blurriness or smoothness. We

divided the frequency band in to three parts (three radial bands) for low, medium and high frequency. Figure 6.7 displays an overall analysis of an image of brushed metal jig surface, using 2D Fourier transform. It includes three main components: The original grayscale image showing the raw visual data (Top image), the magnitude spectrum derived from the image's 2D Fourier Transform highlighting the frequency content (Middle image), and a plot of the energy ratios across three distinct frequency bands (Bottom image), presented on a logarithmic scale. This analysis helps in understanding the distribution of energy within the image, indicating areas of sharpness and detail.

The ratio of the energy of each band to the total energy of the spectrum is calculated and plotted as a function of height. As it is depicted in Figure 6.8, the ratio decreases for the low frequency (blurry and smooth object) band and increases for the medium and high frequency (with details and sharp) where reaching the height where the image is in focus. The blue curve represents the energy ratio for the low-frequency band. In focused images, where fine details are distinguishable, the energy ratio tends to decrease. This decrease suggests that the overall structure dominates the image content. Conversely, the green and red curves show the energy ratios for medium and high-frequency bands, respectively. In focused images, these bands exhibit an increase in energy ratio. This increase indicates a greater presence of detailed features and textures, which are better captured at higher frequencies.

c) Gradient methods Edge detection algorithms are important in digital image processing, serving as the foundation for analysing image sharpness based on high-frequency content distinctions. These algorithms operate on the principle that well-focused images have significantly more high-frequency content compared to their defocused counterparts. This high-frequency content is characterised by substantial differences in intensity between neighbouring pixels, which indicate the sharpness of the edges within the image. To effectively use this high-frequency information, edge detection techniques use convolution masks. These masks are applied to the image to derive intensity gradients through high pass filtering, which helps identify and enhance the edges. In the following sections, we will delve deeper into specific edge detection algorithms, like Sobel, Canny, and Laplace, examining their methodologies, performance, and implications in further detail.

- **Sobel Operator:** The Sobel operator is employed in edge detection algorithms to highlight edges within an image. By operating as a discrete differentiation operator, this operator approximates the gradient of the image's edges. The Sobel operator returns the gradient vector for every pixel. It performs horizontally and vertically by convolving the image with small, sep-

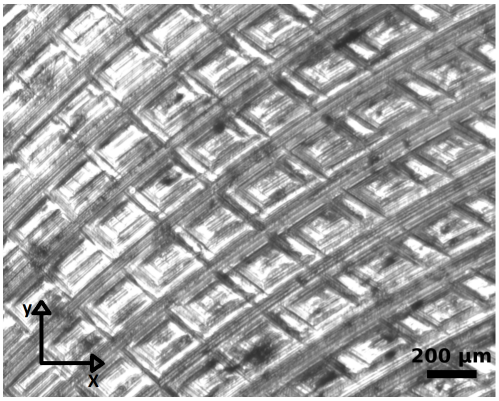

(a) Original Image (surface of brushed metal jig).

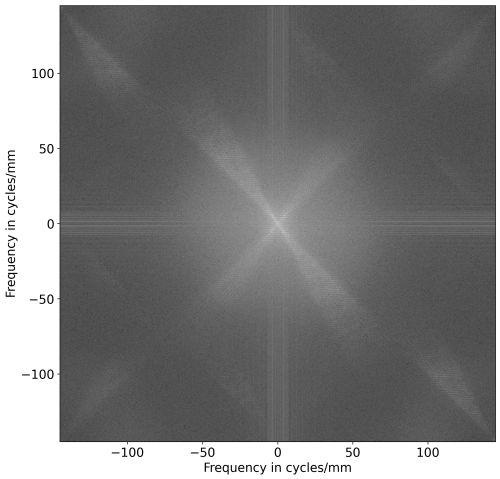

(b) Magnitude Spectrum.

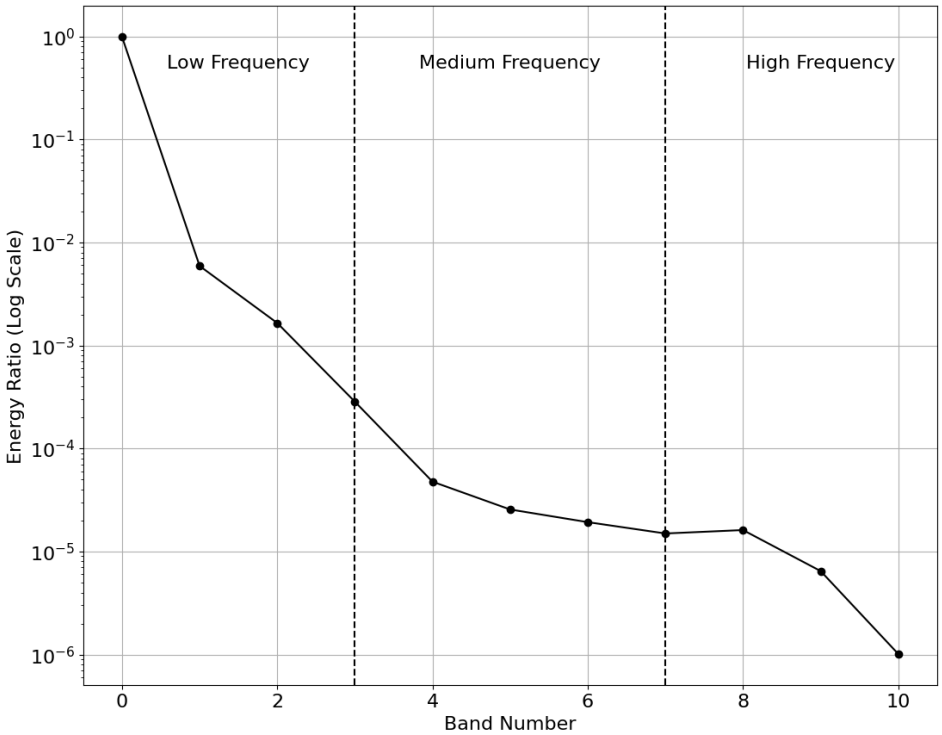

(c) Energy Ratio.

Figure 6.7: This figure presents the (a) original grayscale image, (b) the magnitude spectrum derived from the image's 2D Fourier Transform, (c) and a plot of the energy ratios for ten distinct frequency bands on a logarithmic scale. The bands are divided to three parts (low, medium and high frequency) which shows on the plot

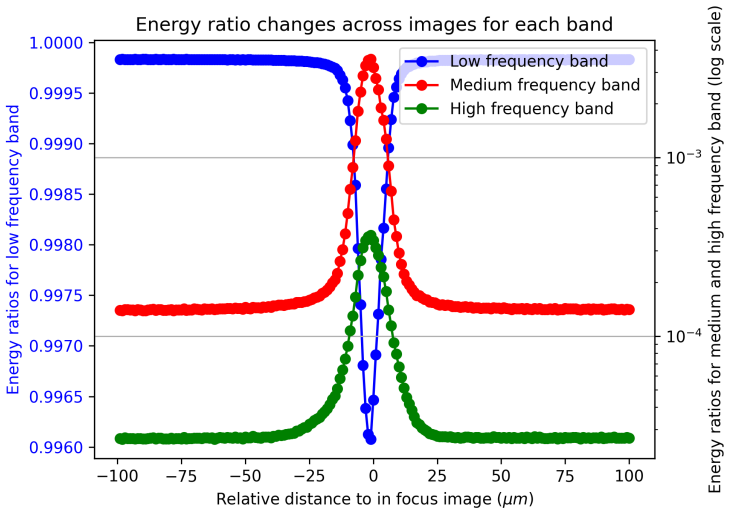

Figure 6.8: The plot illustrates the energy ratios for low (blue-linear scale), medium (green-log scale), and high frequency (red-log scale) bands, which were derived from frequency domain analysis for different sequence of images. The analysed surface is the same as Figure 6.7

arable filters. The computational efficiency of the Sobel operator is due to the separability of the kernel. The gradient approximation it provides is simple, particularly regarding capturing fluctuations in frequency within the image. In order to approximate the derivatives, the operator employs two 3x3 kernels: one to account for horizontal changes and the other for vertical changes. Multiplying the x and y derivative filters by a one-dimensional Gaussian filter yields each kernel. Because a Gaussian filter is commonly used for blurring, the Sobel operator simultaneously computes gradients and applies smoothing, rendering it less sensitive to noise, but on the other side, it reduces the details of the image. The Sobel-x operator is defined as:

$$\text{Sobel-x} = \begin{bmatrix} 1 \\ 2 \\ 1 \end{bmatrix} * \begin{bmatrix} -1 & 0 & 1 \end{bmatrix} = \begin{bmatrix} -1 & 0 & 1 \\ -2 & 0 & 2 \\ -1 & 0 & 1 \end{bmatrix}$$

The Sobel-Y operator is defined as:

$$\text{Sobel-y} = \begin{bmatrix} -1 \\ 0 \\ 1 \end{bmatrix} * \begin{bmatrix} 1 & 2 & 1 \end{bmatrix} = \begin{bmatrix} -1 & -2 & -1 \\ 0 & 0 & 0 \\ 1 & 2 & 1 \end{bmatrix}$$

One approach to derive a sharpness metric is to sum the gradient magnitudes across the entire image.

- **Canny Operator:** The Canny edge detector is an edge detection operator. The algorithm itself takes a picture and extracts edges in different steps. The Canny edge detector approximate a Gaussian filter as the sum of four exponential elements. Here are the steps towards finding the edge by Canny detector:

  (a) Calculating the intensity gradient of the image involves determining the edge strength by finding the gradient of the image intensity at each pixel.

  (b) Suppression of false edges, known as non-maximum suppression, scans the image to retain only the local maxima in the gradient magnitude that correspond to edges.

  (c) Hysteresis thresholding utilizes two thresholds, high and low, to identify strong and weak edges.

  (d) Strong edges are included in the final edge map, while weak edges are only included if connected to strong edges.

  In this method the sharpness is measured the same as Sobel and it has been shown in Figure 6.9e for set of pictures of back side of the sensor.

- **Laplacian Operator:** The Laplacian Operator is a derivative-based tool employed for edge detection within images. Unlike the Sobel or Canny operators, which are first-order derivative masks, the Laplacian Operator is distinguished by being a second-order derivative mask. The primary function of the Laplacian is to highlight areas where there is a rapid change in intensity, making it particularly useful for identifying edges.

6.3.3 Performance on backside of functional sensor in nominal condition

After introducing various metrics for measuring sharpness in this section, we present plots 6.9 of the normalized sharpness on the sensor's back side using different methods. The measurements range from $1mm$ below to $1mm$ above the sharpest image, with the images scanned in steps of $1\mu m$. However, in the plots, for better presentation only every $10\mu m$ step is shown. All the introduced metrics show good performance in detecting the sharpest image. The sharpness increases as the image approaches optimal focus, but decreases once it moves away from it. The plots show that the Energy Ratio and edge-based methods (Canny, Sobel, and Laplace) demonstrate sharp, narrow peaks, indicating their sensitivity to fine details like edges. On the other hand, Entropy and Standard Deviation show more gradual curves, reflecting their focus on image texture and overall pixel distribution rather than just edges.

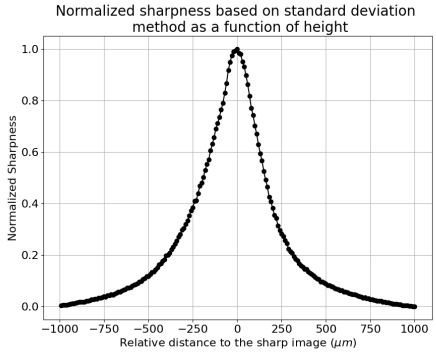

(a) Standard deviation.

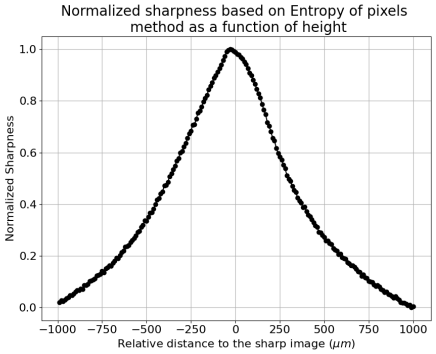

(b) Entropy.

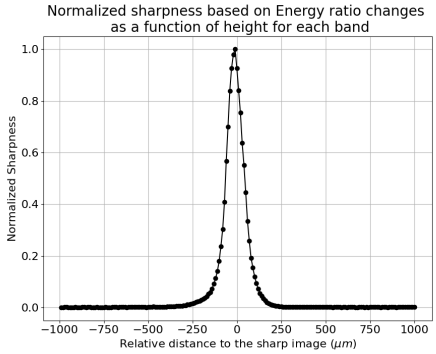

(c) Frequency ratio.

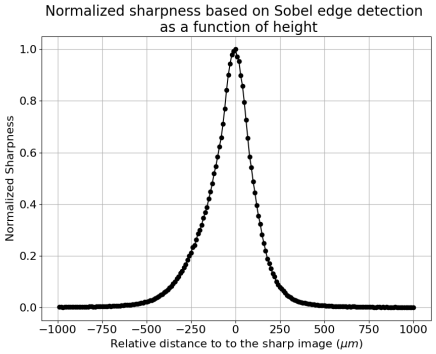

(d) Sobel filter.

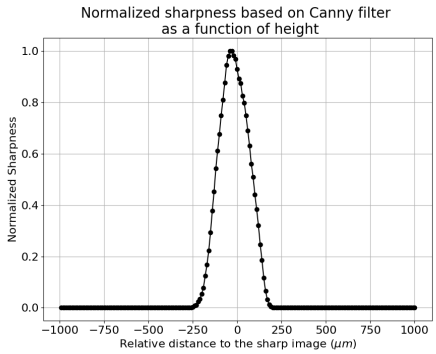

(e) Canny filter.

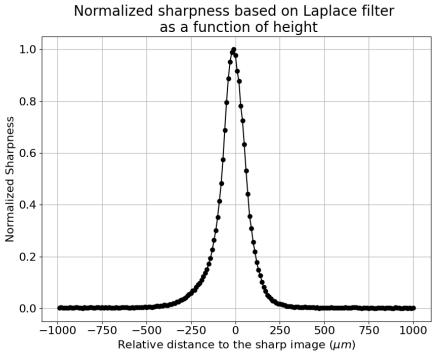

(f) Laplace filter.

Figure 6.9: Sharpness as a function of camera height for different algorithms for the back side of a functional sensor.

The following sections will analyse these techniques for detecting sharpness. The comparison will focus on their effectiveness in the presence of noise, as well as evaluate their performance in terms of brightness, accuracy, Full Width at Half Maximum (FWHM), execution time, number of false positives, sensitivity, and adaptability across desired different surfaces.

6.3.4 Noise analysis

One aspect investigated in this study is the effect of noise on images and its impact on the algorithms used to determine the sharpest image. The objective is to identify the algorithm that is most robust against noise. The height measurement system, which utilizes both a lens and a camera, is susceptible to noise; typically, lenses introduce blurring noise, while cameras contribute to image noise. To examine this, we introduced random salt-and-pepper noise (white dot noise) to the set of backside of sensor images and assessed its influence on the proposed methods. We analyzed the impact of noise on the sharpness algorithms by adding white pixels to each image. The noise fraction is defined as the fraction of pixels for which the gray intensity value was changed into white. The images originated from the backside of the functional sensor. Each method, return different value. Figure 6.10 plots the absolute value of change in the position of the sharpest image, compared to the original dataset, against the noise percentage from 1 to 10%. For each noise level, a Gaussian function is fitted to the sharpness values obtained from each metric as a function of height, within a range of approximately $120\mu m$ around the maximum value.

Entropy and Laplace exhibited the best performance in noisy environments, with deviations of less than 3 μm compared to the other methods. Standard Deviation performed reasonably well but was less robust than Entropy or Laplace. The Energy Ratio method was significantly impacted by noise, showing a large spread and pronounced positional shifts of the calculated sharpest image as the noise level increased. A similar trend was observed with the Canny filter, which also tended to produce secondary maxima under noisy conditions. In conclusion, Entropy proved to be the most reliable method for sharpness calculation in noisy environments, followed closely by Laplace. Standard Deviation, Canny, and Sobel offered moderate performance but degraded significantly at higher noise levels, whereas Energy Ratio was the most noise-sensitive method.

6.3.5 Execution time analysis

Another aspect of our investigation focused on the execution time of the sharpness algorithms. To get reliable measurements, we employed a timer, iterating over each algorithm 100 times to compute the average execution time per loop. The

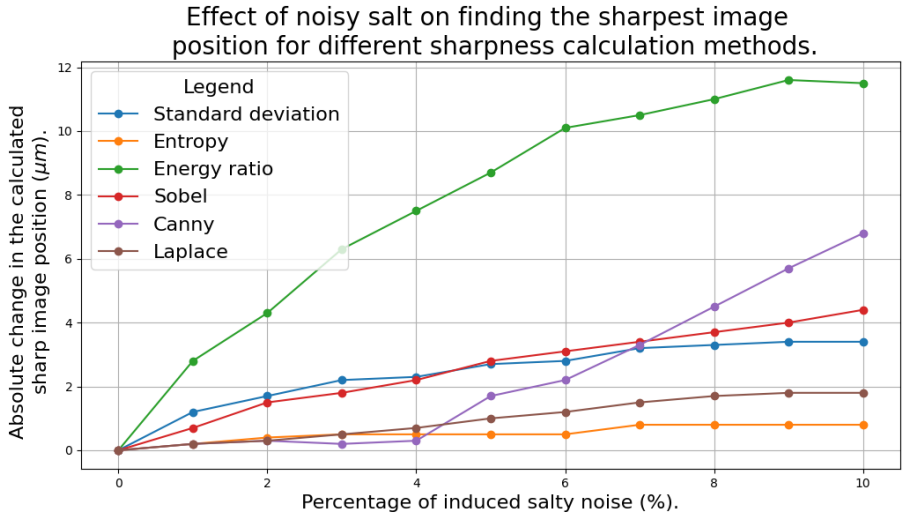

Figure 6.10: This plot illustrates the absolute change in the calculated position of the sharpest image, as compared to the original dataset, in relation to the percentage of salt-and-pepper noise for different algorithm.

algorithms were developed in Python and were run on a commercial laptop. The average times were then compiled across the entire dataset of the backside of the sensor's images. For each sensor, approximately 10 height measurements should be done. Since there are gluing of 12 sensors per day, this amounts to a total of 120 measurements. Therefore, any algorithm that takes more than 10 seconds to run is not suitable for this application. These results are presented in Table 6.5. Among the evaluated sharpness measurement methods, the Entropy, Laplace, and Canny algorithms demonstrated the quickest execution times. Next, the standard deviation method and the Sobel filter are placed. However, the Sobel filter's execution time exceeds the previously mentioned limit. In contrast, the Energy Ratio method was markedly slower, requiring approximately 100 to 600 times more time to determine the sharpest image compared to the Laplace and Entropy methods, respectively. This significant difference in execution time may be attributed to the computational complexity and the amount of data processing required by the Energy Ratio method.

The overall measurement time is influenced not only by the image processing speed but also by the motor's movement speed along the Z-axis. On average, the measurement of each point—including image acquisition, processing, and motor displacement over a 1 mm range with 200 steps, performed in the metrology setup using the Laplace filter—took approximately 55 s.

Table 6.5: Timing analysis of the sharpness algorithms. Average time of execution of different sharpness algorithms.

Algorithm	Average execution time per image[3] (ms)
Entropy Method	0.3
Laplace Filter	2.26
Canny Filter	2.85
Standard Deviation	7.5
Sobel Filter	30.33
Energy Ratio	205.97

6.3.6 Full width at half maximum analysis

An additional parameter investigated in evaluating the sharpness algorithms is the FWHM of the curve of sharpness as a function of distance to surface. A narrower FWHM indicates superior sensitivity, as it reveals that sharpness values are closely clustered around the peak. Conversely, a wider FWHM implies a broader dispersion of sharpness values across images, indicating greater variability. This variability necessitates a wider scanning range to find the sharpest image, potentially increasing the complexity and time required for analysis. The Table 6.6 outlines the FWHM values for various algorithms, measured by fitting a Gaussian function to the data using the formula $FWHM = 2\sqrt{2\ln 2}\sigma$. According to this table, the Energy Ratio method exhibits the smallest FWHM, indicating it as the most high spatial resolution among the tested methods. The resolution capabilities of Energy ratio and edge detection algorithms (Laplace, Canny and Sobel) surpass those of statistical methods (Standard Deviation and Entropy), which have the highest FWHM values.

Table 6.6: FWHM of different algorithm are sorted in this table.

Algorithm	FWHM (μm)
Energy Ratio	116
Laplace Filter	161
Canny Filter	201
Sobel Filter	249
Standard Deviation	420
Entropy	726

[3]Image size: 1280×1024 pixels

6.3.7 Accuracy analysis

Different methods of measuring sharpness yield unique values for the most in-focus or sharpest image. To assess the accuracy of these methods, we used gauges of predetermined thickness, ranging from 1 to $10mm$ with increments of $0.5mm$, accurate to sub-micrometer levels. In this experiment, both surfaces of the gauges were intended to be probed to determine the sharpest image. However, since the gauges are opaque, they were positioned on a flat base surface, configured in such a way that the microscope's image captured half of the top surface of the gauge and half of the base surface. Weights were placed on each gauge, but improper mechanical contact between the two surfaces led to measurement errors. Both the top and base surfaces were scanned, and the positions of the sharpest images were derived to determine the gauge widths. The residual errors in the calculated widths are depicted in Figures 6.11a and 6.11b. According to these plots, the Sobel, Energy Ratio, Canny, and Laplace algorithms exhibit minimal residuals, ranked from lowest to highest in accuracy. The Energy Ratio method has the smallest standard deviation, indicating consistent performance, while the Sobel method shows the largest deviation among them. Generally, the Laplace algorithm measured higher values compared to others, suggesting a tendency to overestimate. These filters meet the criteria for non-contact height measurement. Conversely, despite its fluctuations, the Entropy method demonstrated the poorest accuracy among all tested methods, rendering it unsuitable for precise non-contact optical height measurements.

6.3.8 Repeatability analysis

The repeatability of the sharpness measurements obtained from various algorithms was evaluated in this study. This assessment involved repeatedly measuring the width of a single $3mm$ gauge 100 times to assess measurement consistency while minimizing scan time and movement between the gauge's top and bottom surfaces. The chosen gauge allowed for the capture of two distinct peak signals, facilitating a reliable evaluation. The width of the $3mm$ gauge was measured, and Figure 6.12 presents a histogram of these measurements across the 100 trials. The mean value and standard deviation for each algorithm are also provided. According to the gauge's datasheet, the width is $3000.0 \pm 0.11\mu m$ [67]. The absolute difference between the thickness of the gauge and the calculated thickness are listed in Table 6.7. The Energy Ratio method demonstrated a small mean discrepancy of $4\mu m$ from the actual gauge width, with a standard deviation of $0.69\mu m$, indicating high precision and minimal variability. The Laplace algorithm followed closely, exhibiting an $8\mu m$ discrepancy and a standard deviation of $0.79\mu m$. The Entropy and standard deviation algorithms, while providing mean values closer to the actual

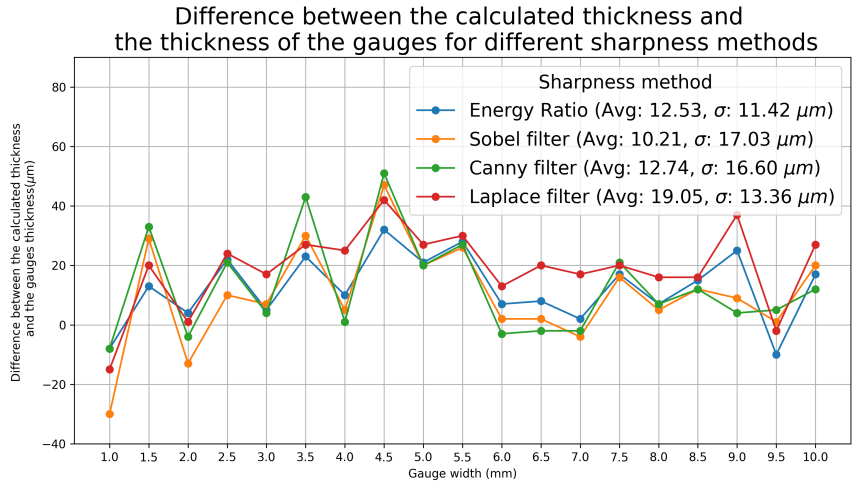

(a) Accuracy for sharpness measurement based on the Energy ratio, Sobel filter, Cany filter and Laplace filter methods.

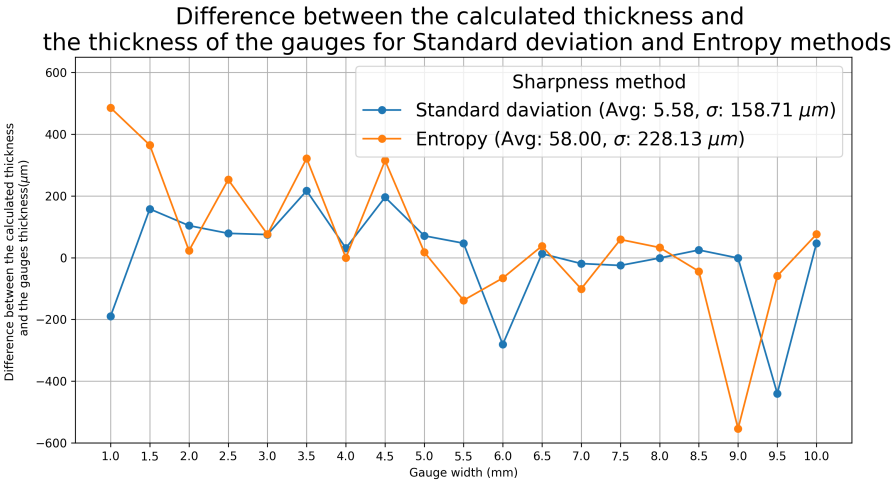

(b) Accuracy for sharpness measurement based on the Standard deviation and Entropy methods.

Figure 6.11: Difference between the true thickness and the calculated thickness of the gauges for different sharpness methods is shown. Since the range of change of the Standard deviation and Entropy are more than the others algorithms then they seperated in another plot (b). In picture (a), the plot of Errors between the measured and calculated widths of the gauges for Sobel, Canny, Laplace and Energy ratio are shown.

width than those obtained by the Sobel and Canny filter methods, showed greater data spread. In conclusion, although the Entropy and standard deviation methods yielded mean values close to the actual gauge width, their broader data spread suggests they are less precise compared to the more consistent results of the Sobel and Canny filters. These findings highlight the varying levels of repeatability and precision among the different sharpness measurement algorithms, with the Energy Ratio and Laplace methods demonstrating superior performance.

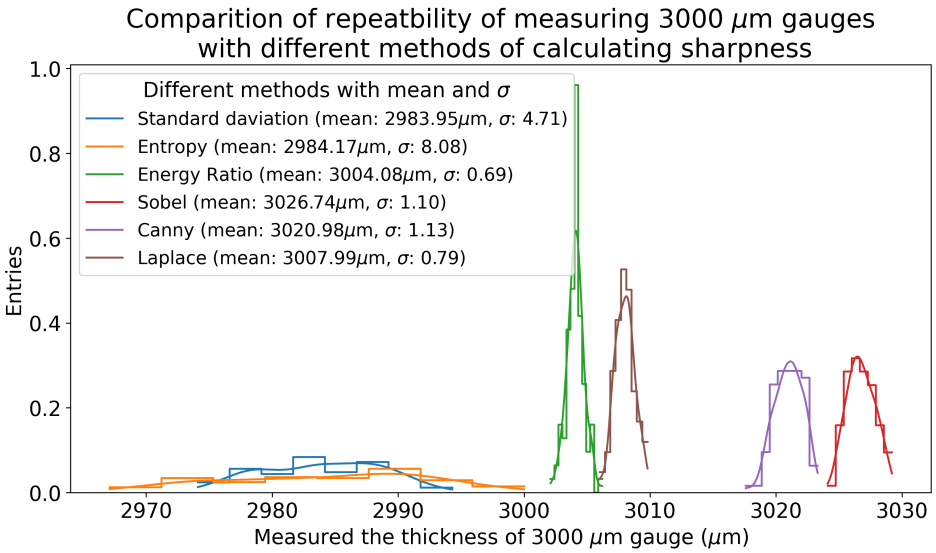

Figure 6.12: Histogram of repeatability or accuracy of the sharpness measurement algorithm.

Table 6.7: Absolute difference between the thickness of the gauge and the calculated thickness.

Algorithm	Absolute difference (μm)
Energy Ratio	4.08 ± 0.69
Laplace Filter	7.99 ± 0.79
Entropy	15.83 ± 8.08
Standard Deviation	16.05 ± 4.71
Canny Filter	20.98 ± 1.13
Sobel Filter	26.74 ± 1.1

6.3.9 Brightness analysis

Enhancing perceived sharpness is achieved by making edges within an image more distinct through proper contrast. In a sharp image, the differences between pixel intensities are clearly distinguishable, typically represented in an ideal intensity histogram by two peaks corresponding to low and high pixel intensities. Changes in environmental lighting can shift these histogram peaks to the right (with an increase in light) or to the left (with a decrease), affecting the distribution of pixel intensities. Unless these peaks exceed the histogram's minimum or maximum thresholds, the sharpness algorithms should remain independent of brightness changes. However, in extremely dark or bright environments, where the peaks do exceed these bounds, sharpness can be significantly impacted. This effect is illustrated in Figure 6.13, which shows the changes in the derived position of the sharpest image compared to the original images under varying light conditions. Furthermore, contrast adjustments can compress or expand the range between the peaks of the intensity histogram, affecting the image's overall sharpness. The influence of contrast modifications is depicted in Figure 6.14. For instance, low contrast in images can make surfaces appear more homogeneous, as seen in images of a Kapton strip, where the surface texture details are less pronounced.

The Laplace filter provides the most consistent results under varying brightness conditions, while the Energy Ratio method remains stable up to moderate brightness changes. The Entropy and Standard Deviation methods, along with the Sobel filter, are more affected by brightness, showing larger deviations as brightness increases.

6.3.10 Image size analysis

The study also examined how changes in image size impact the performance of sharpness algorithms. The image under study in each set of pictures was cropped to different sizes and subjected to the respective sharpness algorithm. Figure 6.15 shows the plotted absolute changes in the calculated position of the sharpest point, relative to the diagonal size of the original image (measured at 1639 pixels). The findings suggest that as the image size decreases, the accuracy of sharpness measurement decreases as well. However, it should be mentioned that for images smaller than 327 pixels in diagonal size, algorithms like Sobel, Canny, and Laplace still provide accurate results. Despite being accurate, false maximums were seen in smaller images, suggesting that the algorithms may struggle to consistently identify the sharpest points in reduced image sizes. It is important to take into account image size when utilizing these algorithms in practical applications.

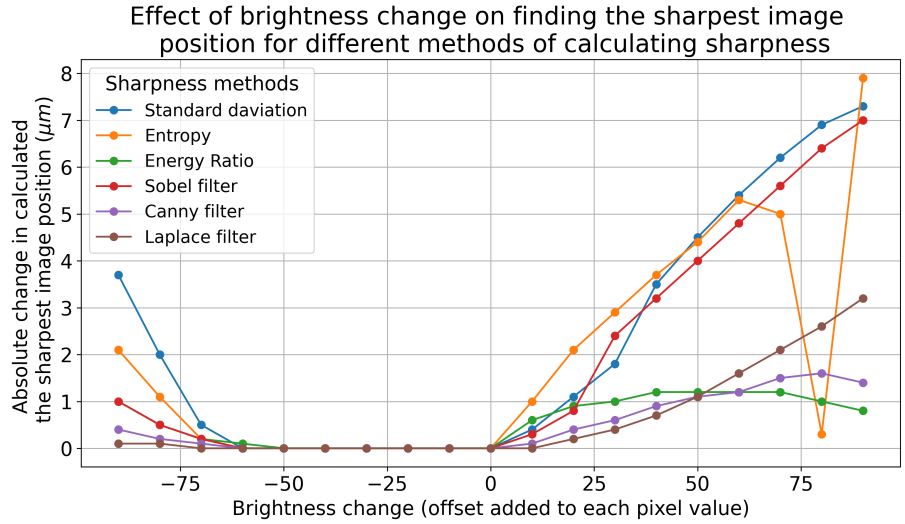

Figure 6.13: Effect of brightness change on the different sharpness measurement algorithm. At high brightness, the entropy method shows fluctuations in locating the sharpest image, caused by feature loss from saturation. This demonstrates the method's sensitivity under such conditions.

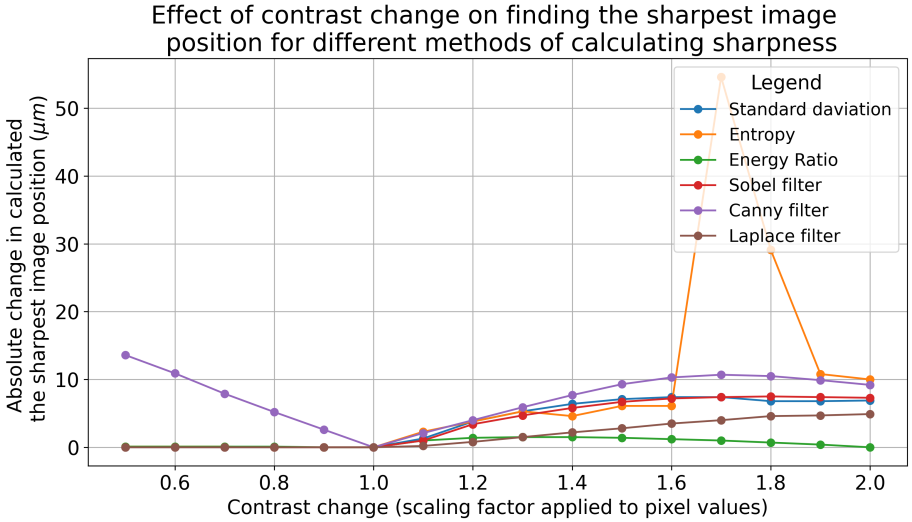

Figure 6.14: Effect of contrast change on the different sharpness measurement algorithm. At high contrast, the entropy method shows fluctuations in locating the sharpest image, caused by feature loss from saturation. This demonstrates the method's sensitivity under such conditions.

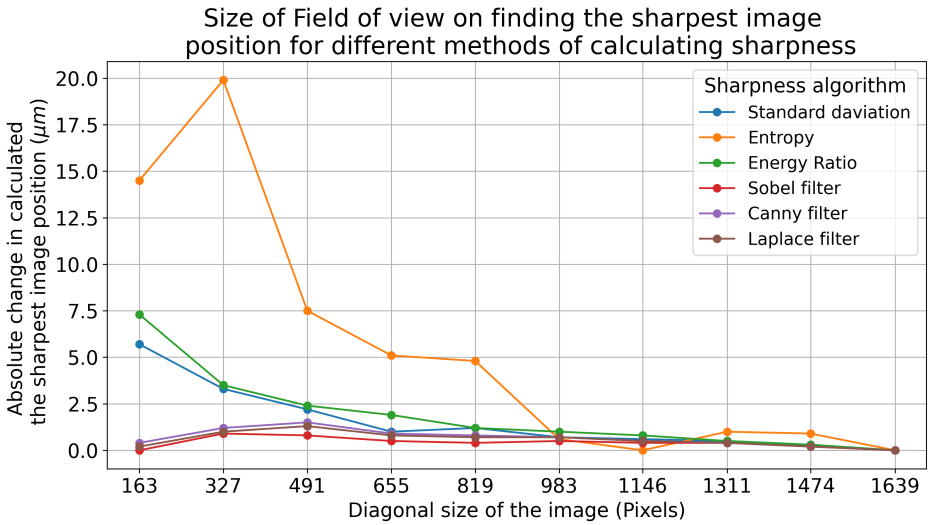

Figure 6.15: Absolute change of calculated the sharpest image position as a function of diagonal size of field of view.

6.3.11 Conclusion

This section introduces various sharpness algorithms, including Standard Deviation, Entropy, Energy Ratio, Sobel Filter, Canny Filter, and Laplace Filter, for non-contact height measurement applications. These methods were evaluated based on execution time, accuracy, precision, sensitivity, and their performance under noise, image size, contrast, and brightness variations. Table 6.8 presents a comparative analysis of the performance metrics for various sharpness enhancement algorithms.

Among these methods, the Laplace Filter demonstrated the best overall performance and is suitable for non-contact optical height measurements especially on sensitive and fragile sensor surfaces. The method is robust against noise; at 10% noise levels, it introduces only a 2 μm change in identifying the sharpest image position. Its precision and accuracy ($\sim 8 \pm 0.8\mu m$) fall within the required range (less than $2.5\mu m$). Additionally, the Laplace Filter provides a narrow sharpness curve as a function of height, indicating good sensitivity. Its results are minimally affected by image size (less than $2\mu m$) and by brightness and contrast (less than $5\mu m$). These properties make the Laplace Filter a reliable metric for sharpness measurement in non-contact optical height measurement methods.

Table 6.8: Performance evaluation of sharpness algorithms.

Parameter	**Standard deviation**	**Entropy**	**Energy ratio**	**Sobel**	**Canny**	**Laplace**
Execution Time (ms)	7.5	0.3	205.97	30.33	2.85	2.26
Noise sensitivity at 10% (μm)	~ 3.5	~ 1	~ 11.5	~ 4.5	~ 7	~ 2
Repeatability (μm)	16.05	15.83	4.08	26.74	20.98	7.99
Precision (μm)	4.71	8.08	0.69	1.1	1.13	0.79
FWHM (μm)	420	726	116	249	201	161
Image size sensitivity	Small	High	Small	Small	Small	Small
Contrast sensitivity	Small	High	Small	Small	Medium	Small
Brightness sensitivity	High	High	Small	High	Small	Small

6.4 Displacement laser sensor

By utilising Laser triangulation-based displacement sensors, these sensors provide precise and contactless measurements of distances and displacements. In the next section, we will explore the basic operational principles of triangular laser sensors, illustrating their use of geometric relationships for precise measurements.

6.4.1 Principle of working

The triangular displacement laser sensor works based on the principle of triangulation. A laser emits a beam towards the target object and captures the reflected beam using a lens and sensor positioned at a predetermined angle relative to the laser source. The displacement can be precisely calculated by observing the shift in the position of the reflected light on the sensor, which varies with the distance from the object (see Figure 6.16). The efficacy of the laser sensor is impacted by the surface characteristics of the objects it measures, including factors like reflectivity and color. In order to successfully integrate this sensor into a gluing machine, it is of the utmost importance to carry out performance tests that are customized to the particular surfaces encountered in the assembly process. This

step will ensure that the sensor's measurements maintain accuracy even when dealing with various materials and conditions in the 2S module assembly process. The ZX1-LD50A81 5M CMOS Laser Sensor has been chosen for testing in the gluing machine application. The sensor specifications, which include an analog current output are detailed in Table 6.9. These data are measured on the standard target object (white ceramic at a temperature of 25 °C) by manufacter[68]. Linearity and resolution may vary depending on target object and we need to investigate it on the target surfaces we use during module assembly.

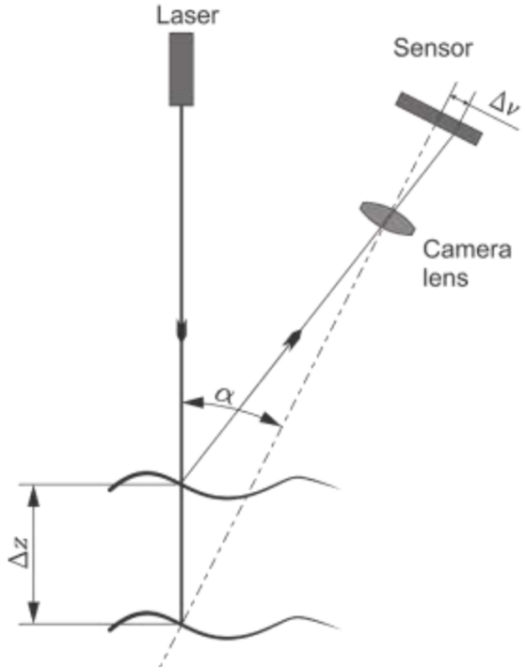

Figure 6.16: Principle of the Laser Triangulation Sensor. The illumination laser beam is represented by the red line. The reflected laser light is represented by the dashed lines when the piecework is shifted to a different position [69].

Table 6.9: Specifications of ZX1-LD50A81 CMOS Laser Sensor. These data are measured standard picework (white ceramic at a temperature of 25 °C) by manufacter[68].

Attribute	**Specification**
Model	ZX1-LD50A81
Light Source (Wavelength)	660 nm, 1 mW max
Measurement Range	40 to 60 mm
Resolution[4]	2 μm
Spot Diameter	0.17 mm
Analog Output	Current output: 4 to 20 mA
Digital Output	PNP
Linearity[5]	±0.15% Full Scale
Digital Output Response Time	1-100 ms
Temperature Characteristic	0.03% Full Scale/°C
Ambient Illumination	On received light surface: 7,500 lx or less (incandescent light)
Weight	Packet approx. 450 g, Sensor approx. 330 g
Price[6]	623.00 Euro

6.4.2 Calibration and Linearity

First, we developed a prototype board to convert the output current (4 to 20 mA) to voltage, digitize it, and calibrate the digital output to height. We chose a 100Ω resistor for the shunt resistor. To achieve a $2\mu m$ resolution, it is necessary to use a 14-bit Analog to Digital Converter (ADC), so we selected a 16-bit ADC. For calibration, the ADC output was measured while scanning the height along the z-axis (over a length of 12 mm with a step size of 0.2 mm) at 100 different points on the surface. A white liquid was used as a flat surface to minimize the effect of target surface tilt in this test. Figure 6.17, shows one of measurements, the raw value versus the Z stage position. The data are shown in blue color with error bar and the fitted line is shown by red dash color. The error of data is calculated as the standard deviation of 100 samples taken on different points on the surface. After fitting a line, the average of calibration coefficients were obtained and are

[4]Defined in Standard Mode for Omron's standard target object (white ceramic) after executing Smart Tuning. The resolution indicates the repetition accuracy for a still workpiece. Not an indication of the distance accuracy.

[5]Indicates the error with respect to the ideal straight line of the displacement output in the case of measuring Omron's standard target object (white ceramic) at a temperature of $25°C$.

[6]Quoted by frederik.cousse@rexel.be on 13/10/2020.

shown in Equation 6.3. The intercept of the plot is an arbitrary value and can be set to zero during the calibration process.

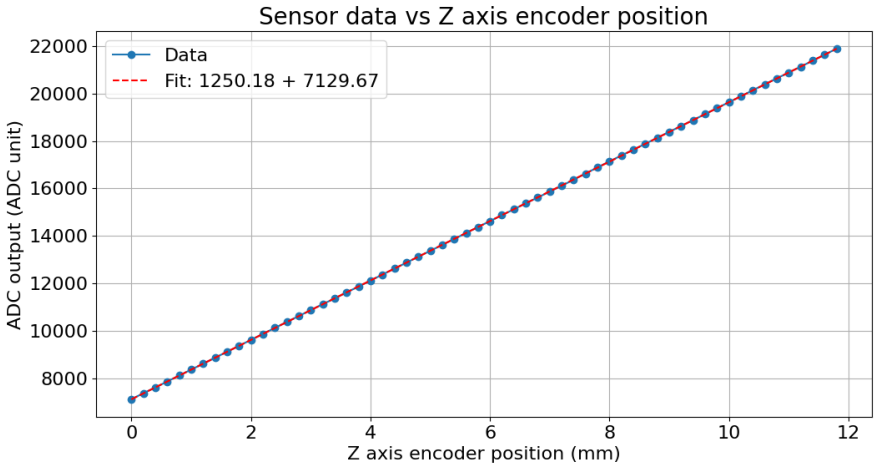

Figure 6.17: ADC raw output data versus sample (white liquid) position. The plot displays sensor data (blue markers with error bars) and a fitted linear model (red dashed line). The error bars represent the standard deviation of 100 samples taken at different surface points for each height.

$$ADC\ raw\ data\ [ADC\ unit] = 1250.21 \pm 0.09 \left[\frac{ADC\ unit}{mm}\right] \times Z\ stage\ position\ [mm] + 7032.48 \pm 63.13 \left[\frac{1}{mm}\right] \tag{6.3}$$

After calibration, the average of the residual plot (difference between Z elevator stage and sensor's output) versus the Z encoder position over 100 measurements was analyzed to determine the linearity of the sensor's output and how accurately it corresponds to actual changes in height across its measurement range. The linearity of the laser sensor and readout system was tested over a white liquid with 0.2 mm steps and 0.1 mm steps for the back side of a functional sensor over a 12 mm range. In Figure 6.18 top, the linearity on the white liquid surface and Figure 6.18 bottom, the linearity on the backside of a functional sensor are illustrated. The blue solid line represents the mean residual values at each Z-axis position, computed from 100 repeated measurements on different points. The red error bars indicate the standard deviation (σ) of the residuals at each Z-axis position. The maximum and minimum residual values recorded at each position

also are shown in blue and orange dash-dot line respectively. For the white liquid, a non-linearity around $10\mu m$ for 7.3 mm and 8.2 mm was observed. For the rest of the scanned range, the maximum non-linearity was less than $5\mu m$. According to the residual plot of the back side of a functional sensor the average of the residual value lie between -10 to $10\mu m$ across the measured range, indicating a generally well-calibrated system. Figure 6.19 shows the linearity error (% of Full Scale, 20 mm) of the Omron sensor from the datasheet, measured on different surface materials for comparison. The tested materials include white ceramic (solid blue line), SUS304 with a mirror finish (dashed pink line), and a substrate (dash-dot orange line). The x-axis represents the displacement in millimeters relative to the measurement center distance, where negative values correspond to the far side (target surface) and positive values represent the near side (sensor side).

In our analysis, due to the movement range limitation of the Z-stage elevator, the measurements covered only 12 mm from the far side.

6.4.3 Performance on different surfaces

After the calibration, the performance of the laser sensor was investigated on different surfaces at various heights. For each surface, the sensor output as a function of the z-stage position (over a length of 12 mm with a step size of 0.1 mm) was measured at 100 different points to determine the average performance of the laser sensor for that surface type. For each height scan, the calibration coefficient was derived by fitting a linear function. The histogram of the conversion coefficients for the backside of a functional sensor, along with a fitted Gaussian function, is showed in Figure 6.20 (top). The mean (μ) and standard deviation (σ) of the fitted Gaussian function, as well as the standard deviation of the conversion coefficient, are listed in Table 6.10. Additionally, the histogram of residuals for different heights across 100 measurements is shown in Figure 6.20 (bottom). The standard deviation (σ) of the fitted Gaussian function for the residuals was taken as the laser sensor precision for each surface, which is also listed in Table 6.20.

In this test, the measurements were limited to 12 mm from the far side of the laser sensor due to the limitations of the Z stage elevator. However, this is not a problem because the tip of the glue dispensing needle will be placed within the near quarter of the range close to the sensor. Since needle heights vary, a safe margin should be considered to ensure the tip of the needle remains within the measurement range.

While checking the performance of the laser sensor on different surfaces, some spikes (out of expected range) were observed on very brushed, shiny, and reflective surfaces. These spikes were ignored during data preprocessing before analyzing the data.

Table 6.10 includes the average conversion coefficients for different objects.

Figure 6.18: Top: The residuals of the measurements on surface of white liquid with the respect to the fitted line. Bottom: The residuals of the measurements on surface of back side of a functional sensor.

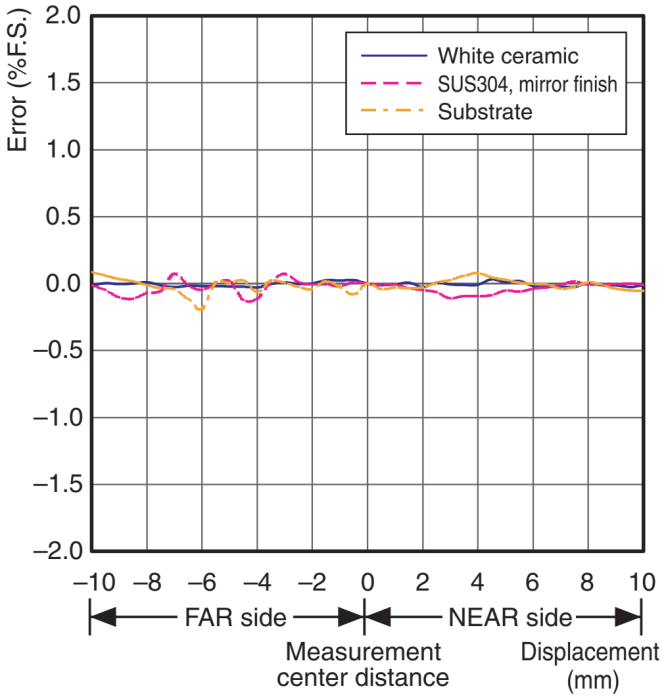

Figure 6.19: Linearity error (% of Full Scale range, 12 mm) of the laser sensor for different target materials according to the datasheet.

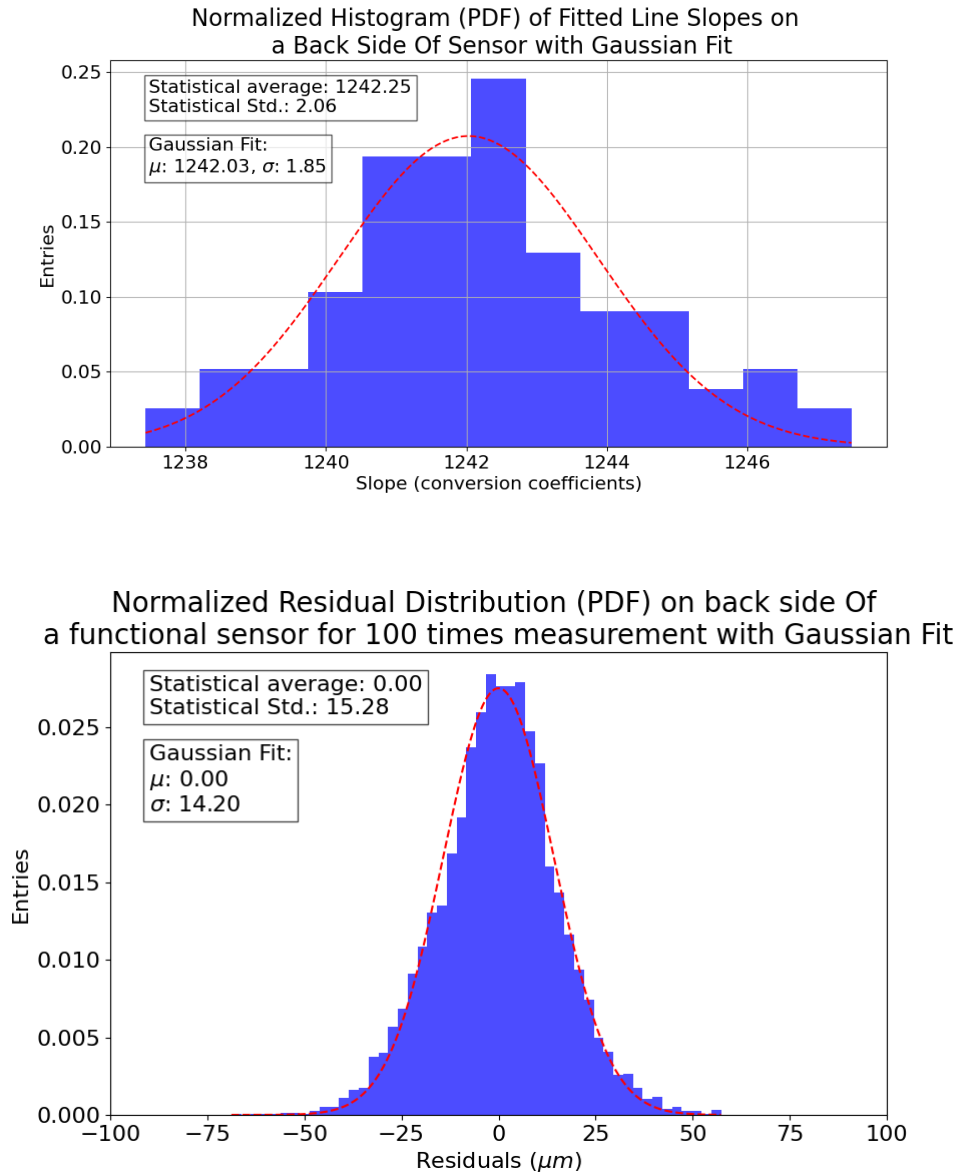

Figure 6.20: Top: Normalized histogram (PDF) of fitted line slopes (coefficient conversion) on backside of a functional sensor and (bottom) normalized residuals of the measurements with the respect to the fitted line distribution (PDF) on the same surface for 100 times measurement with Gaussian Fit. with Gaussian Fit ADC raw output data versus sample position. The data are shown in blue color and the fitted line is shown by red dash color.

According to the maximum allowed precision defined in the requirements section ($20\mu m$), the maximum permissible deviation from the average value of the conversion coefficient is ±2 [ADC unit/mm]. Consequently, the front side of the functional sensor requires its own calibration coefficient (It is notable that the measurement points on the front side of the functional sensor were selected along a line within the strip area and oriented perpendicular to the strip direction). With this laser sensor, reliable measurements cannot be performed on the top side within the strip region. However, it has been demonstrated that height measurements can be carried out on the top side outside the strip pattern. Moreover, the precision of the laser sensor on the front side of the functional sensor ($48.39\mu m$) exceeds the acceptable precision threshold. For the remaining surfaces, the average conversion coefficient can be used, and it is not necessary to update its value for each surface and the precision of the laser sensor on the jig (brushed metal), hybrid, Kapton strip, and the backside of the functional sensor is within the acceptable range ($20\mu m$) and maximum precision was observed on surface of bridge as $14.11\mu m$.

Table 6.10: Calibration results for conversion coefficient between ADC output and mm with residual standard deviation for different surfaces.

Surface	Avg. Slope (ADC unit/mm)	Std. Slope (ADC unit/mm)	Std. Residuals (Precision) (μm)
Jig (brushed metal)	1242.11 ± 1.79	2.08	13.4
Hybrid	1243.33 ± 1.96	1.89	12.48
Kapton strip	1242.85 ± 0.78	0.94	6.69
Front side of a functional sensor[7]	1239.46 ± 2.44	2.09	48.39
Back side of a functional sensor	1242.03 ± 1.85	2.06	14.02
Bridge	1242.28 ± 2.41	2.63	14.11
Average	1242.3	-	-
Maximum[8]	-	-	14.11

Note: The average slope (Avg. Slope) is obtained from the mean (μ) value of a Gaussian function fitted to the histogram of slope measurements at 100 different points over range of $12mm$ and step of $0.1mm$, with the standard deviation (σ) chosen as the uncertainty. For comparison, the statistical standard deviation is also presented in the Std. Slope column. The standard deviation (σ) derived from fitting a Gaussian function to the residuals plot of 100 measurements is chosen as the precision and is presented in the Std. Residuals column.

6.4.4 Resolution

To investigate the resolution of the laser sensor and readout system, we used the Z elevator and the backside of the functional sensor (the most fragile target) as the reference object. The Z-stage was moved up in steps of $1\mu m$ (the smallest possible increment). Then, the differences between consecutive height sensor readings were calculated. The smallest non-zero difference indicates the resolution of the height sensor. And the maximum resolution defined as the maximum required steps to move until the output laser sensor changes. In Table 6.11, the percentage of the minimum change of the laser sensor and readout system for $1\mu m$ movement of the sample is presented. According to the table, it appears that the laser sensor and readout system have a maximum resolution of $2\mu m$ on the backside of a functional sensor. Therefore, with the laser sensor and readout system, a resolution better than $2\mu m$ is achieved.

Table 6.11: Percentage of the minimum change of the laser sensor and readout system for $1\mu m$ of movement of the sample (back side of a functional module).

Change of reading for $1\mu m$ height shift of Z elevator	Percentage (%) in 12000 measurements
0	23.76
1	53.62
2	22.62

6.4.5 Inclination effect

According to the laser sensor datasheet, any inclination of the sensor introduces errors in position measurement. Figure 6.21 illustrates the errors caused by side-to-side and front-to-back inclinations, based on data from the datasheet [68]. The datasheet specifies a maximum inclination error of 0.7%. However, in our setup, the laser sensor is fixed, and calibration compensates for this inaccuracy. As shown in Figure 6.21 and observed in experiments on shiny surfaces, the inclination of the laser sensor has a significant impact on measurement accuracy. This factor contributed to the decision to select the ZX2 series laser sensor for the gluing robot.

[7]The points were selected along a line within the strip area and oriented perpendicular to the strip direction.

[8]Front side of a functional sensor is excluded.

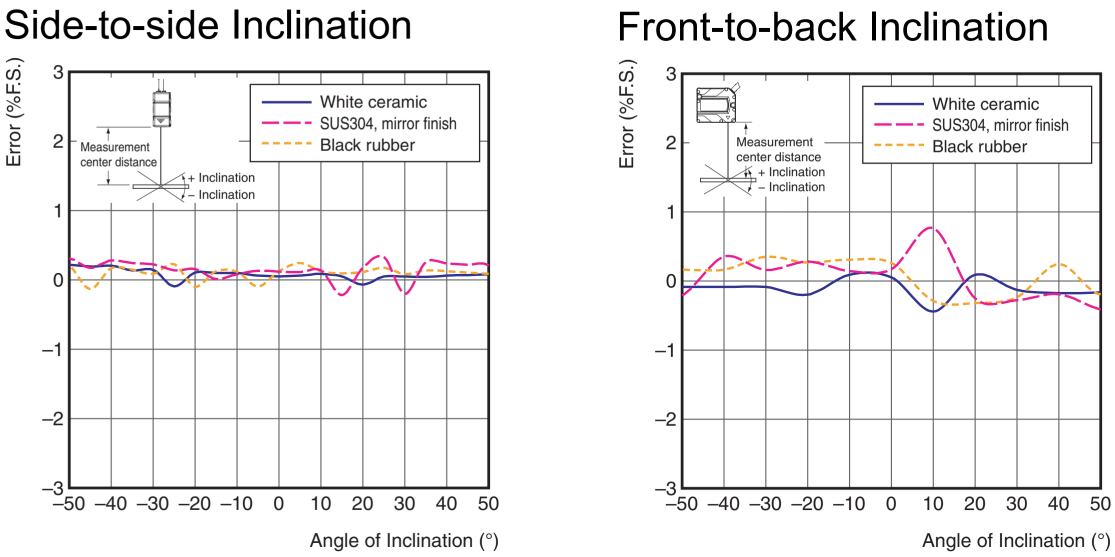

Figure 6.21: Inclination effect on laser sensor accuracy. Left: Side to side inclination effect. Right: Front to back inclination effect[68].

6.4.6 XY calibration

To calibrate the X and Y positions in the gluing robot, it is important to know the edge detection precision. To investigate edge detection accuracy, a sensor gluing jig was used to measure the performance of edge detection at different edges and angles (around of 0, 45, 90, 135, and 180 degrees). A schematic of the jig, indicating the scanned edge numbers and the scanning direction, is provided in Figure 6.22. To ensure that edge detection is independent of the scanning direction (i.e., from high to low or low to high), the difference between the detected edge positions when scanning in the +x direction and then in the -x direction was considered as the edge detection error of the laser sensor. It is notable that the front-back side of the laser sensor, which includes the plane formed by the emitted laser beam and its reflected beam from the surface, was aligned along the y-direction. For each edge, the measurement was repeated 100 times, and the mean value along with the standard deviation for different edges is reported in Table 6.12. The maximum error in edge detection was found to be $15 \pm 7\mu m$, which meets the gluing robot requirements for X and Y calibration and position detection. The precision requirement for XY calibration is not as strict as for the z axis, allowing for a greater tolerance ($\sim 100\mu m$).

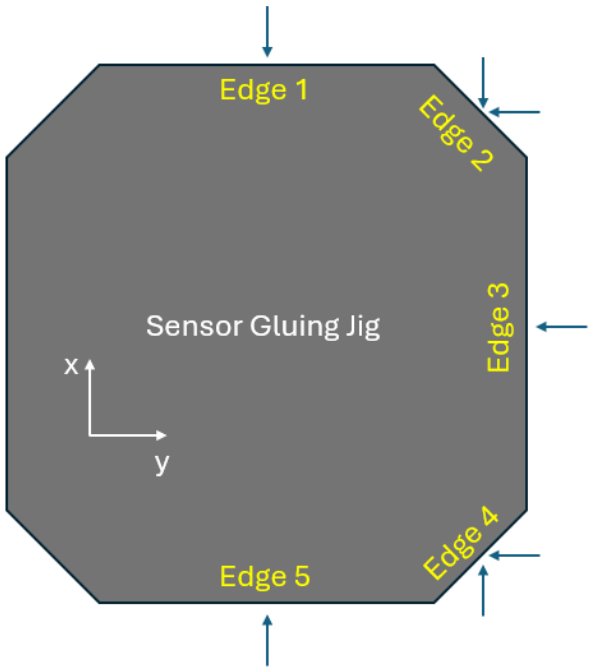

Figure 6.22: Schematic of the sensor gluing jig, indicating the scanned edge numbers and the scanning direction.

Table 6.12: Summary of the edge detection for different angles. The precision is obtained as the standard deviation of 100 measurements.

Edge number	**Scanning direction**	**Avg. of difference between two detected edge from two directions**
1	x	10 ± 8 μm
2	x	15 ± 7 μm
	y	11 ± 5 μm
3	y	14 ± 3 μm
4	x	8 ± 5 μm
	y	3 ± 7 μm
5	x	6 ± 6 μm

6.4.7 Conclusion

In this section, we examined various properties of the triangular displacement laser sensor. A precision of $14.02\mu m$, a linearity of $\sim \pm 10\mu m$ (within a 12 mm scanning range), and a resolution of $2\mu m$ were achieved on the back side of a functional sensor (the most fragile part). The results demonstrate that the sensor meets the requirements of the gluing robot and could be an excellent solution for height measurement. A summary of the laser sensor's measured specifications for the back side of a functional sensor is presented in Table 6.13.

Table 6.13: Summary of the laser sensor's measured specifications on the back side of a functional sensor.

Attribute	**Specification**
Height measurement precision	$14.02\mu m$
Linearity	$\sim \pm 10\mu m$
Resolution	$2\mu m$
XY calibration precision[9]	$15 \pm 7\mu m$

6.5 Optical height measurement vs displacement laser sensor

In the two previous sections (6.3,6.4), we investigated two different solutions to achieve robust and precise height measurements for the gluing robot. Both methods meet the accuracy and precision requirements of the gluing robot, but the

[9]Sensor gluing jig (Aluminium).

optical height measurement shows better performance in this regard. XY calibration and object detection using image processing are faster compared to the laser sensor. However, the laser sensor provides faster data reading, while the optical height measurement relies on Z probing, which is significantly slower. Price is an important factor since several height measurement system are required for the gluing robots. The optical height measurement system ($\sim 4kEuro$) is significantly more expensive compared to the laser sensor ($600Euro$). While optical height measurement works on all types of surfaces encountered during 2S module assembly, the triangular displacement laser sensor has lower performance on shiny and reflective surfaces. In the next section, the design of the readout system will be discussed.

Table 6.14: Comparison between investigated specifications of optical height measurement and triangular displacement laser sensor.

Attribute	**Optical Height measurement (Laplace)**	**Laser sensor**
Precision μm	~ 1 μm	14.11 μm
Repeatability μm	8 μm	± 10 μm
X and Y position detection	2×1.15 μm	15 ± 7 μm
Range of measurement (Z axis)	160 μm (FWHM)	20 mm
Measurement time	Depends on Z axis motor speed On the order of 1 minute	100 ms
Price	$4k$ $Euro$	600 $Euro$
Weight	$276g$	$330g$

6.6 Displacement laser sensor readout design

We have opted to utilize the ZX1-LD50A81 and ZX2-LD5005M (new version) laser sensors due to their acceptable accuracy and reliability. However, the current market shortage of amplifiers, digitizers and serial connectors for those sensors, coupled with the necessity of a controller board for reliable communication with the robot controller, presents a challenge. To address this, we have designed a versatile PCB board that serves multiple functions. This board is capable of converting the analog current output from the laser sensors into a voltage. This voltage is then digitized using an ADC. A microcontroller processes this digital data and communicates it to the gluing robot central controller via a serial protocol. Furthermore, the board is equipped to send digital controlling commands to the laser sensors. Given the differing voltage levels required by various components of the board, we

have incorporated voltage converters to ensure compatibility and proper operation. The board requires two power lines: a 15 V supply for the laser sensors and a 5 V supply for the microcontroller and other digital integrated circuits. Additionally, our design includes the capability to provide signal copies to other controllers and manage the sending and receiving of digital signals. In the Figure 6.23 a block diagram of the different sections is pictured. In the following sections, each component of this board will be discussed in detail to provide a comprehensive understanding of its functionality and significance.

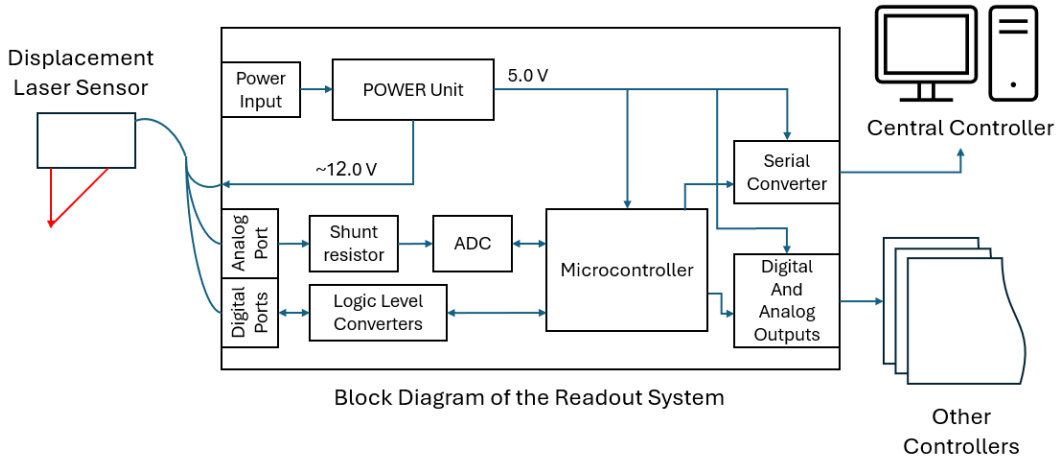

Figure 6.23: Block diagram of the read out system for the displacement laser sensor (see the text).

6.6.1 Analog to digital converter

The laser sensor (ZX1-LD50A81) has a $4-20mA$ analog current output. Analog current is a standard way to transfer signals in industry to make them immune to noise and to prevent voltage drops over long cable lengths. The first step is to convert the analog current to voltage for digitizing. A shunt resistor is used to measure current by creating a small, known voltage drop proportional to the current passing through it. This voltage drop is then measured to determine the current. According to the datasheet of ZX1-LD50A81, the maximum load that can be used is 300Ω. Choosing the shunt resistor is a trade-off between noise and power dissipation. The power dissipation on the shunt resistor increases the temperature due to the current flowing through it. A resistance of 100Ω is used to convert $4-20mA$ to voltage because it converts the current to $0.4-2V$, which is easy to handle. Thus, at $20mA$, there would be $40mW$ power dissipation, requiring a resistor with a low temperature coefficient and high precision. According to

the minimum allowed voltage change, we selected a resistor with a emperature Coefficient of Resistance (TCR) of $2.0ppm/°C$. After converting current to voltage, an ADC to digitize the voltage is necessary. Since the target resolution is $2\mu m$ over a range of $20mm$, we need an ADC with a resolution better than 14 bits. We chose the ADS1115. It is a delta-sigma ADC with 16-bit resolution and I2C protocol for communication, offering 2 differential or 4 single-ended inputs. The most important properties of the ADC are listed in Table 6.15. The modulator frequency of the ADC is $250kHz$, meaning that the delta-sigma ADC samples the input signal at this rate. The Nyquist frequency, which is half of the sampling frequency, is $125kHz$. Any signal components above $125kHz$ will fold back (alias) into the frequency range of interest, potentially distorting the desired signal. To avoid aliasing effects, we need an anti-aliasing low pass filter on the ADC input channels. To avoid using large capacitors, which directly affect the response time, a 2^{nd} order RC filter is designed. In Figure 6.24, the Bode diagram of the filter is depicted on the left, and the step response of the filter is shown on the right side which causes around 40 ms delay for stability before data sampling. To make the circuit immune to noise and to the effects of track resistance, we placed the shunt resistor as close to the anti-aliasing filter and ADC as possible.

Table 6.15: Important Specifications for ADS1115 ADC

Parameters	Value
Resolution	16 bits
Data Rate	8, 16, 32, 64, 128, 250, 475, 860 Sample per Second (SPS)
Modulator frequency	250 kHz
Offset Error (Differential Inputs)	±3 LSB
Gain Error	0.01% (typ), 0.15% (max)
Differential input impedance Full Scale Range =±2.048V	$4.9M\Omega$
Power Supply Voltage Range	2.0 V to 5.5 V
Supply Current (Operating)	150 μA (typ), 300 μA (max)

6.6.2 Power supply

In the design, two linear voltage regulators are used to step down the input voltage from 24V to 12V and then from 12V to 5V. Linear regulators were used because they produce less electrical noise compared to switching regulators. This is particularly important in this design where noise can interfere with signal integrity. On the other hand due to their lower efficiency, linear regulators generate more heat.

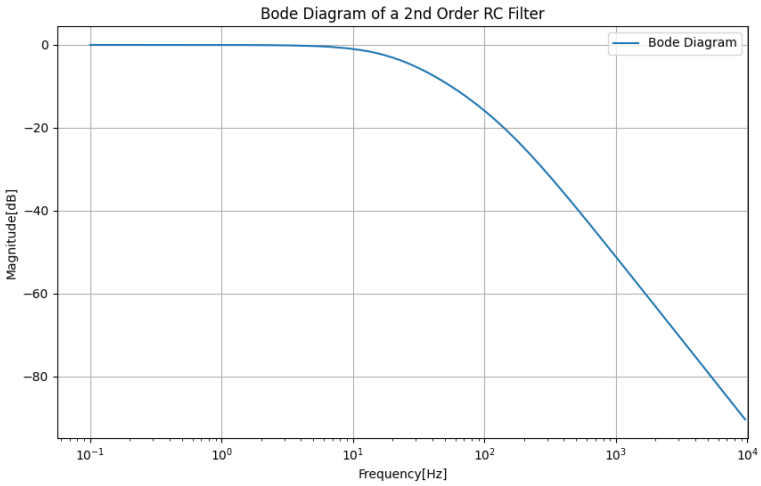

Figure 6.24: Bode diagram of the second order low pass anti-aliasing filter.

This necessitates the use of heatsinks to manage thermal dissipation, which is considered in this design. The L7812CP regulator handles the first stage, converting 24V to 12V, and the 7805CP regulator handles the second stage, converting 12V to 5V. The circuit includes protective features such as fuses and diodes to guard against reverse polarity, as well as LED indicators to provide visual feedback for each voltage level. Analog signals are sent to the microcontroller for power monitoring, and Zener diodes are used for protection.

6.6.3 Processor unit

The CY8C4A45AZI microcontroller was used for this design due to its versatile features and robust performance. This microcontroller offers a blend of high-performance analog and digital peripherals, making it suitable for complex mixed-signal applications which fulfill the requirements of the readout system. The Smart I/O block can perform logical operations on input pins to the chip and on output signals, enabling better control of the digital input and output of the laser sensor. This microcontroller was chosen to maintain consistency and compatibility with other projects developed in our lab, ensuring streamlined development and easier maintenance across multiple projects.

6.6.4 Interfaces

To manage the difference in logic levels between the sensor and the microcontroller, we designed logic level converters using transistors. The digitized data provided

by the ADC from ZX1-LD50A81 is then sent to the main controller via a serial converter, which allows USB communication.

The ZX2-LD5005M sensor uses an RS-232 protocol for communication. To interface with this sensor, we use a MAX-232 IC to convert the RS-232 signals to TTL levels that the microcontroller can read. We also provide an analog output proportional to the laser sensor's current output, which is isolated using an operational amplifier to ensure signal integrity and prevent interference. Additionally, a digital output is generated based on a threshold that can be adjusted using a variable resistor. An LED indicator is included to show the status of this digital output, providing clear visual feedback.

To facilitate communication with other controllers, our design includes digital inputs and outputs as well as an analog output from the microcontroller. A DIP switch is included to select the operating mode of the controller, switching between the ZX1 and ZX2 series of laser sensors. An LCD module and keys are included in the design for communication with users.

6.6.5 Conclusion

In conclusion, the design of the displacement laser sensor readout system for the gluing robot is both innovative and precise. By integrating advanced laser sensors such as the ZX1-LD50A81 and ZX2-LD5005M, the system achieves high precision in height measurement. The custom-designed PCB plays a crucial role in this integration, converting the analog current output of the sensors into a digital format using an ADC, which is then processed by a microcontroller. This setup ensures accurate data collection and communication with the robot controller via serial protocols.

But ZX1 series suffer low efficiency on shiny and reflective surface. This issue is mitigated in the ZX2 series of triangular displacement laser sensors. The use of a high-speed and dynamic range image sensor and a step-less laser power adjustment algorithm enables stable measurements for any color or surface conditions, from metals to substrates, rubber, and transparent objects [70]. After comparing the two solutions, we decided to continue with the new version of the laser sensor (ZX2) for the gluing robot.

6.7 Application in components quality check

As part of quality assurance, we conduct a geometrical inspection of components prior to assembly. One key aspect of this inspection is assessing the flatness of AlCF bridges. Flatness is defined as the distance between the highest and lowest points relative to a plane of the surface. To measure flatness of the AlCF bridges,

we used optical height measurement method with a metrology setup equipped with an XYZ stage. The sample was securely fixed on the carrier, and the height of various points on the surface of interest was measured. Subsequently, a plane was fitted to the data to account for any tilt in the surface. The distance between the highest and lowest points relative to this fitted plane was then calculated. The sum of these distances is considered the maximum non-flatness. The criteria for flatness for each section of the AlCF bridges are presented in Figure 5.3. For the common zone flatness measurement, a $270gr$ weight should be place on the A area. Table 6.16 provides the measured flatness for two of the long AlCF bridges and short stump bridge it was measured $0.002mm$. These AlCF bridges were used in $2S-18-5-BEL-00003$.

Table 6.16: Flatness measurements of different parts of $1.8mm$ AlCF bridges.

Type	A [$< 0.5mm$]	B [$< 0.01mm$]	C [$< 0.01mm$]	D [$< 0.1mm$]
Long	0.039 mm	0.001 mm	0.003 mm	0.076 mm
Long	0.060 mm	0.004 mm	0.004 mm	0.067 mm

Additionally, the flatness of a strip sensor was measured. The 3D vision of back side of the sensor (34348-005) which left free (no vacuum underneath) on XYZ stage of metrology is measured based on the laser height measurements, is illustrated in Figure 6.25. To remove noise in data and smoothen the surface a Gaussian filter was used. A plane was fitted on the measured height to remove the effect of the table tilt. Then the distance between the maximum and minimum value measured ($90\mu m$) as the flatness of the sensor. Which is shown as the red arrow in Figure 6.25. Also, the minimum and maximum are shown with black circle.

6.8 Conclusion

In this chapter, two non-contact approaches for height measurement in the gluing process of 2S module assembly were studied and implemented. The first approach, based on image processing and sharpness evaluation, achieved a resolution of about 1 μm with a repeatability of approximately 8 μm. This method also provided improved positioning capability in the x and y directions. Nevertheless, its application is limited by factors such as a restricted measurement range, longer acquisition times, and the high cost of the optical components required, particularly the lens with long focal length and shallow depth of field.

The second approach, employing a triangulation-based laser displacement sensor, demonstrated a precision of around 14 μm when tested on the backside of functional silicon sensors. It offered a wider measurement range (40-60 mm), fast

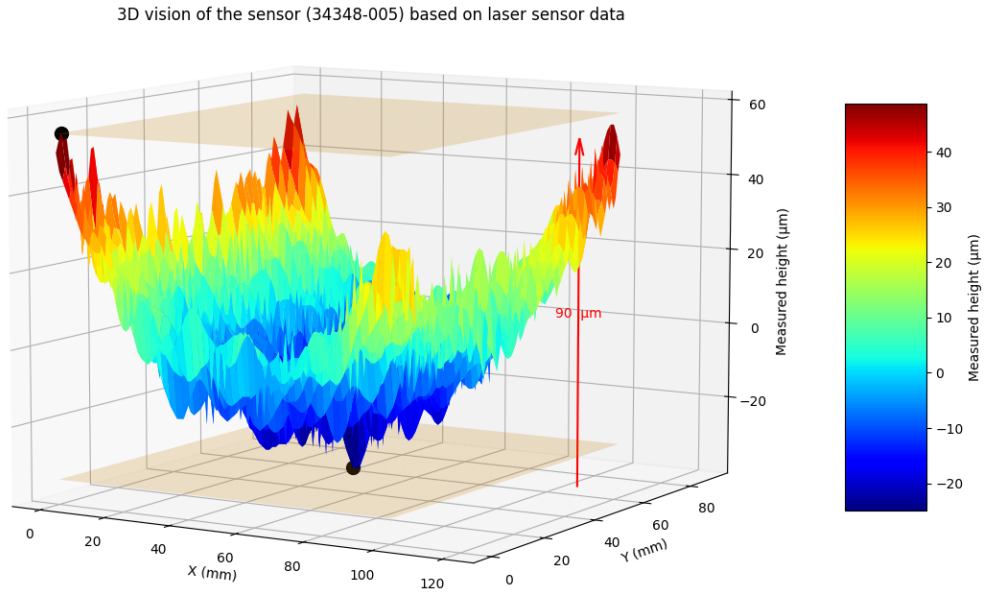

Figure 6.25: 3D vision of the Silicon Sensor during flatness measurement. Red (Blue) color shows high (low) altitude.

measurement time (100 ms), and a cost-effective solution compared to the optical setup. To support this approach, I designed and implemented a custom PCB for reliable readout and control of the ZX1 sensor, and developed dedicated software to integrate the device into the prototype gluing robot.

The optical image-based method was successfully applied for AlCF flatness measurements, while the triangulation laser sensor was deployed for measuring the flatness of silicon sensors. Together, these developments enabled automated, accurate, and efficient height monitoring during the gluing process, contributing directly to the quality assurance of 2S module assembly.

My contributions in this chapter are as follows:

- I conducted a comparative study between image-based height measurement algorithms and a triangular displacement laser sensor.
- I performed the calibration procedure for the laser sensor and analyzed its performance on a range of surfaces with different optical and structural properties.
- I designed and implemented a custom PCB to interface with the ZX1 laser sensor, ensuring reliable data acquisition and control.

- I developed a dedicated software library to integrate the ZX1 laser sensor with the prototype gluing robot, enabling automated measurements during the detector module assembly process.
- I applied the optical height measurement approach for AlCF flatness measurements and used the triangular laser sensor for sensor flatness measurements.

Chapter 7

2S Module Performance in Asynchronous Beam

In my doctoral thesis, I conduct a detailed analysis of the 2S module $2S-18-5-BEL-00003$ which hereafter will be called Device Under Test (DUT), incorporated with multiple 2S modules in a beam test at CERN, In the context of a common beam test between the CMS tracker upgrade project and the MUonE project. In this chapter, I will first provide an introduction to the MUonE project and the beam line. This will be followed by a presentation of key definitions relevant to the study. Finally, I will present the results of my analysis.

7.1 The MuonE project

The muon anomalous magnetic moment is not only one of the most precisely measured parameters in particle physics but also a critical component of the Standard Model. Its precise calculation and measurement serve as a stringent test for the validity of the model. For over two decades, observations from the Brookhaven National Laboratory (BNL) and more recently, the Fermi National Accelerator Laboratory (FNAL) g-2 experiment, have consistently indicated a significant deviation from theoretical predictions, a deviation currently quantified at 4.2σ. While the direct measurements of α_μ at BNL and FNAL face challenges related to magnetic field uniformity, systematic errors, statistical limitations, and theoretical uncertainties, the MUonE experiment is a proposed experiment that is meant to provide a valuable complementary approach. By independently measuring the hadronic vacuum polarization, MUonE has the potential to reduce theoretical uncertainties and offer a different perspective that can enhance our overall understanding of the muon's anomalous magnetic moment. The MUonE experiment is innovatively designed to independently and accurately ascertain the leading hadronic contribu-

tion to the muon anomalous magnetic moment, symbolized as $\alpha_\mu = \frac{g_\mu - 2}{2}$. This is achieved through a distinctive method that involves measuring the hadronic part of the running electromagnetic coupling α in a region of momentum transfer that is crucial for understanding the muon g-2 anomaly. This is pursued through a detailed analysis of the differential cross-section of $\mu - e$ elastic scattering. The experiment is planned to take advantage of the high-intensity, $160GeV$ muon beam at CERN, which interacts with the atomic electrons of a light target material made from low-Z materials, such as Beryllium or Carbon, each $3cm$ thick, to minimize multiple scattering, interspersed with 40 stations of Silicon trackers (2S module) for measuring the trajectories of outgoing muons and electrons. The silicon tracker considered are the CMS 2S modules used in a different way as they would be used in CMS: The beam particles arrive asynchronous with respect to the signal sampling clock, leading to performance that are specific to such an operation mode. This will be explained later in this chapter. The stub data is the only data that is planned to be used by MUonE. Using only stub data allows reading out every clock cycle at 40 MHz frequency. This readout mode allows to cope with the high intensity of the M2 muon beam.

The setup concludes with an electromagnetic calorimeter for systematic checks and a muon filter. In the Figure 7.1, the layout of the MuonE experiment is depicted.

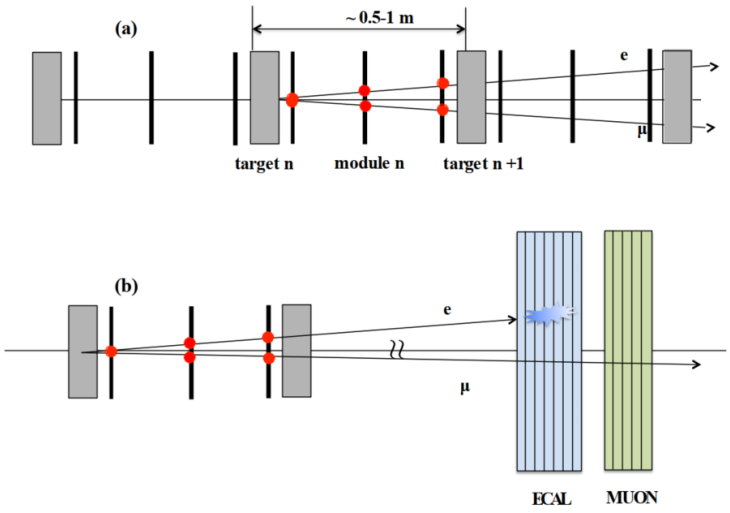

Figure 7.1: Scheme of a MUonE experiment: (a) modules sequence and (b) last module. The schematics are not on scale.

Common beam test between the MUonE project and the CMS tracker upgrade

project are organized in order to test the simultaneous calibration and readout of many modules for the first time. [71].

7.2 Beam line

The M2 beamline is situated in the North Area of Super Proton Synchrotron (SPS). This setup delivers high-energy and high-intensity beams of muons and hadrons, as well as low-intensity electron beams for calibration, towards the EHN2 experimental area. The schematics layout of M2 for horizontal (top) and vertical (bottom) view are shown in Figure 7.2. This beamline, running over approximately 1130 m, starts with six high-gradient quadrupoles designed for high acceptance, notably important for creating intense secondary Pion beams for muon generation. The beamline then employs a horizontal momentum selection system capable of handling momentum variations up to ±10%. Following this is a 600 m long Focusing-Defocusing (FODO) section allowing for the decay of these secondary particles into muons. The beamline is fitted with nine motorised Beryllium absorbers, measur-

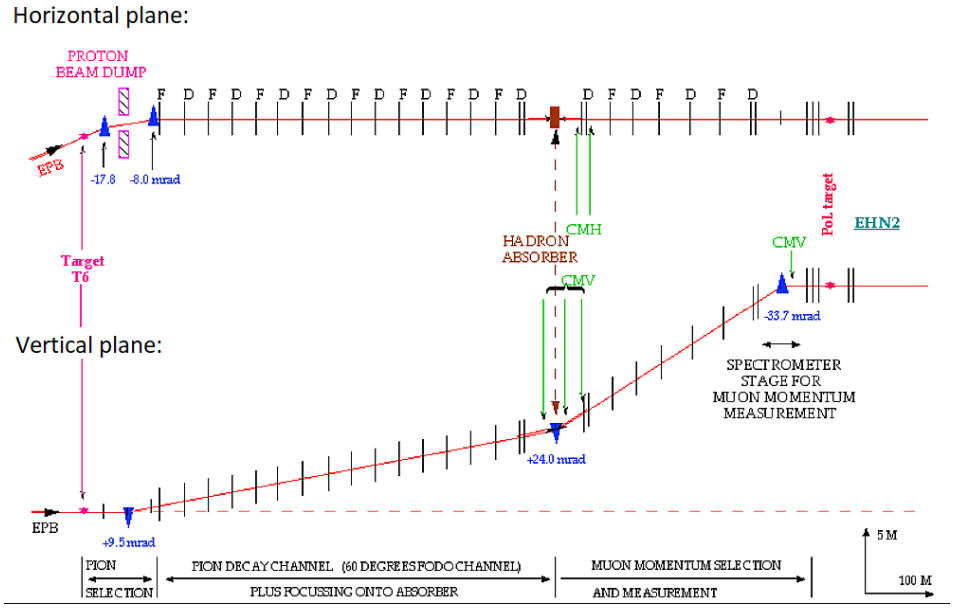

Figure 7.2: Schematics layout of M2 for horizontal (top) and vertical (bottom) view are depicted here.

ing up to 9.9 metres in length, to filter out leftover hadrons for various operating modes, such as hadron or muon beams. The contamination of hadrons in the muon beam is between 10^{-6} to 10^{-5}. A second 400 m Focusing-Defocusing (FODO) section complete with magnetic collimators selects the final muon momentum and

removes any scattered muons from the beam. Advanced instrumentation, including scintillator hodoscopes and Cherenkov detectors, are installed for momentum measurement and beam particle identification. The beamline's design ensures that the beam is focused at the experiment site in EHN2[72].

The upgraded M2 muon beam at CERN SPS is designed to handle high muon fluxes, derived from a primary proton beam of $400 GeV/c$. The intensity of this primary beam ranges between 10^{12} and 10^{13} protons per SPS spill. These protons, striking a primary Beryllium target, produce muons transported through the beamline to the detector. For a typical beam energy of around 160 GeV, the maximum muon intensity reaches about 5×10^7 μ^- per spill (with 10^{12} protons on target). The SPS cycle in fixed-target operation lasts about 14.8 seconds, which includes a 4.8-second spill duration, allowing up to four cycles per minute. In the Table 7.1 a summary of the available operation modes of the M2 beamline is presented and beam parameters for COMPASS are listed in the Table 7.2.

The beam size is around 20 mm in both dimensions, with an angular divergence. However, the halo component of the muon beam is notable, estimated to be about 27% of the total beam intensity.

At the Cerenkov Differential Counters with Achromatic Ring Focus (CEDAR) point in the M2 line, the way the beam spreads out is shown in Figure 7.3. We see that the beam spreads widely in both the x and y directions, which means it has long tails.

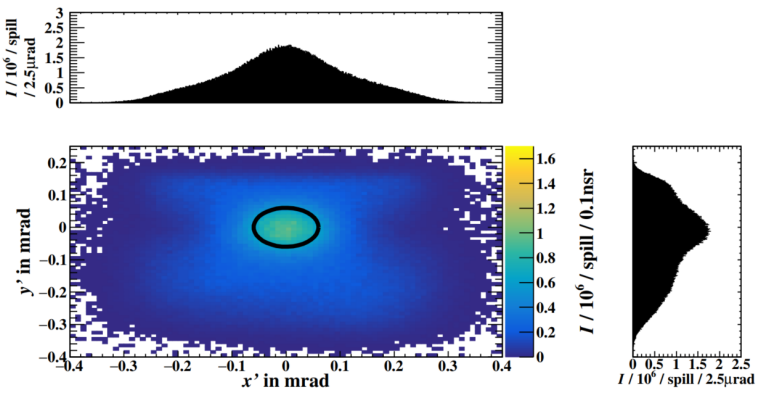

Figure 7.3: The beam divergence at the CEDAR location in M2.

In this beam test we used high intensity mode of Muons, up to 2×10^8 muons per spill, $50 MHz$ asynchronous rate with beam energy of around 160 GeV.

Table 7.1: Overview of the M2 beamline's operational configurations. This includes the momentum of secondary beams for tertiary beam applications.

Beam Mode	Polarity and Momentum [GeV/c]	Max. Flux [ppp/4.8 s]	Typical $\Delta p/p$ (%)	Typical RMS spot at target	Polarisation	Absorber [9.9 m Be]
Muons	+208/ + 190 +172/ + 160	$\sim 10^8$ $2.5 \cdot 10^8$	3%	8×8 mm^2	80%	IN
Hadrons	+190 −190 Max. 280	10^8 (RP) $4 \cdot 10^8$ (with dedicated dump)	-	5×5 mm^2	-	OUT
Electrons	−10 to −40	$< 2 \cdot 10^4$	-	$> 10 \times 10$ mm^2	-	OUT

Table 7.2: Beam parameters for COMPASS[73]

Beam Parameters for COMPASS	Measured
Beam momentum P_μ/P_π	$160/172 GeV/c$
Muon flux at COMPASS per SPS cycle	2.5×10^8
Spot size at COMPASS target ($\sigma_{dx} \times \sigma_{dy}$)	$8mm \times 8mm$
Divergence at COMPASS target ($\sigma_{dx} \times \sigma_{dy}$)	$0.4mrad \times 0.8mrad$
Muon halo within 50 mm from beam axis	16%
Halo in experiment ($6 \times 4m^2$) at $\lvert x, y \rvert > 150mm$	7%

7.3 Layout of the beam test setup

In this section, the beam test setup layout and the modules configuration will be discussed. The setup was located upstream of the COMPASS experiment, and data collection was conducted from September to October 2022. Phase 1 of the setup of the modules contains 4 modules, one assembled in Belgium DUT and 3 in Perugia. The layout of the beam test setup and the order and spatial configuration of the modules are depicted in Figures 7.4 and 7.5. Figure 7.6 show pictures of the setup box and data taking equipments.

The modules were tilted at a 13-degree angle to achieve the best resolution. The tilt involves increasing the chance of shared charge between strips next to each other. This leads to more clusters where two strips are active above the threshold, providing a better estimation of where the particle's track crosses.

The modules were placed in a specific pattern, with the strips alternating between the x and y directions. This arrangement was chosen to measure two coordinates that are orthogonal to the direction of the beam for tracking. The distance between each pair of modules in x and y direction is about 70cm.

During our experiments, we encountered some issues with data collection. The DUT or 2S-18-5-BEL-00003 is module 1, located as shown in Figure 7.4. Notably, there was no data coming from CIC 1 of module 3. This dead area will be accounted for in the event selection, as will be described later.

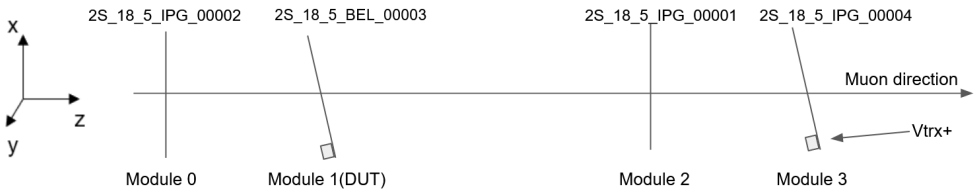

Figure 7.4: The layout of the beam test setup and the spatial configuration of the modules.

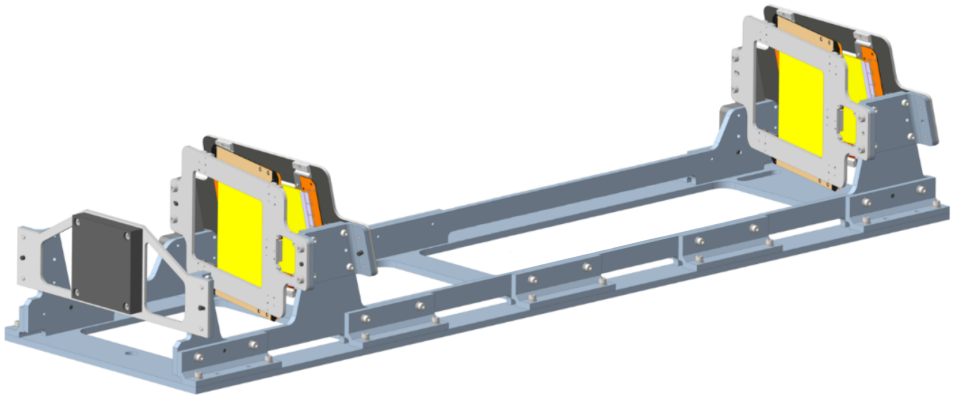

Figure 7.5: The CAD representation of the beam test setup.

7.4 DAQ system

The modules in beam test were read-out optically by a Serenity board. Serenity is a platform used for advanced telecommunications computing. It's made up of three main parts. First, there's a carrier card, which supplies basic services like power and clocking. It also has connections for optical and electrical signals. This

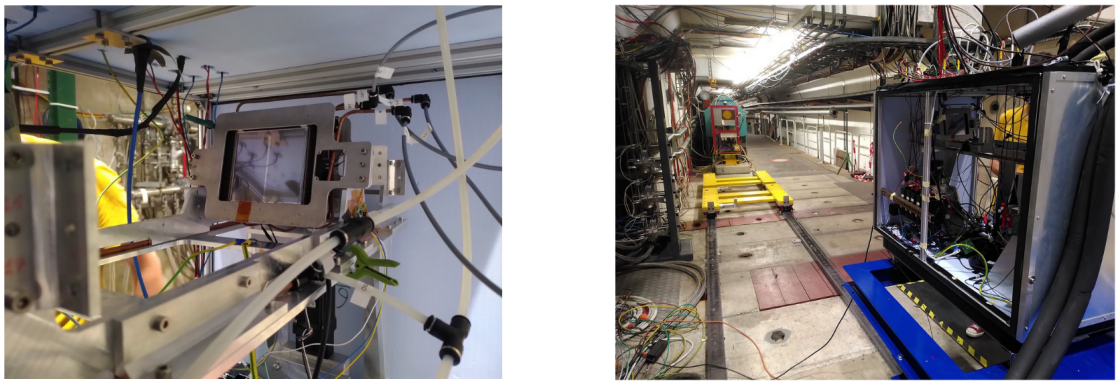

Figure 7.6: Left: Picture of the 2S modules in the setup box. Right: Picture of the setup box including 2S modules, DAQ equipments, cooling system and beam line.

card includes a special controller and a CPU that manages the board. Second, there are daughter cards. These are the parts where data processing happens on FPGA (Xilinx Virtex or KintexUltrascale+ devices).

The system has general and adaptable firmware and software. Regarding the connections for the daughter cards, they offer up to 144 serial optical links (up to $25Gb/s$ each), typically divided into 72 for transmitting and 72 for receiving. These are connected through Samtec Firefly connectors [74][75]. The picture of the Serenity carrier card is shown in Figure 7.7.

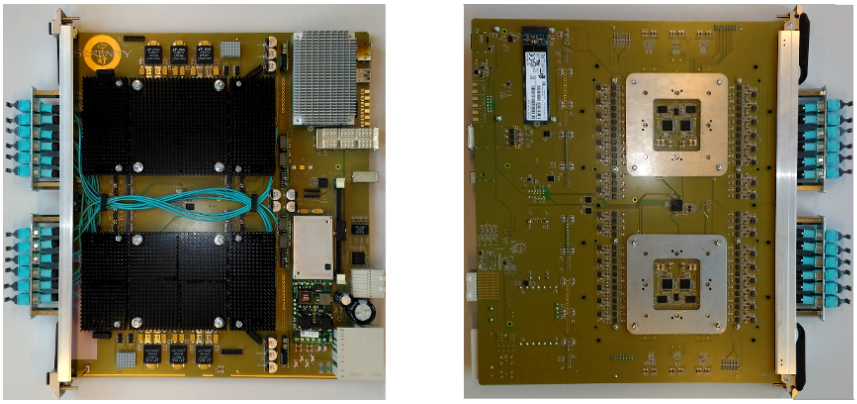

Figure 7.7: Serenity carrier card.

Initially, stubs data is unpacked on the board and sent to two DAQ computers via dual Ethernet links, each with a capacity of $10Gbps$. Upon completion of a run, the data is transferred to disk storage system.

The data received from the Serenity board is in a raw format. It contains all

stubs at a 40MHz readout rate. This data is organized by the board into packets, which are then grouped into links, and finally, these links are stored as files. Notably, the majority of this data is empty due to the higher sampling frequency compared to beam rate, and the files are raw and uncompressed, resulting in a substantial volume of largely irrelevant data that needs to be compressed into a more manageable format.

The first step in this compression process involves the removal of empty links. This is accomplished using a tool known as a 'skimmer,' which is automatically activated following data transfer. Despite the reduction in data volume at this stage, much of the output remains irrelevant.

At this point, the files predominantly contain empty events and are not in a user-friendly format. A decoding process is required, typically converting the data into ROOT format. This conversion is carried out by an unpacker script. This step further reduces the size of the data files, preserving mainly the non-zero information in a flat tree structure that is more accessible.

The trees include all the stubs, organized by BX. Since a stub may appear in BX_y in the first module and BX_z in the next module, both corresponding to the same particle, it may be necessary to combine consecutive BXs. This is achieved through a mini-framework, which allows the user to request the next "multi-event" —a collection of all relevant stubs from consecutive BXs that correspond to the same event. The framework gathers all relevant stubs into vectors, which remain separated by BX.

This framework allows users to easily request the next 'multi-event,' following which all corresponding stubs, still categorized by BX, are collated. For those unconcerned with the event timing, sets of stubs collected during each multi-event are also made available, organized by module. Figure 7.8 shows data path from 2S modules to storage for analysis.

In my analysis, I employed two distinct experimental runs, which are outlined below. These runs were integral to the study as they encompassed a Bias Voltage Scan and a Two-Dimensional (2D) Scan, wherein both the Bias Voltage and the Comparator Threshold (V_{CTH}) were methodically scanned.

- RUN_2022: This particular run focused on the Bias Voltage Scan. It was conducted in August 2022. The emphasis of this run was to systematically vary and record the bias voltage parameters from 0 to 900 Volts for the device under test 2S-18-5-BEL-00003. This provided insights into their impact on the 2S module performance.

- RUN_3061: In September 2022, RUN 3061 was executed. This run was distinctively characterised as a Two-Dimensional (2D) Scan. It was not limited to just the Bias Voltage parameters, as in the previous run, but

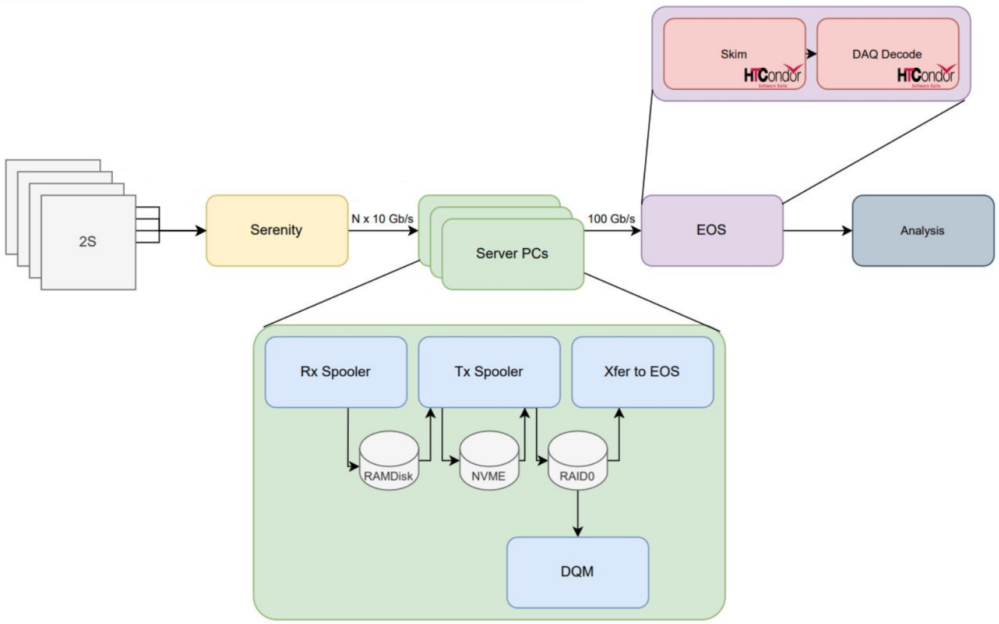

Figure 7.8: The diagram illustrates the data flow from 2S sensor modules to final storage. Data is collected by the Serenity board at a 40 MHz clock cycle frequency, where stubs are aggregated into packets, packets into links, and links into files. Server PCs handle the processing, with the data transferred at high speed (up to $100 Gbps$) to the disk storage system. To reduce the large volume of data, a "skimmer" automatically removes empty links after transfer, significantly reducing the data size. Decoding and further processing convert the raw output into usable formats like ROOT files for analysis.

also included an extensive scan of the V_{CTH} with 15 V_{CTH} (2340 electrons) steps and varying from 400 to 595 V_{CTH} unit (156 to 30576 electrons). This comprehensive approach allowed for a better understanding of 2S module behaviour versus the bias Voltage and the V_{CTH}. This offered a multifaceted perspective on the system's operational dynamics.

7.5 2S module properties (DUT)

The DUT is labelled 2S-18-5-BEL-00003. It is the first fully functional module equipped with a service hybrid and optical read out, built in Brussels at the IIHE. This module has 5 cooling points and the space between the sensors (AlCF thickness) is $1.8mm$. The part numbers and versions of the components used in the modules for the beam test are listed in Table 7.3. Before examining the module's performance in a particle beam, its status was characterised in detail during assembly. The current-voltage (I-V) characteristics of the sensor were measured at different stages of the assembly. The pedestal and noise of each readout channel were also measured during calibration runs, at different assembly stages and at the beam test site.

7.5.1 Sensor characterization

- **CV curve measurement** According to Equation 3.6, there is a linear dependence expected between $1/C^2$ and the sensor bias voltage, where C is sensor total capacitance, until the depleted voltage region reaches the sensor backplane. Apart from the detector geometry, which is fixed, the slope of the curve and the full depletion voltage are determined by the sensor bulk resistivity ρ. Therefore, details of the sensor production process always include a measurement of the C-V curve. The $1/C^2$ versus voltage curves of both sensors of the DUT taken at KIT and Hamamatsu are shown in Figure 7.9. Very similar, sign excellent reproducibility of the production process. A depletion voltage of $290V$ is observed, which corresponds to a resistivity of $2.92k\Omega cm$ for the top sensor and $2.96\ k\Omega cm$ for the bottom sensor. Both numbers within the specified range given in Table 3.1.

- **IV curve measurement** IV curve measurement are performed at several steps of the module assembly to check that no damage was incurred by the sensors during shipping, handling, gluing, bonding, etc. Such damage would typically result in an increase of leakage current. Sensors with a leakage current above specifications should be investigated to understand the cause of the damage and eventually be discarded. The bias voltage is applied to the sensor backplane from the jig for bare sensor, and from the HV pigtail after it has been glued and bonded to the sensor backplane. The sensor bias ring is grounded by contacting it with a Karl Suss probe needle. This needle is positioned manually under a microscope. The IV curve measured in Brussels on the top and bottom sensor of the DUT are shown in Figure 7.10. The top sensor current shows instabilities. Notably, a kink in the IV current is visible at $500V$, followed by a rapid increase of the current when increasing the bias voltage. The current in the top sensor does not comply with specification after the step of sandwich gluing.

- **Electrical noise** Measuring the electrical noise of the channels brings a lot of information about the module quality. The noise is defined as the Root Mean Square (RMS) of a Gaussian curve fitted to the derivative of the S-curve. It corresponds to the Root Mean Square (RMS) of the channel pedestal. For a module that is biased with $V_{bias} \geq V_{depletion}$, an overall noise level of about 1000 e^- is desirable in order to maintain efficient operation at the higher radiation doses foreseen at HL-LHC[3]. Then the noise depends on the strip capacitance connected to the input of each pre-amplifire. A lower noise is seen for disconnected strips, and a larger noise is seen for strips which are shorted together. Eventually the full depletion voltage can also be found by measuring the noise as a function of bias voltage, since the strip capacitance

Table 7.3: The table lists the part numbers and versions of the components used in the modules for the beam test.

Module number	Module 0	Module 1 (DUT)	Module 2	Module 3
Part number	2S-18-5-IPG-00002	2S-18-5-BEL-00003	2S-18-5-IPG-00001	2S-18-5-IPG-00004
Top sensor	36240-009-2	34357-014-2	36241-030-2	34332-005-2
Bottom sensor	36241-042-2	34357-031-2	36241-006-2	34332-041-2
SEH	2SSEH-201000024	2SSEH-201000027	2SSEH-201000028	2SSEH-201000021
FEH-L	2SFEH18L-201000243	2SFEH18L-201000248	2SFEH18L-201000241	2SFEH18L-201000234
FEH-R	2SFEH18R-201000342	2SFEH18R-201000347	2SFEH18R-201000343	2SFEH18R-201000212
CBC version	3.1	3.1	3.1	3.1
CIC version	2	2	2	2
LpGBT version	0	0	0	0
Spacing between sensors	1.8 mm	1.8 mm	1.8 mm	1.8 mm
Number of cooling points	5	5	5	5

is inversely proportional to the depleted depth. In Figure 7.11 the noise of each channel of the DUT biased at $400V$ is showed. The average noise is around $7V_{CTH}$ units for top strips, and around $9V_{CTH}$ units for bottom strips, consistent with other prototypes built with the same version of the readout hybrids. No disconnected, nor shorted strip appears in this graph, indicating that all strips are active in the DUT. Calibration of each module was done separately during calibration by acquisition software $Phase2-ACF$ before data taking in the beam test site.

7.6 Beam profile

Beam profile plots help us assess the functionality of each detector by analyzing the spatial distribution of stubs. These plots are created by directly including all stubs in each BX before applying any event selection filter. The data were collected while the detectors were operating under normal conditions, with a bias voltage of 400 V and a threshold voltage set to 550 V_{CTH} units. From the beam profiles of detector 0 (Figure 7.12), DUT (Figure 7.13), and detector 2 (Figure 7.14), we observe consistent and expected patterns which indicates that these detectors are functioning properly. However, in detector 3 (Figure 7.15), as mentioned, CIC 1 is dead zones, and there are inefficiencies in strips numbered 762 to 764 in CIC 0. We also observed that the beam is wider in the y-direction (Figure 7.13) compared to the x-direction (Figure 7.12). The FWHM in the x-direction was measured to be 322 strips, and in the y-direction, it was 833 strips. Considering the strip pitch, this corresponds to a beam size of approximately 2.9 cm in the x-direction and 7.5 cm in the y-direction

7.7 Event selection

In data preprocessing the stubs from successive non-emptyBX were merged together, up to a maximum of 5 consecutive events. Due to the asynchronous beam, clock edges are difficult to align in all detectors at the same time therefore the signal from the same particle can be recorded in successive BX for different detectors. To analyze the data, we used specific selection criteria for the events. These criteria include:

- We only looked at events where exactly one stub was detected in each of modules 0, 2, and 3.

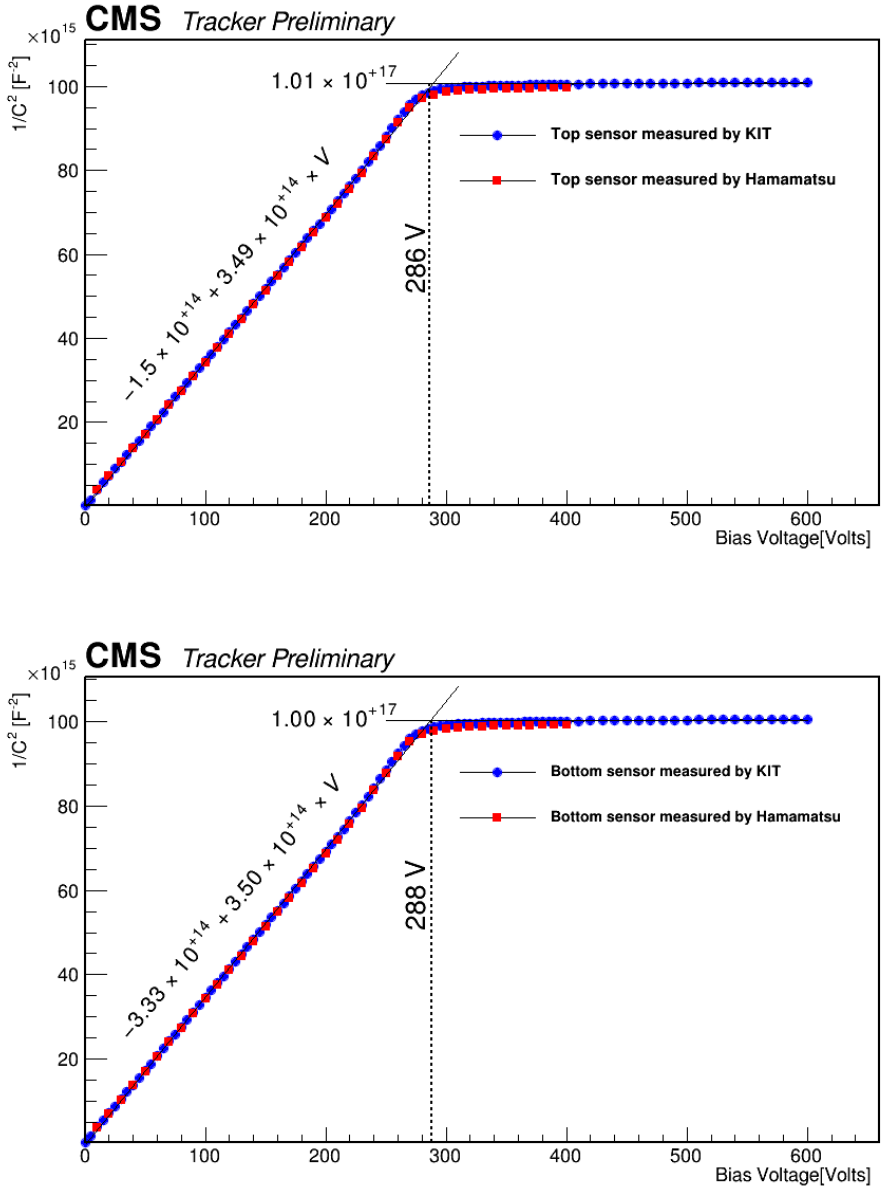

Figure 7.9: Plot of CV measurement for both top (top plot) and bottom (bottom plot) sensors of the DUT. The depletion voltage can extract from this plot at $288V$. The data was measured by KIT before sending the sensors to IIHE. As reported by KIT the temperature was $19.9°C$ and humidity was less than 12% during CV measurement.

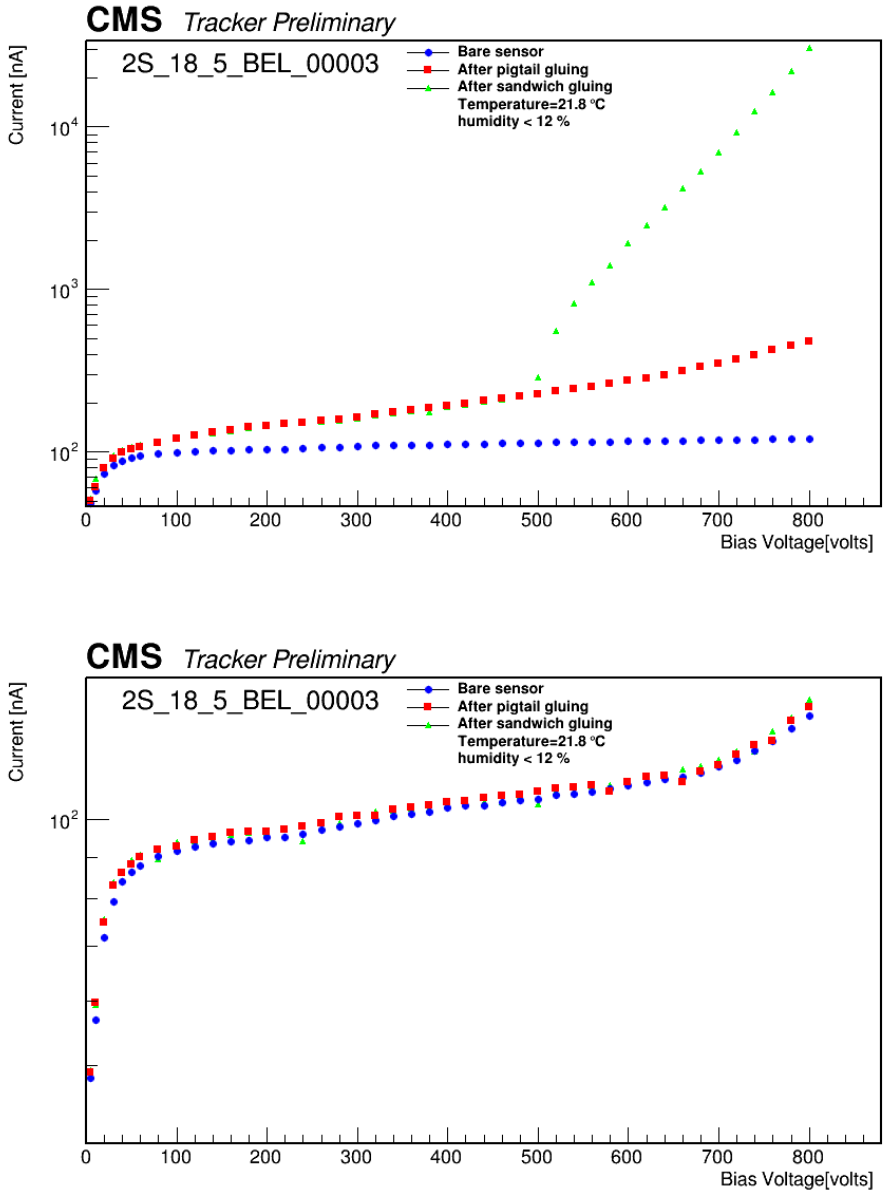

Figure 7.10: IV curve for top sensor (top) and bottom sensor (bottom) of the DUT after each step of module assembly. Measurements were taken at an ambient temperature of 21.8°C with humidity levels maintained below 12%. The measurement was taken at IIHE in Brussels.

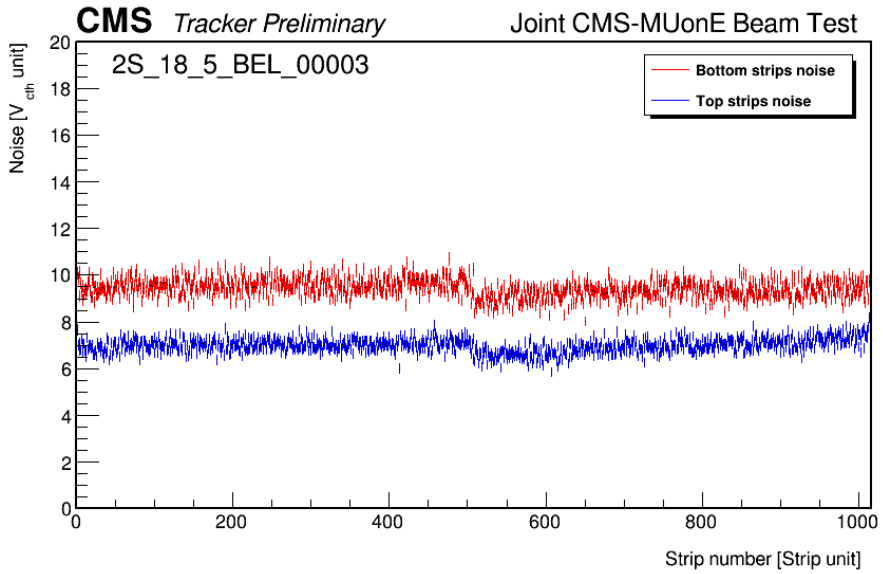

Figure 7.11: Electrical noise of the strips during the calibration of DUT for top and bottom sensor is shown. The average noise is around 7 V_{CTH} unit for top strips, and around 9 V_{CTH} unit for bottom strips.

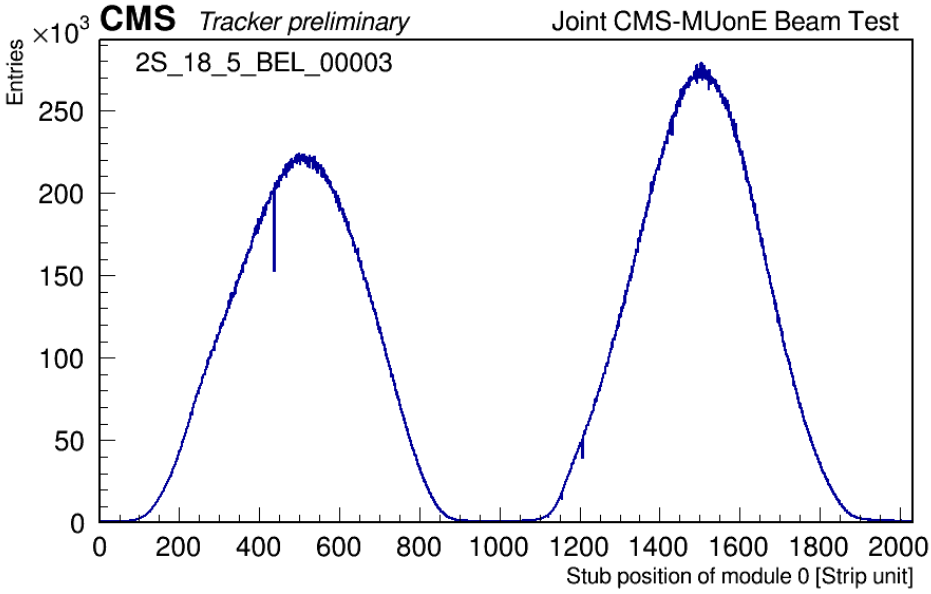

Figure 7.12: Profile of the beam for the module 0 for the left (channels 0-1016) and right (channels 1017-2032) hybrids.

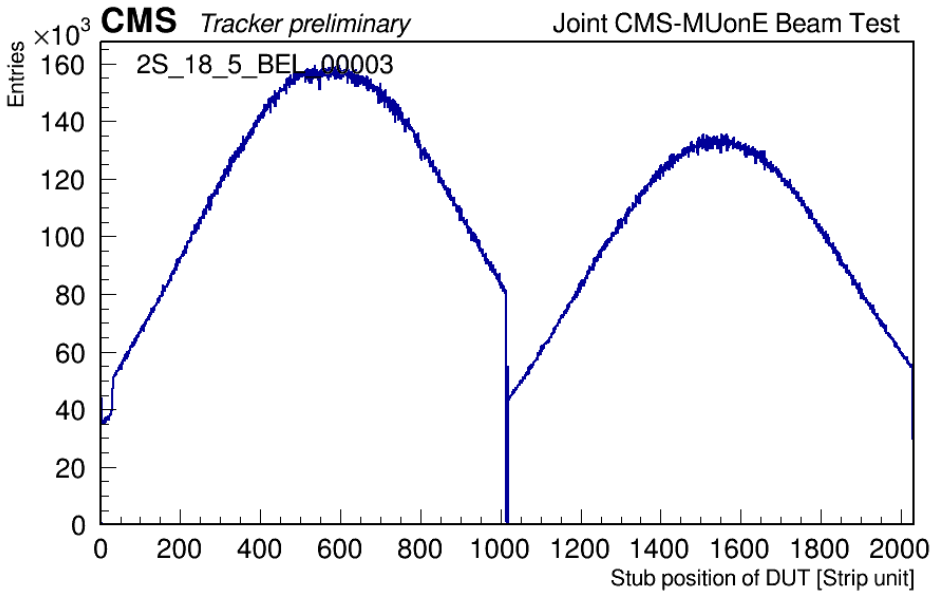

Figure 7.13: Profile of the beam for the DUT for the left (channels 0-1016) and right (channels 1017-2032) hybrids.

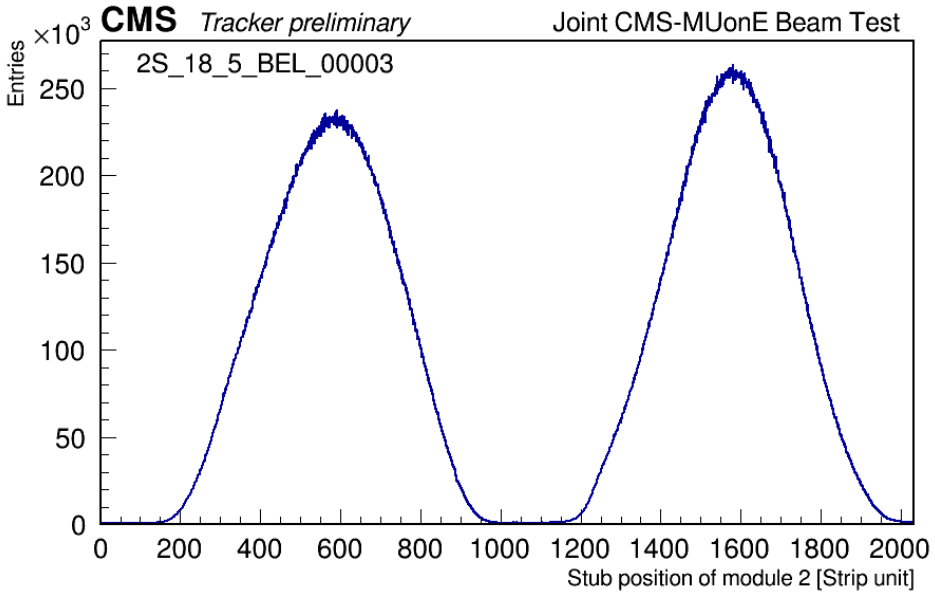

Figure 7.14: Profile of the beam for the module 2 for the left (channels 0-1016) and right (channels 1017-2032) hybrids.

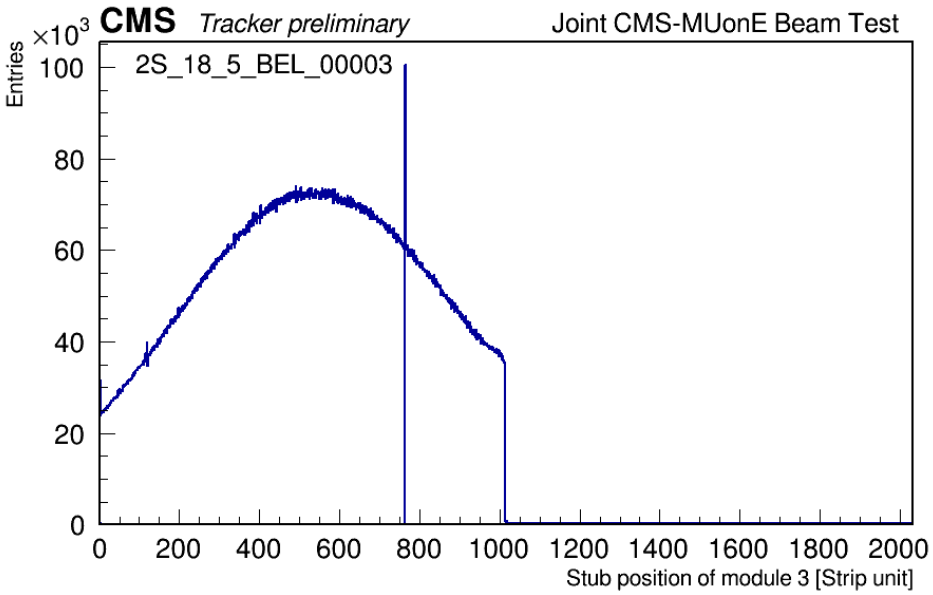

Figure 7.15: Profile of the beam for the module 3 for the left (channels 0-1016) and right (channels 1017-2032) hybrids.

- We used the histogram of the stubs' bend numbers to filter and select particles parallel to the beam axis. As shown in Figure 7.18, we chose particles with a bend number ranging from −1 to 1.
- The stubs in modules 0 and 2 needed to align with a straight track, suggesting they were part of the same particle path.
- For module 0, we required the seed cluster to be located between strip numbers 250 to 375 or 1200 to 1400. This was to make sure we did not consider tracks at the very edges of the strips in our DUT, where data might be less reliable.

Since we didn't get data from half of module 3, we only considered the corresponding half of the DUT. This approach ensured consistency in our analysis.

7.8 Alignment

For the alignment analysis, the run with all the modules operating at nominal condition, bias voltage of 400 V, and V_{CTH} = 550 $V_{CTH}unit$ has been selected. The initial step involves determining the shift in the direction perpendicular to the strips, as well as a position tilt around the strip direction between two planes

of modules aligned in the same direction (specifically, module 0 and module 2 in the y direction and DUT and module 3 in the x direction). We first created a plot showing the stub combinations between two modules. This plot for the DUT and module 3 is shown in Figure 7.16. To ease the extraction of the alignment parameters, we projected it onto the y-axis for each x-axis bin and selected the most probable value. We had to disregard 5%(50*strip*) of the first and 25%(254 *strips*) of the last bins on the x-axis due to a lack of data at the low and high ends along the strips. After that, we fitted a line to the plot showing the selected most probable values of the stubs in module 3 versus DUT. We repeated this process for modules 2 and 0. The formulas 7.1, 7.2, and 7.3 effectively represent the correlation found between these two sets of modules.

$$Y_{2,0} = X_{0,0} \times 1.01341 + 69.6 \tag{7.1}$$

$$Y_{2,1} = X_{0,1} \times 1.01196 + 59.2 \tag{7.2}$$

$$Y_{3,0} = X_{1,0} \times 0.98779 - 28.6 \tag{7.3}$$

where $Y_{2,0}$ is stub position in CIC 0 of module 2, $X_{0,0}$ is position of seed cluster in CIC 0 of module 0, $Y_{2,1}$ is stub position in CIC 1 of module 2, $X_{0,1}$ is position of seed cluster in CIC 1 of module 0, $Y_{3,0}$ is stub position in CIC 0 of module 3, $X_{1,0}$ is position of seed cluster in CIC 0 of module 1 (DUT). To evaluate the fit's accuracy, we looked at the residual plot, which is shown in Figure 7.17 on a logarithmic scale.

The residual is the difference between where the stub actually is in the DUT and where we predict it to be (extrapolated) based on its position in module 3 according to the alignment computed above.

The width of the residual is comparable to beam spread in Y mentioned in Table 7.2:

$$\frac{0.8\ mrad \times 70\ cm}{90\ \mu m\ pitch} = 6.2\ strip \tag{7.4}$$

while the fitted Gaussian width is 4.26 strip. The tail can possibly be attributed to the significant beam halo also mentioned in Table 7.2 (if this halo has a different angular distribution than the main beam) We fitted a Gaussian function to the residual plot for values ranging from −10 to 10 strips. A selection window for stubs in the DUT was set to a width of ±30 strips, which roughly correspond to 6 times the width. To be efficient, a stub must be found in the DUT within this window.

7.9 Fiducial area

The area of the silicon strip module that is expected to be most optimally sensitive to incoming particles is known as the fiducial area. It is within this area

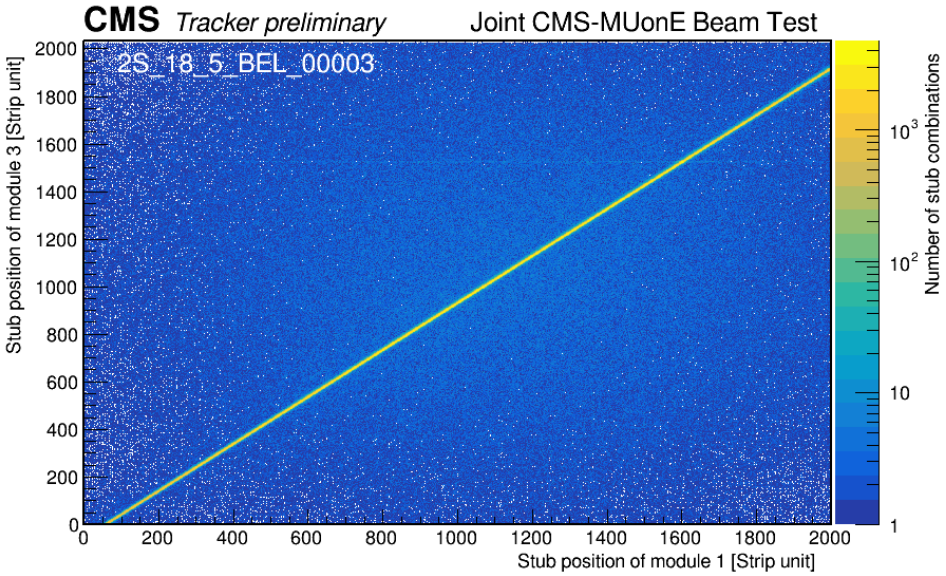

Figure 7.16: The number of stub combinations as a function of stub position in CIC0 of DUT and module 3 is depicted.

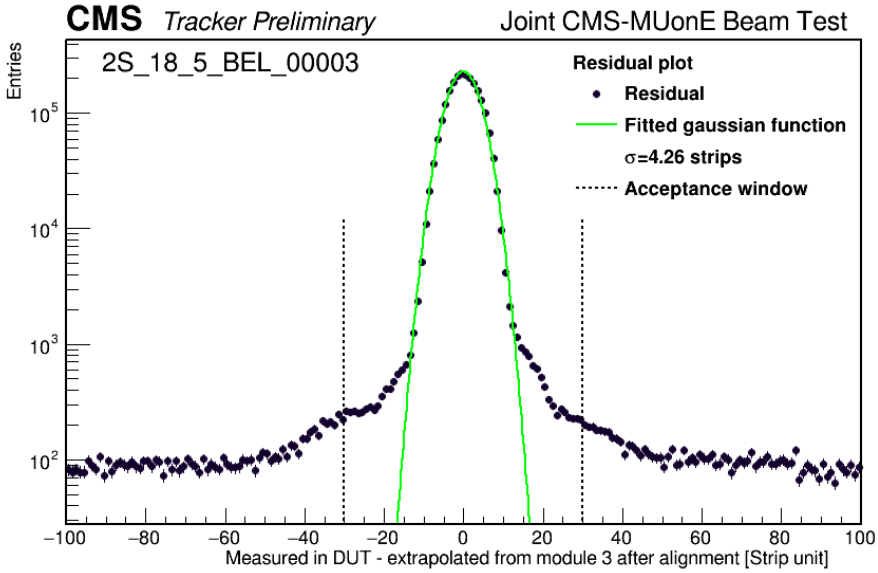

Figure 7.17: Residual plot of calculated alignment has been shown here for CIC0 of the DUT and 3.

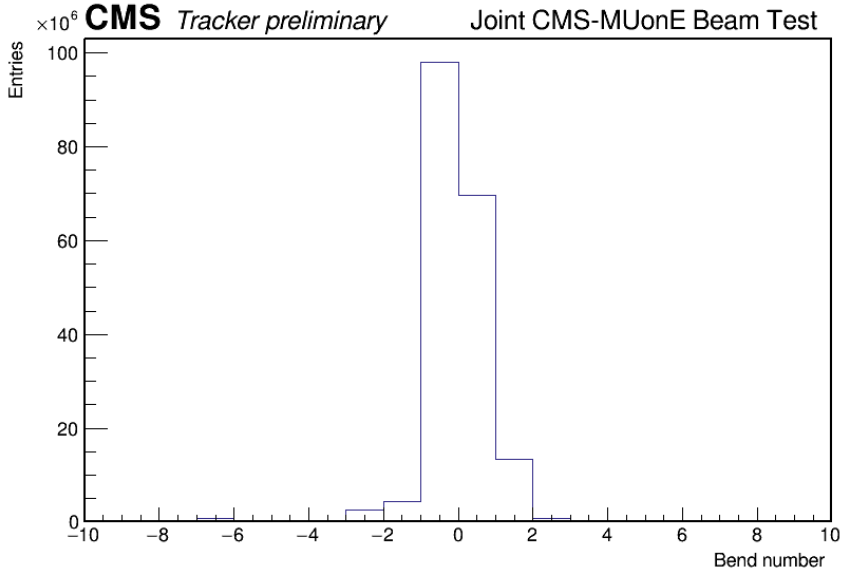

Figure 7.18: Bend number histogram for all the stubs pass through in the module 3.

that the detector's response is well-characterized and calibrated, ensuring valid measurements. The fiducial area excludes edges and regions where the detector's response might be uncertain, inconsistent, or influenced by edge effects, noise, or other factor. This could compromise the quality of the data.

When measuring the DUT efficiency, the zone at the ends of the strips in the DUT were excluded from the fiducial region. This was achieved by requesting stubs to be reconstructed in strip coordinate between 250 and 375 in module 0 when estimating the DUT efficiency in channels CBC0 to CBC3 (respectively between 1200 and 1400 for DUT efficiency in channels CBC 4 to CBC 7). In the Figure 7.19 and 7.20, the fiducial area is shown for both first quarters of the module 0. The color code indicates the stub reconstruction efficiency, studied in section 7.10.1.

7.10 Performance as a function of V_{bias}

This section presents the results for stub reconstruction efficiency, off-track occupancy, and seed cluster multiplicity as a function of bias voltage. These results will be discussed while all the modules was fixed with the V_{CTH} set to ~ 7200 electrons (V_{CTH} = 550 V_{CTH} unit, while pedestal was measured 596 V_{CTH} units as shown in Figure 7.24) and only bias voltage of DUT was changed.

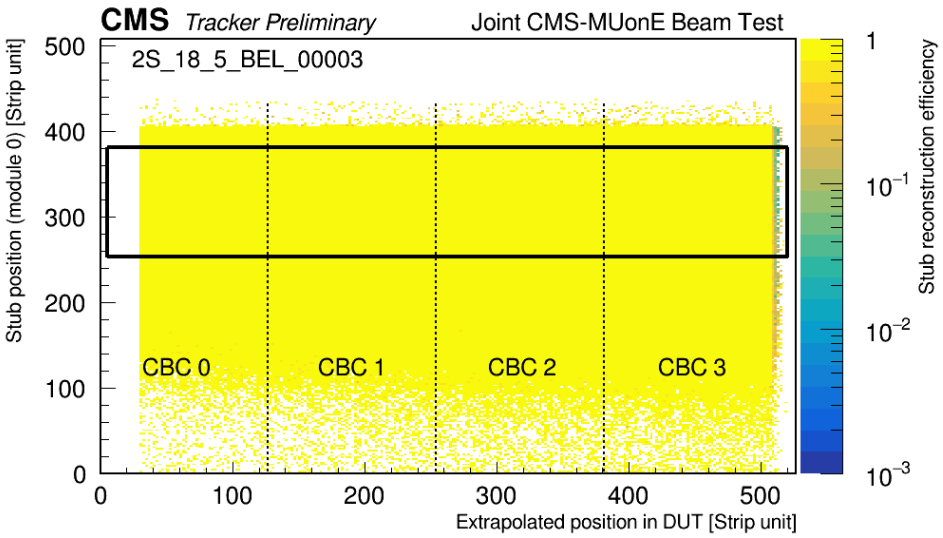

Figure 7.19: Stub reconstruction efficiency as a function of extrapolated position in DUT and stub position in module 0, in the second quarter. The selected region is shown by the black rectangle.

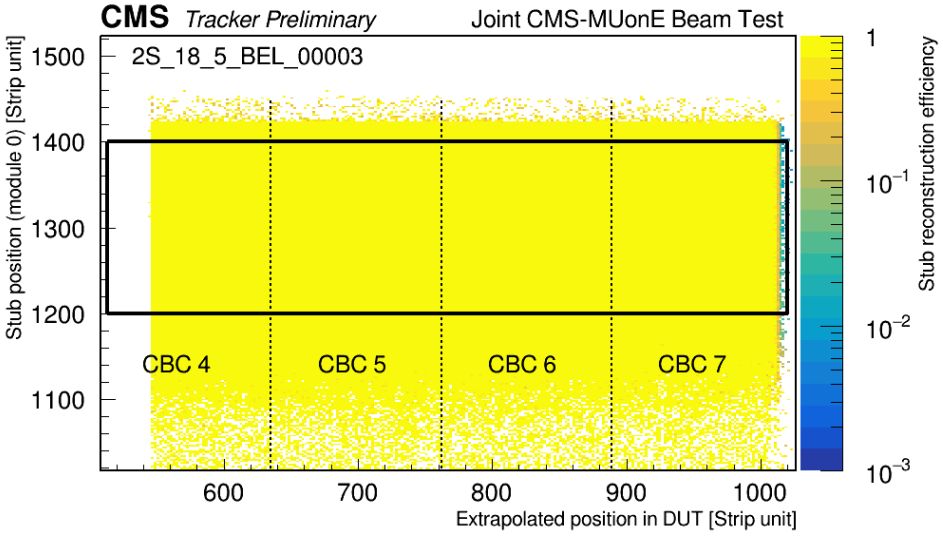

Figure 7.20: Stub reconstruction efficiency as a function of extrapolated position in DUT and stub position in module 0, in the first quarter. The selected region is shown by the black rectangle.

7.10.1 Efficiency as a function of V_{bias}

The detector's SCR increases as the voltage rises until it is fully depleted at the depletion voltage. According to the CV measurements (Figure 7.9) of both detector sensors, it needs about 300 V to reach full depletion.

During data taking for bias voltage scan, the V_{CTH} of all the modules was set on the nominal operation condition on ~ 7200 electron (V_{CTH} = $46V_{CTH}$ $unit$). The bias voltage of all other modules were set at higher their full depletion voltage (400V). The data selection was described in Section 7.7. For each voltage level measurement, several data (ntuples) were available. We also looked at how consistent the detector's performance was at the same voltage levels to see if the power supply was stable. The results didn't show any increasing or decreasing pattern versus time, and we removed any out-of-range data points. Then, we selected the best-fitting value on the graph of data set (the ntuples) for each bias voltage to represent the detector's efficiency at that voltage.

The efficiency is defined as:

$$\epsilon = \frac{\begin{array}{c}\text{denominator \&\& stub in DUT within the selection window} \\ \text{of } \pm 30 \text{ strips around the extrapolated stub position}\end{array}}{\begin{array}{c}\text{Number of selected events with a stub extrapolated} \\ \text{in the DUT fiducial region}\end{array}} \tag{7.5}$$

The stub reconstruction efficiency as a function of applied bias voltage for the CBC 1 to CBC 7 of DUT are shown in Figure 7.21 top and in the bottom the percentage difference from average value is depicted. In the plot, the uncertainty are shown, are smaller than the size of the marker. Analyzing the percentage difference from the average value of different CBCs at each voltage, shows that there are fluctuations in efficiency for voltages from 0 to $169V$. As the bias voltage approaches the full depletion voltage (~ $290V$), the percentage differences converge, and the different CBCs show similar behavior for bias voltages above the full depletion voltage.

At $289V$, the efficiency for CBCs attained were around 95%, and for voltages greater than 289 V, similar or higher efficiencies were observed. However, we noticed that it actually takes more than 676 V to reach the plateau. This was more than we expected, and finally, an average efficiency around 96.5% was reached at $V_{bias} \geq 676$ V for different CBCs of the DUT. The asynchronous nature of the beam in this particular experiment is the reason of relatively low value of efficiency in compared to earlier results [76] and will be discussed in more detail in Section 7.12.1. At very low voltages, near zero, efficiency around 0.7% was measured. This could be due to the electrical noise of the electronic read-out system of the detector, as it has the highest capacity at low depletion voltages.

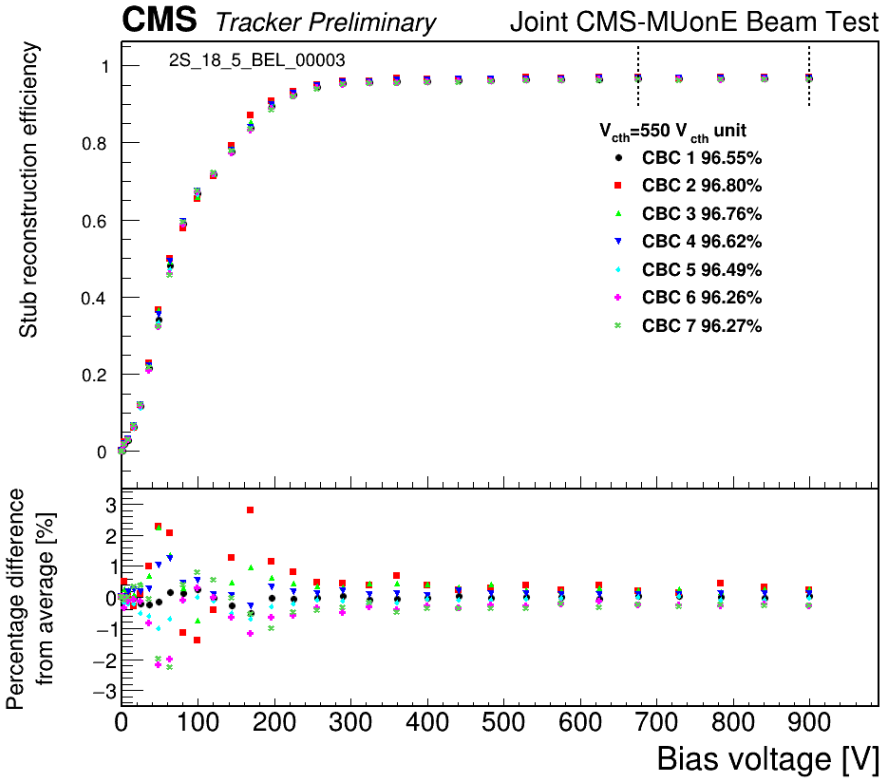

Figure 7.21: The stub reconstruction efficiency as a function of applied bias voltage for CBC number 2 to 7 of CIC 0 of DUT (top) and percentage difference from average value (bottom). Different CBCs show similar behaviour for bias voltage higher than full depletion voltage($\sim 290V$).

7.10.2 Off-track occupancy versus V_{bias}

An off-track stub is defined as a stub that is reconstructed in the DUT outside the acceptance window around the extrapolated beam particle track. The off-track occupancy is defined as:

$$\text{Off-track occupancy} = \frac{\text{Total number of off-track stub in selected event}}{\text{Number of selected events}} \tag{7.6}$$

In this analysis the off-track as a function of the expected strip position in DUT is obtained. Then the average of off-track level over the strips of the DUT was calculated. To obtain off-track occupancy, all stub inside the fiducial area are considered. Figure 7.22 shows the off-track occupancy as a function of bias voltage (left axis) together with the stub reconstruction efficiency for CBC 1 (right axis), for threshold of about ~ 7200 electrons (V_{CTH} = 550V_{CTH} *unit*). There is a considerable decrease in the off-track stub occupancy until it reaches the full depletion voltage, after which it remains below the percent level.

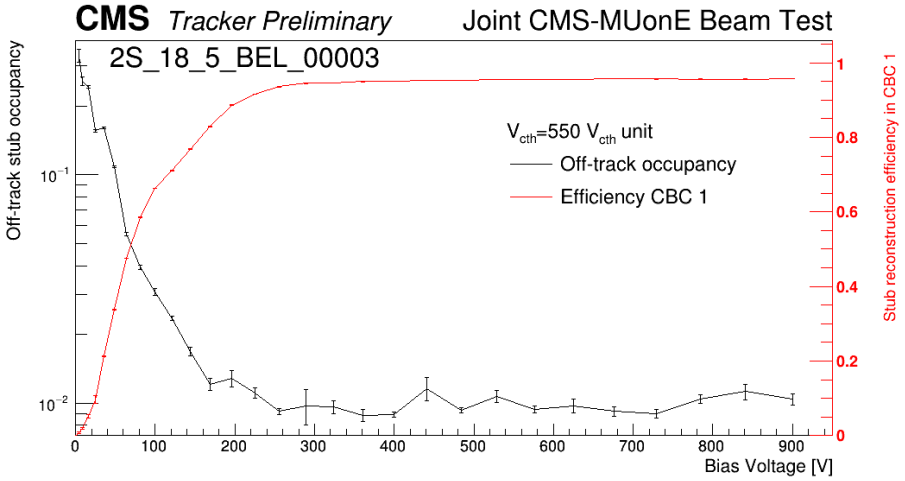

Figure 7.22: Off-track occupancy in the DUT and the stub reconstruction efficiency in CBC 1 as a function of applied bias voltage for nominal threshold V_{CTH} = 550V_{CTH} *unit*. The off-track occupancy decreases when the bias voltage approach the full depletion voltage and roughly remains fixed for voltages higher than that.

7.10.3 Seed cluster multiplicity versus V_{bias}

The multiplicity of the seed cluster, also investigated by looking at stubs with seed cluster multiplicities. Odd stub multiplicity is defined as seed cluster with

size of 1 or 3 while even stub multiplicity means a seed cluster size of 2. The multiplicities versus bias voltage is investigated and has been shown in Figure 7.23. The percentage of stubs with odd multiplicity increased from $4V$ to $49V$. Then it decreases until the depletion voltage and remains roughly fixed. This is because at higher bias voltages, the depleted region increases, and as a result, the clusters become wider, and fewer single-strip clusters are observed. The decrease in the fraction of odd clusters at low bias voltages is due to significant electronic noise, which would lead to a reduction in the average cluster size. This increase in noise at unchanged V_{CTH} threshold value causes the coincidence of noise in both sensors to form a stub.

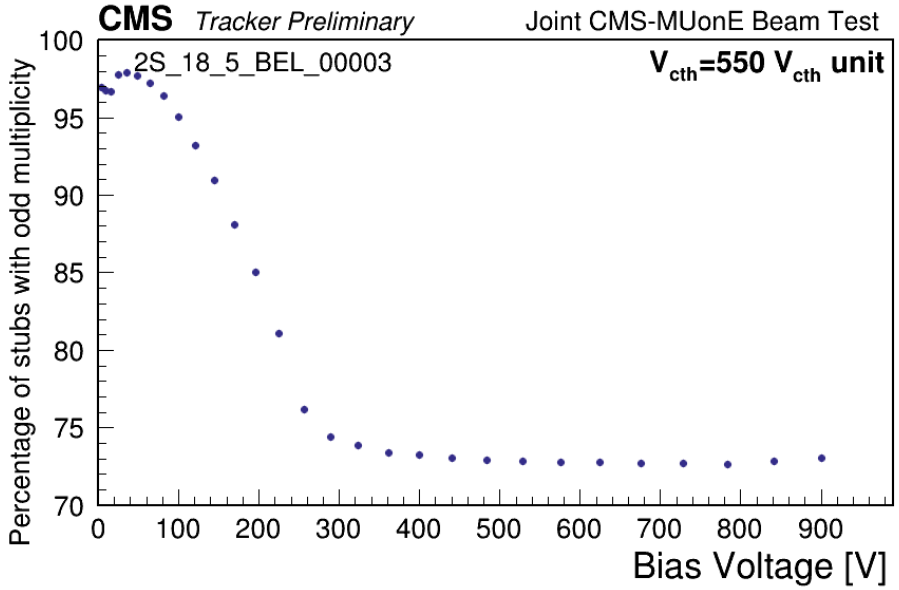

Figure 7.23: The stub multiplicity is displayed as a function of bias voltage. The drop at low voltage is due to significant noise distribution. Then the stub multiplicity decreases as bias voltage approach to full depleting voltage and for higher voltages, it remains fixed.

7.11 Performance as a function of signal threshold

This section will present the results for stub reconstruction efficiency, off-track occupancy, and seed cluster multiplicity as a function of V_{CTH} in DUT, followed by a discussion of these results while the bias voltage of all the modules was

fixed and only the comparator threshold of the DUT was changed. The threshold baseline was calibrated to a level of 596 V_{CTH} units as shown in Figure 7.24. In

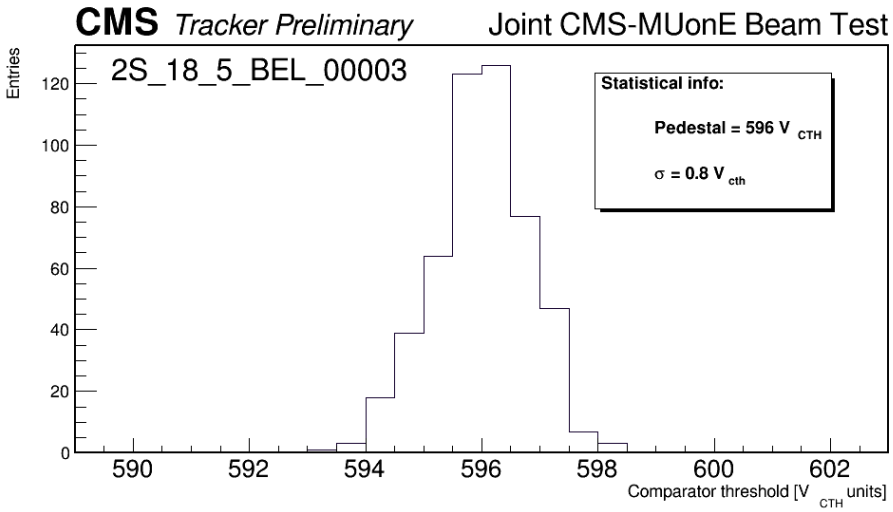

Figure 7.24: Pedestal distribution for CBC 0 is shown in this plot.

the following text, the signal threshold in V_{CTH} is defined as the distance to the pedestal value in V_{CTH} unit.

7.11.1 Efficiency as a function of signal threshold

Another parameter of the detector scanned during the beam test was V_{CTH}. To find a nominal value for the V_{CTH} we selected a run with bias voltage higher than full depleting voltage ($400V$) and investigated the efficiency versus the V_{CTH} which changed by step of 2340 electrons (15 V_{CTH}). The efficiency for CBC numbers 1 to 7 on CIC 0 within the DUT versus the V_{CTH} are shown in Figure 7.25 (top). The maximum efficiency was observed ~ 7200 electrons (46 V_{CTH} unit). The low efficiency in the low V_{CTH} is due to the noise contribution.

In the bottom plot, we show the percentage difference from the average stub reconstruction efficiency for each CBC at various signal thresholds, all measured at a fixed voltage of 400 V. At high signal thresholds, the percentage differences are reach to 2% for some different CBCs. CBC 3 and 5 have the most close behavior to the average value. As the signal threshold decreases, these differences converge and have a minimum around to 7200 electrons ($46V_{\mathrm{CTH}}unit$), indicating similar stub reconstruction efficiencies among the CBCs.

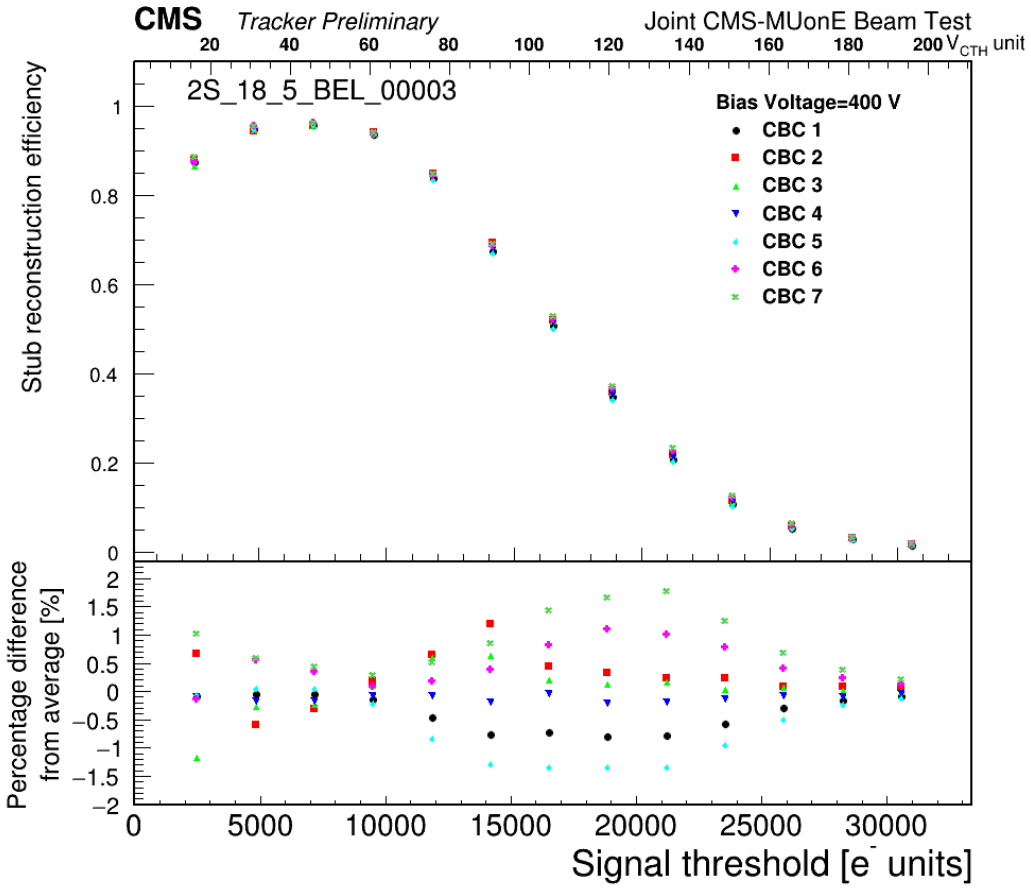

Figure 7.25: (Top) Stub reconstruction efficiency as a function of V_{CTH} for CBC numbers 1 to 7 of CIC 0 in the DUT. (Bottom) Percentage difference from the average value of stub reconstruction efficiency for different CBCs at each signal threshold, at a fixed voltage of $400V$. Around a signal threshold of 7200 electrons ($46V_{\mathrm{CTH}}$), there is minimal difference among the CBCs, and they show the same stub reconstruction efficiency.

7.11.2 Off-track occupancy versus signal threshold

Off-track is an important parameter for understanding the background noise level and the detector's ability to discriminate between signal and background. It is defined in Section 7.10.2. To understand the low efficiency in low V_{CTH} it is important to study off-track occupancy.

Off-track hits can be caused by secondary particles (those created from the decay or interaction of primary particles), noise in the detector, or particles from unrelated background events.

In the Figure 7.26 the stub reconstruction and off-track occupancy versus comparator threshold for the DUT module which was operated with a nominal bias voltage of 400 Volts is shown. At low thresholds, we observed significant off-track occupancy due to noise. By increasing the signal threshold, the off-track occupancy decreases and reaches a stable value at 7200 electrons ($46 V_{\mathrm{CTH}} units$). It remains fix until around $19,000$ electrons ($116 V_{\mathrm{CTH}} units$), and then it decreases once more. On the other hand, the efficiency increases until 7200 electrons ($46 V_{\mathrm{CTH}} units$) by decreasing the thresholds. It is notable that this signal threshold value corresponds to 5-7 times the RMS of the noise, as described in Figure 7.11. As the off-track occupancy increases sharply beyond this point, the efficiency decreases. This suggests that the high off-track occupancy at low thresholds could be related to the low efficiency due to one of the data suppression algorithms in the front-end hybrids.

According to the data sheet of the CBC the stub data taking is designed to handle a limited amount of data at each BX. Because of this, it can only process up to three Stubs for every BX. If a chip has more than three Stubs during a BX, the CBC will only select and send out the three Stubs that have the smallest address numbers. In this case, Stub Gathering Logic will indicate this by including a Stub Overflow Flag in the data packet and sends it out. In this analysis, data packets with the Stub Overflow flag were excluded. In addition, in the CIC there is a selection process based on the stub bend is used. This means that stubs with smaller bends are given priority because they are likely to come from tracks with higher momentum p_T.

7.11.3 Seed cluster multiplicity versus signal threshold

The multiplicity of the seed cluster is defined in Section 7.10.3. In the Figure 7.27 the stub multiplicity versus V_{CTH} for bias voltage of 400 V is depicted. The smooth decrease with decreasing threshold is understood to be caused by widening clusters, and the fluctuations at very low thresholds to be due to high noise occupancy. A drop in stub reconstruction efficiency has been observed for a V_{CTH} lower than 4836 electron ($30 V_{CTH}$) could be due to noise contribution which can observed in

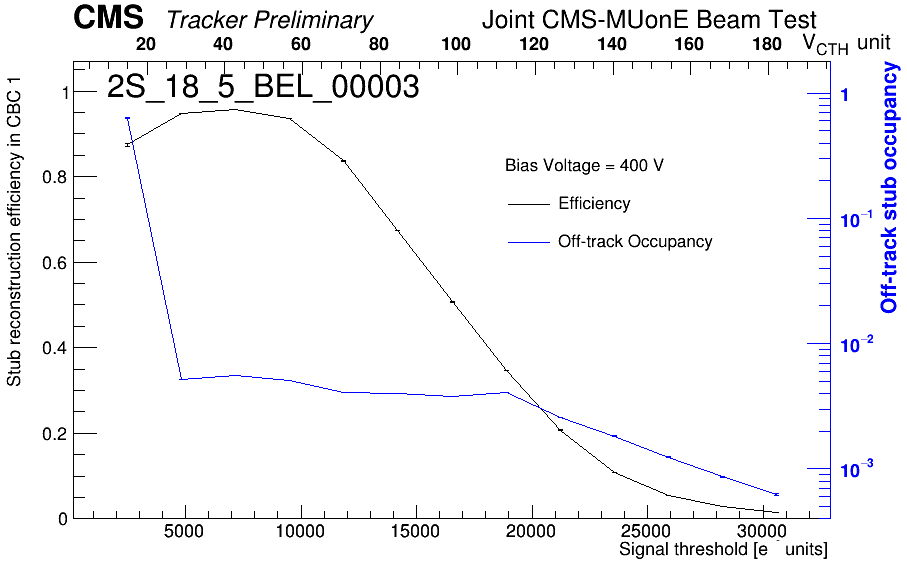

Figure 7.26: The stub reconstruction efficiency in CBC 1 (black circles) and occupancy of off-track stubs for DUT (red rectangles) is shown in logarithmic scale as a function of comparator threshold. The efficiency drops in low signal threshold to be due to high noise occupancy.

the fraction of stub with odd multiplicity.

7.11.4 Efficiency versus V_{bias} and signal threshold

In this section the Efficiency as a function of comparator threshold and bias voltages will be discussed. The efficiency of stub reconstruction for the first quarter of DUT, measured as a function of the comparator threshold with step of 2340 electrons (15 V_{CTH}) across various bias voltages, is presented in the Figure 7.28. The efficiency is increased as V_{CTH} increased and it reached to the maximum value for $550V_{\mathrm{CTH}}$ unit and it reduced again. It is recognized that the observed decrease in efficiency at exceedingly low thresholds can be attributed to data truncation phenomena, which occur when the noise occupancy surpasses acceptable levels. The plot show that for voltages less than the depletion voltage $(e.g.100V)$, an efficiency of 80% was reached for 4836 electrons (31 V_{CTH} unit). In this analysis 1 V_{CTH} considered 156 electrons.

7.11.5 Calculating collected charge

The stub reconstruction efficiency as a function of signal threshold reflects the detector's sensitivity to signal discrimination and provides insight into the distri-

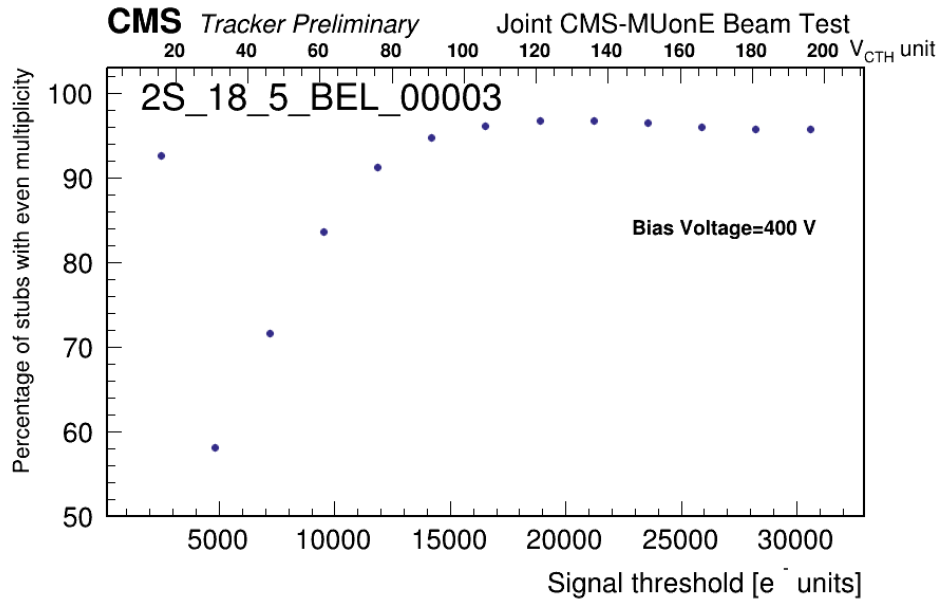

Figure 7.27: The stub multiplicity is displayed as a function of comparator threshold. It decreases by decreasing signal threshold until 4836 electrons ($30V_{CTH}$) and then a fluctuation observed at very low signal threshold which is due to noise.

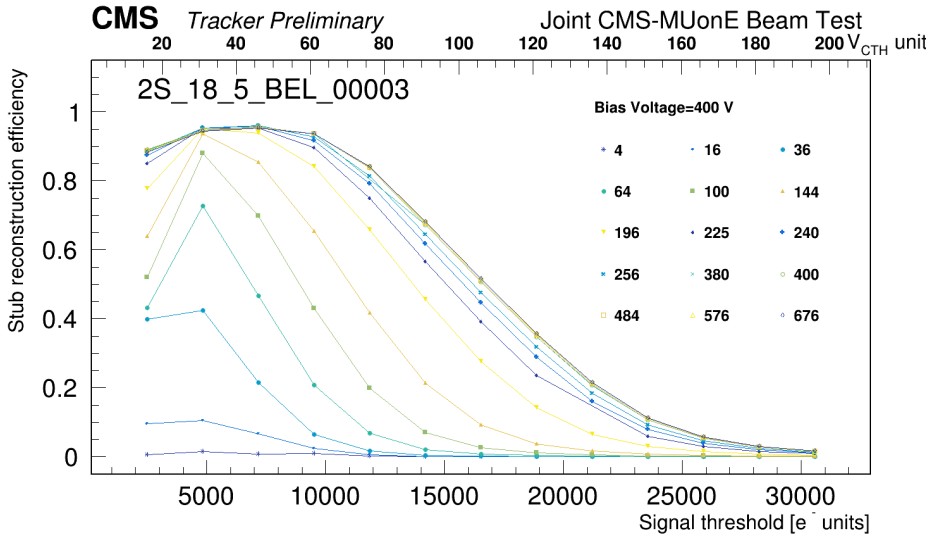

Figure 7.28: The stub reconstruction efficiency in the first quarter of the DUT as a function of comparator threshold for different bias voltages is depicted.

bution of deposited charge in the active area of silicon sensor under different bias voltages. Assuming equal efficiency for both sensors, the numerical derivative of the square root of the stub reconstruction efficiency is shown in Figure 7.29. For bias voltages higher than the full depletion voltage, the curves converge, indicating saturation in performance. In this regime, changes in bias voltage no longer significantly affect the collected charge, and the maximum of the distribution appears around 20×10^3 electrons, which is consistent with the expected value of approximately 21.8×10^3 electron-hole pairs generated by a MIP in 290 μm of silicon. As the bias voltage decreases, the peak shifts toward lower signal thresholds, indicating reduced collected charge due to incomplete depletion region.

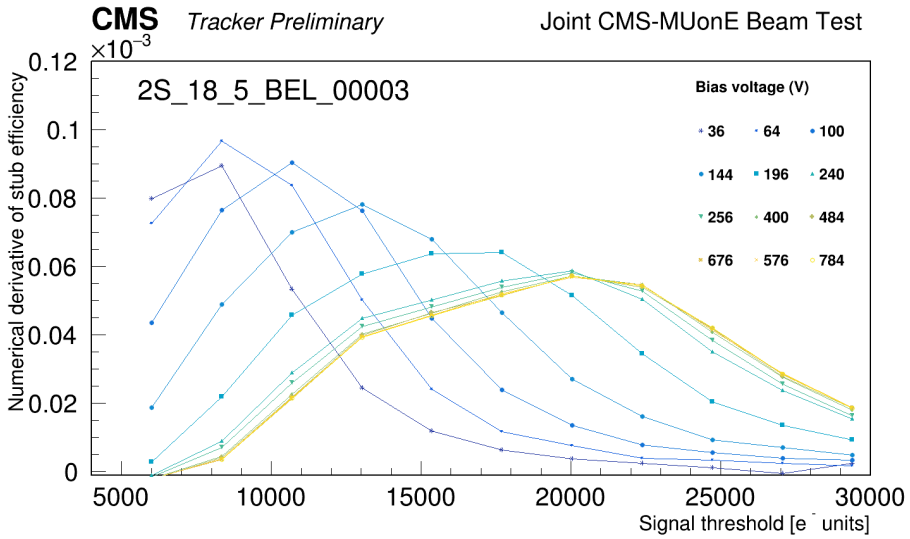

Figure 7.29: Numerical derivative of the square root of stub reconstruction efficiency as a function of signal threshold which indicate collected charge in the detector as a function of signal threshold for different bias voltages is depicted. For bias voltage higher than 240 V, it shows a maximum around 20×10^3 e^-.

7.12 Uniformity of the efficiency at nominal setting

After scanning the bias voltage and V_{CTH} and analyzing the efficiency, we selected a value where the DUT exhibits high efficiency. We will present the efficiency versus strip number to demonstrate how uniform the response is.

The stub reconstruction efficiency is defined in Section 7.10.1.

In the Figure 7.30 and 7.31 the stub reconstruction efficiency as a function of extrapolated position the DUT is shown, split by quadrant. The efficiency per read-out chip is extrapolated from a linear fit on the corresponding strips.

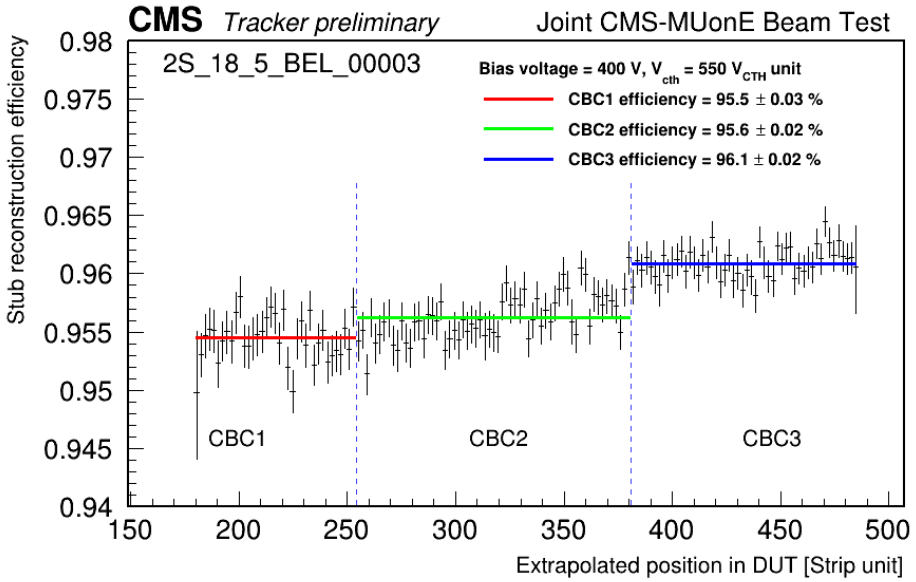

Figure 7.30: The stub reconstruction efficiency as a function of extrapolated position for the first quarter of the DUT is shown.

7.12.1 Effect of asynchronous data taking

Relatively low efficiency measured in this particular beam test could be caused by timing effects. These timing effects could be time-walk effects, noise or the dead time in the logic detection. Dr. Martin Delcourt from Vrije Universiteit Brussel did a detailed timing analysis and simulation on how timing and inefficiency are related. His research found that even small differences in the electronic parts, like a 2% change in amplifier gain, can make the VCTH thresholds vary from one CBC to another[77]. Even small changes in gain can have a measurable impact on efficiency, shifting the inefficient region in time[76].

The study also pointed out that adding a delay between the DUT and other modules can result in fluctuations in observed efficiency. Because of these delays, the inefficiency can vary from 80% to 97%. This shows how important the timing of these signals is to our ability to measure efficiency accurately.

In the electronic detector system, a DLL within the chip enables the programmable delays, specifically allowing timing adjustments in fractions of a clock

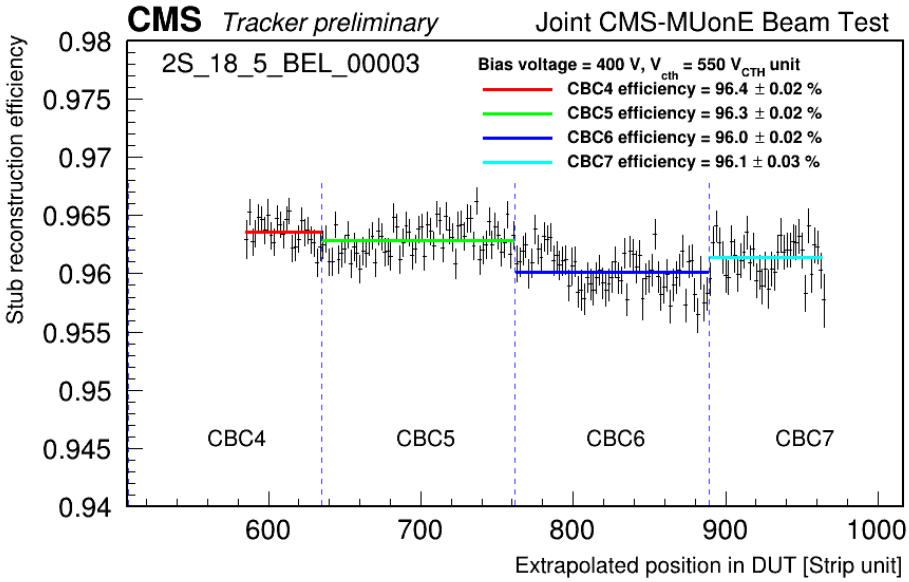

Figure 7.31: The stub reconstruction efficiency as a function of extrapolated position for the second quarter of the DUT is shown.

cycle. This feature provides flexibility to introduce delays in increments of approximately $1ns$. Another beam test was conducted a year later (2023) with 12 modules, where in a run by scanning this parameter, a timing scan was performed to investigate timing between modules.

The first module (DUT in that setup) was kept at a DLL of 12ns. By selecting events at the edge of the clock, the performance of the module was measured versus time. By assuming uniform timing profiles for all three modules, which can be represented by two error functions, and by scanning the observed data, the timing profile parameters were fine-tuned to match the measured delays. The result is shown in Figure 7.32. The black dots are the observed data, and the red plot is the simulation fitted data, and the blue plot is single module response. The results show low efficiency at the clock edge.

Furthermore, to study how the inefficiency at the clock edge might impact the measurements presented earlier, a simulation was conducted. I used the fitted parameters to model the probability of detecting a particle when it arrives near the clock edge. Then, the average value of the detection probability around the clock edge was calculated for three detectors and one DUT according to Figure 7.7. For a time range of -12.5 to $12.5\,\mathrm{ns}$, the detection probability for a single module decreases from 1% to 0.5634%, and the average detection probability of 96.3% was achieved. What is being measured is not an intrinsic property of a module but is in fact coming from the structure of the setup.

$$\epsilon_{DUT} = \frac{\int \epsilon_{DUT}(t).\epsilon_0(t).\epsilon_2(t).\epsilon_3(t)\,dt}{\int \epsilon_0(t).\epsilon_2(t).\epsilon_3(t)\,dt} \tag{7.7}$$

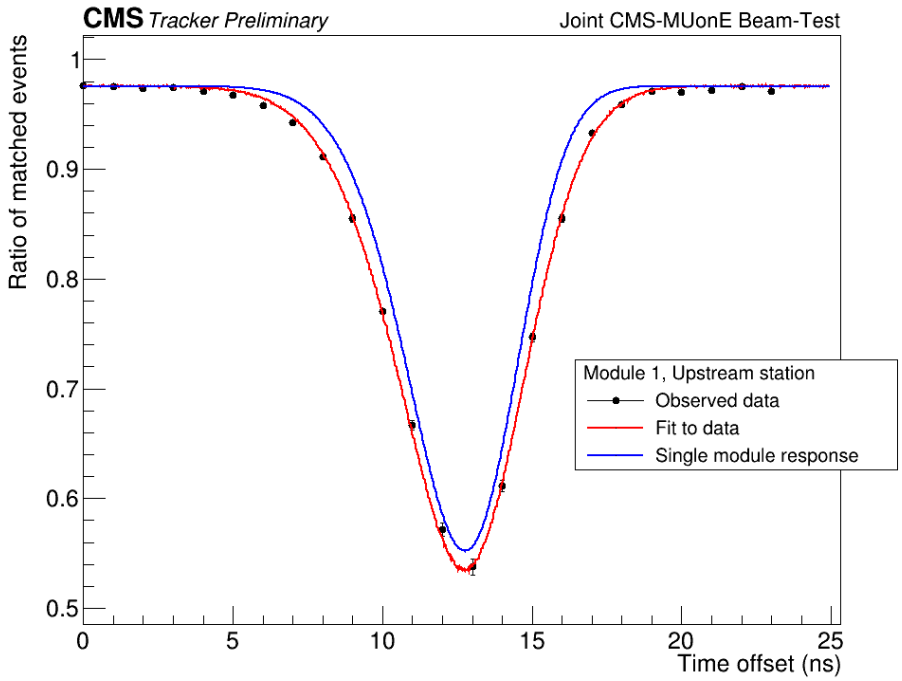

Figure 7.32: The probability of observing a stub in subsequent $25ns$ bins is determined by the delay between the device tested and the two reference modules. The data is fitted to a simulation that models the in-time detection efficiency of all modules using two error functions. The simulation is also compared to the corresponding single module detection efficiency.

7.13 Conclusion

In this chapter, we explored the performance of module 2S-18-5-BEL-00003, focusing on its efficiency and operational characteristics. Our investigation revealed that the module's efficiency ranges between 94.2% and 96.3%, a variance attributed to the read-out chip used. This efficiency is notably lower than what was recorded in previous assessments, a discrepancy stems from the asynchronous nature of the beam impacting the module's performance.

We further examined the module's operational range by methodically adjusting the bias voltage and comparator threshold. Maximum efficiency is reached at

a bias voltage higher than 400 V and a comparator threshold of 46 V_{CTH} unit (~ 7200 electron). Additionally, our findings indicate that the module's efficiency remains stable across a wide range of high bias voltages, showcasing its resilience to variations in voltage.

The study also delved into the module's off-track occupancy, an area of interest due to its potential impact on stub reconstruction efficiency. A noticeable decline in this efficiency at very low thresholds was identified, likely a result of noise contributions. These were discerned through measurements of both off-tracks occupancy and multiplicity, suggesting a correlation between increased noise and reduced efficiency. At nominal bias voltage ($\geq 400V$), comparator threshold in the range 31 to 61 V_{CTH} unit (4836 to 9516 electrons) correspond to close to maximum efficiency ($\geq 96\%$).

In terms of stub multiplicity, our analysis highlighted a trend where lower threshold values were associated with a higher fraction of stubs featuring an even seed cluster multiplicity. This observation implies that lowering the V_{CTH} values even further, to around 4831 electron (31 V_{CTH} units), could enhance the module's spatial resolution. This is in contrast to the ~ 7200 electron (46 V_{CTH} unit) signal cut-off identified as optimal for achieving maximum efficiency, suggesting a trade-off between efficiency and resolution in the module's operation.

In summary, our comprehensive evaluation of module 2S-18-5-BEL-00003 has provided valuable insights into its efficiency and operational dynamics. While it demonstrates high efficiency within a specific range, its performance is influenced by external factors such as the asynchronous nature of the beam and noise contributions. The findings underscore the importance of optimizing operational parameters to balance efficiency with other critical performance metrics, such as spatial resolution.

My contributions in this chapter are as follows:

- I actively participated in the data analysis of the 2S module during the asynchronous muon beam test.
- I developed a dedicated C++ code to read and process stub data.
- I performed coarse alignment of the module with respect to the beam and reference detectors.
- I measured the uniformity of efficiency across the sensor strips.
- I investigated module efficiency, off-track occupancy, and stub parity as a function of bias voltage and signal threshold.

Chapter 8

Digital Diagnostic Monitoring Interface

In this chapter, the Digital Diagnostic Monitoring Interface (DDMI) is discussed, along with its significance for system testing, including the back-end board, firmware, and software used to test 2S modules in the DAQ system of the outer tracker for quality assurance and validation of reliable communication. First, the architecture of the hardware, firmware and software is reviewed. Then, the results of optical power variations under different environmental conditions are presented and discussed. Finally, the reliable and safe optical power margin is analyzed by investigating the Bit Error Rate (BER).

8.1 Introduction

One of the motivations for integrating optical power monitoring is the early detection of VTRx deterioration. It has been observed that, at high temperatures ($\sim 40\ ^{\circ}C$) within the VTRx module, adhesive components release gases that contaminate the fibers, leading to a reduction in optical power [78]. Such degradation in optical connectivity compromises communication performance and may ultimately result in a complete loss of control or data transmission across the entire link. By monitoring optical power levels, deviations from nominal operating conditions can be detected, enabling the initiation of necessary maintenance routines, such as adjusting the optical transmitter bias current or replacing modules where possible.

Furthermore, optical power monitoring is essential for several other diagnostic and optimization tasks. These include scanning the transmitted optical power of the VTRx+ module across various configuration parameters—such as laser bias current and modulation—to characterize its performance. Additionally, monitoring optical power is necessary to determine the communication system's safe

margin or optical power budget by analyzing the BER as a function of optical power. This process ensures that the link operates reliably under various conditions and remains within acceptable performance limits. The DDMI [79] integrated into Small Form-factor Pluggable (SFP) [80] transceivers is a valuable tool that not only provides information about key diagnostic parameters of the optical transmission but also enables monitoring of both received and transmitted optical power. This monitoring offers insight into the health and performance of the SFP module, the connected fiber optic cable, and the VTRx+. In the next section, the architecture of the test bench DAQ system prepared at the IIHE for the present development, from front-end to back-end, will be discussed in detail.

8.2 Test bench DAQ architecture

The test bench consists of the module assembly setup (Figure 8.1), which is installed in the IIHE clean room as part of the CMS tracker upgrade construction. It is composed of two main sections: the front-end electronics and the back-end electronics. Communication between these sections is entirely optical. For this study, the front-end consists of a 2S module, while the back-end comprises a μTCA FC7 board connected to a DAQ PC via Ethernet. The 2S module is equipped with its SEH, which integrates all the necessary chips and electronic components, including the lpGBT and VTRx+, to enable high-speed optical data transmission.

8.2.1 VTRx+ transceiver

The Versatile Link Plus (VL+) project [81] aims to provide multi-gigabit-per-second optical data transmission for the readout and control of the HL-LHC experiments. On the detector side, it comprises two main components: the lpGBT chip and the VTRx+ transceiver. Both components have been designed to operate reliably under the harsh conditions encountered in HL-LHC experiments, including radiation, strong magnetic fields, and temperature variations. Figure 8.2 (left) illustrates a block diagram of the VTRx+ transceiver. This block diagram presents a schematic overview of the VTRx+, highlighting the key components: Transmit Optical Sub-Assembly (TOSA), Laser Diode Driver (LDD), Receiver Optical Sub-Assembly (ROSA) including TIA and PIN photodiode. These components are common to the SFP and will be discussed in the related section. Figure 8.2 (right) shows a prototype of a VTRx+ module with its optical fiber pigtail terminating in an MT connector [82]. The VTRx+ is designed for multi-gigabit optical transmission, supporting an asymmetric uplink and downlink data rate. In our case, a 10.24 Gbps uplink and a 2.56 Gbps downlink are used. The VTRx+ incorporates four VCSEL in an array configuration, operating at 850 ± 10 nm in multimode

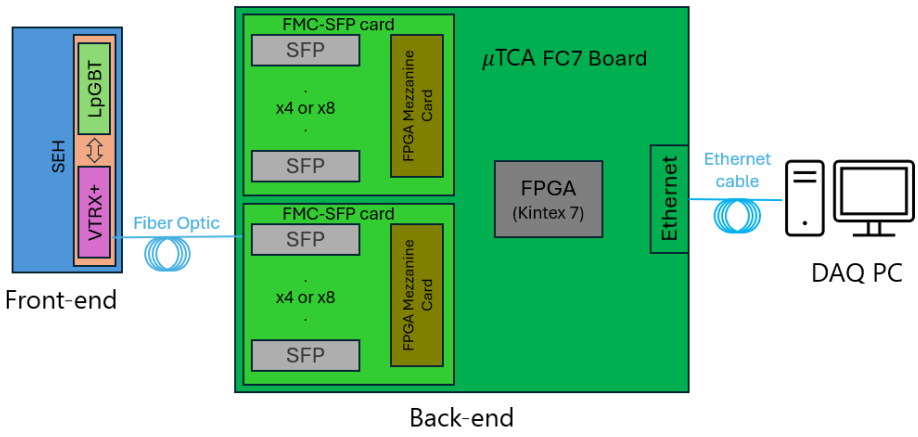

Figure 8.1: Block diagram of the DAQ system, including (left) the lpGBT and VTRx+ on the SEH at the front-end, which facilitate high-speed optical data transmission over fiber optics; (middle) a μTCA FC7 board at the back-end, equipped with SFP modules and two SFP-FMC mezzanine cards; and (right) the DAQ PC, connected to the FC7 board via Ethernet.

(MM). Additional specifications of the VTRx+ are summarized in Table 8.1. The schematic of the light coupling unit is presented in Figure 8.3. The VTRx+ fea-

Table 8.1: Summary of VTRx+ specifications[83].

Specification	Value
Radiation tolerance	1 MGy 1×10^{15} $neutrons/cm^2$
Temperature range	-35 *to* 60 $°C$
Magnetic field	4 T
Data rate, Upstream	10.24 Gbps
Data rate, Downstream	2.56 Gbps
Center wavelength	850 nm
Tx OMA*1	> -1.6 dBm (691.8 μW)
Rx Sensitivity	< -12.5 dBm (56.2μW)
Responsivity Photo diode (-25 to 60 $°C$)	> 0.45 (A/W)
Power budget, Upstream	> 7.3 dB (5.37 mW)
Power budget, Downstream	> 11.5 dB (14.1 mW)

*1 : Transmitter Optical Modulation Amplitude.

tures an I2C interface. Additionally, it can provide information about the average

optical power of the received light through its Received Signal Strength Indicator (RSSI), which provides a current output proportional to the average photocurrent flowing in the photodetector bias circuit [84].

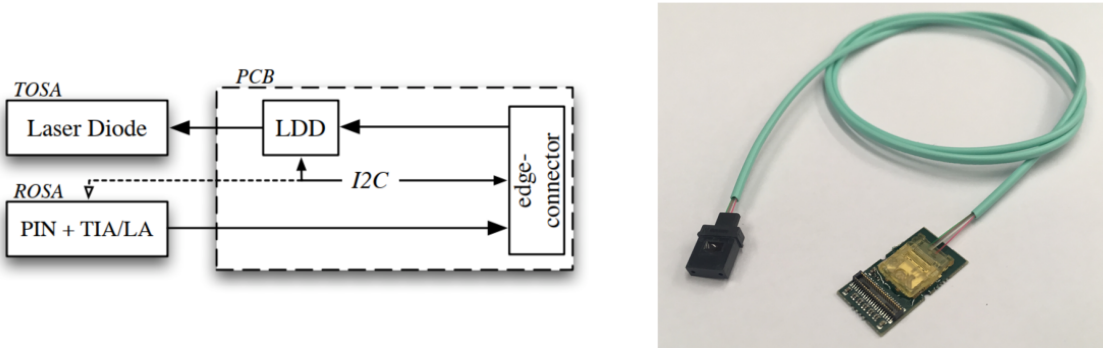

Figure 8.2: Left: Block diagram of the VTRx+ module showing the TOSA, LDD, TIA, and PIN photodiode. Right: Photo of the VTRx+ module displaying the transceiver, pigtail, and MT fiber connector.

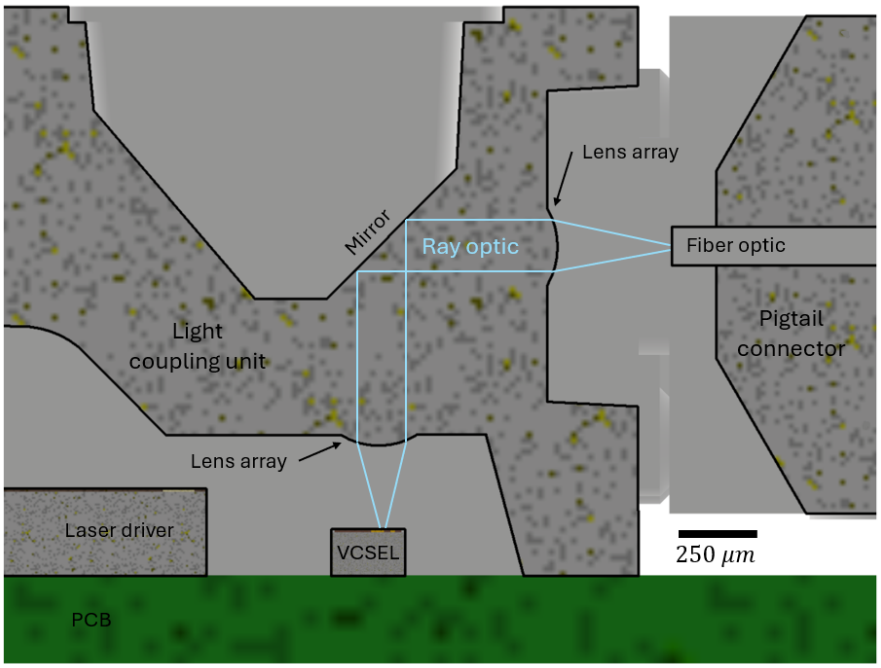

Figure 8.3: Partial 2D cross-sectional schematic of the VTRx+ module, showing selected components including the light coupling unit, VCSEL, pigtail connector, laser driver, and PCB section.

8.2.2 SFP

On the back-end side of the test bench, the optical link terminates at an SFP transceiver. Since the back-end electronics in CMS are typically shielded from radiation, a Commercial-Off-the-Shelf (COTS) component can be used. However, the selected transceiver must be compatible with the VTRx+. Therefore, a multimode SFP+ [85] with supporting the speed of 10.24 Gbps has been chosen. The specifications of the SFP+ are listed in Table 8.2. A picture of the standard SFP

Table 8.2: Key specifications of the SFP transceiver module from FS [85].

Parameter	Value
Data rate	9.95 - 10.5 Gb/s
Wave length	840 - 860 nm
Bit Rate Error	10^{-12}
Tx Optical Modulation Amplitude (OMA)	-1.5 dBm (708 μW)
Receiver Sensitivity (OMA)[a]	-11.1 dBm (78 μW)
Supply Voltage	3.14 - 3.46 V
Operating Temperature	0 - 70 $°C$

[a]Measured with BER $< 10^{-12}$ and Pseudo Random Binary Sequence (PRBS)31.

is shown in Figure 8.4 (top), while the block diagram of its main components is presented in Figure 8.4 (bottom).

SFP optical transceivers are typically divided into three main blocks:

- The Transmitter (Tx) block is responsible for converting electrical signals into optical signals. It consists of an electro-optical interface called the TOSA, which includes a laser diode. The laser diode is driven by an LDD that converts electrical digital voltage signals into current, enabling the laser diode to emit light signals.

- The Receiver (Rx) block is responsible for converting incoming optical signals into electrical signals. It consists of an opto-electrical interface known as the ROSA, which includes a photodiode and a TIA. The TIA amplifies the current signals received from the photodiode, converting them into voltage signals. Additionally, the Rx block may include a post-amplifier that further enhances these electrical signals to improve the signal-to-noise ratio, ensuring they are strong enough for digital processing.

- The control block monitors and manages the operation of the optical transceiver. It includes a microcontroller that controls various functions, such as the

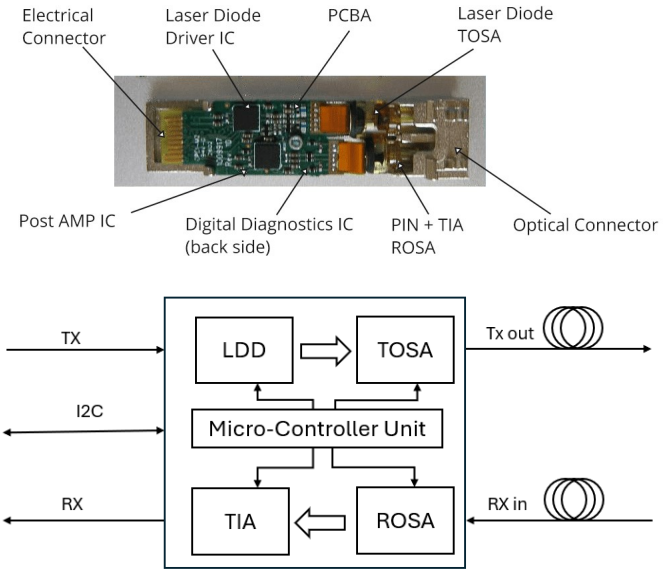

Figure 8.4: Top: Photo of the SFP module and its components [86]. Bottom: Block diagram illustrating the SFP's functionalities, including the TOSA, LDD, ROSA, TIA, and the main controller.

LDD and the TIA. An ADC digitizes various analog measurements, including module voltage, diode bias current, temperature, received optical power (RX power), and transmitted optical power (TX power). The control block also includes memory that stores relevant information such as the vendor ID, SFP specifications, monitored diagnostic data, and calibration parameters. This data can be accessed via an I2C serial bus for configuration and monitoring, which will be discussed in detail later.

For this work, a standard SFP+ module with embedded DDMI was used. This interface is defined by the SFF-8472 standard [79]. SFP modules are factory-calibrated but can also be calibrated externally. A status register indicating whether the DDMI is calibrated internally or externally. For the SFP module used in the test setup, the status register was checked and confirmed that the device had been factory-calibrated. Additionally, the calibration coefficients were verified to be 1, and the offset was confirmed to be zero. Therefore, no external calibration process was necessary and, the data was read directly from memory. Measured parameters are reported in 16-bit data fields, consisting of two concatenated bytes. These 16-bit fields provide a wide dynamic range.

The developed I2C block that I developed utilizes a single two-byte read sequence over the 2-wire interface to retrieve multi-byte fields from the diagnostic

monitoring data structure (see 8.2.5.1). This approach ensures data coherence. If this sequence is not used, a partially updated multi-byte field might be transferred to the host, leading to potential inconsistencies. The following sections provide additional details on the diagnostic parameters:

- **Internally measured transceiver temperature:** Represented as a 16-bit value in increments of 1/256 degrees Celsius, with a total range of −128 $°C$ to +128 $°C$. The accuracy of the temperature measurement varies by vendor but must be within ±3 $°C$ across the specified operating condition.
- **Internally measured transceiver supply voltage:** Represented as a 16-bit unsigned integer, where the voltage is defined as the full 16-bit value (0 – 65535) with an LSB equal to 100 μV, providing a total range of 0 V to +6.55 V. Accuracy is vendor-specific but must be better than ±3% of the manufacturer's nominal value over the specified operating temperature and voltage range.
- **Measured TX bias current:** Represented as a 16-bit unsigned integer, where the current is defined as the full 16-bit value (0 – 65535) with an LSB equal to 2 μA, resulting in a total range of 0 to 131 mA. Accuracy is vendor-specific but must be better than ±10% of the manufacturer's nominal value over the specified operating temperature and voltage.
- **Measured TX (RX) received optical power:** This value represents the average transmitted (received) optical power and is expressed as a 16-bit unsigned integer, where the power is defined as the full 16-bit value (0–65535) with an LSB equal to 0.1 μW, covering a range of 0 to 6.5535 mW (~ −40 to +8.2 dBm). Absolute accuracy depends on the exact optical wavelength. For the vendor-specified wavelength, accuracy must be better than ±3 dB over the specified temperature and voltage range [79].

Table 8.3 presents the required range and accuracy of the measurements for various parameters.

Table 8.3: Digital Diagnostic Information

Parameter	**Range**	**Accuracy**	**Unit**
Temperature	−128° to +128°	±3°	degrees Celsius
Voltage	0 V to +6.55 V	±3%	Volts
Tx Bias Current	0 to 131 mA	±10%	mA
Tx Output Power	0 to 6.5535 mW	±3 dB	mW
Rx Power	0 to 6.5535 mW	±3 dB	mW

8.2.3 FC7

The FC7 board is the successor to the CMS GLIB Advanced Mezzanine Card (AMC) card and was originally developed for applications such as the CMS Pixel Front-End Driver[87]. This evolution has made the FC7 highly versatile for the DAQ of system test for the outer tracker upgrade. In Figure 8.5, the front side (top image) and the backside of the board are shown, with the main components highlighted. The FC7 board is built around the Xilinx Kintex-7 (XC7K420T) FPGA and follows the FMC standard. It provides a flexible and reusable platform with Multi-Gigabit Transceivers (MGTs) that support data rates of up to 10 Gbps, along with a wide range of configurable I/O options. The FC7 is an AMC, designed to be fully compatible with the μTCA crate architecture. Key features of the FC7 include:

- **Xilinx Kintex-7 XC7K420T-2 FPGA:** Capable of supporting 32 data lines at rates of up to 10 Gbps, essential for high-speed data transmission.
- **AMC connector:** Provides high-speed connectivity through 12 ports, supporting various Multi-Gigabit Transceiver protocols for CMS applications.
- **FMC connector:** The FC7 utilizes FPGA Mezzanine Cards (FMCs), specifically of the Low Pin Count (LPC) type, each providing 34 differential I/O connections. Additionally, the board supports 20 high-speed serial lanes (12 to the back-end and 8 to the front-end), enabling high-bandwidth protocols such as the GigaBit Transceiver (GBT) protocol for communication with the front-end electronics.
- **4 Gb DDR3 RAM:** Supports high-speed memory transfers of up to 30 Gbps.
- **MicroSD slot:** Used for storing firmware images.
- **Microcontroller:** Implements the Module Management Controller, managing system monitoring and power control.

To simplify development, the FC7 firmware is divided into two main sections: the system core and the user logic. Basic functions, such as Gigabit Ethernet via IPBus, clock configuration, power control, MMC communication, SD card programming, and system monitoring, are managed by the system core, which is provided by the FC7 development team. The user logic section is where application-specific development takes place. The SFP DDMI functionality is implemented into this section. For communication with the back-end, data is typically transmitted over the IPBus protocol or through dedicated pins on the AMC connector.For this work, the FC7 was connected to a dedicated PCB backplane as part of the quality assurance test system. This backplane serves as an interface for data transmission using the Ethernet protocol.

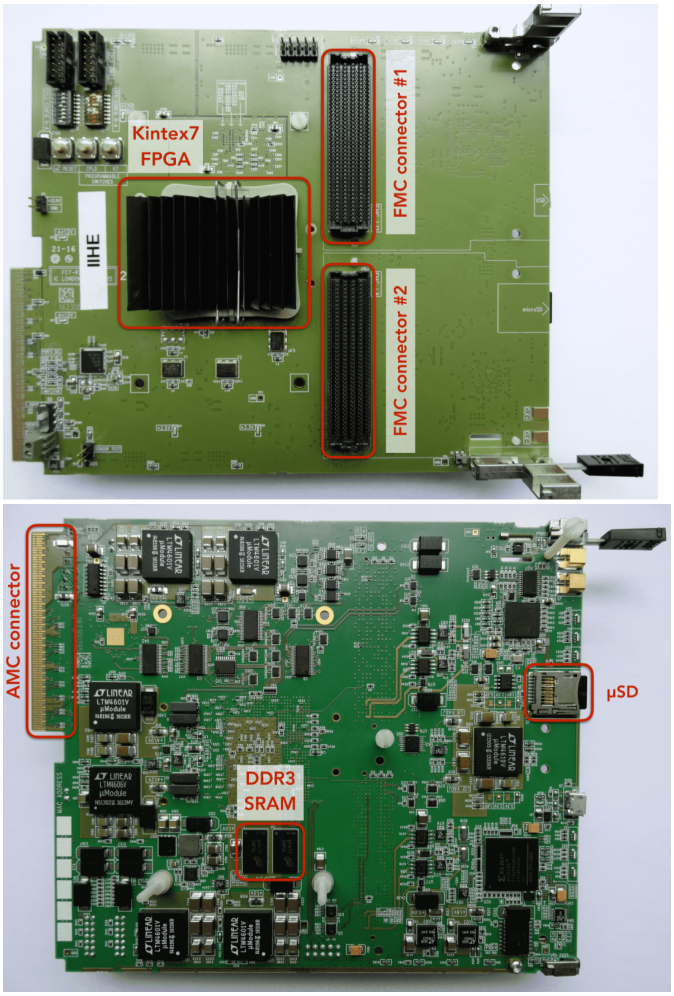

Figure 8.5: The FC7 AMC card is illustrated, with key components highlighted by red rectangles on the front (top) and back (bottom) surfaces [88].

8.2.4 FMC-SFP card

To connect the SFP modules to the FC7 board, an FPGA Mezzanine Card (FMC) is used. The FMC-SFP board is designed to provide high-speed serial I/O interfaces via a High Pin Count (HPC) connector, following the VITA 57 standard. There are two variations of these cards based on the number of supported SFP modules: the FM-S14 and FM-S18, which support up to four and eight SFP/SFP+ module interfaces, respectively. These interfaces connect directly to the Multi-Gigabit Transceivers (MGTs) of the FPGA. The FMC-SFP card supports both SFP and SFP+ modules and is capable of handling various standard voltage levels, ensuring compatibility across a wide range of Xilinx FPGA families, both legacy and modern.A block diagram and an image of the FM-S14 are shown in Figure 8.6. This design prioritizes high-speed data transfer and adaptability, making it well-suited for applications requiring reliable and high-performance serial communication within FPGA-based systems [89].

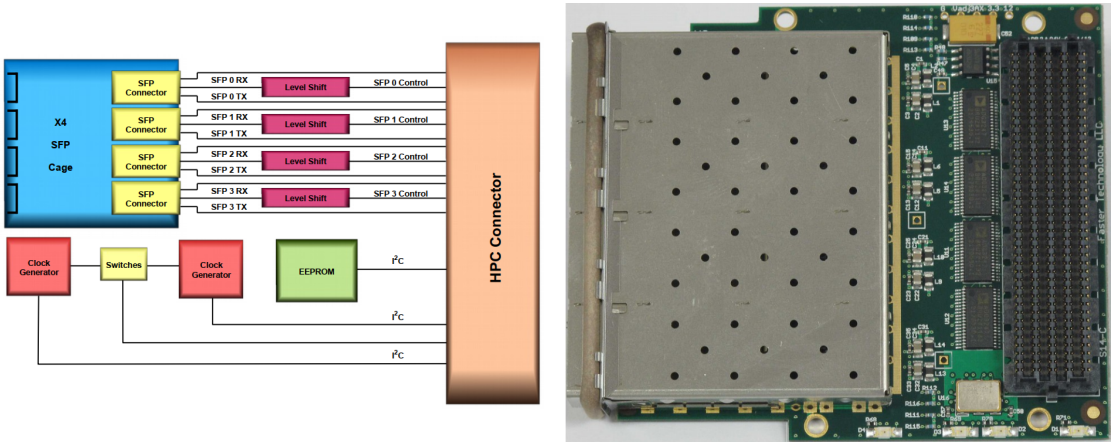

Figure 8.6: Left: Functional block diagram of the FMC-S14. Right: Photo of the FMC-S14 showing its components.

8.2.5 μDTC and IPBus

The micro Data, Trigger and Control (uDTC) project is a firmware initiative based on the FC7 general DAQ card. Its primary objective is to develop the fundamental firmware required for testing setups involving all CMS Tracker Phase II chips, hybrids, modules, and multi-modules. The uDTC firmware [90] is built on the FC7 DAQ card, which incorporates a Kintex-7 FPGA. The FC7 FPGA firmware includes system-level components that enable communication with peripheral devices on the FC7 board and support IPBus communication. IPBus serves as the

primary protocol for communication between the user and the board. This section provides a general overview of the firmware, followed by a detailed discussion of the blocks involved in DDMI.

The top-level structure of the user firmware for uDTC is illustrated in Figure 8.7. More detailed information on the top-level blocks can be found in [90]. The firmware operates at a clock speed of 40 MHz, dictated by the LHC clock, which is essential for the operation of the front-end chips. The Physical Interface Abstraction Layer (PIAL) functions as an intermediary between the FPGA and the front-end devices connected via the FMC connectors. Within this abstraction layer, incoming data is parsed into a predefined bus, which is then forwarded to the data readout block. Additionally, the PIAL receives slow control commands from the Command Processor Block.

The communication protocol between the FC7 board and the DAQ software is based on IPbus. IPbus is a high-performance, Ethernet-based control protocol specifically designed for reading from and writing to FPGA-based, memory-mapped hardware devices used in particle physics experiments[91]. The IPbus system has three main components:

- **Firmware**, which runs on the hardware (FPGA) and interprets IPbus commands.
- **ControlHub**, a software application that manages simultaneous access from multiple clients and ensures reliable communication of data packets.
- *μHAL* **(Micro Hardware Access Library)**, a C++/Python API that interfaces with devices and facilitates the development of control software.

IPBus control in uDTC closely follows the IPBus slave structure defined by the FC7 development team. The system core hosts the IPBus master, which issues commands to the slaves, each assigned a specific address space. In uDTC, three such slaves are implemented:

- **IPBus Decoder Config:** Contains all configuration settings for the uDTC firmware. This block also stores default values for configuration registers, which are applied when a reset command is issued.
- **IPBus Decoder Control:** Manages all control registers for the uDTC firmware.
- **IPBus Decoder Status:** Stores status registers for the uDTC firmware, used to monitor various blocks.

All interfaces to and from the IPBus slaves are organized into VHDL record structures, which are defined in the section corresponding to each controlled block.

A key feature of the uDTC IPBus structure is its optimized memory allocation (registers), enhancing code synthesis efficiency and improving resource utilization.

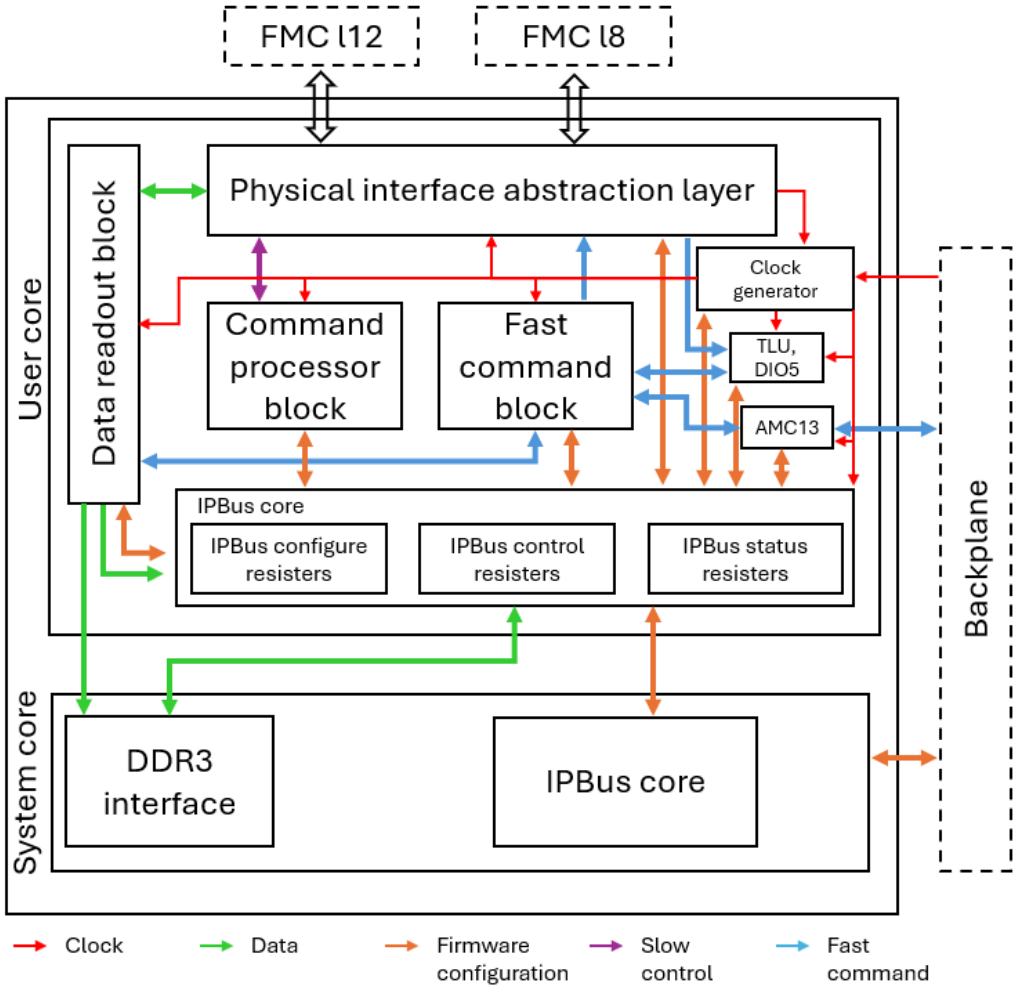

Figure 8.7: Block diagram of the top-level view of the firmware of the uDTC project. The DDMI is implemented in a separate block in the user core.

8.2.5.1 DDMI block

This section provides a detailed discussion of the DDMI block. In terms of communication, within the developed system, the FC7 and FPGA function as master devices, while the SFP module operates as a slave. The I2C protocol is used for communication [92], where the master initiates and controls data transfer, and the

SFP module responds. The block diagram of the DDMI and its communication with IPBus is shown in Figure 8.8. In this diagram, the DDMI, including the I2C interface and the bidirectional demultiplexer, is highlighted in a green rectangle. The communication between the DDMI and IPBus registers is represented in orange, while the physical tracks of the I2C lines extending from the bidirectional demultiplexer to the SFP module's memory are shown in black.

The developed I2C block reads diagnostic data directly by addressing specific memory locations. This process requires first writing the memory pointer address. After each write operation, an acknowledgment from the slave is checked. If the SFP module fails to send the first acknowledgment, which typically indicates the absence of the module, the I2C block returns error code 1. If the second acknowledgment fails, which may indicate a data transfer issue, the I2C block detects, processes, and reports the corresponding error. To ensure data coherence, the I2C block sends an acknowledgment after reading the first byte, which moves the pointer to the next byte, allowing sequential byte-by-byte data retrieval. This approach helps maintain the integrity and accuracy of the transferred data. A counter is implemented within the I2C block to generate a 20 kHz clock from the main system frequency of 40 MHz. This slower clock is essential for controlling the timing of data transmission on the I2C bus. A secondary signal, with a 90-degree phase shift, is also generated to prepare the data value before sending each bit during the write process and to read the data after the clock signal during the read process. This ensures proper synchronization between the clock and data signals.

A bidirectional demultiplexer block was developed and integrated with the I2C block to connect each plugin on the FMC-SFP board to the I2C signals. The bidirectional demultiplexer supports 4 to 8 SFP channels, enabling the selection of a specific SFP module for I2C communication based on the channel selection signal input. When the appropriate channel is selected, the corresponding Serial Data (SDA) and Serial Clock (SCL) lines are driven, ensuring communication with only the selected SFP module. Additionally, the firmware includes provisions for synthesis and bitstream generation based on the hardware configuration (optical-quad SFP or optical-octa SFP). Both FM-S14 and FM-S18 channels were tested and verified individually using an SFP module and a fiber optic loopback.

Additionally, a chronograph of the I2C communication trace captured with a Picoscope 2206 [93] is displayed in Figure 8.9. This illustrates the process of data transmission between the FC7 and the SFP module. The blue waveform represents the data signal, while the red waveform corresponds to the clock signal, operating at a frequency of 20 kHz. The decoded I2C protocol data, including the start signal, addresses, acknowledgment signals, exchanged data bytes, and stop signal during communication, is shown beneath the waveforms. The x-axis represents time and

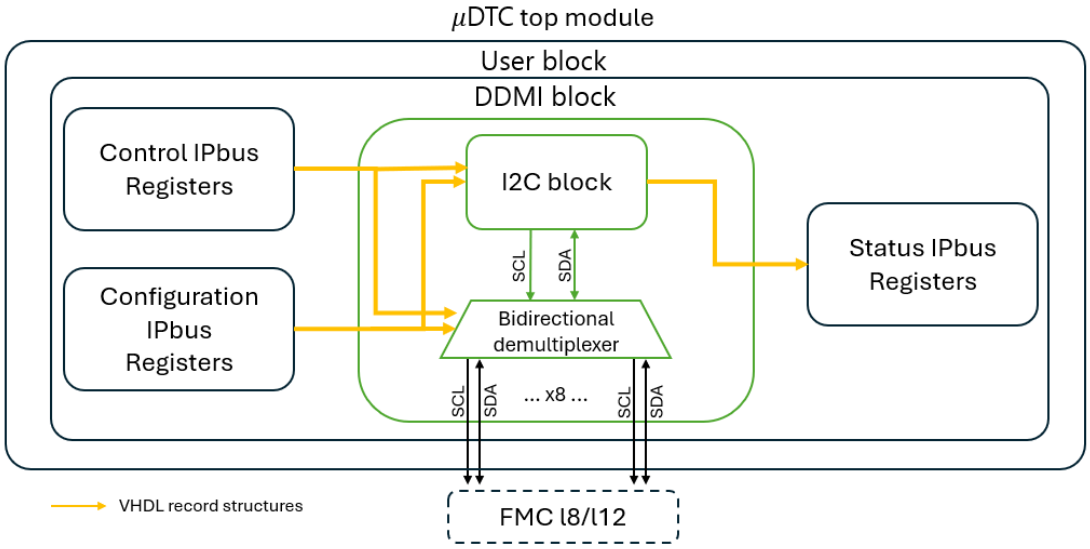

Figure 8.8: Architecture of the DDMI implementation and its data path with other IPBus blocks in uDTC.

displays the total communication duration, which is approximately 2.347 ms, while the y-axis represents voltage. In this instance, data is read from addresses 100 and 101 of a single-mode SFP module, which correspond to the measured RX optical power. The value read by Ph_2ACF is a reasonable value of 355.1 μW, confirming reliable data retrieval from the back-end to the DAQ software.

8.2.6 Ph2_ACF

The Phase-2 Acquisition and Control Framework (ph2acf) framework is designed to facilitate efficient control and communication between hardware and firmware components in the CMS Tracker Phase II system. The C++ middleware Application Programming Interface (API) simplifies firmware interaction by abstracting complex calls and handshaking into accessible functions. Additionally, ph2acf includes a C++ object-based library that models system components, such as CBCs, hybrids, and boards, along with their associated properties, including status and values. The framework also implements functions to send and receive IPBus commands, which are essential for communication with the firmware blocks. I developed, implemented and tested functions in ph2acf to send control commands and read data through IPBus for communication with the DDMI block in the firmware. This integration ensures reliable data acquisition and control within Phase II testing and operation.

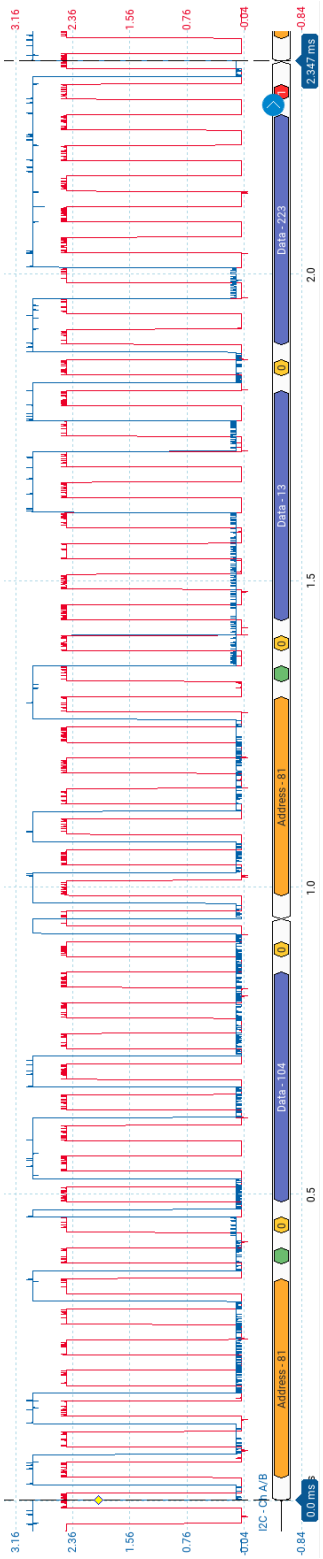

Figure 8.9: I2C communication trace captured by a Picoscope 2206, illustrating the interaction between an I2C master and an SFP module during the reading of transmitted optical power. The red waveform represents the clock signal at a frequency of 20 kHz, while the blue waveform corresponds to the data signal. The decoded I2C data includes the start signal, addresses, acknowledgment signals, exchanged data bytes, Not Acknowledge (NACK), and stop signal during communication. The final measured received optical power, as reported by the software, is 355.1 μW. The x-axis represents time (spanning approximately 2.347 ms), while the y-axis represents voltage levels.

8.3 Optical power measurement validation

Testing and validation of the transmitted (Tx) and received (Rx) optical power, as read by the DDMI block, were performed in three steps, each progressively more realistic. These steps included:

- An SFP-to-SFP loopback.
- An SFP-to-SFP connection with a power meter using a fiber optic splitter.
- A 2S module equipped with a VTRx+ and an SFP.

The following sections provide a detailed explanation of these setups and the corresponding results.

- **SFP-SFP Loopback:** In this setup, a 5 m fiber-optic cable (see Table 8.4) was used to create a loop between the TOSA and ROSA of an SFP module (see Table 8.2). The transmitted and received optical power were measured every minute over a period of approximately 7 hours. The experimental setup was placed in a cleanroom with the temperature controlled at $21 \pm 1°C$. The results are shown in Figure 8.10. The top plot represents the transmitted optical power, with an average measured value of 711.19 μW (−1.48 dBm), which aligns well with the SFP datasheet specification of 707.9 μW (−1.5 dBm). It was also observed that the transmitted power fluctuated by approximately ±11.1 μW (+0.1 dBm, −0.05 dBm) around the mean value. This fluctuation could be attributed to the power control loop dynamics of the laser driver. Such variations are generally negligible in most fiber-optic link budgets, which often accommodate total tolerances of ±1 dB or more. The average received optical power, shown in the bottom plot of Figure 8.10, was measured to be 557.32 μW (~ −2.54 dBm). This value is lower than the transmitted optical power by 153.87 μW (1.06 dBm), a difference that could be attributed to misaligned or poorly seated connectors as well as connector losses. Additionally, the transmitted optical power was measured using an external power meter, which recorded a value of approximately 540 μW (-2.6 dBm). The specifications of this power meter are listed in Table 8.5.

  The initial drop observed in the receiver plot may be due to the relaxation of the connector over time. To check this hypothesis, an experiment was conducted to assess the variation in received optical power due to connection mismatches. The TX and RX cables were disconnected and reconnected to the SFP 100 times. After each reconnection, the transmitted and received optical power were measured 100 times, and the average values were recorded.

Table 8.4: Specifications of the fiber optic cable used in the loopback tests [94].

Specification	**Value**
Manufacturer	FS
Fiber Mode	OM3
Insertion Loss	$\leq 0.3\ dB$
Connector Types	Lucent Connector (LC)-LC
Polish Type	Ultra Physical Contact (UPC)-UPC
Connector Ferrule	Zirconia Ceramic
Fiber Count	Duplex
Cable Jacket	PVC
Attenuation at 850 nm	$3.0\ dB/km$

Table 8.5: Specifications of the FOPM-201 Optical Power Meter [85].

Specification	**FOPM-201**
Measurement Range	-70 to 10 dBm
Calibrated Wavelengths	850/1300/1310/1490/1550/1625 nm
Resolution	0.01 dB
Accuracy	SM: ±0.2 dB, MM: ±0.6 dB
Linearity	±2%
Detector Type	InGaAs
Response Range	700-1700 nm
Optical Connector	2.5mm FC/SC/ST
Cable Type	SMF & MMF

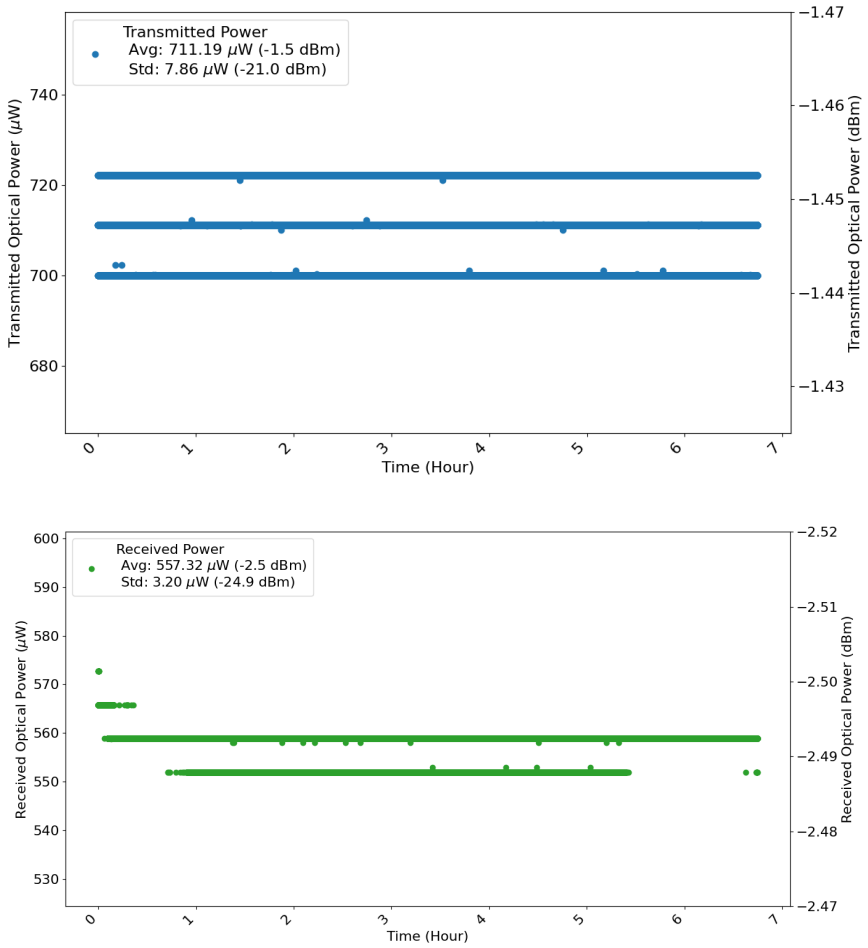

Figure 8.10: Transmitted (top, blue) and received (bottom, green) optical power via fiber optic loopback as a function of time.

Figure 8.11 presents the average transmitted and received optical power after each reconnection.

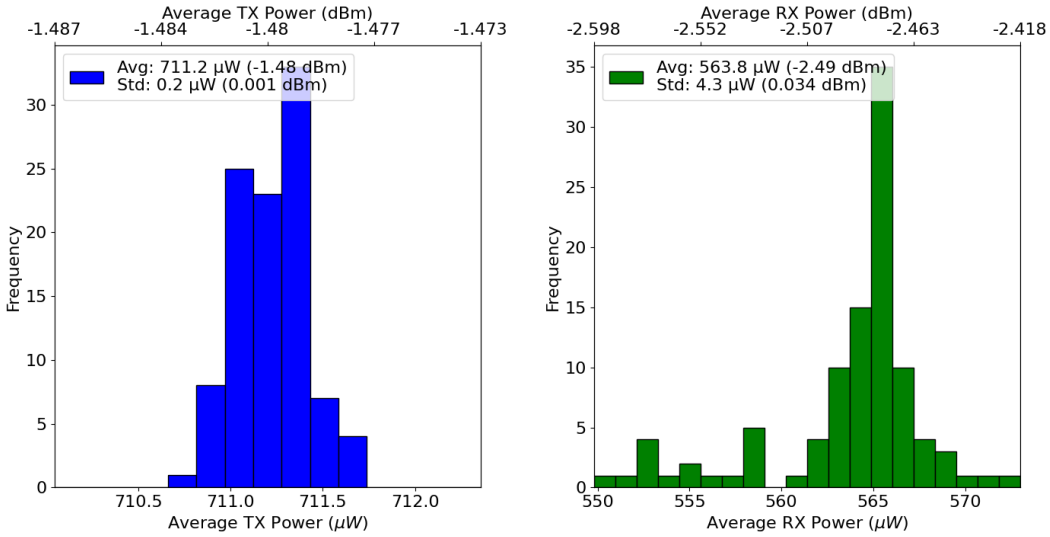

Figure 8.11: Histograms showing the distribution of average transmitting optical power (left) and receiving optical power (right) after 100 fiber optic reconnections in the SFP loopback test (see text). The legends display the calculated average and standard deviation of the optical power values. The TX Power is around 0.711 mW (-1.48 dBm), as expected according to the datasheet of the SFP. The RX Power shows variability with a total range around $23\mu W$ (0.18 dBm) and statistical standard deviation of 4.3 μW (0.034 dBm), indicating that reconnection quality affects the received optical power.

The plot shows that the transmitted optical power (TX Power) is approximately 711 μW (-1.48 dBm), as expected. However, the average received optical power (RX Power) is around 563.8 μW (-2.49 dBm) and varies with a total range of about 23 μW (0.18 dBm) and statistical standard deviation of 4.3 μW (0.034 dBm), indicating that connection quality affects the received optical power. Even after accounting for mechanical mismatches, the loss between the transmitted and measured received optical power exceeds the insertion loss of each end of the LC connector (0.3 dB). This suggests that additional real-world factors, such as dust, misalignment, reflection, and measurement tolerances, contribute to the observed loss, often pushing it closer to 1 dB. Thus, a total difference of approximately 1 dB between the transmitted power of -1.5 dBm and the received power of -2.48 dBm is

reasonable for a fiber optic connection with two LC/UPC connectors. This does not indicate a faulty connector or fiber optic cable.

- **SFP-SFP and Power Meter:** To simultaneously read and validate the data, a 50/50 fiber optic splitter was used. The fiber splitter is a passive optical device designed to distribute optical power by splitting a single optical signal into multiple outputs. Additional specifications are listed in Table 8.6. Since the splitter fibers are single-mode, a 1310 nm single-mode SFP was used for this verification. The key specifications of the SFP are provided in Table 8.7. As the input and output ports of the fiber optic splitter are of the Square Connector (SC) type, two SC-to-LC converters were used to interface with the SFP. The block diagram of the setup, along with measured values at different points using both a power meter and the SFP receiver via ph2acf, is shown in Figure 8.12. No significant deviation was observed between the data obtained from the two methods (power meter and the developed optical power monitoring block), indicating that they provide consistent results and validate each other. The slight deviation observed could be attributed to connection mismatches or losses.

Table 8.6: Key specifications of the fiber splitter [95].

Specification	**Value**
Operating Wavelength	$1260 - 1650\ nm$
Configuration Type	1×2
Split Ratio	Symmetrical
Fiber Mode	Single mode
Insertion Loss	$\leq 4.1\ dB$
Wavelength Dependent Loss	$\leq 0.3\ dBm$

- **SFP-VTRx+:** Following validation using the power meter, a 2S module (2S_18_6_BEL-01002) equipped with a VTRx+ (VTRx+_030.0cm_16611010854) was connected to the SFP. The 2S module was placed inside the burn-in system, where the temperature was maintained at 26 ± 0.05°C for 108 hours. A block diagram of the burn-in setup is shown in Figure 8.13. The received optical power over time is presented in Figure 8.14. The average received optical power was measured as $1305.2 \pm 7.6\,\mu W$ (1.16 ± 0.03 dBm). In this setup, although the temperature was kept constant, a slight increase in received optical power was observed. However, the low standard deviation indicates a high level of consistency in the data. To compare this result to the expected VTRx+ transmitted optical power, a histogram of the typical transmitted optical power by VTRx+ for different batches as a function of

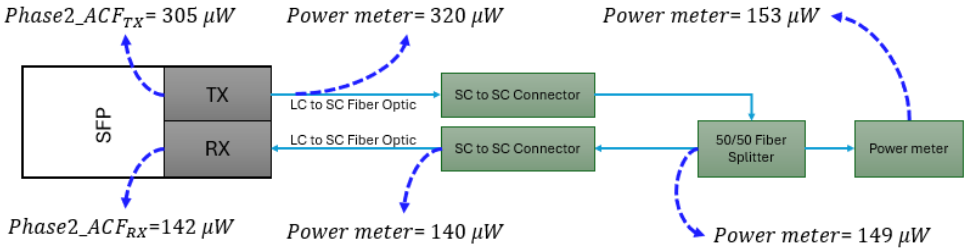

Figure 8.12: Block diagram of the optical power measurement setup using a fiber optic splitter. The setup illustrates the SFP transceiver (TX/RX) connected to a 50/50 fiber splitter via SC-to-SC converters. One output of the splitter is connected to the power meter, while the other is connected to the receiver of the SFP module. Power measurements were taken at various points in the system, with values indicated in the diagram. The measurements obtained using the developed feature in ph2acf closely align with the optical power values recorded by the power meter, demonstrating consistency and minimal deviation in the measured optical power levels.

Table 8.7: Specifications of the SFP-10GSR-85 and SFP-1G-LX-31 transceiver modules from FS.

Parameter	**850 nm MMF**	**1320 nm MMF**
Manufacture	FS	FS
Part Number	SFP-10GSR-85	SFP-1G-LX-31
Max Data Rate	10.3125 Gbps	1.25 Gbps
Wavelength	850 nm	1310 nm
Bit Rate Error	10^{-12}	–
TX Power	-7.3 to -1 dBm	-9.5 to -3 dBm
Receiver Sensitivity	$< -11.1\ dBm$	$< -20\ dBm$
Receiver Overload	$-1\ dBm$	$-3\ dBm$
Temperature Range	0 to 70 $°C$	$-40\ +85°C$
Core Size	50/125 μm	9/125 μm

OMA is presented in Figure 8.15. Most VTRx+ transceivers exhibit a transmitted optical power ranging from 1.0 mW (0 dBm) to 1.3 mW (1.14 dBm), while the acceptance threshold is approximately 0.7 mW (-1.55 dBm). The average received optical power from the VTRx+ in the burn-in setup therefore aligns with the typical transmitted optical power distribution of VTRx+ transceivers.

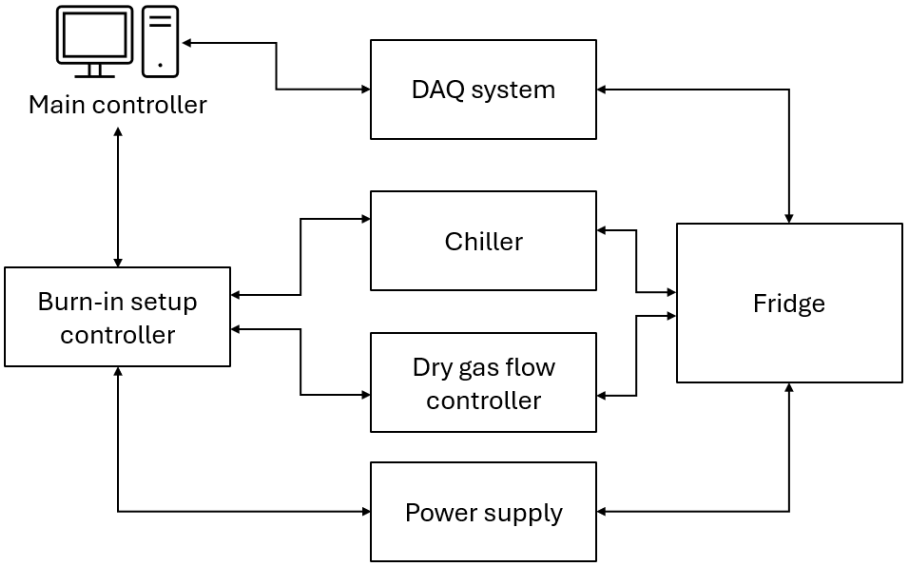

Figure 8.13: Block diagram of the burn-in setup.

8.4 VTRx+ transmitted optical power vs. temperature

Since the 2S modules will operate at low temperatures, a study was conducted to evaluate the relationship between VTRx+ transmitted (Tx) optical power and temperature. A series of 2S modules were subjected to thermal cycling based on their availability. In the burn-in setup, a temperature sensor was mounted on the frame of the 2S module carrier, near the right FEH, as shown in Figure 8.16. The temperature and transmitted optical power were recorded each 152.55 s. In the first experiment, a 2S module (2S_18_6_BEL-00104) equipped with a VTRx+ (VTRx+_12.0cm_16611002541) was subjected to thermal cycling from 30°C to -30°C over five cycles. The duration of each cycle was as follows: one cycle of 32 hours, two cycles of 11 hours each, and two cycles of 22 hours each. The results

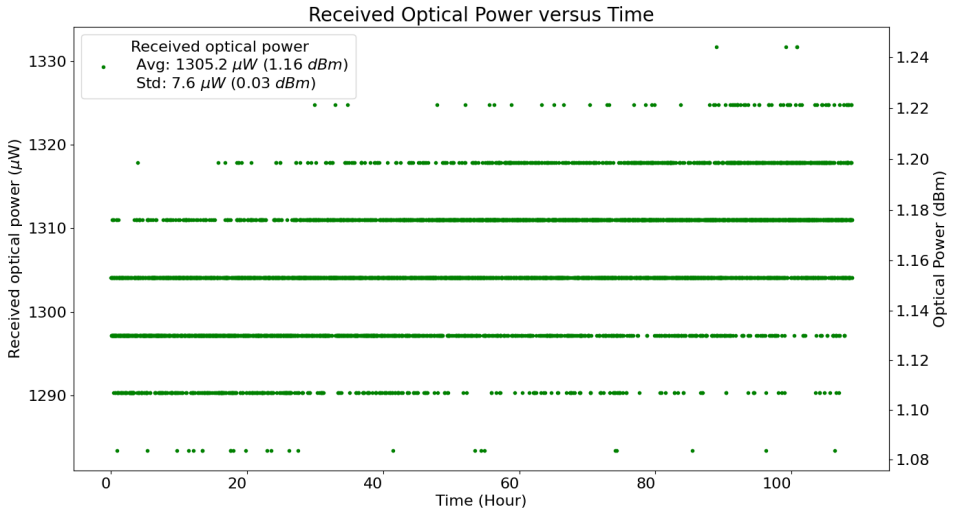

Figure 8.14: Received optical power from VTRx+ (VTRx+_030.0cm_16611010854) as a function of time at a fixed temperature of $26 \pm 0.05°C$ over a duration of 108 hours.

from the different cycles are presented in Figure 8.17. The top plot shows the received optical power versus temperature measured on the module carrier plate during the temperature increase (ramp-up), while the bottom plot represents the same data during the temperature decrease (ramp-down). High repeatability in the received optical power was observed across different cycles, indicating that the thermal ramp was slow enough for all components to reach thermal equilibrium. In the plotted graph, two distinct oscillatory behaviors are evident. The first is a low-frequency fluctuation that spans a larger range of data points, creating a broad wave-like pattern. Superimposed on this trend is a higher-frequency oscillation, with a temperature-dependent period of approximately 3.7-4.6°C and smaller amplitude variations (around 70 μW between each local minimum and maximum), introducing finer fluctuations throughout the dataset. This combination suggests an underlying periodic behavior at two different scales. Additionally, a hysteresis effect was observed in the received optical power, with a difference between the ramp-up and ramp-down plots.

In the second experiment, the RSSI and the 2S module temperature sensor, in addition to the optical power, were recorded for four modules. An offset of approximately 5°C was observed between the carrier plate temperature sensor and the 2S module temperature sensor on the pigtail. Figure 8.18 presents the received optical power at the back-end (transmitted by VTRx+) for different modules (see

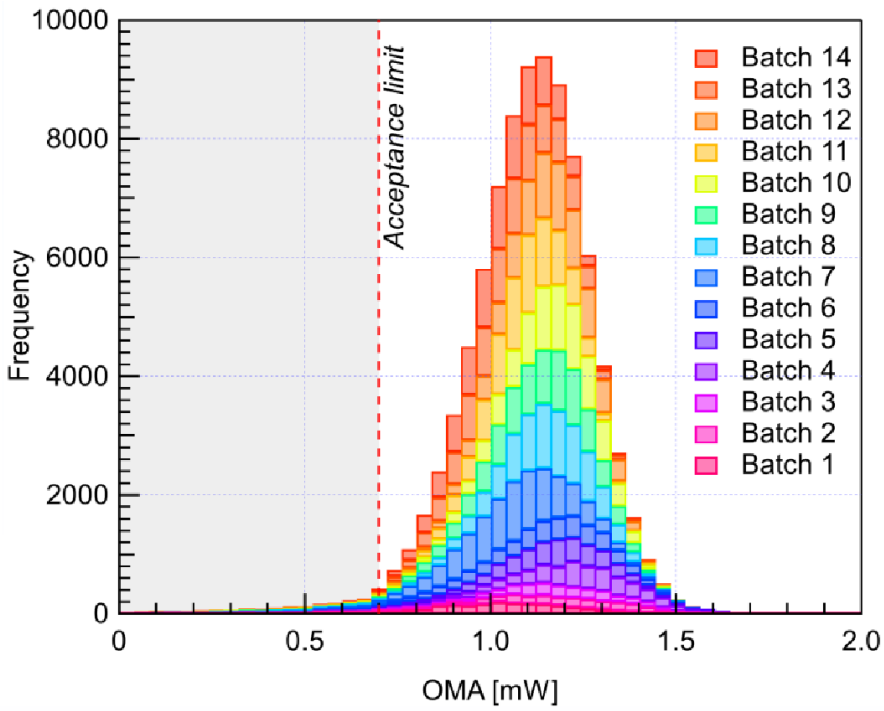

Figure 8.15: Histogram of the transmitted (Tx) optical power of VTRx+ as a function of OMA. Most modules exhibit a Tx optical power between 1.0 mW (0 dBm) and 1.3 mW (1.14 dBm), while the acceptance limit is approximately 0.7 mW (-1.55 dBm) [96].

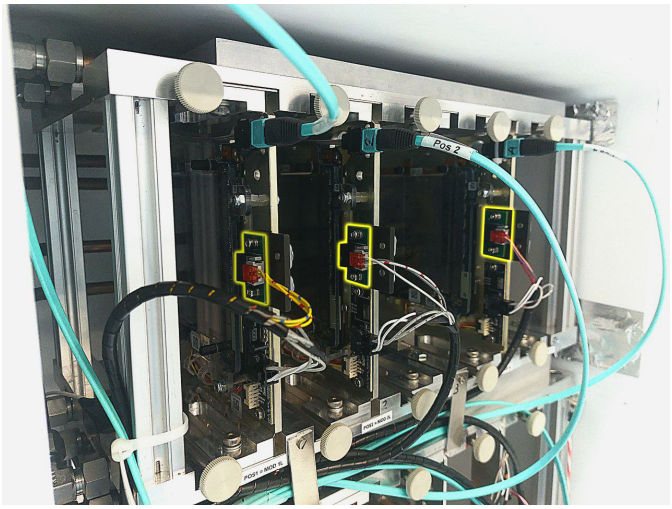

Figure 8.16: Image of the modules on the carrier frame inside the burn-in system. The temperature sensors are highlighted in yellow. The VTRx+ modules are located at the bottom left of the modules in these images.

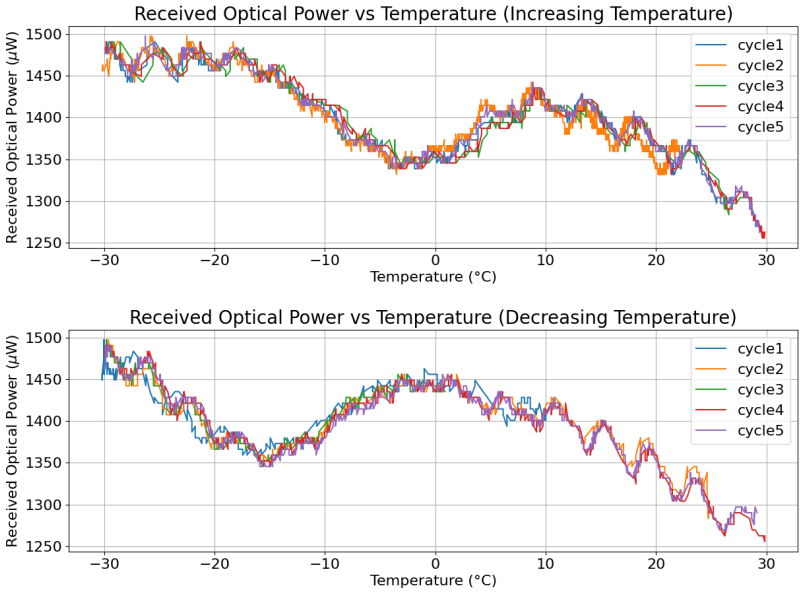

Figure 8.17: Received optical power as a function of temperature over five cycles during increasing (top) and decreasing (bottom) temperature ramps, ranging from $-30°C$ to $30°C$, (2S module 2S_18_6_BEL-00104 equipped with VTRx+ VTRx+_12.0cm_16611002541). The overall trend indicates a reduction in optical power as the temperature increases. Variations between cycles are observed, particularly in the mid-temperature range ($-10°C$ to $20°C$), which may be attributed to mechanical expansion and contraction or the thermal sensitivity of optical components. The system exhibits good consistency across cycles, indicating stable behavior under repeated temperature changes, though minor deviations suggest possible temperature-dependent effects such as thermal hysteresis.

Table 8.8: Part numbers and serial numbers of the modules and VTRx+ units in the burn-in setup.

Module	Part name	VTRx+ serial number
Module 1	2S_18_6_BEL_10001	VTRx+_12.0cm_16611011513
Module 2	2S_18_6_BEL_10002	VTRx+_12.0cm_16611014921
Module 3[a]	2S_18_6_BEL_01002	VTRx+_030.0cm_16611010854
Module 4	2S_40_6_BEL_10002	VTRx+_12.0cm_16611015040

[a]Kick off module.

Table 8.8) as a function of the 2S module temperature sensor during a thermal cycle from 20°C to -30°C. In general, the received optical power plot exhibits an overall upward-sloping envelope, indicating a positive correlation between temperature and received power within this range. This behavior contradicts the expected trend [97] and the general pattern observed in Figure 8.17. Temperature changes can cause thermal expansion, potentially shifting the lens on the light coupling unit relative to the VCSEL of the VTRx+ and altering the received optical power [96][98]. Periodic wave-like ripples or oscillations similar to those in Figure 8.17 are also observed in the received optical power. The amplitude of these oscillations varies with temperature and differs between modules.

Figure 8.19 displays the RSSI signal at the front-end (transmitted by the SFP) for different modules. Except for module 3 (red plot), the RSSI plots exhibit an upward trend, indicating a positive correlation between RSSI and temperature. No high-frequency fluctuations were observed in the RSSI plots. Additionally, for module 1 and module 4 (blue and black plots, respectively), the same low-frequency fluctuations observed in the received optical power plot (Figure 8.18) are present in the RSSI plots. Furthermore, hysteresis was observed in the plots between the temperature ramp-up and ramp-down phases, which was more pronounced in plots exhibiting low-frequency fluctuations with larger amplitudes. However, the underlying origin of this behavior is not yet fully understood.

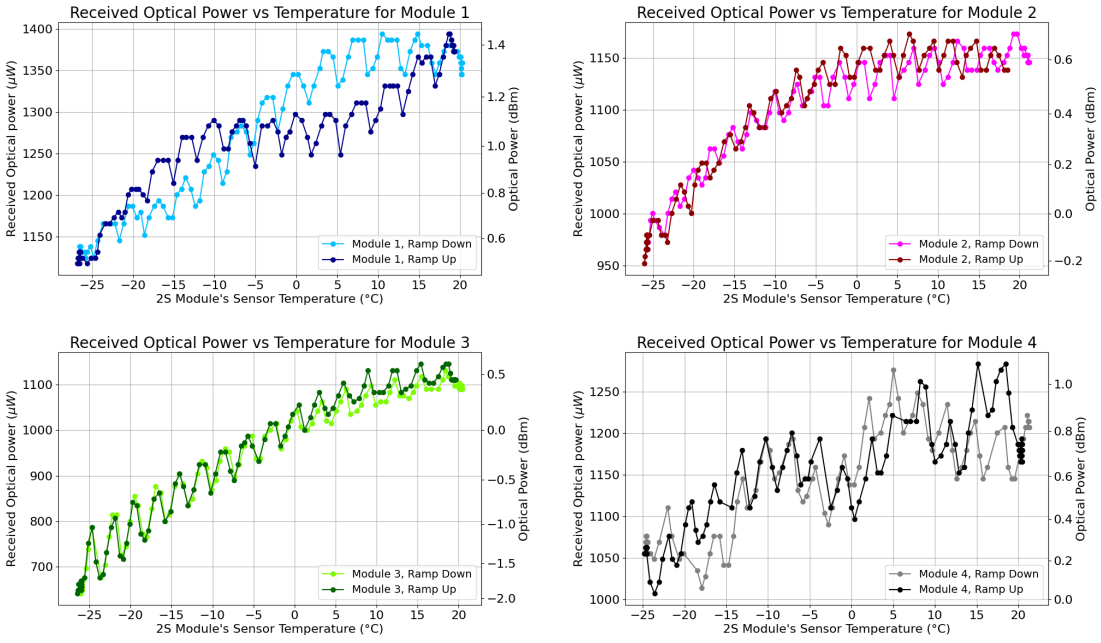

Figure 8.18: Received optical power measured with the DDMI block for different modules as a function of temperature.

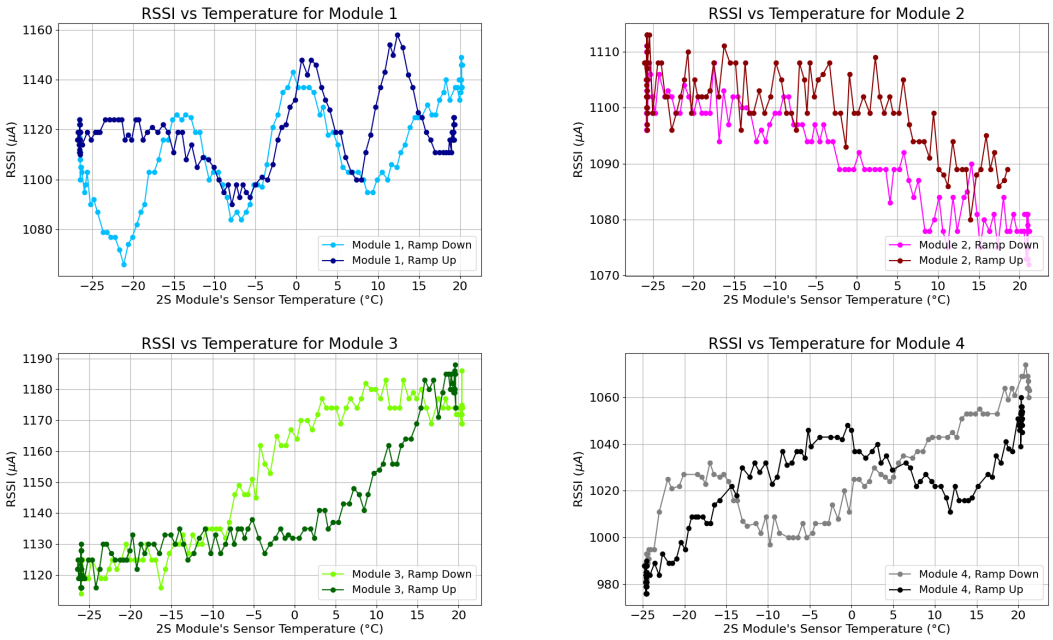

Figure 8.19: RSSI for different modules as a function of temperature.

The plots show periodic fluctuations in the received optical power as the temperature changes. To analyze these variations in greater detail, a polynomial (degree of 3) was first fitted to the data to remove the baseline and overall trend, and the residual values were extracted. A Hamming window was then applied to the residuals, followed by a Fast Fourier Transform (FFT) to identify the dominant frequency components in the signal. The results of the FFT analysis are shown in Figure 8.20. All four module plots exhibit a significant peak around 0.35 $1/°C$, suggesting that temperature variations induce optical power fluctuations with a period of approximately $2.8°C$. A second observed peak appears at approximately twice the fundamental frequency, indicating that it is likely a harmonic. The observed peaks lower than the main peak (i.e., below approximately 0.25 $1/°C$) may be attributed to changes in the speckle pattern generated within the multimode optical fiber. These variations can result from microbending effects induced by mechanical stress when the fiber optic is subjected to temperature changes[99]. The main frequency peaks for different modules are listed in Table 8.9 for both the ramp-up and ramp-down phases.

This specific periodic variation in intensity as a function of temperature, observed in the received optical power, may be attributed to a shift in the fringes of the interference pattern formed within the light coupling unit of the VTRx+. This shift suggests a thermally induced change in the Optical Path Length (OPL),

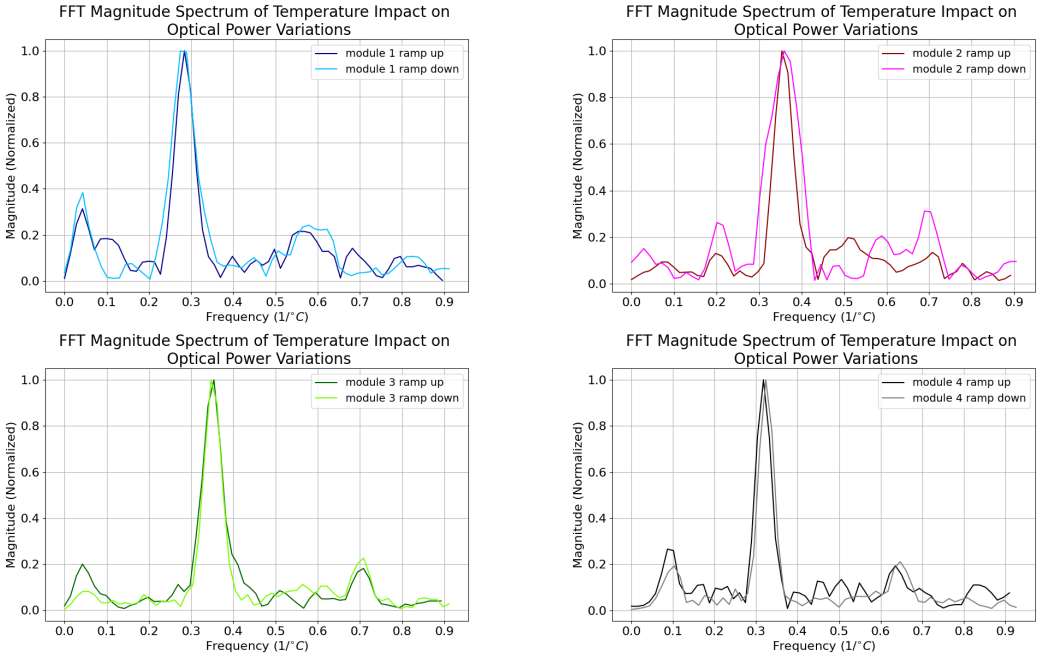

Figure 8.20: FFT analysis of received optical power fluctuations as a function of temperature. The spectrum reveals periodic components in the signal, suggesting underlying thermal effects influencing optical transmission.

Table 8.9: Significant peak values observed in the FFT of received optical power as a function of temperature, along with the corresponding temperatures for different modules during the thermal cycle.

Module	Significant peak ramp down $[1/°C]$ $(°C)$	Significant peak ramp up $[1/°C]$ $(°C)$
Module 1	0.284 (3.517)	0.289 (3.455)
Module 2	0.354 (2.826)	0.359 (2.786)
Module 3	0.354 (2.824)	0.347 (2.88)
Module 4	0.318 (3.147)	0.323 (3.092)

which can be analyzed using the interference Equation (8.1):

$$m\ \lambda = 2\ n\ \Delta d \tag{8.1}$$

where m is the number of fringe shifts, λ is the laser wavelength, n is the refractive index of the light coupling unit, and Δd represents the change in OPL within the light coupling unit induced by temperature variations. By applying the interference formula and measuring the number of displaced fringes, the thermal expansion of the optical system can be determined as a function of temperature. Additionally, substituting the observed temperature variation into the equation for linear thermal expansion enables the estimation of the initial physical dimensions of the optical system at the reference temperature.

$$\Delta d = d_0\ \alpha\ \Delta\theta \tag{8.2}$$

where d_0 is the initial length of the light coupling unit, α is the coefficient of linear thermal expansion for the plastic material, and $\Delta\theta$ represents the temperature change. For these calculations, the laser wavelength (λ) is assumed to be 850 nm, the refractive index of the light coupling unit (n) is taken as 1.63 [100] for ULTEM [96], and the coefficient of linear thermal expansion for the light coupling unit (α) is assumed to be $55.8{\times}10^{-6}$ $(1/^{\circ}C)$[101]. The calculated thermal expansion and initial dimensions of the interference-based optical system within the plastic enclosure for four VTRx+ modules are summarized in Table 8.10. Detailed calculations for Module 1 are provided in Appendix Y.

Table 8.10: Initial dimensions of the interference-based optical system within the light coupling unit for four modules, calculated based on fringe shifts and thermal expansion analysis.

Module	θ_0 $(^{\circ}C)$	θ_1 $(^{\circ}C)$	m	OPL (μm)	Initial length (mm)
Module 1, ↘	18.3	-23.6	12	3.13	1.338
Module 1, ↗	18	-23.4	12	3.13	1.354
Module 2, ↘	19.2	-22.2	15	3.91	1.693
Module 2, ↗	18.1	-21.6	15	3.91	1.766
Module 3, ↘	18.4	-22.2	14	3.65	1.611
Module 3, ↗	18	-21.9	14	3.65	1.640
Module 4, ↘	18.4	-22	13	3.39	1.504
Module 4, ↗	18.5	-22.3	13	3.39	1.489

↘ : Ramp down.
↗ : Ramp up.

In another experiment, the effect of fiber optics on optical power as a function of temperature was investigated. In this test, an MT loopback was used in the burn-in setup. The transmitter and receiver were both SFP modules, with a segment of fiber optic cable (approximately 1.3 m) placed inside the burn-in setup and subjected to thermal cycling, while the transceivers remained outside the burn-in setup in a cleanroom environment. The results for four fiber optic cables used in the VTRx+ optical power versus temperature measurement are shown in Figure 8.21. The x-axis represents the temperature measured by the burn-in setup sensor, which was attached to the carrier frame. The results indicate periodic fluctuations of approximately $\pm 50 \mu W$ (0.39 dBm) in the received optical power for channels 1 and 3, occurring every $20°C$. For channels 2 and 4, a smaller variation of about $\pm 15 \mu W$ (0.25 dBm) was observed. Additionally, hysteresis was present in all plots. While these results confirm that temperature variations affect optical power in the fiber optic cable, which explains the low-frequency fluctuations observed in received optical power and RSSI versus temperature, the magnitude of these fluctuations is not as significant as those observed when the VTRx+ was subjected to thermal cycling. One possible explanation for these optical power changes is the movement of the light coupling units above the VCSEL transmitter laser [96]. An average change in optical power of approximately 160 μW (0.6 dBm) was observed across a temperature range of $20°C$ to $-30°C$, with 50 μW (0.39 dBm) attributed to the thermal impact on the fiber optic cable.

8.5 Transient response of VTRx+ after power-on

In this test, three modules were placed in the burn-in setup while powered off. The temperature was then set to -30°C, and the received optical power was measured every 22.6 ms. Afterward, the modules were powered on.

In Figure 8.22 (left), the results are shown for 600 s, while the right plot provides a zoomed-in view of the first 100 s, with a moving average (computed over 100 points) displayed in red for the three modules. These plots indicate that it takes approximately 80 to 100 s for the optical power to stabilize. For module 3 (green), a significant fluctuation between two distinct values, with a difference of $70 \mu W$ (0.4 dBm) in optical power, is observed between 200 s and 400 s before eventually stabilizing after 600 s.

At first glance, the oscillations in the plots suggest that the source of fringe interference is located near the laser transmitter, which serves as the primary heat source. Given the fact that the interferometric fringes in the VTRx+ optical system shift approximately every 3°C, we calculated the final temperature around

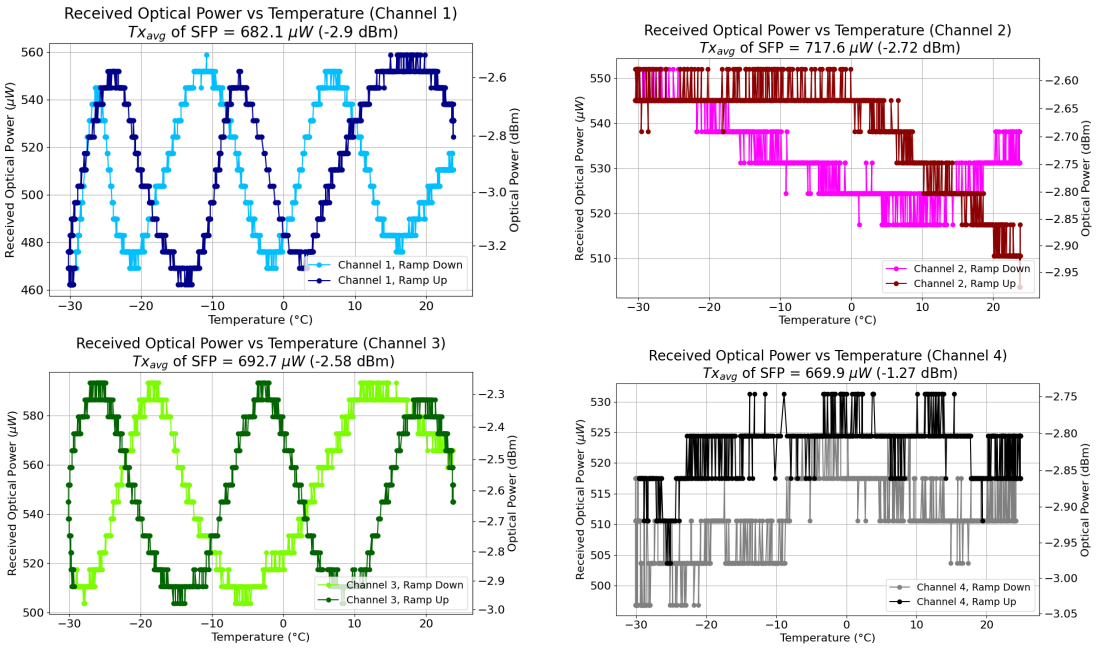

Figure 8.21: Received optical power as a function of temperature for three channels with the fiber optics in a loopback configuration. An SFP module was used as both the transmitter and receiver.

the VCSEL laser. For this calculation, the initial temperature was assumed to be -25°C, based on the observed offset between the burn-in setup sensor temperature and the embedded 2S module sensor temperature. For each half-period (maximum or minimum), a 1.5°C temperature increase was considered from the first observed minimum of the optical power versus temperature. The temperature plot as a function of time for different modules, along with the Exponential Decay 8.3 fit (Equation 8.3), is shown in Figure 8.23.

$$T(t) = Ae^{-t/\tau} + T_0 \tag{8.3}$$

The fitted parameters of the function (Equation 8.3), along with their averages for modules 1, 3, and 4, are listed in Table 8.11.

The fitted parameters are consistent and according to the average values, and the final temperature ($t \to \infty$) will reach to $-7.2°C$ and the average time constant obtained 22.4 s.

In this section, the temperature of the VTRx+ was measured by a novel and indirect method and around 16 $°C$ increment temperature in compare to the operational temperature was calculated.

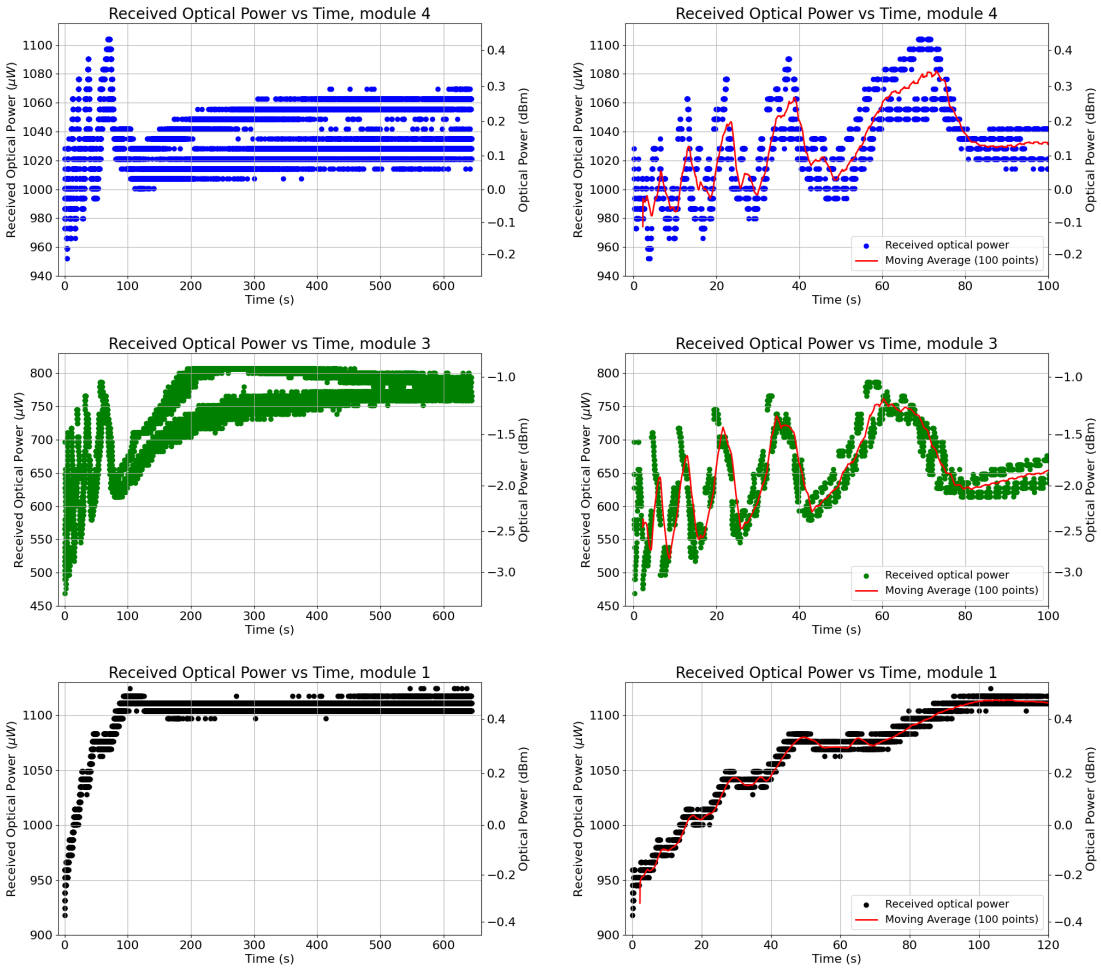

Figure 8.22: Received optical power as a function of time for three modules measured after powering on at -30°C for approximately 600 s (left). The right plot provides a zoomed-in view of the first 100 s with a moving average.

Table 8.11: Exponential decay fit parameters for different modules, including average values.

Module	A ($^\circ C$)	τ (s)	T_0 ($^\circ C$)
Module 1	-16.305	18.249	-7.359
Module 3	-17.061	23.552	-7.027
Module 4	-17.152	25.538	-7.240
Average	-16.839	22.446	-7.209

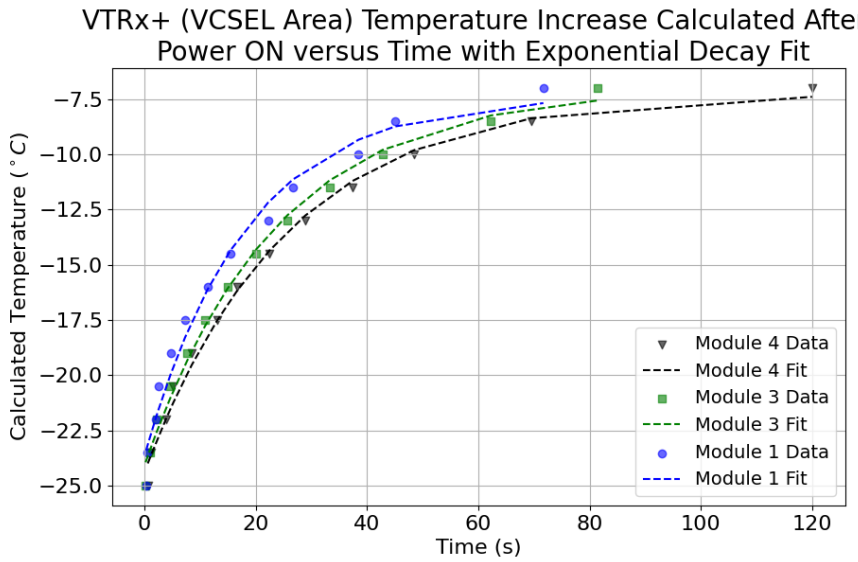

Figure 8.23: Calculated temperature of the VTRx+ as a function of time after power-on for modules 1, 3, and 4.

8.6 Bit error rate vs. optical power

Another application of the DDMI that I developed is the investigation of the safe margin for optical power. One key parameter in this context is the BER, which quantifies the number of incorrectly received bits relative to the total number of transmitted bits. BER becomes particularly critical as optical power decreases. In standard communication protocols, the BER is required to remain below 10^{-12} to ensure reliable data transmission. By analyzing the relationship between BER and optical power, we can determine the optical power threshold at which the system's performance significantly degrades.

The lpGBT uplink (10.24 Gbps) frame includes a Forward Error Correction (FEC) frame of either 20 or 48 bits[42]. In this study, the BER is defined as the ratio of the number of FEC frames containing at least one bit error to the total number of bits transmitted over a communication link, as given in Equation 8.4:

$$BER = \frac{\text{number of frames with at least one bit error}}{\text{total number of bits transmitted}} \tag{8.4}$$

For this setup, an optical attenuator (coupled to a stepper motor) was placed in series along the fiber, between the VTRx+ (transmitter) and the SFP (receiver). At each step, the average optical power was measured over 100 data points, with the statistical standard deviation chosen as the error. The BER was then measured (implemented in ph2acf using a PRBS7 sequence generated as a built-in test

pattern of the lpGBT[1]) for the transmission of approximately 1.2×10^{12} bits. This test was repeated at two different temperatures, 20°C and -30°C, for modules 1, 3, and 4. The rate of frames with at least one bit error as a function of average received optical power is shown in Figures 8.24, 8.25, and 8.26 for modules 1, 3, and 4, respectively, on a logarithmic scale. In general, as the received optical power decreases, the BER increases, demonstrating the expected deterioration in signal quality at lower optical power levels.

For module 1 (Figure 8.24), a non-zero BER at -30°C (blue) starts at 43.7 μW (-13.6 dBm), which is at a higher optical power compared to the BER at 20°C (red). It increases smoothly until reaching 30 μW (-45.2 dBm), at which point both plots at the two temperatures exhibit the same behavior, increasing exponentially as optical power decreases. Communication loss occurs at approximately 22 μW (-16.5 dBm) for -30°C, while for 20°C, it occurs at approximately 16.5 μW (-17.8 dBm).

For module 3 (Figure 8.25), the non-zero BER at -30°C (blue) is approximately two orders of magnitude lower than at the same optical power level at 20°C (red). For this module, the BER at 20°C (red) starts at 23 μW (-16.4 dBm), with communication loss occurring at 19.6 μW (-17 dBm). At -30°C (blue), the BER starts at 21 μW (-16.8 dBm), and communication loss occurs at 18 μW (-17.4 dBm).

For module 4 (Figure 8.26), similar to module 1, the non-zero BER at -30°C (blue) starts at a higher optical power (28 μW, -15.5 dBm) compared to 20°C (red). It increases slightly until reaching approximately 20 μW (-17 dBm), then rises significantly until communication loss occurs at 14.5 μW (-18.4 dBm). At lower optical power levels, the BER at -30°C (blue) is approximately two orders of magnitude lower than at 20°C (red). The BER at 20°C (red) starts at approximately 24 μW (-16.2 dBm) and increases until communication loss occurs at 13.5 μW (-18.7 dBm).

Overall, errors begin to appear at an optical power of approximately 30 μW (-15.2 dBm), while communication loss occurs at around 18 μW (-17.5 dBm). The summary of the BER versus optical power results is provided in Table 8.12, including the average transmitted optical power from the VTRx+, which indicates a significant range between the transmitted optical power and the lowest measurable BER. Such a broad range is highly desirable, as it ensures reliable data transmission and tolerance against power fluctuations.

[1]The PRBS generator is located in the front-end (eLink of LpGBT), while the PRBS checker is in the back-end (FC7)

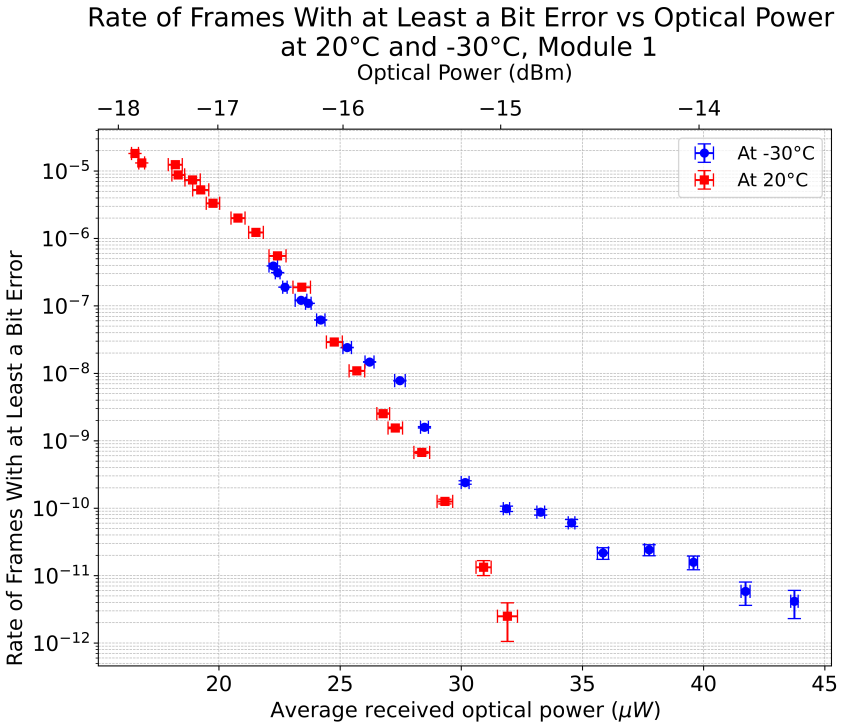

Figure 8.24: BER as a function of received optical power for module 1 at two different temperatures.

Table 8.12: Summary of BER versus optical power results, including the optical power at the error threshold, the minimum optical power before connection loss, and the average transmitted optical power of the VTRx+ at 20°C and -30°C.

Module	Error occurrence threshold μW (dBm)	Communication Lost μW (dBm)	$Tx_{avg.}$ μW (dBm)
Module 1 at 20°C	32 (-15)	16.5 (-17.8)	1350 (1.3)
Module 1 at -30°C	43.7 (-13.6)	22.2 (-16.5)	1100 (0.4)
Module 3 at 20°C	23 (-16.4)	19.6 (-17)	1100 (0.4)
Module 3 at -30°C	21 (-16.8)	18 (-17.4)	700 (-1.5)
Module 4 at 20°C	23.8 (-16.2)	13.5 (-18.7)	1200 (0.8)
Module 4 at -30°C	28 (-15.5)	14.5 (-18.4)	1000 (0)

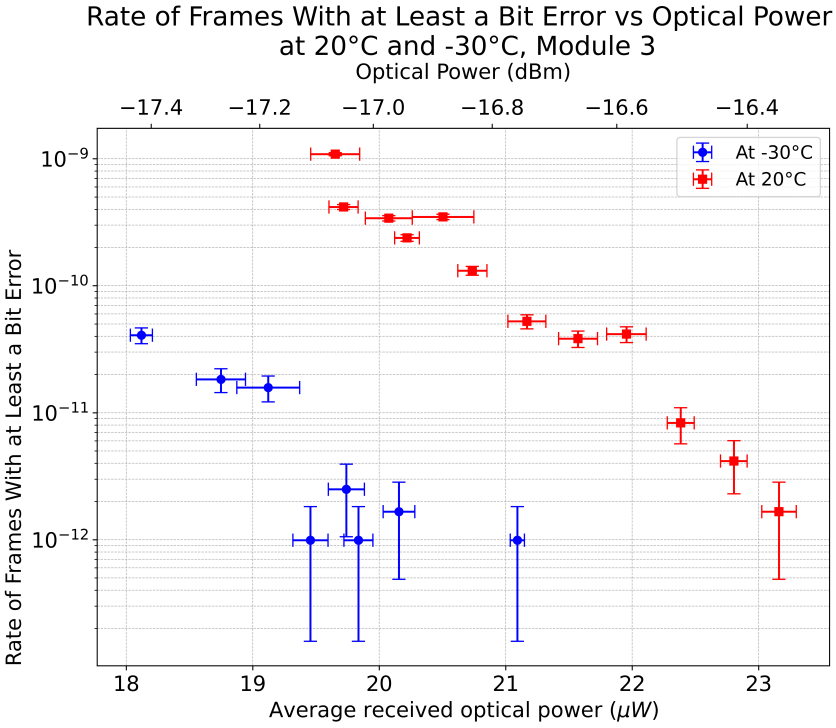

Figure 8.25: BER as a function of received optical power for module 3 at two different temperatures.

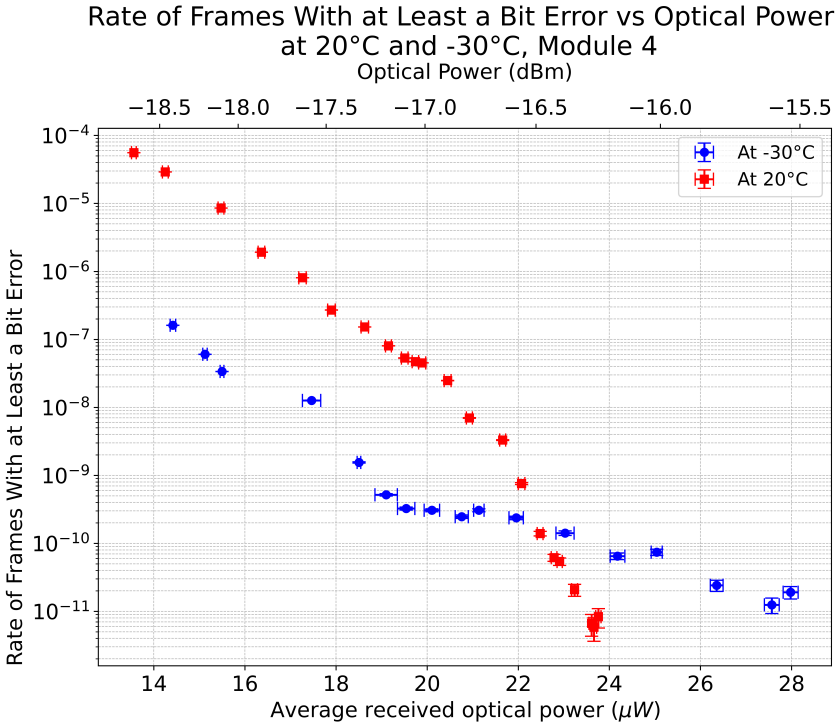

Figure 8.26: BER as a function of received optical power for module 4 at two different temperatures.

8.7 Calibration of RSSI output in test system

Additionally, after calibrating optical power as a function of the attenuator position in a loopback configuration, the attenuator was placed between the SFP (transmitter) and VTRx+ (receiver) for module 4. By reducing the optical power, the RSSI signal was monitored. The results of RSSI versus optical power are shown in Figure 8.27 with a fitted line. The relationship between RSSI and optical power was extracted and is given by the following equation:

$$\text{Optical Power}\,(\mu\text{W}) = 1.394 \times \text{RSSI}\,(\mu\text{A}) - 691.05 \tag{8.5}$$

By defining the responsivity as the ratio of the photodetector current to the optical input power which is important to characterize the photodiode, it was calculated to be 0.72 A/W for the VTRx+ mounted on Module 4 at -25 $°C$. The last RSSI signal value before communication loss was recorded as 508.5 μA, corresponding to an optical power of 19.5 μW (-17.1 dBm).

This section demonstrated the use of DDMI for RSSI calibration and VTRx+ responsivity measurement.

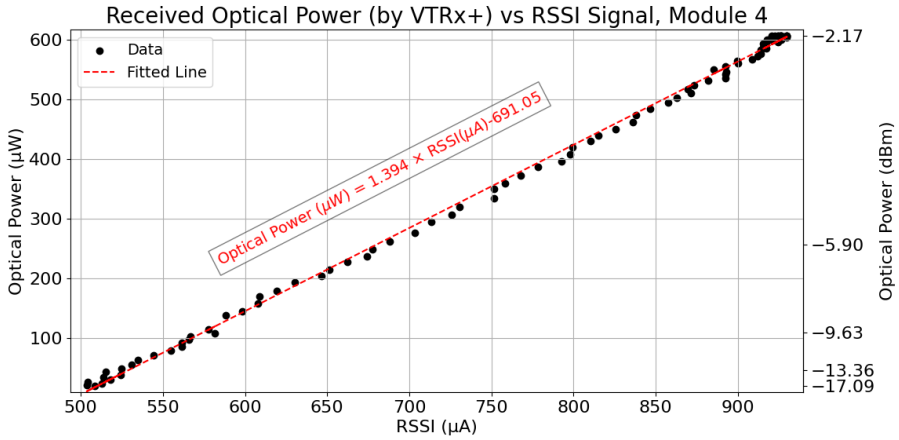

Figure 8.27: RSSI signal as a function of transmitted optical power for module 4 at -25°C.

8.8 Conclusion

In this chapter, the development of the DDMI for the uDTC and ph2acf was discussed. The system architecture was outlined, followed by a description of the validation setup used to ensure the reliability of implementation to the system.

The relationship between received optical power and temperature was investigated. On average, a change of approximately 160 μW (0.6 dBm) in optical power was observed with a temperature change from 20°C to -25°C, with 50 μW (0.39 dBm) attributable to thermal effects on the fiber optics. Modulation across the temperature range were observed, with a periodicity of 3 $°C$. This modulation seems related to the fringe shift in the interferometric pattern formed in the optical system of the light coupling unit.

The transient response of the VTRx+ after power-on was also examined and addressed to heat exchange of VCSEL, and stability achieved after 80 to 100 s depends on the VTRx+ module. Additionally, based on the fluctuations observed in the received optical power due to fringe shifts, the average final temperature of the light coupling unit, close to the VCSEL laser array, was calculated to be -7.2°C while the VTRx+ and 2S module were at their operating temperatures of -25 $°C$.

Furthermore, BER versus optical power was measured at 20°C and -25°C. Errors in data were observed for optical power levels below 30 μW (-15.5 dBm), with communication loss occurring around 18 μW (-17.5 dBm).

Additionally, the conversion coefficient of the RSSI signal to optical power was derived.

This work demonstrates the practical utility of DDMI as a tool for reliability assurance and health monitoring in optical communication systems, while offering insights into the environmental factors affecting optical power transmission.

My contributions in this chapter are as follows:

- I developed the DDMI block in VHDL and integrated it into the DAQ system firmware.
- I implemented the supporting C++ software to enable communication and data readout via IPbus.
- I measured the received optical power as a function of temperature and analyzed its fluctuations.
- I characterized the transient response in the transmitted optical power of the VTRx+.
- I investigated Bit Error Rate (using a plugin developed by collaborators) as a function of optical power.
- I calibrated the RSSI response (plugin developed by collaborators) against optical power.
- I measured the responsivity of the VTRx+ photodiode, ensuring proper calibration of the optical monitoring system.

Chapter 9

Conclusion and Perspectives

The HL-LHC represents a significant step forward in high-energy physics experiments. This ambitious program requires improvements in detector technology, necessitating extensive upgrades. These upgrades are necessary to handle an increased pileup of up to 200 events (60 events at end of RUN 3) in the final luminosity plan, as well as to withstand high radiation levels, with total fluences equivalent to up to 3×10^{14} 1-MeV neutrons / cm^2 at the nearest distance from the beam where the 2S modules studied in this thesis will be placed.

The 2S modules considered in this thesis must be assembled and tested with highly precise and reliable assembly tools and procedures, in order to meet the required precision and contribute to the first trigger level (L1) of the new CMS detector. This requires precise assembly techniques and strict quality control of the components.

This thesis focuses on one of the main technological and methodological challenges in producing the 2S modules for the CMS Outer Tracker at IIHE and CMS. This work has made important contributions in four main areas:

The initial focus was on the mechanical assembly of 2S modules inside the cleanroom at IIHE. In order to measure the height of the glue dispensing robot head relative to the surface of the 2S module components to be glued, two non-contact methods were studied in detail: one based on optical sharpness analysis and the other using a triangular displacement laser sensor. The optical sharpness analysis method achieved a resolution of approximately 1 μm and a repeatability of 8 μm. It also offers more accurate positioning in the x and y directions. However, it has a number of limitations: a limited measurement range, the measurement time is order 50 seconds per height measurement, and the lens is very expensive ($\sim 4k$ *Euro*) due to its very specific features (long focal length, small depth of field). On the other hand, the displacement laser sensor demonstrated a precision of around 14 μm when measuring on the backside of the functional sensor detector. It supports a larger measurement range from 40 mm to 60 mm, offers a short

measurement time of 100 ms, and is relatively cost-effective. A dedicated readout system was designed and implemented to integrate the displacement laser sensor into the gluing robot.

Two of these displacement laser sensors (ZX2) were installed in the gluing machines and the production line relies on them. From July to September 2025, the IIHE successfully assembled about 200 of 2S modules without any reported issues related to the measurement of the height of the dispensing syringe.

Beyond tests at the assembly line, the 2S modules must demonstrate their performance under realistic operational conditions. To contribute to this demonstration, a beam test where four 2S module prototypes were exposed to an asynchronous high-energy muon beam was conducted by a collaboration of the CMS tracker community and the MUonE community. One of these prototypes, labelled 2S-18-5-BEL-00003, was made at the IIHE. This beam test, where only the stub data were read out, provided an interesting test bed to understand what kind of performance monitoring can be envisaged when using online stub data rather than offline data. However, due to the asynchonous nature of the beam, the phase between the beam trigger and the readout clock is different for each particle, which causes the signal sampling times to jitter. These conditions, planned for the MUonE experiment, are fundamentally different from the synchronous data taking conditions at the HL-LHC, for which the 2S modules have been designed. A muon detection efficiency higher than 96% was obtained when biasing the sensors at voltages higher than 400V and setting the signal comparator threshold in the range 4800-9500 electrons. The inefficiency was understood to be due to the trigger jitter. Yet, our results indicate that there should be margin in the detector settings for efficient operation in the future MUonE experiment. The rate of stubs due to noise was also studied from the off-track occupancy, defined as the occupancy of the module outside a window defined around the track reconstructed in the other 3 modules. At very low thresholds, high off-track occupancy was observed, indicating increased noise contributions and resulting in reduced efficiency in this signal threshold region. A correlation was identified between increased off-track occupancy and reduced stub-finding efficiency, particularly at low thresholds. Another feature studied is the parity of the size of the stub seed cluster, as a function of threshold. As the threshold decreases from 9500 to 4800 electrons, the fraction of two-strip seed clusters increases, indicating that the spatial resolution of the module improves. Decreasing the threshold further results in a decrease of the fraction of two-strip clusters, indicating that noise starts to contaminate the stubs and that the module parameters become suboptimal. The cluster parity thus provides rich information for an initial setting of the detector parameters with only online data, without having to reconstruct tracks.

At the time of thesis submission, the MUonE collaboration was organizing a

time-structured run in 2025, involving three stations composed of six 2S modules, seven of which were built at the IIHE. The findings of this study are anticipated to provide valuable input for both MUonE and CMS in optimizing their detector and DAQ systems.

In a context that is somewhat broader than the construction of 2S modules, a Digital Diagnostic Monitoring Interface (DDMI) was developed for diagnosing and testing the optical transceivers in the system test, as well as for evaluating the reliability of fiber-optic communication. After validating the integration of the DDMI into the DAQ of the 2S module test systems, based of the FC7 board, the relationship between received optical power and temperature was investigated. On average, a fluctuation of 160 μW (0.6 dBm) in received optical power was observed. This variation could result from several factors, such as thermal effects in the laser emitter or mechanical shifts due to thermal expansion in the light coupling unit. In addition, minor fluctuations in received optical power within each 3 °C temperature interval were attributed to fringe shifts in the interferometric pattern formed within the optical system of the light coupling unit. Using this method, the actual temperature of the VCSEL region was indirectly measured as approximately -7.2 °C, while the system was operating in an environment set to -25 °C. Furthermore, the transient time required to reach thermal equilibrium after powering on was found to be between 80 and 100 seconds. The DDMI was also used to measure the BER as a function of received optical power at two different temperatures: 20 °C and -25 °C. Bit errors began to appear when the optical power dropped below 30 μW (−17.5 dBm). Additionally, the responsivity of the PIN receiver in the VTRx+ module was measured as 0.72 A/W at a temperature of -25 °C. Overall, the DDMI proved to be a powerful tool for testing, quality control, and ensuring reliable operation of the optical readout chain. It also offers potential for future investigations into the effects of radiation on optical transceivers.

In conclusion, this thesis has presented a set of practical tools and validated procedures that contribute significantly to the overall readiness of the CMS Outer Tracker upgrade in the HL-LHC era. Through the development and demonstration of effective non-contact height measurement techniques for assembly robots, the integration of a digital diagnostic monitoring interface for optical transmitters, and the performance study of a 2S module in a beam test, this work prepares the way for the large-scale construction and integration of 2S modules as the HL-LHC program progresses toward implementation.

List of Presentations

Below is a list of conference presentations and contributions I gave during my PhD studies:

1. **"Study of Fundamental Characteristics of a 2S Module in a Particle Beam Using 40 MHz Stub Data,"** A. Khalilzadeh, P. Vanlaer, M. Delcourt, *Belgian Physical Society General Scientific Meeting 2025*, Louvain-la-Neuve.

2. **"Module Quality Assurance for the CMS Outer Tracker Phase-2 Upgrade,"** A. Khalilzadeh, P. Vanlaer, M. Delcourt on behalf of the CMS Tracker Detector group, *TWEPP 2024*, Glasgow.

3. **"Characterization of Basic Properties of a 2S Module in a Particle Beam Using 40 MHz Stub Data,"** M. Delcourt, A. Khalilzadeh, P. Vanlaer on behalf of the CMS Tracker Detector group and MUonE collaboration, *CMS Upgrade Days at CERN 2023*, Geneva.

4. Manuscript in preparation:**"A versatile software for the new CMS tracker module qualification for the LHC High Luminosity upgrade,"** CMS Collaboration, targeting JINST, Reference: CMS PAPER dinardo-003 (with contributions to the DAQ system test).

Appendix A

Calculation of Initial Length Based on Fringe Shift and Thermal Expansion

Displacement Calculation

The optical path difference resulting in a fringe shift in an interferometric setup is given by:

$$m\lambda = 2n\Delta d \tag{A.1}$$

where:

- $m = 12$: observed fringe shift for Module 1 during a temperature change,
- $\lambda = 850\,\text{nm}$: wavelength of the VTRx+ laser,
- $n = 1.63$: refractive index of the ULTEM plastic.

Solving for the displacement Δd:

$$\Delta d = \frac{m\lambda}{2n} \tag{A.2}$$

Substituting the known values:

$$\Delta d = \frac{12 \times 850 \times 10^{-9}}{2 \times 1.63} \tag{A.3}$$

$$\Delta d = \frac{10.2 \times 10^{-6}}{3.26} = 3.13 \times 10^{-6}\,\text{m} = 3.13\,\mu\text{m} \tag{A.4}$$

Thermal Expansion Calculation

The linear thermal expansion of a material is given by:

$$\Delta d = d_0 \alpha \Delta\theta \tag{A.5}$$

where:

- $\alpha = 55.8 \times 10^{-6}\,^{\circ}\mathrm{C}^{-1}$: linear thermal expansion coefficient of the material,
- $T_0 = 18.3^{\circ}\mathrm{C}$: initial temperature,
- $T_1 = -23.6^{\circ}\mathrm{C}$: final temperature,
- $\Delta\theta = T_1 - T_0 = -23.6 - 18.3 = -41.9^{\circ}\mathrm{C}$.

Rearranging to solve for the initial length d_0:

$$d_0 = \frac{\Delta d}{\alpha \Delta\theta} \tag{A.6}$$

Substituting the values:

$$d_0 = \frac{3.13 \times 10^{-6}}{(55.8 \times 10^{-6}) \times (-41.9)} \tag{A.7}$$

$$d_0 = \frac{3.13}{55.8 \times 41.9} \tag{A.8}$$

$$d_0 = \frac{3.13}{2338.02} = 1.338\,\mathrm{mm} \tag{A.9}$$

Thus, the calculated initial length of Module 1 is approximately 1.338 mm.

References

[1] G Abbiendi. Status of the MUonE experiment. *Physica Scripta*, 97(5):054007, Apr 2022.

[2] Lyndon Evans and Philip Bryant. LHC Machine. *Journal of Instrumentation*, 3(08):S08001, Aug 2008.

[3] The CMS Collaboration. The Phase-2 Upgrade of the CMS Tracker, 2017. CERN-LHCC-2017-009, CMS-TDR-014.

[4] The CMS collaboration. Development of the CMS detector for the CERN LHC Run 3. *Journal of Instrumentation*, 19(05):P05064, May 2024.

[5] CMS Collaboration. Public CMS Luminosity Information. `https://twiki.cern.ch/twiki/bin/view/CMSPublic/LumiPublicResults#Full_summary_proton_proton_colli`, 2025. Accessed: 29 June 2025.

[6] Fabienne Landua. The CERN accelerator complex layout in 2022. Complexe des accélérateurs du CERN en janvier 2022. 2022. General Photo.

[7] Tai Sakuma. Cutaway diagrams of CMS detector. 2019. `https://cds.cern.ch/record/2665537`.

[8] *The CMS magnet project: Technical Design Report*. Technical design report. CMS. CERN, Geneva, 1997. CERN-LHCC-97-010 ; CMS-TDR-1.

[9] The CMS Collaboration. The CMS Phase-1 pixel detector upgrade. *Journal of Instrumentation*, 16(02):P02027, Feb 2021.

[10] N. Demaria. Status of CMS silicon strip tracker. *Nuclear Physics B - Proceedings Supplements*, 125:198–205, 2003. Innovative Particle and Radiation Detectors.

[11] J. Fernandez. The CMS silicon strip tracker. *Nuclear Instruments and Methods in Physics Research Section A: Accelerators, Spectrometers, Detectors*

and Associated Equipment, 573(1):257–259, 2007. Proceedings of the 7th International Conference on Position-Sensitive Detectors.

[12] Paolo Azzurri. The CMS Silicon Strip Tracker. *Journal of Physics: Conference Series*, 41(1):127, May 2006.

[13] CMS Collaboration. CMS Silicon Strip Tracker Performance Results with 2024 Data, 2025. CMS Performance Note,CMS DP -2025/020.

[14] CMS Collaboration. CMS Strip Tracker Offline Performance Plots 2024. `https://twiki.cern.ch/twiki/bin/view/CMSPublic/StripsOfflinePlots2024`, 2024. accessed 2025-07-07.

[15] Suvankar Roy Chowdhury on behalf of the CMS Collaboration. Performance of the CMS Silicon Strip Tracker. `https://journals.jps.jp/doi/abs/10.7566/JPSCP.42.011006`, 2023.

[16] The CMS Collaboration. Performance of the CMS electromagnetic calorimeter in pp collisions at $\sqrt{s}$ = 13 TeV. *JINST*, 19:P09004, 2024. CMS-EGM-18-002, CERN-EP-2024-014, CMS-EGM-18-002-003.

[17] Andrea Benaglia. The CMS ECAL performance with examples, 2014. CMS-CR-2013-430.

[18] The CMS collaboration. The CMS trigger system. *Journal of Instrumentation*, 12(01):P01020, Jan 2017.

[19] CERN. LHC/HL-LHC Plan. `https://hilumilhc.web.cern.ch/content/hl-lhc-project`, 1 2025. Accessed on 10 May 2025.

[20] CERN. High-Luminosity LHC. `https://home.cern/resources/faqs/high-luminosity-lhc`, 2023. Accessed: 2025-07-11.

[21] Highlights of the HL-LHC physics projections by ATLAS and CMS, 2025. ATL-PHYS-PUB-2025-018 CMS-HIG-25-002.

[22] Burkhard Schmidt. The High-Luminosity upgrade of the LHC: Physics and Technology Challenges for the Accelerator and the Experiments. *Journal of Physics: Conference Series*, 706(2):022002, Apr 2016.

[23] Giacomo Sguazzoni. The CMS Pixel Detector for the High Luminosity LHC, 2024. CMS-CR-2022-276.

[24] The Phase-2 Upgrade of the CMS Level-1 Trigger, 2020. CERN-LHCC-2020-004, CMS-TDR-021.

[25] Fabio Cossutti. Precision Timing with the CMS MIP Timing Detector for High-Luminosity LHC, 2024. CMS-CR-2024-219.

[26] Bora Akgun. An overview of the CMS High Granularity Calorimeter, 2024. CMS-CR-2024-307.

[27] Ka Wa Ho. The CMS ECAL upgrade for the High-Luminosity LHC era, 2023. CMS-CR-2023-181.

[28] Moritz Oliver Wiehe. The CMS High Granularity Calorimeter for the High Luminosity LHC, 2022. CMS-CR-2022-047.

[29] Antonello Pellecchia and on behalf of the CMS Muon group. The upgrade of the CMS muon system for the high luminosity LHC. *Journal of Instrumentation*, 19(02):C02077, Feb 2024.

[30] The Phase-2 Upgrade of the CMS Muon Detectors, 2017. CERN-LHCC-2017-012, CMS-TDR-016.

[31] Jeroen Guido Hegeman. The CMS Data Acquisition System for the Phase-2 Upgrade, 2018. CMS-CR-2018-099.

[32] W. Adam and et al. Experimental study of different silicon sensor options for the upgrade of the CMS Outer Tracker. *Journal of Instrumentation*, 15(04):P04017, Apr 2020.

[33] S. Navas and et al. Review of Particle Physics. *Phys. Rev. D*, 110:030001, Aug 2024.

[34] M Huhtinen and F Faccio. Computational method to estimate Single Event Upset rates in an accelerator environment. *Nuclear Instruments and Methods in Physics Research Section A: Accelerators, Spectrometers, Detectors and Associated Equipment*, 450(1):155–172, 2000.

[35] W. Shockley and W. T. Read. Statistics of the Recombinations of Holes and Electrons. *Phys. Rev.*, 87:835–842, Sep 1952.

[36] W. Shockley. Currents to conductors induced by a moving point charge. *J. Appl. Phys.*, 9(10):635–636, 1938.

[37] S. Ramo. Currents Induced by Electron Motion. *Proceedings of the IRE*, 27(9):584–585, 1939.

[38] The Tracker group of the CMS collaboration and et al. Selection of the silicon sensor thickness for the Phase-2 upgrade of the CMS Outer Tracker. *Journal of Instrumentation*, 16(11):P11028, Nov 2021.

[39] Frank Hartmann. *Evolution of Silicon Sensor Technology in Particle Physics: Basics and Applications*, volume 3 of *Springer Tracts in Modern Physics*. Springer Cham, 3 edition, 2024.

[40] Mark Prydderch. *CBC3.1 User Manual*. Science & Technology Facilities Council Technology, July 2019.

[41] G. Bergamin, L. Caponetto, A. Caratelli, D. Ceresa, G. Galbit, S. Jain, K. Kloukinas, B. Nodari, S. Scarfi, and S. Viret. CIC2/2.1 Technical Specification. `https://cern.sharepoint.com/sites/Tracker-Upgrade/Electronics/CIC/Shared%20Documents/Specifications/CIC2_specs_v1p4.pdf`, 2022.

[42] Paulo Moreira and et al. lpGBT documentation: release. `https://cds.cern.ch/record/2809058`, 2022.

[43] Jan Troska, Alexander Brandon-Bravo, Stephane Detraz, Andrea Kraxner, Lauri Olanterä, Carmelo Scarcella, Christophe Sigaud, Csaba Soos, and Francois Vasey. The VTRx+, an optical link module for data transmission at HL-LHC. *PoS*, TWEPP-17:048, 2017.

[44] A. Honma, A. La Rosa, and A. Mussgiller. Draft 2S Module Specifications, June 2022. Internal CMS Documentation; Institutions: Brown University, CERN, DESY, EDMS NO. 2642509 v.3.

[45] Buchanan and et al. Assessment of Two Advanced Aluminium-Based Metal Matrix Composites for Application to High Energy Physics Detectors. *Materials*, 16(1), 2023.

[46] DuPont Electronics & Industrial. Kapton®MT Polyimide Film — Technical Data Sheet. `https://www.dupont.com/content/dam/electronics/amer/us/en/electronics/public/documents/en/EI-10144-Kapton-MT-Data-Sheet.pdf`, 2023. Accessed: 2025-01-16.

[47] CMS Module Working Group. 2S Module Assembly Procedure, October 2021. Internal CMS Documentation, EDMS NO. 2642512 v.1.

[48] Keithley Instruments. *Keithley 6517A Electrometer/High Resistance Meter Datasheet*, 2005. Document Number: 6517A-900-01 Rev. D.

[49] U. Heintz, A. Dierlamm, O. Pooth, and A. Mussgiller. QC Document for Preproduction and Production Modules (v4), May 2025. Accessed on 11 June 2025.

[50] CERN Tracker Group. Long Bridge: Dimensional and Flatness Specifications for 2S Module Assembly. https://edms.cern.ch/document/1978714/AE, 2020. Accessed: 2025-06-01.

[51] CERN Tracker Group. Short Bridge: Dimensional and Flatness Specifications for 2S Module Assembly. https://edms.cern.ch/document/1762094/AG, 2023. Accessed: 2025-06-01.

[52] Accelonix / Hesse GmbH. Bondjet BJ820 Fine Wire Wedge Bonder. Brochure, September 2016. Available at: https://accelonix.nl/wp-content/uploads/bros-mk-bondjet-bj820-en-20160901.pdf (accessed 2025-01-16).

[53] Dow Inc. SYLGARD™ 186 Silicone Elastomer Technical Data Sheet. https://www.dow.com/en-us/document-viewer.html?randomVar=3158061458582113620&docPath=/content/dam/dcc/documents/11/11-1253-sylgard-186-silicone-elastomer.pdf, 2025. Document ID: 11-1253.

[54] Polytec PT GmbH. Polytec TC 437 Thermally Conductive Adhesive Technical Data Sheet. https://www.polytecstore.fr/polytec_images/documents/FT_PT/tc/polytec-tc-437_engl.pdf, 2017. Version 1/2017.

[55] Arjun Chaliyath. High Precision Automated Metrology of the 2S Modules for the CMS Phase-II Tracker Upgrade. Poster presentation at BPS2025: Belgian Physical Society General Scientific Meeting, May 2025. Louvain-la-Neuve, Belgium.

[56] Royce Instruments. Royce 650 Universal Bond Tester. https://accelonix.nl/product/micro-electronics/bond-testing/multitest-bond-tester-kopie/, 2025.

[57] Stefan Maier and Roland Koppenhöfer. *OT Module Test Bench and Readout GUI (GIPHT)*. Karlsruhe Institute of Technology, Karlsruhe, Germany, v4.0 edition, November 2024. Accessed: 2025-06-01.

[58] Rohde & Schwarz GmbH & Co. KG. R&S® HMP4000 Power Supply Series. https://www.rohde-schwarz.com/nl/products/test-and-measurement/dc-power-supplies/rs-hmp4000-power-supply-series_63493-47360.html, 2025.

[59] Keithley Instruments. Models 2410 and 2410-C SourceMeter® Specifications. https://www.tek.com/en/documents/specification/models-2410-and-2410-c-sourcemeter-specifications, 2025.

[60] Nicolas Maximilian Rowert. *Assembly and Characterization of a First Functional 2S Module for the CMS Phase-2 Upgrade at LHC*. PhD thesis, RWTH Aachen University, 2018. CERN-THESIS-2018-400.

[61] Christian Käseberg. Doppelseitige Vermessung von 2S-Modulen für das Upgrade des CMS-Spurdetektors. Master's thesis, Aachen, Germany, Jul 2017.

[62] The Imaging Source Europe GmbH. DFK 33UX264 Technical Reference Manual. `https://s1-dl.theimagingsource.com/api/2.5/packages/documentation/manual-trm/trmdfk33ux264/2edd95c0-09c5-5d98-baa9-05796b0d6248/trmdfk33ux264.en_US.pdf`, 2025. Version 1.3, April 10, 2025.

[63] Lensation GmbH. TC5M-30-65C Object-Side Telecentric Lens Technical Data Sheet. `https://www.lensation.de/pdf/TC5M-30-65C.pdf`, 2020. Version 1.0, August 2020. Accessed: 2025-06-01.

[64] OWIS GmbH. LTM-80-75-HSM Precision Linear Stage Technical Data Sheet. `https://www.owis.eu/produkte/artikel/LTM-80-75-HSM`, 2025. Order Number: 41.083.75AD.

[65] OWIS GmbH. HVM-60N-12-HiSM Elevator Stage Technical Data Sheet. `https://www.owis.eu/en/products/article/HVM-60N-12-HiSM/0`, 2025. Order Number: 42.A60.12AW.

[66] Jason P. de Villiers. A comparison of image sharpness metrics and real-time sharpening methods with GPU implementations. In James E. Gain and Patrick C. Marais, editors, *Proceedings of the 7th International Conference on Computer Graphics, Virtual Reality, Visualisation and Interaction in Africa, Afrigraph 2010, Franschhoek, South Africa, June 21-23, 2010*, pages 53–62. ACM, 2010.

[67] Schut Gauge. *Schut Gauge Blocks*, 2024. S.N.: 15067.

[68] OMRON. *Smart Sensor Laser Sensor with Built-in Amplifier ZX1*, 4 2024.

[69] Primož Poredoš, Klemen Povsic, Boštjan Novak, and Matija Jezeršek. Three-Dimensional Measurements of Bodies in Motion Based on Multiple- Laser-Plane Triangulation. *Revista Tecnica de la Facultad de Ingenieria Universidad del Zulia*, 38:53–61, 01 2015.

[70] OMRON. *Smart Sensors Laser Sensors CMOS Type ZX2*, 4 2024.

[71] G. Abbiendi and et al. Measuring the leading hadronic contribution to the muon G-2 via μe scattering. *The European Physical Journal C*, 77(3), 2017.

[72] Johannes Bernhard et al. Studies for New Experiments at the CERN M2 Beamline within "Physics Beyond Colliders": AMBER/COMPASS++, NA64μ, MuonE. *AIP Conf. Proc.*, 2249(1):030035, 2020. CERN-PBC-Notes-2021-009.

[73] Johannes BERNHARD, Dipanwita BANNERJEE, and Lau GATIGNON. Review of the M2 beam at CERN, Feb 2018.

[74] Paolo Prosperi and Guido Magazzu. The DAQPATH readout system of the Serenity boards for the CMS Phase-II Upgrade, 2022. CMS-CR-2022-112.

[75] Andrew Rose. Serenity - An ATCA prototyping platform for CMS Phase-2, 2019. CMS-CR-2018-327.

[76] Martin Delcourt. Commissioning and Study of a CMS 2S Module with 40 MHz Readout. In *Proceedings of the 12th Beam Telescope and Test Beam Workshop*, Edinburgh, UK, Apr 2024.

[77] Martin Delcourt. CMS/MUonE Beam test analysis (Discussion on timing). `https://indico.cern.ch/event/1281484/contributions/5383582/attachments/2638146/4564727/230427_Timing_discussion_muone.pdf`, 2023. Presentation at CERN, April 28, 2023.

[78] O. Groettvik and on behalf of the ALICE collaboration. Installation, integration and first operating experiences of the ALICE ITS upgraded readout system. *Journal of Instrumentation*, 17(04):C04003, Apr 2022.

[79] SFF Committee. SFF-8472 Specification for Diagnostic Monitoring Interface for Optical Transceivers, 2019. Version 12.3.

[80] Small Form Factor Committee. SFF-8431 Specifications for Enhanced Small Form Factor Pluggable Module SFP+, Jul 2013.

[81] L Amaral, S Dris, A Gerardin, T Huffman, C Issever, A J Pacheco, M Jones, S Kwan, S C Lee, Z Liang, T Liu, Z Meng, A Prosser, S Padadopoulos, I Papakonstanstinou, C Sigaud, S Silva, C Soos, P Stejskal, J Troska, F Vasey, P Vichoudis, T Weidberg, A Xiang, and J Ye. The versatile link, a common project for super-LHC. *Journal of Instrumentation*, 4(12):P12003, Dec 2009.

[82] Simao Machado Jeremy Blanc. Versatile Link Plus Terminated Cords and Cables Specifications. `https://edms.cern.ch/document/2045621/1`, July 2019. EDMS NO. 2045621.

[83] Alan Prosser. Versatile Link Plus Technical Specification, part 1 SYSTEM. https://edms.cern.ch/document/1719328/1, Aug 2019. EDMS NO. 1719328.

[84] J. Troska. Versatile Link Technical Specification, part 2.1.4. Transimpedance amplifier for use in versatile transceiver. https://edms.cern.ch/document/1141160/1, Jan 2012. EDMS NO. 1141160.

[85] FS.com. FSP-10GSR-85: 10GBASE-SR SFP+ Optical Transceiver, 2024. Accessed: 2024-09-19.

[86] Sheldon. What is Inside an SFP Module - Understanding TOSA, ROSA, BOSA. https://www.fs.com/blog/what-is-inside-an-sfp-module-understanding-tosa-rosa-bosa-12210.html, March 2024. Accessed: 2025-04-15.

[87] M. Pesaresi, M. Barros Marin, G. Hall, M. Hansen, G. Iles, A. Rose, F. Vasey, and P. Vichoudis. The FC7 AMC for generic DAQ & control applications in CMS. *JINST*, 10(03):C03036, 2015.

[88] Jarne Theo De Clercq. *The Upgraded Outer Tracker for the CMS Detector at the High Luminosity LHC, and Search for Composite Standard Model Dark Matter with CMS at the LHC*. PhD thesis, Vrije U., Brussels, 2019. CERN-THESIS-2019-278.

[89] Faster Technology. FMC Quad SFP/SFP+ Datasheet. https://www.fastertechnology.com/product/fmc-quad-sfp-sfp/, 2024. Accessed: 2024-09-19.

[90] Laurent Charles, Jarne De Clercq, Mykyta Haranko, Jelena Luetic, and Stefano Mersi. *d19c User's and Developer's Manual*, 2018. Version: March 4, 2018.

[91] C. Ghabrous Larrea, K. Harder, D. Newbold, D. Sankey, A. Rose, A. Thea, and T. Williams. IPbus: a flexible Ethernet-based control system for xTCA hardware. *Journal of Instrumentation*, 10(02):C02019, Feb 2015.

[92] Joseph Wu. *A Basic Guide to I2C*. Texas Instruments Incorporated, November 2022. Technical Document - Application Note.

[93] Pico Technology. *PicoScope 2206: 50 MHz USB Oscilloscope*, 2023. Accessed: 2025-02-20.

[94] FS.com. LC/UPC to LC/UPC Duplex OM3 Multimode Fiber Optic Patch Cable, 2024. Accessed: 2024-09-19.

[95] FS.com. LC UPC to LC UPC Duplex OM3 Multimode PVC (OFNR) 2.0mm Fiber Optic Patch Cable, 2024. Accessed: 2024-09-19.

[96] Csaba Soos. The Versatile Link+ Transceiver Story. `https://indico.cern.ch/event/1389968/`, October 2024. EP-ESE Electronics Seminar.

[97] Farah Z Jasim, Khalid Omar, Zainuriah Hassan, et al. Temperature effect on VCSEL output performance. *J. Optoelectron. Adv. Mater*, 3:1136–1138, 2009.

[98] Csaba Soos. Versatile Link+ Transceiver Production. Presentation at the Topical Workshop on Electronics for Particle Physics (TWEPP 2022), September 2022. Held in Bergen, Norway.

[99] Juan Arango, Victor Aristizabal, Francisco Vélez, Juan Carrasquilla, Jorge Gomez, Jairo Quijano, and Jorge Herrera-Ramirez. Synthetic dataset of speckle images for fiber optic temperature sensor. *Data in Brief*, 48:109134, 2023.

[100] Xiaoning Zhang, Jun Qiu, Junming Zhao, Xingcan Li, and Linhua Liu. Complex refractive indices measurements of polymers in infrared bands. *Journal of Quantitative Spectroscopy and Radiative Transfer*, 252:107063, 2020.

[101] Technical Products, Inc. Ultem 1000 Material Specifications, 2006. Accessed: 2025-04-25.